Numerical Modeling and Prediction of Irreversibilities in Sub- and Supercritical Turbulent Near-Wall Flows

Dem Fachbereich Maschinenbau
an der Technischen Universität Darmstadt
zur
Erlangung des Grades eines Doktor-Ingenieurs (Dr.-Ing.)
genehmigte

Dissertation

vorgelegt von

Dipl.-Ing. (FH) Florian Ries, M.Sc.

aus Schwetzingen, Deutschland

Berichterstatter:	Prof. Dr. rer. nat. Amsini Sadiki
Mitberichterstatter:	Prof. Dr.-Ing. Johannes Janicka
Mitberichterstatter:	Prof. Dr.-Ing. Markus Klein
Tag der Einreichung:	16.10.2018
Tag der mündlichen Prügung:	26.11.2018

Darmstadt 2018
D17

Ries, Florian
Numerical Modeling and Prediction of Irreversibilities in Sub- and Supercritical Turbulent Near-Wall Flows
Darmstadt, Technische Universität Darmstadt,
Jahr der Veröffentlichung der Dissertation auf TUprints: 2019
URN: urn:nbn:de:tuda-tuprints-91604
Tag der mündlichen Prüfung: 26.11.2018

Erklärung

Hiermit erkläre ich, dass ich die vorliegende Arbeit, abgesehen von den in ihr ausdrücklich genannten Hilfen, selbstständig verfasst habe.

Datum, Unterschrift

Acknowledgements

This PhD thesis was carried out during my work as doctoral candidate in the department of Energy and Power Plant Technology (EKT) at the Technische Universität Darmstadt. I would like to express my sincere gratitude to Prof. Dr.-Ing. Johannes Janicka, head of the department, for giving me the opportunity to work on an exciting PhD project, for providing computer resources and optimum working conditions. I also would like to thank my supervisor Prof. Dr. rer. nat. Amsini Sadiki for his excellent guidance, continuous interest in my research work and constant support during this time. His great interest, wealth of expertise and persistent enthusiasm were necessary to carry out this work.

I am sincerely grateful to Prof. Dr.-Ing. Markus Klein from the Universität der Bundeswehr München for accepting to be co-referent of my thesis work. I would also like to thank him for the time reviewing my thesis.

I would like to thank Prof. Dr. Wolfgang Kollmann for many fruitful and valuable discussions on all matters related to turbulence theory. I hope we can continue these discussions further at the EKT.

Special thanks to all friends and scientific co-workers at the departments EKT and RSM for their cooperation and companionship that have been invaluable in completing this work. In particular, I would like to thank Kaushal Nishad and Yongxiang Li for their friendship and the enormous help during this time. I am also indebted to Kaushal Nishad, Louis Dressler, Yongxiang Li, Adam Zietak and Carl-Philipp Ding for editing my thesis.

Furthermore, I want to thank my Bachelor and Master students Hossein Torkashvand, Judith Elin Vesper, Tim Arnold and Felix Kraft for their nice stay here and the great scientific outcome, which contributed a lot to this work.

A lot of thanks to my family, especially my dear wife Vanessa. This work would have not possible without her dedication, motivation, understanding and hard work for managing our son Ole. I am truthfully thankful to Vanessa for her love and enormous support during this time.

Darmstadt, October 2018
Florian Ries

For my wife Vanessa and my son Ole

Abstract

Most of heat transport and fluid flow occurring in nature and in technical applications are inherently turbulent. On closer inspection of turbulent flows, a wide range of length and time scales can be observed and it is obvious that these turbulent motions are unsteady, irregular and chaotic. Turbulent structures generally increase the disorder of the system resulting in a loss of available mechanical power, which can be expressed in terms of entropy production. This is the fundamental reason for irreversibilities in turbulent heat and fluid flows, and responsible for decreasing thermodynamic efficiency in many engineering devices. In spite of decades of research in the field of numerical simulations, it is still difficult to predict turbulent flows and causes of irreversibilities accurately. In this respect, large eddy simulations (LES) provide a promising approach, especially in dealing with turbulent flows with large scale, unsteady characteristics. Despite the great potential of LES, the extent of its usage for entropy generation analysis and thermodynamic optimization has been insignificant up to now. This can be mainly attributed to the high challenges in modeling of the unresolved irreversibilities in the subgrid.

The present work is focused on the development of a reliable LES framework combined with the second law of thermodynamics that allows to characterize and optimize sub- and supercritical wall-bounded flow applications. This is progressively accomplished in a series of development steps including (1) the development of reliable numerical treatments to simulate turbulent heat and fluid flow in the context of large eddy and direct numerical simulations (DNS), (2) the development of advanced, wall-adapting subgrid-scale models for momentum transport, heat transport and entropy production, and (3) the generation of comprehensive DNS databases that allow to evaluate the present LES framework under realistic flow situations with complex thermodynamic properties. In order to establish the validity of the present approach, the numerical methods and models are systematically assessed by comparison with experimental and DNS reference data. Finally, the proposed LES framework is utilized to characterize supercritical fuel injection processes and to optimize impingement cooling devices based on the concept of entropy generation minimization (EGM).

Important milestones towards LES as a reliable engineering tool for entropy generation analysis are achieved in this work. In particular, a new wall-adapting one-equation subgrid-scale model is proposed, which provides the correct asymptotic behavior in the near-wall region without using any ad-hoc or dynamic procedure. Regarding the subgrid-scale heat flux, a thermodynamically consistent heat flux model suitable for wall-bounded turbulent heat transport is proposed. Finally, using the inertial-convective subrange theory, appropriate closure terms for the subgrid-scale entropy generation related to friction loss and heat transport are derived. The developed LES framework is then used to characterize supercritical injection processes and to optimize impingement cooling. Based on entropy generation analysis, distinctive features of the disintegration process under supercritical conditions are described and optimal designs for impingement cooling devices are identified.

This work demonstrates, that LES combined with second law analysis is a very valuable and viable tool for predictive engineering and design optimization of complex heat and fluid flow applications.

Kurzfassung

Die meisten Strömungs- und Wärmetransportvorgänge in Natur und Technik sind turbulent. Bei genauerer Betrachtung solcher turbulenten Strömungen kann man ein breites Spektrum an instationären, unregelmäßigen und chaotischen Strukturen beobachten. Turbulente Strukturen erhöhen die Unordnung eines Strömungssystems, verbunden mit einem Verlust an verfügbarer mechanischer Energie. Dies kann durch Entropieproduktion beschrieben werden und ist die Hauptursache für Irreversibilitäten in turbulenten Strömungen, welche verantwortlich für thermodynamische Verluste in zahlreichen Ingenieursanwendungen sind. Trotz jahrzehntelanger Forschung auf dem Gebiet der numerischen Berechnungsverfahren bleibt es anspruchsvoll turbulente Strömungen und hierbei auftretende Irreversibilitäten akkurat vorherzusagen. Diesbezüglich bieten vor allem Grobstruktursimulationen (LES) einen vielversprechenden Ansatz zur Berechnung von instationären Strömungen mit großskaligen turbulenten Strukturen. Trotz des großen Potenzials von LES, findet diese Technik hinsichtlich Entropieproduktionsanalysen und thermodynamischer Optimierung kaum Anwendung, welche vor allem der komplizierten Feinstrukturmodellierung von Irreversibilitäten geschuldet ist.

Der Fokus der vorliegenden Arbeit liegt auf der Entwicklung einer verlässlichen LES Methode, die eine Charakterisierung und Optimierung basierend auf dem zweiten Hauptsatz der Thermodynamik von unter- und überkritischen Strömungsanwendungen erlaubt. Dies beinhaltet: (1) die Entwicklung geeigneter numerischer Verfahren zur Berechnung von turbulenten Strömungen mit Wärmetransport im Rahmen von LES und direkten numerischen Simulationen (DNS), (2) die Entwicklung von wandangepassten Feinstrukturmodellen für den Impulstransport, Wärmetransport und Entropieproduktionsraten, und (3) die Erstellung eines umfangreichen DNS Referenzdatensatzes zur Beurteilung der LES Methode unter realitätsnahen Strömungsbedingungen und komplexen thermodynamischen Fluideigenschaften. Die Beurteilung der entwickelten numerischen Methoden und Modelle erfolgt außerdem durch einen systematischen Vergleich mit experimentellen und DNS Daten aus einschlägiger Literatur. Das vorgeschlagene Gesamtmodell wird abschließend zur Charakterisierung von überkritischen Treibstoffeinspritzungen und zur thermodynamischen Optimierung von Prallkühlvorrichtungen genutzt.

In der vorliegenden Arbeit sind wesentliche Meilensteine bezüglich der Entwicklung eines verlässlichen Ingenieurswerkzeugs zur Entropieproduktionsanalyse mittels LES erreicht worden. Besonders hervorzuheben ist hierbei die Entwicklung eines wandangepassten Ein-Gleichungs-Feinstrukturmodells, welches ohne die Verwendung von ad-hoc Verfahren oder dynamischer Prozeduren in der Lage ist, das korrekte Wandverhalten wiederzugeben. Ein weiterer wesentlicher Beitrag ist die Entwicklung eines thermodynamisch konsistenten Wärmeflussmodells. Zusätzlich konnte, basierend auf der Turbulenztheorie, ein analytischer Zusammenhang zwischen der Entropieproduktion in den Feinstrukturskalen und den aufgelösten Grobstrukturskalen gefunden werden. Das entwickelte Gesamtmodell wird abschließend dazu genutzt, um überkritische Treibstoffeinspritzungen zu charakterisieren und Prallkühlvorrichtungen zu optimieren. Die Analyse der Entropieproduktionen erlaubt einerseits die Bestimmung der charakteristischen Merkmale des Strahlzerfalls bei überkritischen Betriebszuständen und andererseits eine thermodynamisch optimale Auslegung von Prallkühlvorrichtungen.

Aus der vorliegenden Arbeit geht klar hervor, dass Entropieproduktionsanalysen mittels LES eine sehr wertvolle und umsetzbare Methode zur Vorausberechnung und Optimierung von komplexen Strömungsanwendungen mit Wärmetransport darstellt.

List of Publications

The content of this thesis is partly based on the following journal and conference publications which have been published during the PhD project.

Journal Publications

[**E1**] A.S. Doost, F. Ries, L.G. Becker, S. Bürkle, A. Wagner, V. Ebert, A. Dreizler, F. di Mare, A. Sadiki, J. Janicka. Residence time calculations for complex swirling flow in combustion chamber using large-eddy simulations. Chem Eng. Sci., 156, pp. 97–114, **2016**, DOI: 10.1016/j.ces.2016.09.001

[**E2**] F. Ries, P. Obando, I. Shevchuk, J. Janicka, A. Sadiki. Numerical analysis of turbulent flow dynamics and heat transport in a round jet at supercritical conditions. Int. J. Heat Fluid Fl., 66, pp. 172–184, **2017**, DOI: 10.1016/j.ijheatfluidflow.2017.06.007

[**E3**] F. Ries, J. Janicka, A. Sadiki. Thermal Transport and Entropy Production Mechanisms in a Turbulent Round Jet at Supercritical Thermodynamic Conditions. Entropy, 19(8), **2017**, DOI: 10.3390/e19080404

[**E4**] F. Ries, Y. Li, M. Rißmann, D. Klingenberg, K. Nishad, B. Böhm, A. Dreizler, J. Janicka, A. Sadiki. Database of Near-Wall Turbulent Flow Properties of a Jet Impinging on a Solid Surface under Different Inclination Angles. Fluids, 3(5), **2018**, DOI: 10.3390/fluids3010005

[**E5**] K. Nishad, F. Ries, J. Janicka, A. Sadiki. Analysis of spray dynamics of urea-water-solution jets in a SCR-DeNOx sytem: An LES based study. Int. J. Heat Fluid Fl., 70, pp. 247–258, **2018**, DOI: 10.1016/j.ijheatfluidflow.2018.02.017

[**E6**] A. Heinrich, F. Ries, G. Kuenne, S. Ganter, C. Hasse, A. Sadiki, J. Janicka. Large Eddy Simulation with tabulated chemistry of an experimental sidewall quenching burner. Int. J. Heat Fluid Fl., 71, pp. 95-110, **2018**, DOI: 10.1016/j.ijheatfluidflow.2018.03.011

[**E7**] F. Ries, Y. Li, D. Klingenberg, K. Nishad, J. Janicka, A. Sadiki. Near-Wall Thermal Processes in an Inclined Impinging Jet: Analysis of Heat Transport and Entropy Generation Mechanisms, Energies, 11(6), 1354, **2018**, DOI 10.3390/en11061354

[**E8**] F. Ries, K. Nishad, L. Dressler, J. Janicka, A. Sadiki. Evaluating Large-Eddy Simulation Results based on Error Analysis. Theor. Comp. Fluid Dyn., pp. 1-20, **2018**, DOI 10.1007/s00162-018-0474-0

Conference Publications

[**E9**] P. Obando, F. Ries, A. Sadiki, J. Janicka. Analysis of fuel disintegration process under supercritical conditions using large eddy simulation. 10th Mediterranean Combustion Symposium MCS-10, Naples, Italy, **2017**

[**E10**] F. Ries, Y. Li, A. Sadiki. Entropy production in near-wall turbulent flow inside a generic air-to-air plate heat exchanger. 6th European Conference on Computational Mechanics ECCM6, Glasgow UK, **2018**

[**E11**] Y. Li, F. Ries, K. Nishad, A. Sadiki. Near-wall modeling of LES for non-equilibrium turbulent flows in an inclined impinging jet with moderate Re-number. 6th European

Conference on Computational Mechanics ECCM6, Glasgow UK, **2018**

[**E12**] F. Ries, Y. Li, K. Nishad, J. Janicka, A. Sadiki. Study of non-equilibrium boundary layers in a generic DEF-injection system using DNS. 12th International ERCOFTAC Symposium on Engineering Turbulence Modelling and Measurements ETMM12, Montpellier France, **2018**

[**E13**] K. Nishad, F. Ries, Y. Li, A. Sadiki, J. Janicka. Large eddy simulation of intake flow in DISI engine using near wall modeling.12th International ERCOFTAC Symposium on Engineering Turbulence Modelling and Measurements ETMM12, Montpellier France, **2018**

List of Master and Bachelor Theses

The following master and bachelor theses were supervised during the PhD project.

Torkashvand, Hossein. Evaluierung von Subgrid-scale Modellen für Large-Eddy-Simulationen wandnaher Strömungen, Master Thesis, Technische Universität Darmstadt, **2015**

Vesper, Judith Elin. Large Eddy Simulation of Heat Transfer Processes in Energy Systems based on Thermodynamically Consistent Models, Master Thesis, Technische Universität Darmstadt, **2016**

Arnold, Tim. Large Eddy Simulation of Thermal Transport in Supercritical Turbulent Pipe and Channel Flow, Bachelor Thesis, Technische Universität Darmstadt, **2017**

Kraft, Felix. Large Eddy Simulation of Heat Transport in a Transcritical Turbulent Boundary Layer, Master Thesis, Technische Universität Darmstadt, **2017**

Contents

List of Figures

List of Tables

Nomenclature

Upper case Latin letters		Units
C_K	Kolmogorov constant	–
C_{OC}	Obukhov-Corrsin constant	–
C_s	Smagorinsky coefficient	–
D	Diameter	m
D_{ij}	Rate of deformation tensor	1/s
$D_{k_{sgs}}$	Diffusion of k_{sgs}	kg/(m s^3)
E	Spectrum of the turbulent kinetic energy	m^3/s^2
$E(\kappa)$	Energy spectrum	m^3/s^2
$\mathcal{G}$	Spatial filtering operator	1/m
H	Height	m
I	Turbulent intensity	–
$\mathbf{C}$	Cross-stress term	m^2/s^2
$\mathbf{L}$	Leonard term	m^2/s^2
L	Characteristic length scale	m
L_{11}	Longitudinal length scale	m
$\mathfrak{L}_{ij}$	Germano identity	m^2/s^2
L_{ij}	Velocity gradient tensor	1/s
M	Molar mass	kg/mol
Ma	Mach number	–
N	Number of statistically independent samples	–
N_q	Entropy generation numbers of heat transport	–
N_{total}	Entropy generation numbers of friction loss and heat transport	–
Nu	Nusselt number	–
N_v	Entropy generation numbers of friction loss	–
P	Modified pressure	kg/(m s^2)
P_k	Production of k	kg/(m s^3)
$P_{k_{sgs}}$	Production of k_{sgs}	kg/(m s^3)
Pr	Prandtl number	–
Pr_{sgs}	Subgrid-scale turbulent Prandtl number	–
P_θ	Production of temperature variance	K/s
Q	Random variable	–
$\mathbf{R}$	Reynolds subgrid tensor	m^2/s^2
R	Ideal gas constant	J/(mol K)
Re	Reynolds number	–
Re_b	Reynolds number based on bulk velocity	–
Re_{crit}	Critical Reynolds number	–
Re_j	Jet Reynolds number	–
Re_τ	Friction Reynolds number	–

R_{ij}	Two-point correlation tensor	–
S	Area	m^2
$\mathbf{S}_{ij}^d$	Traceless symmetric part of the square of the velocity gradient	$1/s^2$
$S(\kappa)$	Surfaces of the spheres with radius	m^2
T	Temperature	K
T_r	Reduced temperature	–
T_τ	Friction temperature	K
U	Characteristic velocity scale	m/s
U^+	Dimensionless velocity in wall unit	–
U_b	Bulk velocity	m/s
U_i	Velocity	m/s
V	Volume	m^3
V_m	Molecular volume	m^3/mol
V_{mc}	Shifted volume increment	m^3/mol
Z	Supply of ψ	–

Lower case Latin letters		**Units**
$\mathbf{r}$	Spatial lag-distance vector	m
a_n	Specific filter coefficient	–
b	Specific model parameter of generalized EoS	–
c_p	Specific heat	J/(kg K)
e	Internal energy	J/kg
e°	Internal energy of ideal reference state	J/kg
e_k	Error measure	–
e_x^{bc}	Error in the boundary conditions	–
e_x^{init}	Error of the initial conditions	–
e_x^{mod}	Physical modeling error	–
e_x^{num}	Numerical error	–
e_x^{rand}	Sampling error	–
e_x^{ref}	Error of the reference data	–
f_ν	Damping factor	–
f_i	Body force per unit mass	m^2/s
h	Sensible enthalpy	J/kg
i	Imaginary unit	–
k	Turbulent kinetic energy	m^2/s^2
k_{sgs}	Subgrid-scale turbulent kinetic energy	m^2/s^2
l_0	Length scale of large scale motions	m
n_i	Unit vector outward normal to boundary S	–
p	pressure	$kg/(m\,s^2)$
p_r	Reduced pressure	$kg/(m\,s^2)$
q_i	Heat flux vector	W/m^2
q_w	Wall heat flux	K/m^2
q_i^{sgs}	Subgrid-scale heat flux vector	W/m^2
r	Heat source	m^2/s^3
s	Entropy density	J/K
t	Time	s
t_{av}	Averaging time	s
u_0	Velocity scale of large scale motions	m/s
u_τ	Friction velocity	m/s
u_K	Kolmogorov velocity scale	m/s

v_i	Normal speed of the displacement	m/s
y^+	Dimensionless wall distance in wall unit	–

Upper case Greek letters		**Units**
Δt	Time interval	s
Δ	Filter width or grid width	m
Φ	Arbitrary extensive quantity	–
Π	Rate of production per unit volume of Φ	–
Π_q	Entropy production rate by heat transport	W/(m^3 K)
Π_q^m	Π_q due to mean gradients	W/(m^3 K)
Π_q^t	Π_q due to fluctuating gradients	W/(m^3 K)
Π_q^{sgs}	Subgrid-scale entropy production rate by heat transport	W/(m^3 K)
Π_v	Entropy production rate by viscous dissipation	W/(m^3 K)
Π_v^m	Π_v due to mean gradients	W/(m^3 K)
Π_v^t	Π_v due to fluctuating gradients	W/(m^3 K)
Π_v^{sgs}	Subgrid-scale entropy production rate by viscous dissipation	W/(m^3 K)
Θ	Specific model parameter of generalized EoS	–
Ξ	Specific model parameter of generalized EoS	–

Lower case Greek letters		**Units**
α	Thermal diffusivity	m^2/s
α_{sgs}	Subgrid-scale thermal diffusivity	m^2/s
δ	Channel half height	m
δ_Θ	Thermal boundary layer	m
δ_{ij}	Kronecker delta δ	–
ϵ_θ	Dissipation rate of temperature variance	K/s
ϵ_k	Dissipation rate of turbulent kinetic energy	kg/(m s^3)
$\epsilon_{\theta_{sgs}}$	Dissipation rate of θ_{sgs}	K/s
$\epsilon_{k_{sgs}}$	Dissipation rate of k_{sgs}	kg/(m s^3)
η_K	Kolmogorov length scale	m
η_B	Bachelor length scale	m
η_{OC}	Obukhov-Corrsin length scale	m
γ	Blending factor	–
κ	von Kármán constant	–
$\boldsymbol{\kappa}$	Wave number vector	m^{-1}
κ_c	Cut-off wave number	m^{-1}
λ	Thermal conductivity	W/(m K)
μ	Dynamic viscosity	Ns/m^2
μ_i	Skewness or kurtosis of the probability distribution	–
ν	Molecular viscosity	Ns/m^2
ν_{sgs}	subgrid-scale viscosity	Ns/m^2
ω	Pitzer acentric factor	–
ψ	Specific value of an arbitrary extensive quantity	–
ρ	Mass density	kg/m^3
ρ_i	Autocovariance	–
ρ_r	Reduced mass density	–
σ	Hard-sphere diameter of gas molecules	m
σ_{ij}	Cauchy stress tensor	m^2/s^2
τ	Integral time scale	s
τ_0	Time scale of large scale motions	s

τ_i	Temporal decorrelation distance of the turbulent quantity	–
τ_K	Kolmogorov time scale	s
τ_θ	Characteristic turbulence time scale	s
τ_{ij}	Deviatoric part of σ_{ij}	m^2/s^2
τ_{ij}^{sgs}	Subfilter stresses	m^2/s^2
τ_w	Wall shear stress	m^2/s^2
θ	Temperature variance	K^2
θ^+	Dimensionless temperature in wall unit	–
θ_{sgs}	Subgrid-scale temperature variance	K^2
φ	Flux per unit area through boundary	–
ξ	Specific model parameter of generalized EoS	–

Abbreviations

σ-model	SIGMA model
AFRL	Air Force Research Laboratory
BD	Blended differencing
CD	Central differencing
CFD	Computational Fluid Dynamics
CFL	Courant-Friedrichs-Lewy-number
CMOS	Complementary metal-oxide-semiconductor
CV	Control Volume
DLR	Deutsche Luft- und Raumfahrt
DNS	Direct Numerical Simulation
EoS	Equation of state
FDF	Filtered density function
FVM	Finite Volume Method
GGDH	Generalized gradient diffusion hypothesis
HHLR	Lichtenberg High Performance Computer
LES	Large Eddy Simulation
LN_2/GH_2	Liquid-nitrogen-gas-hydrogen
LN_2/GHe	Liquid-nitrogen-gas-helium
LN_2/GN_2	Liquid-nitrogen-gas-nitrogen
LO_2-GCH_4	Liquid-oxygen-gas-methane
LO_2-GH_2	Liquid-oxygen-gas-hydrogen
LOX-GH	Liquid-oxygen-gas-hydrogen
MAE	Mean absolute error
MES	Method of Exact Solutions
MILES	Monotone-Integrated Large Eddy Simulation
MMS	Method of Manufactured Solutions
NASA	National Aeronautics and Space Administration
NIST	National Institute of Standards and Technology
nMAE	normalized mean absolute error
ONERA	Office National D'études et de Recherches Aérospatiales
OpenFOAM	OPEN source Field Operation And Manipulation
PISO	Pressure-Implicit with Splitting of Operators
PIV	Particle Image Velocimetry
PR-EoS	Peng-Robinson equation of state
PRC-EoS	Peng-Robinson equation of state with volume correction
RANS	Reynolds-Averaged Navier-Stokes
RK	Runge-Kutta

RK-EoS	Redlich-Kwong equation of state
SGMV	Systematic Grid and Model Variations
SIMPLE	Semi-Implicit Method for Pressure Linked Equations
SRK-EoS	Soave-Redlich-Kwong equation of state
TVD	Total Variation Diminishing
UD	Upwind differencing
vdW-EoS	van der Waals equation of state
WALE	Wall-adapting linear eddy-viscosity model

PART I: FUNDAMENTALS AND MODEL DEVELOPMENT

Chapter 1

Introduction

Most of the heat transport and fluid flows occurring in the nature and in technical devices are inherently turbulent, some examples are hot smoke from a chimney, mixing in internal combustion engines, or geophysical flows like storm clouds. On closer inspection of turbulent flows, a wide range of length and time scales can be observed and it is obvious that these turbulent motions are apparently unsteady, irregular and chaotic. Thereby, the quasi-chaotic and unsteady motions of turbulence churn up the flow and enhance the mixing and heat transport. However, they also increase the disorder of the system associated with an imminent loss of available mechanical power, which is the fundamental reason for irreversibilities in turbulent heat and fluid flows and responsible for the thermodynamic loss in many engineering applications.

In spite of decades of research, it is still impossible to predict turbulent heat and fluid flows analytically, even in simple flow configurations. Instead, numerical simulations are usually employed that allow to produce an approximate solution of the turbulent flow field at some pre-determined locations in space and time. This is known as *Computational Fluid Dynamics*, or short CFD. In this respect, the leading computational approaches to predict the turbulent quantities of interest and practical relevance are: *Direct Numerical Simulations* (DNS), *Large Eddy Simulations* (LES) and approaches based on the solution of the *Reynolds-Averaged Navier-Stokes* equations (RANS). These approaches can be categorized based on their level of description, computation expense, range of applicability and accuracy.

In DNS, no additional turbulence model is required since the wide range of turbulent length and time scales are fully resolved. Due to the high computational cost, this approach is predominantly restricted to heat and fluid flow problems at low-to-moderate Reynolds numbers. In contrast, RANS simulations only solve the Reynolds equations to obtain the mean flow, while the entire spectrum of turbulent motions is described by means of closure models. This leads to a significant reduction of the required computational resources compared to DNS, making simulations of turbulent flows feasible for complex engineering applications with high Reynolds numbers. However, it is well known that the RANS approach is not always accurate for many cases, especially for flows with large scales, unsteady character and supercritical flows. To overcome the limitations of DNS and RANS, many researchers paid more attention towards LES as an alternative method to predict turbulent heat and fluid flows. In LES, large three-dimensional unsteady turbulent motions are explicitly computed, whilst a turbulence closure model accounts for the influence of the unresolved more universal scales. This simplifies the turbulence modeling, improves the predictive capability compared to RANS and makes LES valid for a wide range of flow situations. Therefore, in this work, the LES technique is used to calculate turbulent heat

and fluid flows. In order to validate the LES and to analyze evolving thermal fluid flow processes, DNS data are also generated.

In dealing with the numerical modeling and prediction of irreversibilities in sub- and supercritical wall-bounded flows in the context of LES and DNS, further modeling aspects have to be addressed. First, enhanced thermodynamic and transport property models are required to account for the non-ideal behavior of the fluid under supercritical conditions. In the most CFD studies, cubic equations of state are applied for this purpose, because they provide an adequate accuracy for a wide range of substances and operating conditions, and even more importantly their numerical solution is generally not too demanding. The coefficients for the transport properties in supercritical flows are often described by means of analytical expressions based on the kinetic gas theory including extensions that account for polar, non-polar and associating fluids at low and high pressures. Additionally, look-up table methods are commonly employed in CFD for the calculation of thermodynamic and transport properties, mostly for pure substances. Another important aspect in the case of LES of wall-bounded flows is the near-wall treatment. Close to the wall, turbulent motions are of the order of the viscous length scale, which means that energetic turbulent structures are small in the vicinity of the wall and have to be explicitly resolved in classical LES. As a consequence, in order to obtain reliable predictions of wall-bounded flows, subgrid-scale models must provide the correct asymptotic behavior in the near-wall region. Finally, when using LES to predict irreversibilities in turbulent heat and fluid flows, subgrid-scale closure approaches for the entropy production are required. In this respect, it is worth mentioning that in spite of the known advantages of LES in predicting turbulent flows, the extent of its usage for entropy production analysis has been insignificant. This is largely due to the challenges in the modeling of the unclosed irreversibility effects in the subgrid.

Despite the significant progress in the application of LES to turbulent heat and fluid flows, many issues remain still open, especially in dealing with subgrid-scale modeling strategies in the vicinity of heated walls and entropy production analysis. This motivates the present work, which is focused on the development of a reliable LES framework combined with the second law of thermodynamics that allows to characterize and optimize sub- and supercritical wall-bounded flow applications. In order to demonstrate the applicability and reliability of the present LES framework, two specific flow applications of practical relevance are selected in this thesis, namely, impingement cooling/heating and supercritical fuel injection. The current state of research in the fields of subgrid-scale modeling for wall-bounded flows, entropy generation analysis using CFD, impingement cooling/heating and supercritical fuel injection is briefly outlined in the next section. Subsequently, the concrete research objectives of the present work are summarized followed by a list of the scientific contributions made within this work. At the end of this chapter, the structure of the thesis is outlined.

1.1 State of research

In the last few decades, there has been a great progress in the research field of LES of wall-bounded turbulent heat and fluid flows, which is partially facilitated by the increasing computer power. The most important milestones are briefly summarized below. Then, the current state of research regarding entropy generation analysis using CFD is outlined followed by a short summary of the research progress in impingement cooling and supercritical fuel injection applications.

Subgrid-scale modeling of momentum and heat transport

Numerous subgrid-scale modeling approaches for the momentum transport are reported in the literature. Using an eddy-viscosity hypothesis is the most common procedure, where it is assumed that the subgrid-scale stress tensor acts as an additional diffusion term in the LES equations by introducing a subgrid-scale eddy viscosity. In analogy to RANS, such subgrid-scale models can be divided into algebraic and differential models. The first and simplest algebraic model is that proposed by Smagorinsky [220], which forms a basis for several advanced models and is still used in LES engineering practice. Other important variants of algebraic subgrid-scale models are the dynamic Smagorinsky model [67], the wall-adapting linear eddy-viscosity model (WALE) [163], the sigma model (σ-model) [164], the model of Vreman [238]. For a more detailed overview see Sagaut [203]. In the case of differential subgrid-scale models, one-equation models are often employed. Thereby, a transport equation for the subgrid-scale kinetic energy is used to calculate the subgrid-scale viscosity. The first one-equation model in the context of LES was proposed by Yoshizawa [254]. An important feature of this model is that no assumption of local balance between the subgrid-scale energy production and dissipation rate has been made [151]. It is therefore expected that one-equation models are particularly advantageous in transitional flows and in turbulent flows with large unsteadiness. Based on the Yoshizawa model, several advanced one-equation models have been proposed in the literature, e.g. [210, 91, 107, 151].

One drawback of the classical formulations of the subgrid-scale viscosity models proposed by Smagorinsky and Yoshizawa is that both models cannot distinguish between turbulent fluctuations and laminar flow with mean velocity gradient, which occurs especially in the vicinity of viscous walls [113]. To circumvent this issue, the subgrid-scale viscosity has to be modified in order to reproduce the correct asymptotic behavior in the near-wall region. One possibility is to apply wall damping functions similar to the near-wall treatment of low Reynolds number turbulence models in the RANS context [233]. In this approach the distance to the wall has to be calculated, which requires additional computational resources and is not always unique in the case of complex flow geometries. Another possibility is to use a dynamic procedure as proposed by Germano [67], which automatically adapts the model coefficients in order to provide a proper near-wall behavior. However, as pointed out in [163], the proper asymptotic behavior can be only obtained in such models when the dynamic procedure is applied over homogeneous planes parallel to the walls, which is not feasible in complex geometries. Wall-adapting LES modeling is an alternative approach, which do not require any ad hoc treatment or test filtering approach to reproduce the correct flow behavior in near-wall regions. The SIGMA and WALE models are prominent examples of such an approach.

In principal, many strategies that are used to close the momentum equation can be also applied to model the subgrid-scale heat flux vector. However, in contrast to turbulent fluid flow, small temperature scales are less universal than velocity scales and may exhibit an anisotropic behavior even at smallest scales. Consequently, more advanced subgrid-scale models are required in the case of turbulent heat transport in order to justify the separation and modeling of the small temperature scales. In spite of this, isotropic thermal diffusivity models are mostly employed in the majority of LES studies including heat transport. Thereby, the subgrid-scale heat diffusivity is traditionally represented based on the Reynolds analogy and the concept of turbulent Prandtl number, which is taken to be a constant value close to one in most cases. Many researchers intended to improve the isotropic thermal diffusivity model by using a dynamic procedure to calculate the turbulent Prandtl number [158, 133], including buoyancy effects [61], using a definition of

the thermal diffusivity based on the Kolmogorov scaling [249] or including the effects of local fluid properties in the calculation of the turbulent Prandtl number [176].

As implied by the discussion above, a better representation of the subgrid-scale heat flux vector for complex flow situations can be obtained by accounting for the anisotropic behavior of small temperature scales and introducing a tensor subgrid-scale thermal diffusivity. Some of these models are derived in analogy to the general gradient diffusion hypothesis [51] as it is often applied in the RANS context. Another approach was suggested by Peng and Davidson [184], they developed a non-linear subgrid-scale heat flux model based on considerations regarding the transport equation of the subgrid-scale heat flux. Wang et al. [241, 243, 242] proposed a series of models which includes the resolved strain-rate tensor, rotation rate tensor and the temperature gradient. In contrast to these model formulations, the anisotropic model by Huai and Sadiki [90, 179] is based on the second law of thermodynamics in conjunction with the invariant theory. In this way, the irreversibility requirements of the second law of thermodynamics are automatically fulfilled by the model formulation. Furthermore, scale similarity and mixed models are also available in the literature, e.g. [97]. However, similar to tensor subgrid-scale thermal diffusivity models, such kind of heat flux models are rarely used in LES engineering practice.

Entropy generation analysis using CFD

In the last decades, entropy generation analysis has become an established method in thermal science and engineering, especially in the fields of refrigeration (cryogenics), heat transfer and power plant technology [28]. It is based on the second law of thermodynamics in conjunction with heat transfer and fluid mechanics principles, and it allows to evaluate the significance of irreversibilities related to heat transport and friction in a thermo-fluid system. Irreversibilities essentially cause a degradation of available energy into internal energy in the working fluid, which leads to a reduction of the thermodynamic efficiency of a system [110]. From an engineering perspective, the concept of entropy generation minimization can be therefore useful as a design tool in order to avoid the imminent loss of available mechanical power in thermo-fluid systems [26]. A detailed description of the theoretical background of entropy generation analysis can be found in [27].

When dealing with entropy generation analysis using CFD, usually the local form of the second law is used to investigate thermodynamic irreversibilites. This allows to quantify the overall entropy production of a system and also to examine how irreversibilities are distributed locally throughout the system [213]. Based on the concept of minimal entropy generation and CFD, causes of irreversibilities have been analyzed for a wide range of thermo-fluid processes including laminar and turbulent heat transfer in wall-bounded flows [204, 244, 62, 206, 116, 103], flows under supercritical conditions [195, 171, 156], reacting flows [52, 252, 63] and also in heat transfer in impinging flows [196, 215, 59]. Contributions of the theory and application of entropy generation analysis using CFD for different types of engineering systems are reviewed in [222, 177, 213].

Focusing on turbulent heat and fluid flows, only a few DNS studies are reported in the literature that deal with entropy generation analysis. Okong'o and Bellan [171] employed DNS to investigated entropy generation effects in supercritical transitional mixing layers. They concluded that entropy generation is useful to describe the behavior of small-scale turbulent motions. Farran and Chakraborty [63] conducted DNS of a freely propagating premixed flame and determined the turbulent second law efficiency in comparison to laminar flames. Ries et al. [E3], [E7] generated two comprehensive DNS databases of entropy generation rates of a supercritical injection process and an inclined impinging jet configuration, that is very useful for model development and evaluation in the context

of LES and RANS. In contrast to DNS, entropy generation analysis based on RANS has been carried out in many numerical studies. Mohseni and Bazargan [156] investigated the effect of the variation of wall heat flux in a heated vertical tube at supercritical conditions. They concluded that the performance of the system improves when operating close to the pseudo-boiling point. Shuja et al. [215] studied local entropy generation in an impinging jet and evaluated various turbulence models based on the concept of minimum entropy generation. Herwig and Kock [85, 116] developed wall-functions for the entropy production rates and used their approach to evaluate the heat transfer performance of turbulent shear flows. Besides, numerous other RANS studies are reported in the literature that propose optimal designs of thermodynamic systems based on CFD with second law analysis, e.g. [209, 244, 70].

Entropy generation analysis based on LES are rarely reported in the literature, largely because of the challenges in modeling of the unclosed irreversibility effects in the subgrid. Recently, Safari et al. [202] developed a methodology based on filtered density function (FDF) approach that allows LES predictions of entropy transport and generation in turbulent reacting flows. They used their approach to analyze entropy generation in a turbulent mixing layer and a turbulent non-premixed piloted methane jet flame. Unfortunately, the FDF approach requires the solution of an additional transport equation for the entropy filtered density function along with complex stochastic differential equations to close this transport equation. It is therefore not possible to use the FDF method as a simple post-processing tool, likewise in a commercial CFD code, which impedes its practical application. Entropy generation analysis based on the classical LES approach that includes the subgrid-scale contribution of entropy production rates are still not reported in the literature.

Impingement cooling and heating

Impinging cooling and heating are used in a variety of engineering application as it enables localized high heat transfer, e.g. cooling of electronic components, quenching of metals and glass, cooling of turbine blades or drying of paper and other materials. In this respect, it has been observed that the jet dynamics and heat transfer depends on many parameters, such as nozzle shapes, Reynolds number, inflow conditions, jet-to-plate spacing, target plate inclination, molecular Prandtl number, surface roughness, interaction with cross-flow and many more. This makes the optimization of engineering systems very difficult where thermal control is often carried out by means of impingement cooling. Moreover, the underlying physics in turbulent impinging jets are manifold and not unique since such flows feature very complex dynamics with interlinked effects including stagnation points, shear flow boundary layers, strong streamline curvatures and anomalies in the distribution of Nusselt numbers. It is therefore not surprising that in the last few decades, impinging cooling has been the subject of extensive research to gain insights into the complex physical mechanisms and to identify preferred operating conditions along with practical guidelines for its general usage. An overview of experiments, numerical studies and available empirical correlations of impinging cooling can be found in numerous reviews, e.g., [257, 258, 98, 141, 236, 159, 246, 57].

Focusing on heat transport in impinging jets, several researchers measured local Nusselt numbers for fully-developed circular impinging jets with respect to the jet-to-plate spacing H/D and jet Reynolds number Re_j (see [22, 111, 89, 108]). In these experimental studies, main emphases were placed on a Reynolds number range from 4000–80,000 and a H/D interval from 0.5–12, representing conventional gas jet installations for heat transfer [257]. In this context, it was concluded that heat transfer can be intensified by increasing Re_j

and/or decreasing H/D. Furthermore, it was observed that the variation of the mean wall heat transfer appears non-monotonic in the radial direction with two distinctive peaks occurring in the case of small jet-to-plate spacings ($H/D < 3$ [108]) and above a critical Reynolds number of $Re_{j,crit} > 3000$ [258]. The first peak, which is located in the vicinity of the stagnation point, is believed to be caused by a strong acceleration of the fluid away from the center of the jet and with a flapping of the impingement position [66]. The secondary peak appears approximately two nozzle diameters away from the stagnation point, which is thought to be linked to large-scale vortical structures issuing from the jet shear layer [198]. Further, the influence of nozzle shapes on the heat transfer characteristic of impinging gas jets has been also investigated in various experimental studies, e.g. [129, 34, 81, 235, 228, 150]. In this regard, it was found that the shape of nozzle influences considerably the distribution of the local Nusselt number with the highest heat transfer coefficients in the case of circular orifices compared to elliptical, square, rectangular or triangle shapes. Varying the inclination of the impinged plate, a few experimental studies have explored the effect of target plate inclination angle on the heat transfer distribution of impinging jets, e.g. [251, 169, 42, 8, 10]. It was concluded that the location of peak heat transfer is shifted towards the compression side as the inclination increases [251] and averaged Nusselt numbers increase with decreasing inclination [10]. Other influencing parameters on the heat transfer characteristic of impinging jets like inflow temperature, interaction with cross-flow, acoustic and mechanical excitation, jet arrays, jet inflow oscillation, surface curvature, rotating target plates or surface roughness have been also addressed in numerous experimental studies (see [235, 32, 199, 66, 69, 139, 64, 253]).

Despite significant progress towards a better understanding of the various physical phenomena taking place in impinging jet cooling, many issues remained open due to limitations of present measurement techniques, especially in the vicinity of the impinged wall where steep gradients and small turbulent flow scales make measurements very difficult. In order to circumvent these limitations, several numerical simulations have been initiated. Especially, wall-resolved LES [237, 49, 23, 83, 231, 78, 6, 162] and direct numerical simulation (DNS) [207, 45, 84, 230, 100, 50, 247] have been carried out in order to complement experimental results and to gain further insights into the complex mechanisms of heat transport and fluid flow dynamics in impinging jet cooling. In this regard, Hattori and Nagano [84] provided a comprehensive DNS dataset of fluid flow and heat transport properties for a plane non-inclined impinging jet at $Re_j = 9120$ and different jet-to-plate spacings. In the LES study of Hadžiabdić and Hanjalić [83], the authors analyzed the role of coherent vortical structures on the heat transfer distribution at the wall. They concluded that the impingement of roll-up vortices generated by instabilities in the initial shear layer along with pressure pulsations lead to a flapping of the jet, which is believed to be instrumental in surface renewal process and thus enhances the heat transfer in the stagnation point. Aillaud et al. [6] conducted a wall-resolved LES of a round air jet impinging on a heated surface ($Re_j = 23{,}000$, $H/D = 2$) to explain the origin of the secondary peak in the radial variation of the temporal-mean Nusselt number. It was found that especially the rebound of primary vortices enhances the heat transfer and causes the secondary peak in the spatial distribution of the Nusselt number. Dairay et al. [50] and Wilke and Sesterhenn [247] performed DNS of impinging jet flow at $Re_j = 10{,}000$ and $Re_j = 8000$, respectively, with highly resolved domains and high order numerical schemes. In the first study, the authors analyzed the role of unsteady processes on the wall heat transfer, while in the latter study, the influence of Mach number, Reynolds number and ambient temperature on the velocity and temperature was examined. Recently, Grenson and Deniau [78] performed a wall-resolved LES of a heated impinging jet at Re_j =60,000

in order to analyze the fundamentals of flow and heat transfer in impinging jets under higher Reynolds numbers. Based on the analysis of instantaneous flow topology, turbulent quantities and probability functions, this investigation revealed that hot spots of high convective heat transfer related to unsteady separation and streak-like structures are linked to the secondary peak in the Nusselt number distribution. However, the mechanisms responsible for these streak-like structures near the radial location of the secondary peak remained unclear. Other important aspects like the influence of subgrid-scale modeling in LES of impinging jets [172, 136], flow dynamics and heat transfer characteristics in multiple impinging jets [117, 58], the effect of wall curvature [102, 7], impingement jet in cross-flow [190, 201] or jet impingement onto a rotating disc [106] have been also investigated by means of LES and DNS. With regard to numerical studies of oblique impinging jets, it is worth mentioning that only a few LES studies [74, 33] and no DNS, except the DNS studies of Ries et al. [E4], [E7], have been reported in the literature, even though this specific configuration features very interesting flow properties and is of practical relevance in cooling arrangements for gas turbine blades, allowing to reduce the size of such systems [57], as well as in numerous other applications.

Supercritical fuel injection

Fuel injection under supercritical conditions can be found in various energy conversion applications such as liquid rocket engines, gas turbines or diesel engines [115, 152, 4, 123]. The main reasons to operate under such extreme thermodynamic conditions are to increase the thermal efficiency of processes, to reach higher specific energy conversion rates and/or to enhance heat and mass transport.

Focusing on experimental studies of supercritical fuel injection with application to liquid rocket engines, systematic research programs were initiated in the mid 1990s by the Air Force Research Laboratory (AFRL) in the USA, the Office National D'études et de Recherches Aérospatiales (ONERA) in France and the Deutsche Luft- und Raumfahrt (DLR) in Germany, in order to obtain valuable insights into the complex fuel disintegration process under supercritical conditions. An overview of recent experimental efforts on high-pressure supercritical injection at the AFRL can be found in the article of Chehroudi [40]. Reviews of the experimental studies undertaken at the DLR and ONERA are provided by Oschwald et al. [175] and Habiballah et al. [82], respectively.

The experimental investigations can be divided into three categories with an increasing degree of complexity. Initial studies utilized a single jet of cryogenic nitrogen injected into a warm nitrogen environment with pressures below and above the critical pressure of nitrogen [41, 173, 149]. In this respect, axial and radial profiles of the density were provided that allow a comparison with computational models and enables the characterization of the main features of the disintegration process of the jet. Then, experiments of coaxial jets were performed in order to investigate the mixing effects of co-flowing gas. At AFRL, measurements of a liquid-like nitrogen jet with a gas-like nitrogen co-flow (LN_2/GN_2) were conducted [53], while liquid-like nitrogen and gas-like helium (LN_2-GHe) and liquid-like nitrogen and gas-like hydrogen (LN_2/GH_2) coaxial jets were examined at DLR [146, 147, 174]. Measured quantities such as growth rates, core lengths, turbulent length scales and breakup/mixing regimes were examined. Finally, combustion studies with cryogenic propellants were introduced to gain insights into the complex high pressure coaxial injection processes with subsequent influence on chemical reactions. Shadowgraphy and spontaneous Raman scattering were used at DLR to analyze the flame structure in reactive liquid-like oxygen and gas-like hydrogen (LO_2-GH_2) coaxial jets [146, 148]. At

ONERA, the structure and shape of LO_2-GH_2 jet flames were examined based on measurements of OH radicals and O_2 [36, 105, 82] and it was concluded that combustion is mainly controlled by the large-scale turbulent mixing at high pressure. Moreover, measurements of liquid-like oxygen and gas-like methane (LO_2-GCH_4) were also carried out at ONERA [218, 219].

Regarding numerical simulations of single component injection under supercritical conditions, several researchers applied RANS [149, 112, 217] or LES [185, 211, 160] to gain more reliable predictions for practical applications. The main objective of these contributions was to evaluate the impact of turbulence models and real gas equations of state on the mixing prediction. Despite some attempts to address this issue, a satisfactory answer is still open due to the lack of valuable experimental data at such extreme thermodynamic conditions or comprehensive DNS data under realistic operating conditions. In this respect, Ries et al. [E2], [E3] performed a three-dimensional DNS of the turbulent flow field in a round jet of cryogenic nitrogen, which mimics the experiment by Mayer et al. [149] in terms of geometry, thermodynamics and hydrodynamics, but at a reduced Reynolds number. A comprehensive dataset was provided to support the model development and validation in the context of LES and RANS. Lapenna and Creta [127, 126] performed DNS of a temporal jet configuration and analyzed mixing under supercritical conditions as well as the interaction between turbulent motions and the pseudo-boiling process. Mixing and combustion within supercritical injection processes were also addressed in several LES studies [170, 92, 140, 227]. Ruiz et al. [200] used a two-dimensional DNS to provide a numerical benchmark for high-Reynolds-number supercritical flows with large density gradients in simple configurations containing the essential features of real devices (geometry, thermodynamics, and hydrodynamics). This DNS refers to a mixing layer forming downstream of an injector lip separating a stream of dense oxygen from a stream of light hydrogen, mimicking one experiment by Chehroudi et al. [41]. The authors provided mean and rms velocity, temperature profiles, power spectrum density of the square of transverse velocity, dense core lengths, mixing layer thickness, etc.

Although the experimental and numerical investigations conducted during the last 20 years have contributed considerable to our understanding of the physics and modeling of supercritical fuel injection processes, many phenomena are still not fully understood and no single modeling approach has been yet established as a standard method for such flow conditions, implying the need of further research.

1.2 Research objectives

Based on the current scientific evidence, it is unlikely that turbulent heat and fluid flows can be predicted analytically in the near future. Due to the disadvantages of DNS and RANS approaches, in particular LES seems to be a promising approach to predict complex flow problems accurately and with reasonable computational expense. However, despite the clear advantages of LES, many issues within this approach are still not addressed and further research is required in order to make LES feasible as an engineering tool for the predictive design of complex industrial flow applications. This motivates the present work, which is focused on the development of a reliable LES framework combined with the second law of thermodynamics that allows to characterize and optimize sub- and supercritical wall-bounded flow applications. More specifically, the key objectives of the present work are:

- to develop an accurate and robust numerical treatment for LES of wall-bounded sub- and supercritical flows based on the framework of OpenFOAM.

- to verify and validate the implemented source code in order to ensure that the code is free of programming errors and applicable for the purpose of present use.
- to develop advanced subgrid-scale modeling approaches for heat and fluid flow applicable for wall-bounded flows with strong variation of fluid properties.
- to derive accurate closure models for subgrid-scale entropy production that can be used in a post-processing step for entropy generation analysis.
- to generate comprehensive DNS databases of thermal fluid flow properties and entropy production rates for model development and evaluation.
- to evaluate the subgrid-scale modeling approach and the LES framework by a systematic comparison with DNS reference data.
- to apply the LES framework combined with the second law analysis to characterize supercritical fuel injection processes and to optimize impinging cooling arrangements.

1.3 Scientific contribution

This work contributes to the fields of turbulence modeling and entropy generation analysis in the context of LES of wall-bounded turbulent flows at sub- and supercritical thermodynamic conditions. The main contributions are:

- Generation of a comprehensive DNS database of near-wall thermal flow statistics and entropy generation rates of an inclined impinging jet configuration [E4], [E7]. (see chapter 7)
- Generation of a comprehensive DNS database of thermal flow statistics and entropy generation rates of cryogenic nitrogen injection under supercritical conditions [E2], [E3] (see chapter 8)
- Development of a wall-adapting one-equation subgrid-scale model for wall-bounded turbulent fluid flow. (see section 3.2.3)
- Development of a thermodynamically consistent anisotropic subgrid-scale heat flux model for wall-bounded turbulent heat transport. (see section 3.3.3)
- Derivation of closure models for subgrid-scale entropy production rates by heat transport and friction based on the inertial-convective subrange theory. (see section 3.4)
- Formulation of an evaluation framework for LES results based on error analysis and application of the framework to wall-bounded flows [E8]. (see chapter 9)
- Application of classical LES with second law analysis including the effects of subgrid-scale entropy generation to analyze and optimize thermo-fluid systems for the first time. (see chapter 10)

1.4 Thesis outline

This thesis mainly consists of four parts, divided into eleven chapters. **Part I** provides the theoretical background and mathematical description of wall-bounded turbulent heat and fluid flows under sub- and supercritical thermodynamic conditions as well as their

modeling in the context of LES. This part begins with a short motivation, a summary of the current state of research, a description of the specific research objectives and the main scientific contributions of this work. Subsequently, in chapter 2, the balance laws of thermo-fluid mechanics, thermodynamics of non-ideal fluids, and essential properties of turbulence are briefly reviewed. Modeling of turbulent heat and fluid flows in the context of LES is described in chapter 3. In particular, the concept of LES and classical subgrid-scale modeling approaches for momentum and heat transport are outlined. In this context, a wall-adapting one-equation model, a new anisotropic heat flux model and closure models for the subgrid-scale entropy production are proposed. The focus then shifts to the numerical treatment of turbulent heat and fluid flows in **Part II**. In chapter 4, at first, the second-order finite volume method discretization procedure of the open source C++ library OpenFOAM, which is applied in the present work, is briefly summarized. Subsequently, the pressure correction methods to solve turbulent heat and fluid flow are discussed. These pressure correction methods are added to the OpenFOAM framework as part of this project. The verification and validation of the numerical methods are presented in the chapters 5 and 6, respectively. **Part III** deals with the analysis of irreversibilities in sub- and supercritical flows using DNS. Two specific applications of practical relevance, impingement cooling (chapter 7) and supercritical fuel injection (chapter 8) are examined. In this respect, distinctive features of both applications are analyzed and comprehensive databases are generated for thermal-fluid flow properties and entropy generation rates. These DNS databases are difficult to obtain experimentally and particularly useful for the model development and evaluation of LES. Entropy generation analysis based on LES is discussed **Part IV**. First, the LES modeling approach for momentum transport, heat transport and entropy production rates are evaluated by means of a systematic comparison of LES predictions with reference DNS data (chapter 9). After that, in analogy to part III, entropy generation in impingement cooling applications and supercritical fuel injection processes are examined in chapter 10. In this respect, it is proved that the proposed LES framework provides a promising approach for entropy generation analysis, not only for simple flow configurations, but also for those with complex wall-bounded geometries and complex thermodynamic properties like supercritical flows. Moreover, it is shown that LES with second law analysis can be used as a reliable engineering tool to find thermodynamic optimal designs of thermal devices. Finally in **Part V**, the major findings of this work are summarized and an outlook for further research is motivated.

Chapter 2

Basics of thermo-fluid dynamics

This chapter briefly reviews the balance laws of thermo-fluid mechanics, the thermodynamics of pure non-ideal fluids, and the properties of turbulent heat and fluid flow. Thereby, it is assumed, that the continuum hypothesis holds, which means that all field variables describing the static and dynamic behavior of the fluid can be expressed as continuous functions with respect to space and time. For the sake of simplicity, right-handed Cartesian coordinate system will be used throughout the text and the summation convention applies to repeated subscripts. Further information and explanations of the principles of material theory can be found in e.g. [118, 9, 143, 104, 161].

2.1 Balance laws of thermo-fluid mechanics

In thermo-continuum mechanics any extensive quantity Φ of a material body with the volume V can be defined as

$$\Phi = \int_V \psi dV, \tag{2.1}$$

where $\psi = \rho\phi$ is the specific value of the extensive quantity Φ and ρ is the mass density. The general form of the balance equation for the quantity ψ in spatial description reads [161]

$$\frac{D}{Dt}\int_V \psi dV = \int_S \varphi_i n_i dS + \int_V Z dV + \int_V \Pi dV, \tag{2.2}$$

where D/Dt is the material derivative of Φ, φ_i represents the flux per unit area through the boundary S, Z is the supply of ψ and Π denotes the rate of production (>0) or destruction (<0) per unit volume of Φ. n_i is the unit vector outward normal to boundary S. The flux φ_i is a vector if ψ is a scalar and a tensor if ψ is a vector, while Z and Π have the same tensorial rank as ψ [104]. Equation 2.2 must be true for all volume elements, which leads to the local form of the general balance equation as [93]

$$\frac{\partial \psi}{\partial t} + \frac{\partial}{\partial x_i}\left(\psi U_i - \varphi_i\right) - Z - \Pi = 0, \tag{2.3}$$

where U_i is the fluid velocity. In the case discontinuities exists inside the material body (e.g. in the form of a singular surface S^*), a so-called jump condition can be derived, which reads [104]

$$\left\|\left[\psi\left(U_i - v_i\right) n_i\right]\right\| - \left\|\left[\varphi_i n_i\right]\right\| = 0. \tag{2.4}$$

Here, the brackets $\|[.]\|$ denote the jump of ψ across the discontinuity and v_i is the normal speed of the displacement.

The various fluxes and supply terms in equations 2.2 and 2.3 corresponding to the fundamental properties of mass, momentum, internal energy and entropy are summarized in table 2.1. Additionally, the fluxes and supply terms of the sensible enthalpy balance is included since it is used in the low Mach-number formulation in the numerical solution procedure as described in section 4.2.2.

	ψ	φ_i	Z	Π
mass	ρ	–	–	–
momentum	ρU_i	σ_{ij}	ρf_i	–
energy	ρe	q_j	ρr	$\sigma_{ij} L_{ij}$
sensible enthalpy	ρh	q_j	ρr	$\frac{Dp}{Dt} + \tau_{ij} L_{ij}$
entropy	ρs	q_j / T	–	$\frac{1}{T} \tau_{ij} L_{ij} - \frac{1}{T^2} q_i \frac{\partial T}{\partial x_i}$

Table 2.1: Fluxes and supply terms of balances of thermo-fluid mechanics. Here, ρ is the mass density, U_i the fluid velocity, e the internal energy, h the sensible enthalpy, s the entropy density, σ_{ij} the Cauchy stress tensor, q_i the heat flux vector, T the temperature, f_i a body force per unit mass, r a heat source, $L_{ij} = \frac{\partial U_i}{\partial x_j}$ the velocity gradient tensor, p the pressure and τ_{ij} the deviatoric part of σ_{ij}.

2.2 Constitutive relations

The balance laws of thermo-fluid mechanics as introduced in section 2.1, are totally general and consequently apply to any continuous material and flow system. However, they are independent of the material in the system and therefore insufficient to determine the specific thermo-mechanical behavior of a given material. Moreover, assuming that the body force f_i and the heat source r are known, the five balance equations (the continuity equation, 3 equations of motion and the energy equation) involve 14 independent scalar unknowns (ρ, v_i, $\sigma_{ij} = \sigma_{ji}$, e, q_i) and are therefore mathematically unclosed. Obviously, a set of additional constitutive relations are required to characterize the thermo-mechanical behavior of a given material and to close the balance equations. These constitutive equations are usually formulated for σ_{ij}, q_i, s, e and ρ as a function of kinematic and thermodynamic variables.

For viscous fluids with heat conduction, the general form of the thermo-mechanical constitutive equations for σ_{ij}, q_i, s, e read [161]:

$$\begin{aligned} e &= f\left(\rho, T, \frac{\partial T}{\partial t}, \frac{\partial T}{\partial x_i}, D_{ij}\right), \quad s = f\left(\rho, T, \frac{\partial T}{\partial t}, \frac{\partial T}{\partial x_i}, D_{ij}\right), \\ q_i &= f\left(\rho, T, \frac{\partial T}{\partial t}, \frac{\partial T}{\partial x_i}, D_{ij}\right), \quad \sigma_{ij} = f\left(\rho, T, \frac{\partial T}{\partial t}, \frac{\partial T}{\partial x_i}, D_{ij}\right), \end{aligned} \tag{2.5}$$

where $D_{ij} = \frac{1}{2}\left(\frac{\partial U_i}{\partial x_j} + \frac{\partial U_j}{\partial x_i}\right)$ is the rate of deformation tensor.

2.2.1 Navier-Stokes-Fourier fluid

In the case of a Navier-Stokes-Fourier fluid as assumed in the present work, σ_{ij} depends solely linearly on D_{ij} and q_i is independent of D_{ij} while it depends linearly on $\frac{\partial T}{\partial x_i}$. There-

fore, the constitutive equations for σ_{ij} and q_i can be simplified as

$$\sigma_{ij} = -p\delta_{ij} + 2\mu\left(D_{ij} - \frac{1}{3}D_{kk}\delta_{ij}\right) \tag{2.6}$$

and

$$q_i = -\lambda\frac{\partial T}{\partial x_i}, \tag{2.7}$$

where p is the pressure, λ the thermal conductivity and μ the dynamic viscosity. Furthermore, assuming thermodynamic equilibrium, both the kinetic and caloric equations of state depend only on ρ and T. It follows that

$$e \equiv e|_{eq} = f(\rho, T), \qquad s \equiv s|_{eq} = f(\rho, T) \qquad \text{and} \qquad p \equiv p|_{eq} = f(\rho, T), \tag{2.8}$$

where $.|_{eq}$ denotes equilibrium. The kinetic and caloric equations of state as well as relations for the transport properties μ and λ under sub- and supercritical thermodynamic conditions will be discussed in detail in the following section.

2.2.2 Thermodynamics of real Navier-Stokes fluids

In the most engineering applications of thermo-fluid mechanics, the properties of the working fluid can be accurately described by means of an ideal gas assumption due to moderate thermodynamic operating conditions. Not surprisingly, only little attention is usually paid to the description of caloric and kinetic equations of state when dealing with numerical simulations of engineering applications. However, today there is a great interest in processes that occur at very high pressure such as in propulsion rocket engines, diesel engines or supercritical CO_2 power cycles. Under such extreme operating conditions, where the pressure and temperature can exceed the critical point of the fluid, intermolecular interactions become important and the fluid properties differ considerably from that of a perfect gas. Therefore, enhanced thermodynamic equations of state and transport properties models are required to account for the non-ideal behavior of the fluid. The description of the material behavior of non-ideal fluids is the topic of this section. Thereby, the thermodynamic and transport properties of the fluids are modeled in this work either by analytic equations or using look-up tables. The discussion below is therefore restricted to the methods relevant for this work. A complete overview of the modeling of real fluid properties can be found in [187, 122, 137].

Kinetic equations of state

The intensive thermodynamic properties of a pure fluid are commonly expressed in terms of the dimensionless compressibility factor z, written either as a function of T_r and p_r or of T_r and ρ_r [187]

$$\begin{aligned} z = \frac{pM}{\rho RT} &= f(T_r, p_r) \\ &= f(T_r, \rho_r), \end{aligned} \tag{2.9}$$

where $T_r = T/T_c$ is the reduced temperature, $p_r = p/p_c$ the reduced pressure, $\rho_r = \rho/\rho_c$ the reduced density, M is the molecular weight and $R = 8.3144598J/(molK)$ is the universal gas constant. The subscript "c" denotes the critical value of the thermodynamic properties. The function $f(.,.)$ on the right-hand side of equation 2.9 is called kinetic equation of state and it allows to calculate the unknown property of a pure fluid from the two other

properties that constrain the equilibrium state. For an ideal gas $z = 1$, which leads to the well known ideal gas model. It can be written explicitly for pressure in terms of the intensive properties ρ and T as follows:

$$p = \frac{\rho RT}{M}. \tag{2.10}$$

In the ideal gas model, it is assumed that molecules occupy no volume and exert no intermolecular forces. However, these assumptions are generally not justifiable for real fluids at high pressure. Consequently more complex kinetic equations of state that incorporate intermolecular interactions like attractive, repulsive and chemical forces are required for such thermodynamic conditions. Besides, it is also common practice to tabulate experimentally measured thermodynamic properties instead of using analytic equations as it is done for water in steam tables.

There exist numerous of kinetic equations in the literature for different purposes. In most computational fluid dynamics studies, cubic equations of state are applied, because they provide an adequate accuracy for a wide range of fluids and operating conditions, and even more important their numerical solution is generally not too demanding. Due to these reasons, cubic equations of state are also employed in this work to describe the gaseous and liquid volumetric behavior of pure fluids.

It is possible to represent all common cubic equations of state in a single general form with only four parameters Θ, Ξ, ξ and b [187]. This formulation reads

$$z = \frac{V_m}{V_m - b} - \frac{(\Theta/RT)\, V_m}{(V_m^2 + \xi V_m + \Xi)}, \tag{2.11}$$

where V_m is the molecular volume of the fluid, and Θ, Ξ, ξ, b are specific model parameters that depend on the respective cubic equation of state. The first term on the right hand-side of equation 2.11 represents the repulsive forces, while the second term quantifies attractive interactions. In general, these terms are empirically established to best fit experimental data [122]. A collection of the model parameters of some popular cubic equations are given in table 2.2. Notice that in the case of the Soave-Redlich-Kwong [221] and Peng-Robinson [183] equations an additional parameter ω is introduced. This is the Pitzer acentric factor that accounts for "nonspherical" molecules. Thus, it is expected that kinetic equations of state including ω are better suited for different classes of molecules.

Equation of state	ξ	Ξ	Θ	b
ideal gas	0	0	0	0
van der Waals (1873) [232]	0	0	$\frac{27(RT_c)^2}{64p_c}$	$\frac{RT_c}{8p_c}$
Redlich-Kwong (1949) [192]	b	0	$\frac{0.42748R^2T_c^2}{T_r^{0.5}p_c}$	$\frac{0.08664RT_c}{p_c}$
Soave-Redlich-Kwong (1972) [221]	b	0	$\frac{0.42747R^2T_c^2}{p_c}\cdot(1+(0.48508+1.5517\omega-0.15613\omega^2)(1-T_r^{0.5}))^2$	$\frac{0.08664RT_c}{p_c}$
Peng-Robinson (1976) [183]	$2b$	$-b^2$	$\frac{0.45724R^2T_c^2}{p_c}\cdot(1+(0.37464+1.5423\omega-0.26992\omega^2)(1-T_r^{0.5}))^2$	$\frac{0.0778RT_c}{p_c}$

Table 2.2: Equation parameters of important cubic equations of state.

It is well known, that cubic equations of state yield poor prediction for liquid density, especially at operating conditions near the critical point [145]. One way to circumvent this limitation is to use a so called "volume translation" method as introduced by Martin

[142]. The basic idea of this method is to shift the untranslated molar volume V_m obtained from the equation of state along the volume axis at constant temperature and pressure [144] by an increment of V_{mc}. Several volume-translation methods of this type have been proposed, including methods with a constant correction term, e.g. [142, 182] and more complex forms that depend on both temperature and density [135, 2]. In the present work, the method of Abudour et al. [2] is utilized in conjunction with the Peng-Robinson [183] equation of state as already used in a DNS study of a turbulent jet flow at supercritical conditions by the author [E2], [E3]. An evaluation of this method in comparison to the classical cubic formulations is given in chapter 8 for cryogenic nitrogen at supercritical thermodynamic conditions.

Caloric equations of state

To connect the intensive thermodynamic properties T, p, and ρ with the fundamental properties e and s, additional caloric equations of state are needed. Typically, the fundamental properties are only defined in a relative sense as state properties and expressed in terms of two independent thermodynamic properties such as $e = f(T, p)$ or $e = f(T, \rho)$. Based on this, the relative changes of internal energy e in a system can be written as the sum of a low-pressure reference state e° and the departure function, which accounts for the difference between the real and the ideal state of the property. It follows for $e = f(T, p)$ that

$$e(T,p) = e^\circ(T) + \int_\infty^{V_m} \left[T \left. \frac{\partial p}{\partial T} \right|_{V_m} - p \right] dV_m, \tag{2.12}$$

which can be evaluated for the generalized cubic equation of state in equation 2.11 as

$$e(T,p) = e^\circ(T) + \frac{1}{\sqrt{\xi^2 - 4\Xi}} \left[\Theta - T \frac{\partial \Theta}{\partial T} \right] ln \left[\frac{2V_m + \xi - \sqrt{\xi^2 - 4\Xi}}{2V_m + \xi + \sqrt{\xi^2 - 4\Xi}} \right]. \tag{2.13}$$

The ideal reference state e° is usually calculated by means of ideal gas data. In the present work, 7-coefficient NASA polynomials [35] are utilized for this purpose. Notice, that in the case of ideal gas model, the second term on the right-hand side in equation 2.13 vanishes due to the absence of intermolecular forces. Thus, the caloric state functions being independent of pressure and only a function of temperature in the ideal gas model, e.g. $e^{ig} = e^\circ(T)$ and $s^{ig} = s^\circ(T)$.

Departure functions of the internal energy, enthalpy and entropy for the generalized cubic equation of state are summarized in table 2.3. Departure functions of other thermodynamic properties can be found in [187].

Property	Departure function
Energy, e	$\frac{e-e^\circ}{RT} = \frac{\Theta - T\frac{\partial \Theta}{\partial T}}{RT\sqrt{\xi^2-4\Xi}} ln \left[\frac{2V_m+\xi-\sqrt{\xi^2-4\Xi}}{2V_m+\xi+\sqrt{\xi^2-4\Xi}} \right]$
Enthalpy, h	$\frac{h-h^\circ}{RT} = \frac{\Theta + T\frac{\partial \Theta}{\partial T}}{RT\sqrt{\xi^2-4\Xi}} ln \left[\frac{2V_m+\xi-\sqrt{\xi^2-4\Xi}}{2V_m+\xi+\sqrt{\xi^2-4\Xi}} \right] - 1 + z$
Entropy, s	$\frac{s-s^\circ}{R} = -\frac{\frac{\partial \Theta}{\partial T}}{R\sqrt{\xi^2-4\Xi}} ln \left[\frac{2V_m+\xi-\sqrt{\xi^2-4\Xi}}{2V_m+\xi+\sqrt{\xi^2-4\Xi}} \right] + ln \left[z \left(1 - \frac{b}{V_m} \right) \right]$

Table 2.3: Constant pressure departure function expressions for the generalized cubic equation of state.

The departure functions given in table 2.3 are formulated in a thermodynamically consistent manner. In order to derive also a thermodynamically consistent formulation when a volume translation method is applied, the volume shift needs to be considered in the evaluation of the departure functions as well. Following the procedure described in [144], equation 2.12 can be reformulated for a general volume translation method as

$$(e(T,p) - e^{\circ}(T)) = \underbrace{\int_{\infty}^{V_m} \left[T \left.\frac{\partial p}{\partial T}\right|_{V_m} - p \right] dV_m}_{(I)} - \underbrace{\int_{\infty}^{V_m} \left[T \left.\frac{\partial V_{m_c}}{\partial T}\right|_{V_m} \left.\frac{\partial p}{\partial V_m}\right|_{T} \right] dV_m}_{(II)} + \underbrace{\int_{\infty}^{V_m} \left[T \left.\frac{\partial p}{\partial T}\right|_{V_m} - p \right] \left.\frac{\partial V_{m_c}}{\partial V_m}\right|_{T} dV_m}_{(III)}, \tag{2.14}$$

where the first term on the right-hand side (I) is the contribution by the untranslated volume, which can be directly calculated using the cubic equation of state. The remaining terms (II) and (III) include derivatives of the shifted volume increment V_{mc} and therefore depend on the specific volume translation method applied. For methods with a constant correction term, both integrals (II) and (III) vanish. In the case $V_{mc} = f(T)$, the term (III) is zero and only the second integral (II) contributes to the departure function. Finally, for the most general case $V_{mc} = f(T, V_m)$, both terms (II) and (III) contributes to the departure of the internal energy and need to be calculated to obtain a thermodynamically consistent formulation. The volume translation method applied in this work, the method proposed by Abudour et al. [2], belongs to the most general case where $V_{mc} = f(T, V_m)$.

When applying the volume translation method of Abudour et al. [2], it is worth mentioning that no analytical solution have been found for the terms (II) and (III) in equation 2.14. Alternatively, the integrals could be approximated numerically as reported in [144]. However, it appears that such an approach is too demanding in DNS or LES studies. Therefore, in accordance with other CFD studies of supercritical fluid flow in the literature [160, 144], the volume translation method is applied in this work for improving the density prediction, while neglecting the contribution of the integrals (II) and (III) on caloric properties.

Transport properties

Using the kinetic gas theory, analytic expressions for the molecular viscosity μ and the thermal conductivity λ of dilute gases can be derived. In the most general case these expressions read [187]

$$\mu = (const)\frac{T^{1/2}M^{1/2}}{\sigma^2} \quad \text{and} \quad \lambda = (const)\frac{T^{1/2}}{M^{1/2}\sigma^2}, \tag{2.15}$$

where T is the gas temperature, M the molecular weight, σ is the hard-sphere diameter of the gas molecules and $(const)$ denotes specific constants. Based on these expressions, various relations for the transport coefficients μ and λ were proposed in the literature, e.g. [39, 44, 87, 193], which include also extensions for polar gases at high pressures. A comprehensive description of these methods are provided in [187].

In the present work the correlations of Chung et al. [44] are utilized to calculate the transport coefficients μ and λ. These generalized correlations are based on the kinetic gas theory and account for polar, non-polar and associating fluids at low and high pressures.

The complete model formulation including the empirical model parameters can be found in the original publication of Chung et al. [44]. An evaluation of the thermodynamic and transport models is provided in chapter 8.

2.3 Turbulent heat and fluid flow

In thermo-fluid dynamics, one distinguishes between laminar and turbulent heat and fluid flow. Both regimes, laminar and turbulent, are fully represented by the balance laws of thermo-fluid mechanics (see section 2.1). Thereby, turbulence occurs in flow regimes where momentum convection overwhelms momentum diffusion, such that small disturbances are able to grow leading eventually to a transition from laminar to turbulent state. Whether or not such a transition takes place depends on the Reynolds number, which measures the relative importance of inertial forces to viscous forces within a fluid flow. It is defined for a flow with the characteristic velocity U and the characteristic length scale L as [11]

$$Re = \frac{\rho U L}{\mu}. \tag{2.16}$$

Thereby, turbulent flow is the usual state of fluid motion at high Reynolds numbers (e.g. $Re \gg 2000$ in channel flow), while the flow regime is laminar at low Reynolds numbers.

Most heat transport and fluid flows occurring in the nature and created in engineering applications are turbulent such as hot smoke from a chimney, mixing in an internal combustion engine, or geophysical flows like storm clouds. Figure 2.1 shows planar images of the magnitude velocity (a) and temperature (b) fields of a turbulent injection process of cryogenic nitrogen into a warm nitrogen environment at a jet Reynolds number of $Re_j = 5500$. On closer inspection of the temperature and flow field of the jet, a wide range of length and time scales can be observed and it is obvious that these turbulent motions are unsteady, irregular, seemingly random and chaotic [189]. Thereby, the quasi-chaotic and unsteady motions of the turbulence churn up the flow and enhance the mixing. However they also increase the disorder of the system associated with an imminent loss of available mechanical power. This is in contrast to laminar flow regimes, where the fluid streams in parallel layers without disruption between those layers [21] and mixing processes are mostly dominated by diffusive fluxes rather than turbulent diffusion.

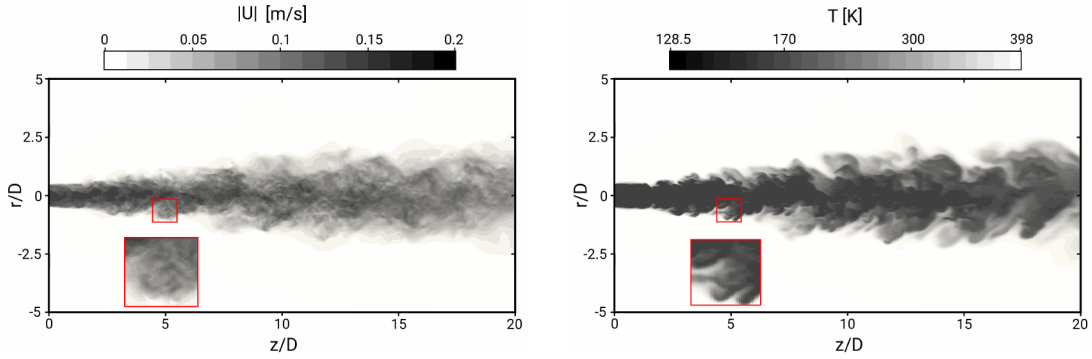

(a) (b)

Figure 2.1: Injection of a turbulent round jet of cryogenic nitrogen into a warm nitrogen environment at a jet Reynolds number of $Re_j = 5500$. Snapshots of the magnitude velocity (a) and temperature (b) fields. DNS results of Ries et al. [E2].

As implied by the above discussion, turbulent heat and fluid flows are locally quasi-stochastic, inherently three dimensional, unsteady, vortical and dissipative. Turbulent flows exhibit a wide distribution of length and time scales which interact with each other. Thereby, energy from large scale motions is transferred to successively smaller and smaller scales until the molecular viscosity or thermal diffusivity are effective in dissipating the energy [189], respectively. Even though these mentioned features of turbulence are common to most turbulent flows and are analyzed in numerous experimental and numerical studies over the last century, it is worth noting that an unique theoretical description of turbulence still does not exist.

The inherently unsteady and random nature of turbulent fields makes statistical methods the appropriate approach for their description. Thereby, in most studies of turbulent heat and fluid flow, statistical moments are utilized to describe the properties of the temperature and flow field. Other important aspects in the description of turbulent heat and fluid flows are the characterization of small-scale turbulence and large-scale motions as well as the way how energy is transfered between these scales. Basic concepts of the statistical description of turbulence and the dynamics of turbulent motions will be given in the following sections. Thereby, only aspects relevant for the understanding of this thesis are provided. Further information and explanations of the vast topic of turbulence theory can be found in e.g. [21, 189, 226].

2.3.1 Statistical description of turbulence

An essential feature of turbulent heat and fluid flow is that the temperature and fluid velocity fields vary significantly and irregularly in both position and time [189]. Consequently, they are random variables and inherently unpredictable. Therefore, in most experimental and numerical studies, statistical methods are utilized to describe the properties of the temperature and flow field, which is also the case in this work.

In turbulent processes, a single random variable Q, e.g. the velocity component in main flow direction or the temperature, is completely characterized by its probability density function $f(V)$ [189], which describes the relative likelihood that Q has the same value of the sample space variable V. Thereby, $f(V)$ can be measured in an experiment or predicted in a numerical simulation with some confidence level. However, instead of examining the entire probability density function $f(V)$, it is often more convenient to describe $f(V)$ by means of statistical moments.

In the case of statistically stationary turbulent flows as assumed in the present work, the time averaged mean, variance and standard deviation of Q integrated over a time interval Δt can be calculated as

$$\mu_1 = \langle Q \rangle = \frac{1}{\Delta t} \int_t^{t+\Delta t} Q\left(t'\right) dt', \tag{2.17}$$

$$\mu_2 = \left\langle Q'^2 \right\rangle = \left\langle \left(Q - \langle Q \rangle\right)^2 \right\rangle, \tag{2.18}$$

$$Q_{rms} = \sqrt{\langle Q'^2 \rangle}, \tag{2.19}$$

where $Q' = Q - \langle Q \rangle$ is the fluctuation of Q. Higher order central moments like the skewness or the kurtosis of the probability distribution can be obtained by

$$\mu_i = \left\langle \left(Q - \langle Q \rangle\right)^i \right\rangle, \tag{2.20}$$

where i denotes the i^{th} statistical moment of the probability density function $f(V)$.

For statistically stationary turbulent processes, information about the correlations between the process at time t and $t+s$ can be obtained by means of the autocovariance

$$\rho_i(s) =< Q_i'(\mathbf{x},t)Q_i'(\mathbf{x},t+s) >, \tag{2.21}$$

from which the integral time scales of the turbulent process can be estimated as

$$\tau_i = \frac{1}{\rho_i(0)} \int_{s=0}^{s\mapsto\infty} \rho_i(s)ds. \tag{2.22}$$

Thereby, τ_i describes the temporal decorrelation distance of the turbulent quantity Q_i.

Information on the spatial structures of random fields can be estimated by means of the two-point correlation tensor [189]

$$R_{ij}(\mathbf{r}) =< Q_i'(\mathbf{x},t)Q_j'(\mathbf{x}+\mathbf{r},t) >, \tag{2.23}$$

where $\mathbf{r}$ is the spatial lag-distance vector. From this, it is possible to define various length scales, e.g. the longitudinal length scale

$$L_{11} = \frac{1}{R_{11}(0)} \int_{r=0}^{r\mapsto\infty} R_{11}(\mathbf{e}_1 r)dr, \tag{2.24}$$

which describes the spatial decorrelation distance of the turbulent quantity Q_1 in x_1-coordinate direction.

Regarding homogeneous turbulence, the correlation tensor $R_{ij}(\mathbf{r})$ is independent of the location $\mathbf{x}$ and Fourier transformation gives the spectrum tensor [189]

$$\Phi_{ij} = \frac{1}{8\pi^3} \iiint_{-\infty}^{\infty} e^{-i\boldsymbol{\kappa}\cdot\mathbf{r}} R_{ij}(\mathbf{r})d\mathbf{r}, \tag{2.25}$$

where $\boldsymbol{\kappa}$ denotes the wavenumber vector and i is the imaginary unit. Integration of Φ_{ij} over a sphere in wave number space and contraction defines the energy spectrum $E(\kappa)$ [113]

$$E(\kappa) = \frac{1}{2} \oint \Phi_{ii}(\boldsymbol{\kappa})dS(\kappa), \tag{2.26}$$

where $S(\kappa)$ are the surfaces of the spheres with radius κ. $E(\kappa)$ describes the distribution of kinetic energy into wavenumber components composing the signal of Q_i with the property

$$\frac{1}{2}\left\langle Q_i'Q_i'\right\rangle = \int_0^{\infty} E(\kappa)d\kappa, \tag{2.27}$$

where the integration is performed over all scalar wave numbers. The energy spectrum is a very useful quantity to analyze turbulent flows qualitatively and plays a central role in the theoretical description of turbulent heat and fluid flow as will be shown later.

In experimental investigations or numerical simulations of turbulent heat and fluid flow, the statistical quantities described above are usually estimated by a finite number of sample averages over a finite time period and/or a finite spatial distance. They consequently contain stochastic errors, that can be estimated using the central limit theorem [130, 29, 229]. Regarding temporal averaging of stationary turbulent flows, statistically independent events occur after approximately two integral time scales, corresponding to the so-called temporal decorrelation distance. By following the procedure described in [229, 29], the

number of statistically independent samples N at position $\mathbf{x}$ can be estimated as $N = \Delta t/(2\tau)$, where Δt is the averaging time and τ is the appropriate integral time scale.

By means of the central limit theorem, the standard deviation of the estimator of mean quantities can be determined as $\sigma_t(\langle Q\rangle) = Q_{rms}/\sqrt{N}$. Similarly, the standard deviation of the estimator of rms quantities is given for normal distribution as $\sigma_t(Q_{rms}) = Q_{rms}/\sqrt{2N}$. Normalizing $\sigma_t(\langle Q\rangle)$ by the expectation of Q and $\sigma_t(\langle Q_{rms}\rangle)$ by the rms value of Q, both at the same position $\mathbf{x}$, leads to the following sampling errors for mean and rms quantities of turbulent flows

$$e_t^{rand}(\langle Q\rangle) = \frac{Q_{rms}}{\langle Q\rangle}\cdot\sqrt{\frac{2\cdot\tau}{\Delta t}}, \quad e_t^{rand}(Q_{rms}) = \sqrt{\frac{\tau}{\Delta t}}. \tag{2.28}$$

Notice that in the case of turbulent flows that are intrinsically not statistically stationary, e.g. in-cylinder flows in internal combustion engines or transition processes, the expression in equation 2.28 are not appropriate to estimate the sampling error. In such cases, ensemble-averaging has to be applied, whereby N is the number of independent samples.

In the case of statistically homogeneous flows, sample averages can be also obtained by means of spatial averaging along a homogeneous direction. Thereby, a statistically independent event occurs after approximately two integral length scales, corresponding to the so-called spatial decorrelation distance. Again, using the central limit theorem leads to the following sampling errors for the spatial mean and rms velocities

$$e_s^{rand}(\langle Q\rangle_s) = \frac{Q_{rms}^s}{\langle Q\rangle_s}\cdot\sqrt{\frac{2\cdot L}{\Delta l}}, \quad e_s^{rand}(Q_{rms}^s) = \sqrt{\frac{L}{\Delta l}}, \tag{2.29}$$

where $< . >_s$ denotes spatial averaging, Q_{rms}^s is the spatial rms value of Q, L is the corresponding integral length scale and Δl is the spatial averaging distance (e.g. the extent of the computational domain).

It remains how the sampling error of other statistical quantities and for arbitrary distributions in turbulent processes can be estimated. For this purpose, table 2.4 provides variances of the estimators of basic statistical moments of turbulent processes. Appropriate values of N can be calculated using equation 2.22 in the case of temporal averaging and using equation 2.24 for spatial averaging. Further estimators of statistical moments utilized in the study of turbulence can be found in [29, 229].

Statistic	μ_2 Gaussian distribution	μ_2 Arbitrary distribution
$\langle Q\rangle$	$\langle Q'^2\rangle/N$	$\langle Q'^2\rangle/N$
$\sqrt{\langle Q'^2\rangle}$	$\langle Q'^2\rangle/(2N)$	$\left(\langle Q'^4\rangle - \langle Q'^2\rangle^2\right)/\left(4\langle Q'^2\rangle N\right)$
$\langle Q'^2\rangle$	$2\langle Q'^2\rangle^2/N$	$\left(\langle Q'^4\rangle - \langle Q'^2\rangle^2\right)/N$
$\langle Q'_iQ'_j\rangle$	$\left(1+\frac{\rho_{ij}^2}{\langle Q_i'^2\rangle\langle Q_j'^2\rangle}\right)\langle Q_i'^2\rangle\langle Q_j'^2\rangle/N$	$\left(\langle Q_i'^2Q_j'^2\rangle - \langle Q_iQ_j\rangle^2\right)/N$

Table 2.4: Variances of estimators of basic statistical moments.

After introducing the basic statistical tools used in the description of turbulent processes, some important statistical quantities of the velocity and temperature fields among their physical interpretation are briefly outlined for further discussion. In the case Q is the velocity vector U_i, one important statistical quantity is the covariance matrix of the

velocity vector, also called Reynolds stress tensor. It stems from the momentum transfer by the fluctuating velocity field and is defined as

$$cov\left(U_i, U_j\right) = \left\langle U_i' U_j' \right\rangle = \left\langle \left(U_i - \left\langle U_i \right\rangle\right)\left(U_j - \left\langle U_j \right\rangle\right) \right\rangle = \left\langle U_i U_j \right\rangle - \left\langle U_i \right\rangle \left\langle U_j \right\rangle, \tag{2.30}$$

where half the trace of the Reynolds stress tensor is the turbulent kinetic energy

$$k = \frac{1}{2}\left\langle U_i' U_i' \right\rangle = \int_0^\infty E_k(\kappa) d\kappa. \tag{2.31}$$

Here $E_k(\kappa)$ is the turbulent kinetic energy spectrum.

Similar to the Reynolds stress tensor, the turbulent heat flux vector describes the heat transport by the fluctuating velocity and temperature fields associated with turbulent diffusion of heat. It is defined by the second order moment of velocity and temperature and can be quantified as

$$\left\langle U_i' T' \right\rangle = \left\langle \left(U_i - \left\langle U_i \right\rangle\right)\left(T - \left\langle T \right\rangle\right) \right\rangle = \left\langle U_i T \right\rangle - \left\langle U_i \right\rangle \left\langle T \right\rangle. \tag{2.32}$$

Usually in turbulent flows with heat transport, the turbulent heat flux overwhelms molecular thermal diffusion and enhances the thermal mixing process.

As the turbulent kinetic energy characterizes the energy of the fluctuating velocity field, the temperature variance characterizes the level of temperature fluctuations. It reads

$$\theta = \frac{1}{2}\left\langle T' T' \right\rangle = \int_0^\infty E_\theta(\kappa) d\kappa, \tag{2.33}$$

where $E_\theta(\kappa)$ is the temperature variance spectrum.

2.3.2 Scales of turbulent motion and the energy cascade

As already mentioned above, turbulence is characterized by a wide range of length and time scales. The physical dimensions of these scales and the way energy is transferred between them are the topics of this section. Thereby, important differences between heat and fluid flow are highlighted. It is important to mention here, that most of the concepts presented below are only valid in the case of fully turbulent flows at sufficiently high Reynolds number with constant physical properties and only away from viscous walls.

Based on the concept of the energy cascade introduced by Richardson [194], turbulence can be considered to be composed of coherent turbulent motions of different size. The generated large scale motions (e.g. by separation) break up and transfer their energy to slightly smaller ones. These large scale motions have dimensions of the order of the flow domain $l_0 = \mathcal{O}\left(\mathcal{L}\right)$ and their energy predominantly comes from the mean flow. These smaller scales undergo a similar break-up process. Within this break up process, energy is transferred to successively smaller and smaller scales until the molecular viscosity or thermal diffusivity are effective in dissipating the energy [189], respectively, and no smaller vortices can be formed. Based on Kolmogorov's similarity theory and his hypothesis of local isotropy [120, 119], the directional tendencies along with all information about the geometry of large scale motions get lost in this chaotic scale-reduction process, leading to universal, homogeneous, isotropic small scales. Important in this context is that energy enters the energy cascade at largest scales, while dissipation is placed at the end of the scale-reduction process.

In the case of turbulent fluid flow, the smallest length, velocity and time scales are of the order of the Kolmogorov scales defined as

$$\eta_K \equiv \left(\frac{\nu^3}{\epsilon_k}\right)^{1/4}, \qquad u_K \equiv \left(\nu \epsilon_k\right)^{1/4}, \qquad \tau_K \equiv \left(\frac{\nu}{\epsilon_k}\right)^{1/2}, \tag{2.34}$$

that depend only on the dissipation rate of turbulent kinetic energy ϵ_k and the viscosity ν. By assuming a scaling of $\epsilon_k \sim u_0^3/l_0$ it follows that the ratio between these smallest scales and the largest turbulent motions are proportional to the Reynolds number as

$$\frac{\eta_K}{l_0} \sim Re^{-3/4}, \qquad \frac{u_K}{u_0} \sim Re^{-1/4}, \qquad \frac{\tau_K}{\tau_0} \sim Re^{-1/2}, \tag{2.35}$$

which shows that smallest scales becomes very small compared to largest scales in the case of high Reynolds numbers.

Regarding the turbulent temperature field, dimensional analysis yields $\eta_T \propto (\alpha\tau)^{1/2}$ for the smallest length scales, where α is the thermal diffusivity and τ the characteristic time scale which differs for low and high Prandtl numbers [203]. For $Pr \leq 1$, smallest length scales are dictated by both, thermal diffusivity α and by viscous dissipation. These are the Obukhov-Corrsin length scales [168, 47]

$$\eta_{OC} \equiv \left(\frac{\alpha^3}{\epsilon_k}\right)^{1/4} = Pr^{-3/4}\eta_K, \tag{2.36}$$

with dimensions equal or larger than the Kolmogorov scales. For $Pr > 1$, viscous diffusion overwhelms thermal diffusion and the smallest temperature length scales are referred to as the Bachelor length scales [20]

$$\eta_B \equiv \left(\frac{\alpha^2\nu}{\epsilon_k}\right)^{1/4} = Pr^{-1/2}\eta_K, \tag{2.37}$$

which are by a factor of $Pr^{-1/2}$ smaller than the Kolmogorov length scales. Obviously, smallest temperature scales are less universal than those of the velocity field and can be significantly smaller for $Pr \gg 1$. Another interesting consequence is that, in contrast to smallest velocity scales, the ratio between smallest and largest temperature scales depend not only on the Reynolds number but also on the molecular Prandtl number.

Next, it is described how the turbulent kinetic energy and the temperature variance are distributed among these turbulent scales of different sizes. This is illustrate in figure 2.2, which shows the wave number spectrum of turbulent kinetic energy (a) and the temperature variance spectra for different Pr numbers (b).

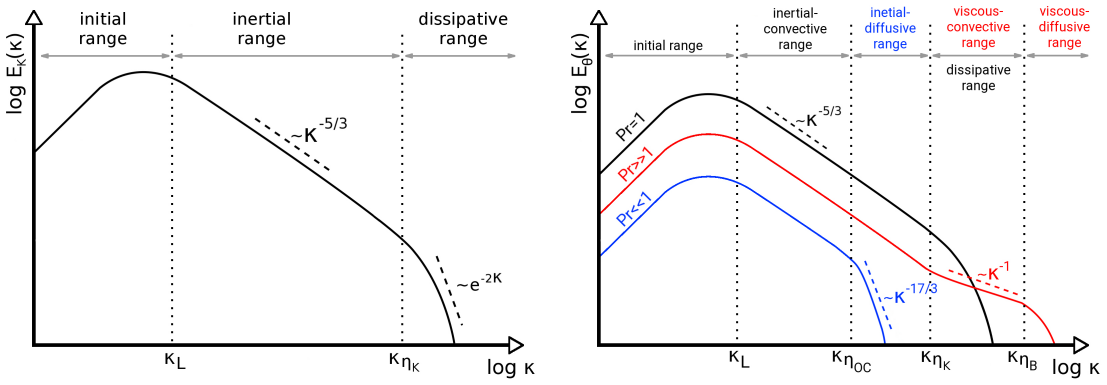

(a) (b)

Figure 2.2: Energy spectrum of a turbulent flow (a) and temperature variance spectra for different Prandtl numbers (b).

Considering the turbulent kinetic energy spectrum depicted in figure 2.2 (a), it can be seen that the bulk of the energy is contained in the large scale motions. This size range is called *energy-containing range* or *initial range* and in the conception of the energy cascade, it is the size range where energy, predominantly fed from the mean flow, enters the cascade. Then, inertia forces spread energy from small to large wave numbers and the directional tendencies of large scale motions get lost. Thereby, molecular-viscous effects can be neglected. This size range is called *inertial range*, where according to Kolmogorov's second similarity hypothesis, $E(\kappa)$ has a universal form determined only by ϵ_k and independent of ν. An expression for the shape of the energy spectrum in the inertial subrange can be obtained straightforward from dimensional analysis as:

$$E_K(\kappa) = C_K \epsilon_k^{2/3} \kappa^{-5/3}, \tag{2.38}$$

where $C_K \approx 1.5$ is the Kolmogorov constant. Finally, at higher wave numbers $\sim \eta_K$, viscous effects are dominant. This size range is called *dissipative range*. Here, turbulent kinetic energy of smallest scales is dissipated into heat.

The energy transfer phenomena becomes more complicated when temperature diffuses in isotropic homogeneous turbulence. The main reason is that the temperature variance spectrum as well as the dynamics of small temperature scales have a less universal character than in turbulent fluid flow as can be seen in figure 2.2 (b). Based on the value of the molecular Prandtl number Pr three different physical regimes associated with different scalar dynamics can be distinguished. For $Pr < 1$, thermal diffusivity is larger than molecular viscosity and the dissipation of smallest temperature scales occurs within the inertial range of the kinetic energy spectrum [203]. Therefore, two inertial ranges exist in the temperature variance spectrum. In the first one, length scales are larger than Obukhov-Corrsin length scales, e.g. $\kappa_{\eta_{OC}} \ll \kappa \ll \kappa_L$, which is called the *inertial-convective range*. These scales are not subjected to viscous and diffusive effects and solely dominated by the stirring induced by velocity fluctuations [203]. Thereby, the form of the temperature variance spectrum is given as

$$E_\theta(\kappa) = C_{OC} \epsilon_\theta \epsilon_k^{-1/3} \kappa^{-5/3}, \tag{2.39}$$

where $C_{OC} = 0.67$ is the Obukhov-Corrsin constant and ϵ_θ is the dissipation rate of temperature variance. The second inertial range, the so-called *inertial-diffusive range* is located within the wave number band of $\kappa_{\eta_K} \ll \kappa \ll \kappa_{\eta_{OC}}$, where thermal-conductive effects are predominant. Here, the temperature variance spectrum is

$$E_\theta(\kappa) = \frac{1}{3} C_K \alpha^{-3} \epsilon_\theta \epsilon_k^{2/3} \kappa^{-17/3}, \tag{2.40}$$

where α is the molecular thermal diffusivity. For $Pr \backsimeq 1$ the shape of the temperature variance spectrum is similar to that of the kinetic energy. Thus, the dynamics and size of temperature and velocity scales are similar, leading to the existence of a unique inertial-convective range in the wave number range of $\kappa_{\eta_K} \ll \kappa \ll \kappa_L$. The shape of this unique inertial-convective range equals equation 2.39. Finally, in the case $Pr \gg 1$, heat conduction has no noticeable influence on small scale temperature fluctuations, while velocity scales are damped by viscous dissipation. Thereby, two inertial ranges exists. Similar to $Pr \leq 1$, the temperature variance spectrum exhibits an inertial-convective subrange within the wave numbers of $\kappa_{\eta_K} \ll \kappa \ll \kappa_L$. In this size range, the shape of the spectra is similar to that of equation 2.39. The second inertial range, the *viscous-convective range*, is located

at high wave numbers within the range of $\kappa_{\eta_B} \ll \kappa \ll \kappa_{\eta_K}$. The associated spectrum is given as

$$E_\theta(\kappa) = \frac{1}{2}\sqrt{\frac{\nu}{\epsilon_k}}\epsilon_\theta \kappa^{-1}. \tag{2.41}$$

Besides the different shapes of the temperature variance spectra for different Prandtl numbers, small temperature scales are also influenced by the interaction of the velocity gradient and the scalar fluctuations, which leads to anisotropic thermal diffusion even at smallest temperature scales.

Chapter 3

LES Modeling of turbulent heat and fluid flow

In dealing with numerical simulations of turbulent heat transport and fluid flow, the leading computational approaches to calculate the turbulent quantities of interest and practical relevance are: direct numerical simulations (DNS), large eddy simulations (LES) and approaches based on the solution of the Reynolds-averaged Navier-Stokes (RANS) equations. These approaches can be categorized based on their level of description, computation expense, range of applicability and accuracy.

In DNS, the wide range of turbulent length and time scales are fully resolved such that no additional turbulence model is required. This means that the spatial and temporal resolution must be as fine enough as the smallest characteristic length and time scales of the continuous fluid flow problem [203], and the computational domain has to be sufficiently large enough to capture largest scales. Since the computational cost increases as $\sim Re^3$ in DNS, this approach is predominantly restricted to heat and fluid flows with low-to-moderate Reynolds numbers [189]. It is therefore not surprisingly that nowadays DNS is mainly applied by scientific groups mostly to generate reference databases for model development or to analyze specific physical processes, but it is usually not used in engineering practice to simulate complex technical applications.

In contrast, RANS simulations only solve the Reynolds equations to obtain the mean flow, while turbulent motions are not explicitly captured. Thereby, the entire spectrum of turbulence is described by means of closure models. On the one hand, this leads to a significant reduction of the required computational resources compared to DNS making simulations of turbulent flows feasible for complex engineering applications with high Reynolds numbers. On the other hand, it is well known that the prediction of complex heat and fluid flows based on RANS is not always accurate for many cases, especially for flows with large scale, unsteady characteristics.

To overcome the limitations of DNS and RANS, many researchers have paid more attention towards LES as an alternative method to predict turbulent flows. In LES, the large three-dimensional unsteady turbulent motions are explicitly computed whilst a turbulence closure model accounts for the influence of the unresolved more universal small scales [113]. The benefit is quite obvious. First, the computational expense of LES is significantly lower than that of DNS, purely a weak function of the Reynolds number when dealing with turbulent flows remote from solids walls. Secondly, only small scale turbulent structures with a small amount of turbulent kinetic energy have to be modeled, which are believed to be universal, homogeneous and isotropic. This simplifies the turbulence modeling, improves the predictive capability compared to RANS and makes LES valid for

a wide range of flow situations. In this way, the LES approach is a compromise between DNS and RANS, well suited for turbulent flows where traditional RANS predictions fail [113] and the computation expense of DNS is too high.

In the present work, the LES technique is used to calculate unsteady turbulent heat transport and fluid flow problems of both, basic interest and engineering applications. By means of this, irreversibilities evolving in such thermo-fluid flows are examined and entropy generation maps are provided. To validate the LES and to analyze evolving processes, DNS data is also generated to support the LES development. This will be addressed in the next chapters. Notice that experimental data from the literature will be also utilized in the validation of LES results for high Reynolds numbers.

In this chapter, first the basic concept of LES is outlined including the theory of scale separation, the applied LES transport equations and the quality assessment of LES results. Thereby, new quality criteria regarding the averaging time in LES statistics are proposed. Then, common subgrid-scale models for the momentum transport are briefly described. In particular, an improved one-equation subgrid-scale kinetic energy model for wall-bounded turbulent flows is presented. Subsequently, classical and extended subgrid-scale models for turbulent heat transport are discussed and a new anisotropy resolving algebraic heat flux model that fulfills the irreversibility requirements of the second law is proposed. Finally, a novel subgrid-scale modeling approach for entropy production rates, essential for the analysis of irreversibilities in thermo-fluid flows, is presented.

3.1 Concept of large eddy simulation

The basic concept of LES is to compute large energy containing turbulent motions explicitly and to use a turbulence closure model to take into account the influence of the unresolved small scales. The rationale of such an approach can be justified on the basis of the turbulence theory. As outlined in section 2.3, large scale turbulent motions cascade into successively smaller and smaller scales until the molecular viscosity is effective in dissipating the smallest scales into heat. Thereby, the directional tendencies along with all information about the geometry of large scale motions get lost in this chaotic scale-reduction process, leading to universal, homogeneous, isotropic smaller scales. The universal, isotropic character of small scales justifies the cut off and modeling of these scales in LES, while the energy containing large scale motions, that are essentially anisotropic, are calculated explicitly within this approach.

Usually, in the most LES approaches, the separation of large and small scales is performed by filtering the flow field such that it can be represented as the sum of a filtered and a residual part. In this context two filtering approaches exist, LES with explicit filtering and LES with implicit filtering. In the explicit filtering approach, a specific filter (typically box or Gaussian) is applied explicitly to the non-linear terms in the discretized balance equations while in the case of implicit filtering the numerical grid itself is assumed to be the LES filter. Both approaches are combined with an additional subgrid-scale closure model to represent the residual part. Besides the filtering approach, other variants of LES are also available in the literature, like the monotone-integrated large eddy simulation procedure (MILES) [30], in which artificial dissipation by a TVD scheme is used as an implicit subgrid scale model. In the present work, LES with implicit filtering is utilized due to its simplicity and robustness. Therefore, the discussion about scale separation, LES transport equations and quality assessment in LES are restricted to topics relevant for LES with implicit filtering. Further details about other variants of LES and filtering can be found in [203].

3.1.1 Scale separation

For a given a turbulent field $\psi(\mathbf{x})$ that contains all scales of motions, the filtered field $\overline{\psi}(\mathbf{x})$ is defined as [189]

$$\overline{\psi}(\mathbf{x}) = \int_{-\infty}^{\infty} G(\mathbf{r}, \mathbf{x})\psi(\mathbf{x} - \mathbf{r})d\mathbf{r} =: G * \psi, \tag{3.1}$$

where $G(\mathbf{r}, \mathbf{x})$ is the convolution or filter kernel. From the convolution theorem it follows that

$$\widehat{\overline{\psi}}(\kappa) = \widehat{G}(\kappa)\widehat{\psi}(\kappa), \tag{3.2}$$

where $\widehat{\cdot}$ denotes the Fourier transform of a quantity. To conserve constant values, the convolution kernel has to fulfill the normalization condition

$$\int_{-\infty}^{\infty} G(\mathbf{r}, \mathbf{x})d\mathbf{r} = \widehat{G}(0) = 1. \tag{3.3}$$

Then the turbulent field $\psi(\mathbf{x})$ can be decomposed into the sum of a filtered and a residual part as

$$\psi(\mathbf{x}) = \overline{\psi}(\mathbf{x}) + \psi'(\mathbf{x}), \tag{3.4}$$

where the large scales motions are represented by the field $\overline{\psi}(\mathbf{x})$ and the small scales by $\psi'(\mathbf{x})$.

In order to be able to apply a filter to the balance laws, the filter has to testify the following three properties [203]:

1. Conservation of constants: $\overline{c} = c$.
2. linearity: $\overline{\phi + \psi} = \overline{\phi} + \overline{\psi}$.
3. Commutation with derivation: $\overline{\partial\psi/\partial x} = \partial\overline{\psi}/\partial x$.

The last property, commutation with derivation, holds only true in the case of homogeneous filters, i.e. filters that are independent of $\mathbf{x}$. This can be shown by finding the partial derivative of expression 3.1 as

$$\frac{\partial\overline{\psi}}{\partial x} = \overline{\frac{\partial\psi}{\partial x}} + \int_{-\infty}^{\infty} \frac{\partial G(\mathbf{r}, \mathbf{x})}{\partial x}\psi(\mathbf{x} - \mathbf{r})d\mathbf{r}, \tag{3.5}$$

where the second part on the right-hand side vanishes only if the filtering length does not vary in respect to x. For inhomogeneous filters, it is found by Ghosal and Moin [72] that the commutation error is of second order in the filter width $\mathcal{O}\left(\Delta^2\right)$. Therefore, the influence of the commutation error might be neglected in a code with second order accuracy as used in this study. Other important features of the filtering approach are: (1) that the filter operation is in general no projection like the Reynolds operator, which means that $\overline{\overline{\psi}} \neq \overline{\psi}$, (2) the filter is not idempotent $\overline{\phi\overline{\psi}} \neq \overline{\phi\psi}$, and (3) filtered subgrid-scale quantities in general do not vanish $\overline{\psi'} \neq 0$, which directly follows from the first point.

The most widely used filter kernels in LES practice are the box filter, the Gaussian filter and the sharp spectral filter. The box filter is simply the volume average over a sphere of radius $1/2\Delta$, the Gaussian filter is the joint normal with mean zero and covariance $\delta_{ij}\Delta^2/12$, and the sharp spectral filter includes all modes with $|\boldsymbol{\kappa}| \geq \kappa_c$ [189], where Δ is the characteristic filter width and κ_c is the cut-off wave number. The filter functions $G(r)$ in physical space and the corresponding filter transfer functions $\widehat{G}(\kappa)$ in wave number space of the box, Gaussian and sharp spectral filters in one-dimension are shown in figure 3.1 (a) and (b), respectively.

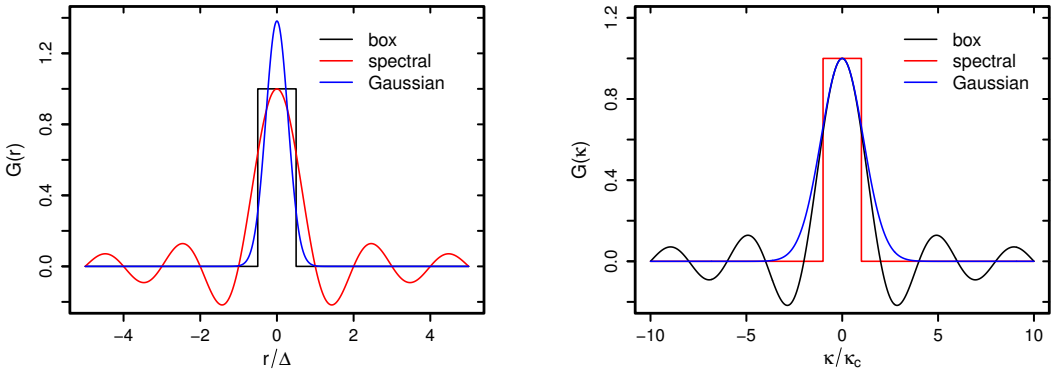

(a) (b)

Figure 3.1: Filter and filter transfer functions in physical (a) and wave number spaces (b).

As it can be seen, the Gaussian filter decreases strictly monotonically with increasing distance in both, physical and wave number space. In contrast, the box and spectral filters exhibit fading oscillations for high wave number and high spatial distance, respectively. As a consequence, box or Gaussian filters are usually utilized in finite volume or finite difference methods, while Gaussian or sharp filters are preferred in spectral codes [113].

Table 3.1 summarizes the one-dimensional filter functions and transfer functions of the box, Gaussian and sharp spectral filters. The extension of these filter functions to the three dimensional case is straightforward by defining them as a function of the radius or as a product of three one dimensional filters. The latter produces an anisotropic filter [113].

Filter	Filter function $G(r)$	Transfer function $\widehat{G}(\kappa)$
Box	$\frac{1}{\Delta} H\left(\frac{1}{2}\Delta - \lvert r\rvert\right)$	$\frac{sin(1/2\kappa\Delta)}{1/2\kappa\Delta}$
Gaussian	$\sqrt{\frac{6}{\pi\Delta^2}}\exp\left(-\frac{6r^2}{\Delta^2}\right)$	$\exp\left(-\frac{\kappa^2\Delta^2}{24}\right)$
Sharp spectral	$\frac{sin(\pi r/\Delta)}{\pi r}$	$H\left(\kappa_c - \lvert\kappa\rvert\right)$

Table 3.1: Filter and filter transfer functions for one dimensional filters.

The discrete form of a filtered quantity at the ith grid point can be expressed as [65]

$$\overline{\psi}_i = G\psi_i = \sum_{n=-M}^{N} a_n \psi_{i+n}, \tag{3.6}$$

with a_n are the specific filter coefficients and the normalization condition

$$\sum_{n=-M}^{N} a_n = 1. \tag{3.7}$$

In the present work, discrete filtering is used in subgrid-scale models with dynamic procedures as it will be described later on. Thereby, the filter coefficients are estimated by the ratio of the face-surface area to cell-surface area.

Finally, in LES of turbulent heat and fluid flow with variable density, usually Favre-filtering is used to simplify the set of LES equations. Thereby, filtered variables are

weighted by the density leading to

$$\widetilde{\psi} = \frac{\overline{\rho\psi}}{\overline{\rho}}. \tag{3.8}$$

By means of this, the turbulent field ψ can be decomposed into a sum of a Favre-filtered and a residual part as

$$\psi = \widetilde{\psi} + \psi'', \tag{3.9}$$

where $(.)''$ denotes the fluctuation with respect to Favre-filtering. Similar to filtering with constant density, the Favre-operator $\widetilde{(.)}$ is linear but does not commute with derivation [65]. However, the commutation error is within the accuracy obtainable by a numerical scheme of second order. It is therefore often neglected in a second order code, which is also the case in this work.

3.1.2 LES transport equations

Applying a commutative filter to the balance laws of an incompressible Newtonian fluid with variable physical properties and Fourier heat flux (see table 2.1) leads to

$$\frac{\partial\overline{\rho}}{\partial t} = -\frac{\partial}{\partial x_i}\left(\overline{\rho}\widetilde{U}_i\right), \tag{3.10}$$

$$\frac{\partial\overline{\rho}\widetilde{U}_i}{\partial t} = -\frac{\partial}{\partial x_j}\left(\overline{\rho}\widetilde{U_iU_j}\right) - \frac{\partial\overline{p}}{\partial x_i} + \frac{\partial\overline{\tau_{ij}}}{\partial x_j} + \overline{\rho}g_i, \tag{3.11}$$

$$\frac{\partial\overline{\rho}\widetilde{h}}{\partial t} = -\frac{\partial}{\partial x_j}\left(\overline{\rho}\widetilde{U_jh}\right) + \frac{\partial}{\partial x_i}\left(\frac{\overline{\lambda}}{\overline{c}_p}\frac{\partial\widetilde{h}}{\partial x_i}\right), \tag{3.12}$$

where the viscous dissipation and the pressure velocity terms in the enthalpy equation are assumed to be small in incompressible flows and therefore neglected. The convective terms $\overline{\rho}\widetilde{U_iU_j}$ and $\overline{\rho}\widetilde{U_jh}$ in the momentum and enthalpy equations are unknown and can not be directly calculated by the Favre-filtered fields. Consequently, both terms have to be modeled in the LES approach. For this purpose, the unknown terms can be decomposed according to Leonard [131] using a triple decomposition as

$$\left(\widetilde{\phi\psi} - \widetilde{\phi}\widetilde{\psi}\right) = \underbrace{\left(\widetilde{\widetilde{\phi}\widetilde{\psi}} - \widetilde{\phi}\widetilde{\psi}\right)}_{\mathbf{L}} + \underbrace{\left(\widetilde{\widetilde{\phi}\psi''} - \widetilde{\widetilde{\psi}\phi''}\right)}_{\mathbf{C}} + \underbrace{\left(\widetilde{\phi''\psi''}\right)}_{\mathbf{R}}, \tag{3.13}$$

where $\mathbf{L}$ is the Leonard term that represents interactions among large scales, $\mathbf{C}$ the cross-stress term which accounts for interactions between the resolved and residual scales, and $\mathbf{R}$ the Reynolds subgrid tensor that represents the interactions between subgrid scales. In the case $\phi = U_i$ and $\psi = U_j$, the left-hand side of equation 3.13 represents the subgrid-scale tensor τ_{ij}^{sgs}. In the case $\phi = U_i$ and $\psi = h$, the left-hand side represents the subgrid-scale heat flux vector q_i^{sgs}.

In contrast to the Reynolds stresses $\mathbf{R}$, the Leonard stresses $\mathbf{L}$ and the cross-stresses $\mathbf{C}$ are not Galilean invariant, i.e. a change of the inertial system changes the terms. Only the sum of them fulfills this demand. Therefore, the Leonard decomposition is not feasible for LES modeling [203]. Instead, the sum of these three terms, $\tau_{ij}^{sgs} = \mathbf{L}_u + \mathbf{C}_u + \mathbf{R}_u$ and $q_i^{sgs} = \mathbf{L}_\theta + \mathbf{C}_\theta + \mathbf{R}_\theta$, is modeled in LES with implicit filtering [113]. Thus, in the case of

LES with implicit filtering the transport equations of mass, momentum and enthalpy can be formulated as [203]

$$\frac{\partial \overline{\rho}}{\partial t} = -\frac{\partial}{\partial x_i}\left(\overline{\rho}\widetilde{U}_i\right), \tag{3.14}$$

$$\frac{\partial \overline{\rho}\widetilde{U}_i}{\partial t} = -\frac{\partial}{\partial x_j}\left(\overline{\rho}\widetilde{U}_i\widetilde{U}_j\right) - \frac{\partial \overline{p}}{\partial x_i} + \frac{\partial}{\partial x_j}\left(\overline{\tau}_{ij} - \overline{\rho}\tau_{ij}^{sgs}\right) + \overline{\rho}g_i, \tag{3.15}$$

$$\frac{\partial \overline{\rho}\widetilde{h}}{\partial t} = -\frac{\partial}{\partial x_j}\left(\overline{\rho}\widetilde{U}_j\widetilde{h}\right) + \frac{\partial}{\partial x_i}\left(\frac{\overline{\lambda}}{\overline{c}_p}\frac{\partial \widetilde{h}}{\partial x_i} - \overline{\rho}q_i^{sgs}\right), \tag{3.16}$$

where the subgrid parts, $\tau_{ij}^{sgs} = \left(\widetilde{U_iU_j} - \widetilde{U}_i\widetilde{U_j}\right)$ and $q_i^{sgs} = \left(\widetilde{U_ih} - \widetilde{U}_i\widetilde{h}\right)$, have to be modeled by means of subgrid-scale models.

3.1.3 Filtered and subgrid-scale quantities

In contrast to a DNS, the temperature and velocity fields and any statistic Q obtained by a LES are filtered quantities and thus depend on the filter width or more specifically on the grid resolution in LES with implicit filtering. To compare statistics obtained by a LES with reference data from DNS or experiments, the residual content of the statistics has to be determined and added to the filtered statistics. Following the procedure described in [186], the mean value of the resolved field denoted by $\langle . \rangle$ is approximately the averaged value predicted by a DNS. Thus, the residual contribution is zero and mean values can be approximated as

$$\langle \overline{\rho} \rangle \approx \langle \rho \rangle, \qquad \left\langle \overline{\rho}\widetilde{Q} \right\rangle \approx \langle \rho Q \rangle, \qquad \left\langle \overline{\rho}\widetilde{Q^2} \right\rangle \approx \langle \rho Q^2 \rangle, \tag{3.17}$$

where it is assumed that the spatial length scale of averaged quantities are small compared to the LES filter. In contrast, the residual contribution of variances or covariances is generally not zero. It can be approximated by adding the averaged residual part as

$$\langle \overline{\rho} \rangle \left(\{Q_i^2\} - \{Q_j\}^2 \right) \approx \underbrace{\left(\left\langle \overline{\rho}\widetilde{Q}_i\widetilde{Q}_j \right\rangle - \frac{\left\langle \overline{\rho}\widetilde{Q}_i \right\rangle \left\langle \overline{\rho}\widetilde{Q}_j \right\rangle}{\langle \overline{\rho} \rangle} \right)}_{resolved} + \underbrace{\left\langle \overline{\rho}\left(\widetilde{Q_iQ_j} - \widetilde{Q}_i\widetilde{Q}_j \right) \right\rangle}_{residual}, \tag{3.18}$$

where $\{.\}$ denotes Favre-averaging. The resolved part can be directly calculated by the LES field, while the residual part has to be modeled. In the case $Q_i = U_i$ and $Q_j = U_j$, the last term on the right-hand side in equation 3.18 denotes the subgrid-scale stress tensor τ_{ij}^{sgs}, while in the case $Q_i = Q_j = T$, the last term represents the subgrid-scale temperature variance θ_{sgs}. It should be mentioned here that the residual part is usually much smaller than the resolved part. Thus, the benefit to add the residual contribution is small if it exists at all. This was shown by the author in [E8] for a LES of turbulent pipe flow. Moreover, as pointed out in [113], the theoretically absurd situation may occur that the resolved part from LES is higher than the corresponding value evaluated from the DNS, due to incorrect subgrid-scale modeling and/or numerical errors. Because of this, the residual part is not added to the resolved statistics in the present work.

Some important subgrid-scale quantities for LES modeling are the subgrid-scale kinetic energy k_{sgs}, its dissipation rate $\epsilon_{k_{sgs}}$, the subgrid-scale temperature variance θ_{sgs} and the dissipation rate of subgrid-scale temperature variance $\epsilon_{\theta_{sgs}}$. Relations between these

subgrid-scale quantities and the resolved velocity and temperature fields can be obtained by applying the inertial-convective subrange theory and the filter operation described above.

Subgrid-scale quantities of the velocity field

Assuming homogeneous isotropic turbulence and the existence of an intermediate range of scales such that the Kolmogorov spectrum is valid (see equation 2.38), then the kinetic energy of the residual motions separated by the sharp spectral filter with the cut-off wave number $\kappa_c = \pi/\Delta$ (see table 3.1) can be calculated as

$$\langle k_{sgs} \rangle = \int_0^\infty \left[1 - \widehat{G}(\kappa)^2\right] E_K(\kappa)\, d\kappa = \frac{3}{2} C_K \langle \epsilon_k \rangle^{2/3} \left(\frac{\pi}{\Delta}\right)^{-2/3}, \tag{3.19}$$

where $\langle . \rangle$ denotes an appropriate averaging and Δ is the grid filter width defined in the present work by the cubic root of the cell volume as $\Delta = (\Delta_x \Delta_y \Delta_z)^{1/3}$. Similarly, the mean square of the resolved part of the rate of deformation tensor $\overline{D}_{ij}$ is given as

$$\left\langle \overline{D}_{ij} \overline{D}_{ij} \right\rangle = \int_0^\infty \kappa^2 \widehat{G}(\kappa)^2 E_k(\kappa)\, d\kappa = 3 C_K \langle \epsilon_k \rangle^{2/3} \left(\frac{\pi}{\Delta}\right)^{4/3}. \tag{3.20}$$

Dividing equation 3.19 by equation 3.20 side by side leads to the following expression of the subgrid-scale turbulent kinetic energy, also known as Yoshizawa's model [203]

$$\langle k_{sgs} \rangle = \frac{2}{\pi^2} \Delta^2 \left\langle \overline{D}_{ij} \overline{D}_{ij} \right\rangle, \tag{3.21}$$

which allows to estimate the kinetic energy of the residual part by means of the resolved velocity field. An alternative approach which was derived in a similar manner by Lilly [132] allows to calculate k_{sgs} directly from the subgrid-scale viscosity ν_{sgs}. It reads

$$\langle k_{sgs} \rangle = \frac{\langle \nu_{sgs} \rangle^2}{\Delta^2 C_k^2}, \tag{3.22}$$

where $C_k = C_S^{4/3} C_\epsilon^{1/3} = 0.094$ for a Smagorinsky constant of $C_S = 0.17$ and with $C_\epsilon = \pi(2/(3C_K))^{3/2} = 0.93$ (see [132, 210]). Notice that for specific flow situations, it is common practice to decrease the value of C_S, which has to be also accounted for in calculating C_k for the sake of consistency. Using equation 3.22 and assuming that $\left\langle \epsilon_{k_{sgs}} \right\rangle \approx \langle \epsilon_k \rangle$, it follows directly from equation 3.19 that the dissipation rate of subgrid-scale kinetic energy is given as

$$\begin{aligned} \left\langle \epsilon_{k_{sgs}} \right\rangle &= \left(\frac{2}{3C_K}\right)^{3/2} \frac{\pi}{\Delta} \langle k_{sgs} \rangle^{3/2} \\ &= \frac{1}{\Delta^4 C_s^4} \langle \nu_{sgs} \rangle^3. \end{aligned} \tag{3.23}$$

Subgrid-scale quantities of the temperature field

In accordance to the kinetic energy spectrum, the temperature variance of the residual motions separated by the cut-off wavenumber ${}_\theta\kappa_c = \kappa_c Pr^{3/4} = \pi/\Delta Pr^{3/4}$ [47] is

$$\langle \theta_{sgs} \rangle = \int_0^\infty \left[1 - \widehat{G}(\kappa)^2\right] E_\theta(\kappa)\, d\kappa = \frac{3}{2} C_{OC} \langle \epsilon_\theta \rangle \langle \epsilon_k \rangle^{-1/3} \left(\frac{\pi}{\Delta}\right)^{-2/3} \langle Pr \rangle^{-1/2}, \tag{3.24}$$

where it is assumed that the shape of $E_\theta(\kappa)$ follows equation 2.39 within the inertial-convective range. For the mean square of the resolved temperature gradient, one obtains

$$\left\langle \frac{\partial \overline{T}}{\partial x_i} \frac{\partial \overline{T}}{\partial x_i} \right\rangle = 2 \int_0^\infty \kappa^2 \widehat{G}(\kappa)^2 E_\theta(\kappa)\, d\kappa = \frac{3}{2} C_{OC} \langle \epsilon_\theta \rangle \langle \epsilon_k \rangle^{-1/3} \left(\frac{\pi}{\Delta} \right)^{4/3} \langle Pr \rangle . \tag{3.25}$$

Dividing equation 3.24 by equation 3.25 side by side leads to the following expression of the subgrid-scale temperature variance

$$\langle \theta_{sgs} \rangle = \frac{1}{\pi^2} \langle Pr \rangle^{-3/2} \Delta^2 \left\langle \frac{\partial \overline{T}}{\partial x_i} \frac{\partial \overline{T}}{\partial x_i} \right\rangle , \tag{3.26}$$

which allows to estimate the temperature variance of the residual part by means of the resolved temperature field. Finally, from equations 3.23, 3.24 and 3.26, and assuming that $\left\langle \epsilon_{\theta_{sgs}} \right\rangle \approx \langle \epsilon_\theta \rangle$, the dissipation rate of subgrid-scale temperature variance is given as

$$\begin{aligned} \left\langle \epsilon_{\theta_{sgs}} \right\rangle &= \frac{2\pi}{3 C_{OC}} \left(\frac{2}{3 C_K} \right)^{1/2} \frac{\langle \theta_{sgs} \rangle \langle k_{sgs} \rangle^{1/2}}{\Delta} \langle Pr \rangle^{1/2} \\ &= \frac{2}{3 C_{OC} \pi^{4/3} C_s^{4/3}} \langle \nu_{sgs} \rangle \left\langle \frac{\partial \overline{T}}{\partial x_i} \frac{\partial \overline{T}}{\partial x_i} \right\rangle \langle Pr \rangle^{-1} . \end{aligned} \tag{3.27}$$

3.1.4 LES quality assessment

With continually increasing computer power, several LES are being carried out demonstrating the capability and prediction accuracy of this technique for both, basic interests and engineering applications, e.g. [99, 73, 157]. Most of these studies are focused on a comparison of predicted first- and second-order statistics with experimental or direct numerical simulations (DNS) data. However, such reference datasets are generally not available for solution verification purpose in new configurations, especially when using LES as an engineering tool for development and conceptual design. Besides, it is worth mentioning that with LES and implicit filtering, the model depends inherently on the grid size, thus linking physical modeling characteristics to numerical characteristics. As a consequence, in contrast to RANS, grid independent LES results do not exist, which impedes the quality assessment in LES. Therefore, assessing, ensuring and predicting the quality, reliability and accuracy of LES are very vital and important.

Categories of spatial resolution assessment measures

Based on the classification by [113, 37], assessment measures for the spatial resolution in LES can be divided into single grid estimators, two grid estimators and systematic grid and model variations (SGMV). Briefly, single grid estimators require only a single grid calculation to assess the quality of a mesh for LES, while in the case of two grid estimators and SGMV, multi grid calculations are needed. Due to their simplicity and good applicability, mostly single grid estimators are used in LES practice. Prominent examples of single grid estimators are the ratio of relative grid size and Kolmogorov length scale, the ratio of subgrid-scale to total turbulent kinetic energy [188] or the subgrid activity parameter [68]. In this context, it is important to mention that such single grid estimators have serious shortcomings to assess the quality of LES, especially close to solid walls and in flows that are not fully developed. Nevertheless, it is expected that they provide useful informations apart from such flow conditions. Multi grid estimators do not exhibit such drawbacks since they include a built-in grid and model sensitivity check [113]. Besides,

also other LES assessment procedures like the *error landscape approach* [153] are used to evaluate LES. This consists of a systematic variation of simulation parameters resulting in a database analysis that allows to gain a general overview of the error behavior in LES. However, such an approach is not applicable for engineering LES practice and it is therefore mostly used to find an optimal refinement strategy or to analyze the error characteristics of LES models. For more detailed discussion on assessment measures for the spatial resolution in LES, the reader is referred to [113, 37].

While quality criteria for the spatial resolution in LES have drawn the interest of many researcher, very little attention has been paid to developed *a priori* and *a posteriori* measures to assess the required averaging time in LES, even though sampling errors can have a significant influence on simulation results as shown by the author in [E8]. To close this gap in the literature, *a priori* and *a posteriori* engineering estimations to predict the minimum record time for the practical use in LES are provided in the following.

A priori estimation of the required averaging time in LES

The expressions for temporal sampling errors derived in section 2.3.1 provide ways to predict *a priori* the minimum record time to obtain basic estimates of statistical quantities with a prescribed degree of accuracy. By assuming a stationary turbulent flow with normal distribution and an even autocorrelation function that follows the expression $\rho_i(s) \sim e^{-\tau_i/t_{av}}$, then the minimum total record times needed to achieve a desired accuracy are summarized in table 3.2. Notice that in the case of engineering estimations, it is further assumed that the hypothesis of "frozen turbulence" [225] is fulfilled and that $\rho_i(s) \approx 0$ for $s \geq 2\tau$. In case of non-stationary turbulent flows, the characteristic time scale can be related to the number of ensemble averages as discussed in section 2.3.1.

Statistical quantity	Record length	Engineering estimation
$\langle \overline{Q} \rangle$	$t_{av} = \frac{2 \cdot \tau \cdot I^2}{e^2}$	$t_{av} = \frac{2 \cdot L_c \cdot I^2}{U_c \cdot e^2}$
$\sqrt{\langle \overline{Q}'^2 \rangle}$	$t_{av} = \frac{\tau}{e^2}$	$t_{av} = \frac{L_c}{U_c e^2}$
$\langle \overline{Q}'^2 \rangle$	$t_{av} = \frac{4 \cdot \tau}{e^2}$	$t_{av} = \frac{4 \cdot L_c}{U_c \cdot e^2}$
$\overline{\rho}_i(s)$	$t_{av} = \frac{2 \cdot \tau \cdot \left(1 - \overline{\rho}_i(s)^2\right)}{e^2}$	$t_{av} = \frac{2 \cdot L_c}{U_c \cdot e^2}$

Table 3.2: Record times for basic estimates in LES. I is the turbulent intensity, τ the integral length scale, e the desired maximal sampling error, L_c a characteristic length scale of large turbulent scales and U_c a characteristic velocity associated to the convection.

The reliability of the engineering estimations of table 3.2 is verified by the author in [E8] for a turbulent pipe flow at $Re_\tau = 180$. Thereby, it was shown that the required averaging time of basic statistics such as mean or rms velocities can be predicted within an accuracy of $\sim 10 - 20\%$ by using the engineering estimations of table 3.2. However, it should be mentioned here that the accuracy of these estimates relies significantly on the guess of the characteristic length scale L_c and the turbulent intensity I. Especially in the case of complex wall-bounded flow geometries the characteristic length scales L_c and turbulent intensities I are difficult to guess. In such cases *a posteriori* quality measures for the averaging time in LES are helpful as proposed below.

***A posteriori* quality measures for the averaging time in LES**

Theoretically, the required record time to obtain basic estimates of statistical quantities with a predetermined degree of accuracy can be estimated *a posteriori* by means of the integral time scale τ of the turbulent process as already described in section 2.3.1. However, it is often very time-consuming and costly to determine τ in a numerical simulation since the entire time history of the turbulence signal has to be stored in a database and post-processed for each location of interest. This is hardly feasible, in particular for daily engineering and practical applications with complex geometries.

As implied by the discussion above, the main task for developing an applicable *a posteriori* quality measure for the averaging time in LES is to estimate the integral time scale of the turbulent process in a post-processing step without using the entire time history of the turbulence signal. By assuming a stationary turbulent flow and that the hypothesis of "frozen turbulence" [225] is fulfilled, the integral time scale may be expressed by means of a characteristic length scale L_c and a characteristic velocity U_c as $\tau \approx L_c/U_c$. Thereby, in the case of convection dominated flows, it seems to be reasonable to assume that U_c is approximately the convection velocity and L_c the turbulent length scale. This leads to the following approximation for the turbulent velocity time scale

$$\tau \approx \frac{k^{3/2}}{\epsilon_k \left\langle |U| \right\rangle}, \tag{3.28}$$

where $\langle |U| \rangle$ denotes the time-averaged magnitude velocity. For a scalar quantity such as the temperature, the integral time scale can be simply approximated as $\tau_\theta \approx 0.5\tau$ [24]. In equation 3.28, the total turbulent kinetic energy k and its dissipation rate ϵ_k have to be calculated. In the context of LES these quantities can be approximated as

$$k \approx \frac{1}{2}\left\langle \overline{U}_i' \overline{U}_i' \right\rangle + \langle k_{sgs} \rangle \quad \text{and} \quad \epsilon_k \approx 2\nu \left\langle \overline{D}_{ij}' \overline{D}_{ij}' \right\rangle + \left\langle \epsilon_{k_{sgs}} \right\rangle, \tag{3.29}$$

where the subgrid-scale quantities $\langle k_{sgs} \rangle$ and $\left\langle \epsilon_{k_{sgs}} \right\rangle$ can be either obtained from transport equations or in the case of algebraic subgrid-scale models calculated by using the expressions derived in section 3.1.3. Based on this, error measures of the averaging time for different basic statistics can be derived using the relations in table 3.2. A reasonable choice of a representative statistic in turbulent flows might be the variance or turbulent kinetic energy. For the turbulent kinetic energy, the error measure reads

$$e_k = \sqrt{\frac{4\tau}{t_{av}}} \approx 2\sqrt{\frac{k^{3/2}}{\epsilon_k \left\langle |U| \right\rangle t_{av}}}. \tag{3.30}$$

An appropriate averaging time in LES is assumed if $e_k \leq 0.05$, which corresponds to a sampling error smaller than 5% with a confidence level of 68%.

Equation 3.30 allows to assess *a posteriori* the averaging time in LES. Thereby, it is expected that equation 3.30 provides useful information about the sampling error in LES of convection dominated flows away from viscous walls. Furthermore, it is easy and inexpensive to apply and therefore well suited for LES engineering practice.

3.2 Subgrid-scale models for the momentum transport

In order to close the filtered momentum transport equations 3.15, the unknown subgrid-scale stress tensor $\tau_{ij}^{sgs} = \left(\widetilde{U_i U_j} - \widetilde{U}_i \widetilde{U}_j\right)$ has to be related to the resolved velocity field.

This is often accomplished based on the eddy viscosity approach, where it is assumed that the subgrid-scale stress tensor acts as an additional diffusion term. Thereby, the isotropic part of τ_{ij}^{sgs} is included into the modified filtered pressure

$$\overline{P} = \overline{p} + \frac{1}{3}\overline{\rho}\tau_{kk}^{sgs} \tag{3.31}$$

and the remaining anisotropic part is expressed by means of an eddy viscosity ν_{sgs} and the Boussinesq approximation as

$$\tau_{\langle ij \rangle}^{sgs} = \tau_{ij}^{sgs} - \frac{1}{3}\tau_{kk}^{sgs}\delta_{ij} = -2\nu_{sgs}\left(\widetilde{D}_{ij} - \frac{1}{3}\widetilde{D}_{kk}\delta_{ij}\right). \tag{3.32}$$

The eddy viscosity is usually modeled by analogy to the mixing length hypothesis based on dimensional analysis via

$$\nu_{sgs} \propto l_0^2/t_0, \tag{3.33}$$

where l_0 and t_0 represent a characteristic length scale and a characteristic velocity time scale, respectively, both are local in space and time.

The concept of eddy viscosity is also used in this work to model the subgrid-scale transport of momentum. Some important representatives of algebraic formulations and differential forms of these modeling approach are discussed in the following sections. In particular, a modified differential k^{sgs}-transport equation model for wall-bounded flows is presented. Evaluations of these subgrid-scale models are provided later in section 9.1. A detailed overview about subgrid-scale modeling of momentum transport can be found in [203].

3.2.1 Algebraic eddy viscosity models

Most of the algebraic subgrid-scale viscosity models used in LES can be generically represented as

$$\nu_{sgs} = \underbrace{(C_m\Delta)^2}_{l_0^2}\underbrace{D_m}_{1/t_0}, \tag{3.34}$$

where the characteristic length scale l_0 is taken to be proportional to the filter width Δ with a model specific proportional coefficient C_m. The operator D_m represents the local characteristic velocity time scale t_0 and its formulation depends on the specific subgrid-scale viscosity model. Usually, D_m is defined by the resolved velocity field and it is a function of space and time. Thereby, it is important that the operator D_m is built in such a way that it is invariant to any coordinate translation or rotation. A description of some popular algebraic eddy viscosity models is given below.

Smagorinsky model

The most popular algebraic subgrid-scale viscosity model is the Smagorinsky model [220], which reads

$$\nu_{sgs} = (C_S\Delta)^2\,|\widetilde{D}_{ij}|, \quad \text{with} \quad |\widetilde{D}_{ij}| = \sqrt{2\widetilde{D}_{ij}\widetilde{D}_{ij}}. \tag{3.35}$$

Here, the characteristic length scale is expressed as $l_0 = C_s\Delta$, where C_S is the Smagorinsky coefficient. The velocity time scale is taken to be the characteristic filtered rate of strain $D_m = \sqrt{2\widetilde{D}_{ij}\widetilde{D}_{ij}}$, which represents an estimation of the velocity fluctuations at the length

scale Δ. In the case of high Reynolds number turbulence and with the filter width Δ in the inertial range, the Smagorinsky coefficient can be estimated as [132]

$$C_S = \frac{1}{\pi}\left(\frac{2}{3C_K}\right)^{3/4} \approx 0.17, \tag{3.36}$$

where a sharp spectral filter is applied. However, this value is only valid for locally isotropic turbulence where the energy transfer from large scales to residual motions is balanced by the dissipation of turbulent kinetic energy. In many cases such as transient flows, this equilibrium condition is not established. This leads researchers to use different values of C_S for different flow situations, typically in the range of $C_S = 0.05...0.2$.

Unfortunately, the specification that the characteristic length scale is given by the expression $l_0 = C_S\Delta$ is only justifiable for Δ within the inertial subrange [189]. Because of this, the Smagorinsky model requires a modification of the grid filter width in the near-wall region. One possibility is to use a van Driest wall damping function. Thereby, the grid filter width Δ is replaced by the expression

$$\Delta_{VD} = min\left[\Delta, \frac{\kappa r}{C_\Delta}\left(1 - e^{\left(-r\cdot A^+/y^+\right)}\right)\right], \tag{3.37}$$

where y^+ is the dimensionless wall distance, $\kappa = 0.41$ the von Kármán constant and $C_\Delta = 0.158$, $A^+ = 26$ are model parameters. This wall damping ensures that the eddy viscosity vanishes in the near wall region proportional to the desirable scaling of $\nu^{sgs} = O(y^3)$.

Dynamic Smagorinsky model

To overcome the limitations of the classical Smagorinsky model, Germano [67] proposed a methodology to determine the local value of C_S dynamically. The basic idea is to apply a test filter $\widehat{(.)}$ with a larger filter width than the grid filter, typically twice the grid filter $\widehat{\Delta} = 2\Delta$, to the resolved velocity field. Then, the local value of the Smagorinsky coefficient can be estimated by assuming that the subtestfilter stresses and the subfilter stresses can be modeled with the same model coefficient.

Using the dynamic procedure, the unresolved fluxes from the first and second filter levels can be formulated as

$$\tau_{ij}^{sgs} = \widetilde{U_iU_j} - \widetilde{U}_i\widetilde{U}_j, \tag{3.38}$$

$$T_{ij} = \widehat{\widetilde{U_iU_j}} - \widehat{\widetilde{U}}_i\widehat{\widetilde{U}}_j. \tag{3.39}$$

Filtering equation 3.38 by means of the test filter and subtracting the result from equation 3.39 yields to the Germano identity

$$\mathfrak{L}_{ij} = T_{ij} - \widehat{\tau}_{ij}^{sgs} = \widehat{\widetilde{U}_i\widetilde{U}_j} - \widehat{\widetilde{U}}_i\widehat{\widetilde{U}}_j. \tag{3.40}$$

Assuming that the subfilter stresses τ_{ij}^{sgs} and the subtestfilter stresses T_{ij} written in terms of the Smagorinsky model can be modeled by the same model constant $c_S = C_S^2$ leads to the model equations

$$\tau_{ij}^{sgs} - \frac{1}{3}\tau_{kk}^{sgs}\delta_{ij} \approx -2c_S\Delta^2|\widetilde{D}_{mn}|\left(\widetilde{D}_{ij} - \frac{1}{3}\widetilde{D}_{kk}\delta_{ij}\right) =: -2c_S m_{ij,} \tag{3.41}$$

$$T_{ij} - \frac{1}{3}T_{kk}\delta_{ij} \approx -2c_S\widehat{\Delta}^2|\widehat{\widetilde{D}}_{mn}|\left(\widehat{\widetilde{D}}_{ij} - \frac{1}{3}\widehat{\widetilde{D}}_{kk}\delta_{ij}\right) =: -2c_S M_{ij}. \tag{3.42}$$

Finally, by inserting equations 3.41 and 3.42 into equation 3.40 and neglecting the variation of c_S one obtains five linearly independent equations

$$2c_S\left(\widehat{m}_{ij} - M_{ij}\right) = \mathfrak{L}_{ij} - \frac{1}{3}\mathfrak{L}_{kk}\delta_{ij}, \tag{3.43}$$

that can be solved for c_S by using the least mean squares approach proposed by Lilly [133] as

$$c_S = \frac{\mathfrak{L}_{ij}\left(\widehat{m}_{ij} - M_{ij}\right)}{2\left(\widehat{m}_{ij} - M_{ij}\right)^2}. \tag{3.44}$$

In order to avoid unphysical values of ν_{sgs}, the model coefficient c_S is usually limited to

$$0 \leq c_S \leq c_{max}. \tag{3.45}$$

Furthermore, appropriate spatial or temporal averaging of c_S, e.g. in homogeneous directions or along fluid particle trajectories, are generally employed to reduce the variability of the model coefficient [189].

Subgrid-scale models based on the Germano procedure such as the dynamic Smagorinsky model are parameter free. This means that the model coefficient is automatically adapted to the local flow structure within the approach. Such models can distinguish between laminar and turbulent flows and provide a proper near wall behavior in the case an appropriate averaging procedure of c_S is applied. Although the second explicit filtering operation can be performed precisely in simple geometries, it may prove to be an issue in the case of complex geometries or moving grids. This has led researchers to develop new subgrid-scale models that provide the correct asymptotic near-wall behavior without using any dynamic or ad-hoc procedures. Representatives of such models are described next.

WALE model

In the wall-adapting linear eddy-viscosity model (WALE) [163] no ad-hoc or dynamic procedure are required to distinguish between laminar and turbulent flows and to reproduce the correct flow behavior at solid walls. Instead the model operator D_m is formulated in such a way that it recovers automatically the proper near-wall scaling for the eddy viscosity. In contrast to Smagorinsky-type models, the model operator is based on the square of the velocity gradient tensor and accounts for the effects of both the strain and the rotation rate of smallest resolved velocity fluctuations. In the WALE model, the subgrid-scale viscosity is expressed as

$$\nu_{sgs} = \left(C_W\Delta\right)^2 \frac{\left(\mathbf{S}^d_{ij}\mathbf{S}^d_{ij}\right)^{3/2}}{\left(\overline{D}_{ij}\overline{D}_{ij}\right)^{5/2} + \left(\mathbf{S}^d_{ij}\mathbf{S}^d_{ij}\right)^{5/4}}, \tag{3.46}$$

where C_W is the model coefficient and $\mathbf{S}^d_{ij}$ is the traceless symmetric part of the square of the velocity gradient tensor

$$\mathbf{S}^d_{ij} = \frac{1}{2}\left(\overline{L}^2_{ij} + \overline{L}^2_{ji}\right) - \frac{1}{3}\delta_{ij}\overline{L}^2_{kk}, \tag{3.47}$$

where $\overline{L}^2_{ij} = \overline{L}_{ik}\overline{L}_{kj}$ is the square of the velocity gradient tensor.

The WALE model coefficient C_W is considered to be a true constant of $C_W = \sqrt{10.6}C_S \approx 0.5$ and it is usually not determined by means of a dynamic procedure.

Sigma model (σ-model)

The operator of the σ-model [164] is based on the singular values of the resolved velocity gradient tensor. It reads

$$\nu_{sgs} = (C_\sigma \Delta)^2 \, \frac{\sigma_3 \, (\sigma_1 - \sigma_2) \, (\sigma_2 - \sigma_3)}{\sigma_1^2}, \tag{3.48}$$

where $C_\sigma = 1.5$ is the model coefficient and σ_i is the i^{th} singular value of the resolved velocity gradient tensor $\overline{L}_{ij}$, which corresponds to the square root of the eigenvalues of $\overline{L}_{ki}\overline{L}_{kj}$. From the definition of the singular values it follows that $\sigma_1 \geq \sigma_2 \geq \sigma_3 \geq 0$. Thus, the modeled ν_{sgs} is always positive by construction.

Similar to the WALE model, to distinguish between laminar and turbulent flows and to reproduce the correct cubic behavior of ν_{sgs} in the vicinity of solid boundaries, no ad-hoc or dynamic procedure is required in the σ-model. Further advantageous properties of the σ-model are that ν_{sgs} vanishes for pure shear and solid rotation flows and in the case of pure axisymmetric contraction/expansion.

3.2.2 Differential subgrid-scale models

Instead of using an algebraic equation to represent the unresolved momentum flux, additional evolution equations for one or more of the subgrid-scale turbulence quantities can be solved in order to account for history and non-equilibrium effects in the unresolved scales. Generally, transport equations for the complete subgrid-scale stress tensor τ_{ij}^{sgs} can be derived. However, such models are very complex and rarely reported in the LES literature, e.g. [56]. Instead, usually one-equation models are employed. Thereby, a transport equation for the subgrid-scale kinetic energy $k_{sgs} = \tau_{ii}^{sgs}/2$ is utilized to calculate the subgrid-scale viscosity. One-equation models are by far the most common higher order models used in LES. Therefore, the following discussion about differential subgrid-scale models is restricted to this approach.

In one-equation models, the subgrid-scale viscosity is expressed by means of a characteristic length scale l_0 and a characteristic velocity scale v_0 as

$$\nu_{sgs} = \underbrace{C_k \Delta}_{l_0} \underbrace{\sqrt{k_{sgs}}}_{v_0}. \tag{3.49}$$

In analogy to the algebraic models, the characteristic length scale l_0 is taken to be proportional to the product of the filter width Δ and a specific model coefficient C_k. The characteristic velocity scale v_0 is represented by the subgrid-scale kinetic energy, which is evaluated by an evolution equation.

Subgrid-scale kinetic energy model

The evolution equation of k_{sgs} can be derived by subtracting the filtered equations of motion from their unfiltered counterpart and multiplying the result by the subgrid-scale velocity. Contraction and isotropic assumptions leads to the one-equation model. One variant, proposed by Yoshizawa [254], reads

$$\frac{\partial \overline{\rho} k_{sgs}}{\partial t} + \frac{\partial}{\partial x_i}\left(\overline{\rho}\widetilde{U}_i k_{sgs}\right) = P_{k_{sgs}} + \epsilon_{k_{sgs}} + D_{k_{sgs}}, \tag{3.50}$$

where $P_{k_{sgs}}$ represents the production, $\epsilon_{k_{sgs}}$ the dissipation and $D_{k_{sgs}}$ the diffusion of k_{sgs}. These three terms are modeled as

$$P_{k_{sgs}} = -\tau_{ij}^{sgs}\widetilde{D}_{ij} = 2\overline{\rho}\nu_{sgs}\left(\widetilde{D}_{ij} - \frac{1}{3}\delta_{ij}\widetilde{D}_{kk}\right)\widetilde{D}_{ij} - \frac{2}{3}k_{sgs}\widetilde{D}_{ii}, \tag{3.51}$$

$$\epsilon_{k_{sgs}} = -\overline{\rho}C_\epsilon\frac{k_{sgs}^{3/2}}{\Delta}, \tag{3.52}$$

$$D_{k_{sgs}} = \frac{\partial}{\partial x_i}\left(\frac{\overline{\rho}\nu_{sgs}}{\sigma_k}\frac{\partial k_{sgs}}{\partial x_i}\right), \tag{3.53}$$

where $\nu_{sgs} = C_k\Delta\sqrt{k_{sgs}}$ (see equation 3.49). The constants are given in [254] as $C_k = 0.1$, $C_\epsilon = 1$ and $\sigma_k = 1$.

An important feature of this model is that no assumption of local balance between the subgrid-scale energy production and dissipation rate has been made [151]. Moreover, it provides a more accurate time scale, which is based on the independent definition of the velocity scale. Therefore, it is expected that the one-equation model is particularly advantageous in regions where the local balance of $P_{k_{sgs}}$ and $\epsilon_{k_{sgs}}$ is violated, e.g. in transitional flows and in turbulent flows with large scale unsteadiness.

Similar to the classical Smagorinsky model, the specification that $l_0 = C_k\Delta$ is not justified in the near-wall region and has to be adjusted. This is usually accomplished by means of van Driest wall damping. Thereby, in analogy to the Smagorinsky model, the grid filter width Δ is replaced by the expression 3.37.

Dynamic subgrid-scale kinetic energy model

The dynamic approach previously described can be also used to obtain the values for C_k and C_ϵ in the one-equation model dynamically. Following the procedure described in [151], the coefficient C_k can be estimated as

$$C_k = \frac{1}{2}\frac{\mathfrak{L}_{ij}M_{ij}}{M_{ij}M_{ij}}, \tag{3.54}$$

where

$$M_{ij} = -\widehat{\Delta}\widehat{K}^{1/2}\left(\widehat{\widetilde{D}}_{ij} - \frac{1}{3}\widehat{\widetilde{D}}_{kk}\delta_{ij}\right) + \Delta\widehat{k_{sgs}^{1/2}\left(\widetilde{D}_{ij} - \tfrac{1}{3}\widetilde{D}_{kk}\delta_{ij}\right)}, \tag{3.55}$$

and

$$K = k_{sgs} + \frac{1}{2}\mathfrak{L}_{ij}. \tag{3.56}$$

In the case of C_ϵ, the dynamic approach reads

$$C_\epsilon = \frac{\nu\left(\widehat{\frac{\partial\widetilde{U}_i}{\partial x_j}\frac{\partial\widetilde{U}_i}{\partial x_j}} - \frac{\partial\widehat{\widetilde{U}}_i}{\partial x_j}\frac{\partial\widehat{\widetilde{U}}_i}{\partial x_j}\right)}{\widehat{K}^{3/2}/\widehat{\Delta} - \widehat{k_{sgs}^{3/2}/\Delta}}, \tag{3.57}$$

which produces only a single equation for the unknown coefficient C_ϵ and can be solved without applying the least squares method. This completes the dynamic subgrid-scale kinetic energy model.

The same limitations of the dynamic procedure are also valid here. Therefore, it is useful to develop a one-equation model that enables the correct asymptotic near-wall behavior without using any dynamic procedure or ad-hoc treatment.

3.2.3 A modified k_{sgs}-transport equation model

In this section a modified one-equation model, namely the σ-k_{sgs}-transport equation model is presented. It combines the advantages of the algebraic σ-model and the one-equation modeling approach. Thus, the essential features of the model are: (1) no dynamic approach or ad-hoc treatments are required to obtain the correct near-wall behavior, (2) it accounts for history and non-equilibrium effects in the unresolved scales, and (3) the model is applicable for a wide range of Reynolds numbers and complex geometries.

Similar to the classical formulation of Yoshizawa [254], the transport equation of the subgrid-scale kinetic energy k_{sgs} is expressed as

$$\frac{\partial \overline{\rho} k_{sgs}}{\partial t} + \frac{\partial}{\partial x_i}\left(\overline{\rho}\widetilde{U}_i k_{sgs}\right) = P_{k_{sgs}} + \epsilon_{k_{sgs}} + D_{k_{sgs}}, \tag{3.58}$$

where $P_{k_{sgs}}$ represents the production, $\epsilon_{k_{sgs}}$ the dissipation and $D_{k_{sgs}}$ the diffusion of k_{sgs}. The pressure diffusion term is usually small in wall-bounded turbulent flows compared to $P_{k_{sgs}}$, $\epsilon_{k_{sgs}}$ and $D_{k_{sgs}}$. It is therefore neglected in the present formulation.

The production term $P_{k_{sgs}}$ is modeled by means of the Boussinesq approximation leading to

$$P_{k_{sgs}} = -\tau_{ij}^{sgs}\widetilde{D}_{ij} = 2\overline{\rho}\nu_{sgs}^{\sigma}\left(\widetilde{D}_{ij} - \frac{1}{3}\delta_{ij}\widetilde{D}_{kk}\right)\widetilde{D}_{ij} - \frac{2}{3}\left(\frac{\nu_{sgs}^{\sigma}}{\Delta C_k}\right)^2 \widetilde{D}_{ii}. \tag{3.59}$$

Here, in contrast to traditional k_{sgs} transport models, e.g. [254, 151], an additional subgrid-scale viscosity ν_{sgs}^{σ} is introduced, which is calculated based on the resolved velocity field rather than using k_{sgs}. In this way, the energy transfer from the resolved to the subgrid-scales is treated correctly as a local and instantaneous dynamic process without any history effects as pointed out in [91, 107]. Furthermore, the correct near-wall behavior of $P_{k_{sgs}} \sim \mathcal{O}\left(y^3\right)$ is automatically obtained by using the subgrid-scale viscosity from the σ-model [164] for ν_{sgs}^{σ} (see equation 3.48).

To take into account the global and history properties of the dissipation $\epsilon_{k_{sgs}}$, it is approximated directly from k_{sgs} as

$$\epsilon_{k_{sgs}} = -\overline{\rho}C_{\epsilon}\frac{k_{sgs}^{3/2}}{\Delta} - 2\overline{\rho}\,\overline{\nu}\frac{\sqrt{k_{sgs}}}{\partial x_i}\frac{\sqrt{k_{sgs}}}{\partial x_i}, \tag{3.60}$$

where the additional dissipation term on the right-hand side accounts for low Reynolds number effects near the wall in order to obtain the correct scaling of $\epsilon_{k_{sgs}} \sim \mathcal{O}\left(y^0\right)$ for $y \to 0$, similar to low-Reynolds models in the RANS-context [128].

The diffusion term is modeled traditionally using a gradient law based on k_{sgs}. It follows that

$$D_{k_{sgs}} = \frac{\partial}{\partial x_i}\left(\overline{\rho}\left(C_k\Delta f_{\nu}\sqrt{k_{sgs}} + \nu\right)\frac{\partial k_{sgs}}{\partial x_i}\right), \tag{3.61}$$

where f_{ν} is a damping factor that will be described later. Considering equation 3.61, it reveals that both terms on the right hand side, turbulent and molecular diffusion of k_{sgs}, follow the correct near-wall behavior of $\sim \mathcal{O}\left(y^3\right)$ and $\sim \mathcal{O}\left(y^0\right)$, respectively.

From the obtained value of k_{sgs}, the subgrid-scale viscosity is computed as

$$\nu_{sgs} = C_k\Delta f_{\nu}\sqrt{k_{sgs}}, \tag{3.62}$$

where f_{ν} is a damping factor, that is required to ensure the correct asymptotic behavior of $\nu_{sgs} \sim \mathcal{O}\left(y^3\right)$ in the vicinity of the wall. In the present model formulation the damping

factor f_ν is selected as

$$f_\nu = min\left[\frac{C_\epsilon k_{sgs}}{2C_k\Delta^2\widetilde{S}_{ij}\widetilde{S}_{ij}}, 1\right], \tag{3.63}$$

which describes essentially the deviation of k_{sgs} from isotropic, homogeneous turbulence and therefore accounts for shear damping effects in the near-wall region. From scaling analysis, it appears that $f_\nu \sim \mathcal{O}\left(y^2\right)$ leading to the correct asymptotic behavior of $\nu_{sgs} \sim \mathcal{O}\left(y^3\right)$ in the present model formulation. Notice that in the subgrid-scale model of Inagaki et al. [94] a similar damping factor based on shear damping effects in the near-wall region is successfully employed for several turbulent flow configurations. Finally, the model constants of the present model are $C_\sigma = 1.5$ (taken from the σ-model [164]) and $C_k = 0.094$, $C_\epsilon = 1.048$ derived from the inertial subrange theory.

3.3 Subgrid-scale models for heat transport

Unlike in turbulent fluid flow, the rationale of LES is less obvious from turbulence theory when dealing with turbulent heat transport. The main reason is that the temperature variance spectrum as well as the dynamics of small temperature scales have a less universal character than velocity scales. As a consequence, the spectral scalar transfer across the LES cutoff may strongly depend on the physical regime it is located in [203]. Moreover, small temperature scales are also influenced by the interaction of the velocity gradient and the scalar fluctuations, which causes anisotropic behavior of the turbulent heat flux even at smallest temperature scales. Consequently, more advanced subgrid-scale models are required in the case of turbulent heat transport in order to justify the cut off and modeling of the small temperature scales, especially in the case of high Prandtl numbers.

Usually, the subgrid-scale scalar flux is modeled to be proportional to the negative gradient of the resolved scalar gradient in analogy to Fourier's or Fick's law. In the case of LES of turbulent heat transport with variable properties, the resolved temperature or enthalpy are scalar quantities expressing the thermal transport. For the sake of consistency with the LES equations applied in this work, the subgrid-scale heat flux models are formulated based on the resolved enthalpy instead of using the temperature. Furthermore, effects of body forces, e.g. gravity force, are not considered in the subgrid-scale model formulations.

In the following sections some important variants of isotropic and anisotropic thermal diffusivity models from the literature are briefly discussed. Then, a new explicit anisotropy resolving algebraic heat flux model that fulfills the second law of thermodynamic is presented. An evaluation of some of these models is given later in section 9.2. More detailed information on the classical heat flux modeling in LES can be found in [203].

3.3.1 Isotropic thermal diffusivity models

The linear eddy diffusivity hypothesis states that the subgrid-scale heat flux vector q_i^{sgs} is aligned with the corresponding filtered enthalpy gradient, with the subgrid-scale heat diffusivity α^{sgs} as a proportional scalar factor. It follows that

$$q_i^{sgs} = \left(\widetilde{U_i h} - \widetilde{U}_i\widetilde{h}\right) = -\alpha^{sgs}\frac{\partial\widetilde{h}}{\partial x_i}, \tag{3.64}$$

where the proportional factor α^{sgs} has to be modeled. For this purpose several modeling approaches are available in the literature.

Constant Pr_{sgs} approach

Traditionally, α^{sgs} is represented based on the Reynolds analogy and the concept of subgrid-scale turbulent Prandtl number Pr_{sgs}. Thereby, the subgrid-scale heat diffusivity is expressed as

$$\alpha^{sgs} = \frac{\nu_{sgs}}{Pr_{sgs}}, \tag{3.65}$$

where the value of the subgrid-scale Prandtl number can be derived by means of the inertial-convective subrange theory as $Pr_{sgs} = 0.42$ [210]. However, many researchers selected values ranging from $Pr_{sgs} = 0.1$ to $Pr_{sgs} = 1$ depending on the specific configuration [203]. This indicates that a universal value of Pr_{sgs} does not exist, which motivates to apply a dynamic procedure to calculate Pr_{sgs}.

Dynamic Pr_{sgs} approach

To overcome the shortcomings of a constant Pr_{sgs}, Moin et al. [158] extended the dynamic procedure of Germano to determine the value of Pr_{sgs} dynamically. This approach was subsequently revised by Lilly [133] in order to improve the numerical stability of the procedure. The final formulation reads

$$\frac{1}{Pr_{sgs}} = -\frac{M_{ik}^2}{\mathfrak{L}_{ik} M_{ik}} \frac{P_j R_j}{R_j^2}, \tag{3.66}$$

where

$$M_{ik} = \widehat{\Delta}^2 |\widehat{\widetilde{D}}_{mn}| \left(\widehat{\widetilde{D}}_{ik} - \frac{1}{3} \widehat{\widetilde{D}}_{ll} \delta_{ik} \right) - \Delta^2 \widehat{|\widetilde{D}_{mn}| \left(\widetilde{D}_{ik} - \tfrac{1}{3} \widetilde{D}_{ll} \delta_{ik} \right)} \tag{3.67}$$

$$R_j = \widehat{\Delta}^2 |\widehat{\widetilde{D}}_{kl}| \widehat{\frac{\partial \widetilde{h}}{\partial x_j}} - \Delta^2 \widehat{|\widetilde{D}_{kl}| \frac{\partial \widetilde{h}}{\partial x_j}}, \tag{3.68}$$

$$P_j = \widehat{\widetilde{U}_j \widetilde{h}} - \widehat{\widetilde{U}}_j \widehat{\widetilde{h}}, \tag{3.69}$$

and $\mathfrak{L}_{ik}$ is calculated from equation 3.40.

Models based on Kolmogorov scaling

Based on the Kolmogorov scaling, Wong and Lilly [249] proposed another scalar thermal diffusivity model as

$$\alpha^{sgs} = \frac{C^{2/3}}{Pr_{sgs}} \Delta^{4/3} \epsilon_k^{1/3} = \frac{C_e}{Pr_{sgs}} \Delta^{4/3}, \tag{3.70}$$

where ϵ_k is the dissipation rate of the turbulent kinetic energy. The coefficients C_e and Pr_{sgs} are determined by means of a dynamic procedure as described in [249]. The advantage of this model is that it excludes the assumption that the dissipation rate equals the subgrid-scale production rate.

3.3.2 Anisotropic thermal diffusivity models

The concept of linear subgrid-scale diffusivity is applicable only for homogeneous isotropic turbulence. However, in more complex flows, it is well known that the turbulent heat flux vector is generally not aligned with the enthalpy gradient even at smallest scales. A better representation of the heat flux vector for such flow situations can be obtained by accounting for the anisotropic behavior of smallest temperature scales and introducing a tensor subgrid-scale thermal diffusivity [19]. Based on this, the subgrid-scale heat flux can be formulated as

$$q_i^{sgs} = -\alpha_{ij}^{sgs} \frac{\partial \widetilde{h}}{\partial x_j}, \tag{3.71}$$

where α_{ij}^{sgs} is the tensor subgrid-scale thermal diffusivity, which has to be modeled.

Models based on the generalized gradient diffusion hypothesis

In the general gradient diffusion hypothesis GGDH, introduced by Daly and Harlow [51], the tensor thermal diffusivity is related to the Reynolds stress tensor. In this respect, a general algebraic expression for the tensor thermal diffusivity is derived from the modeled differential equation for the turbulent heat flux by omitting the transport terms. The models based on the GGDH are often used in the RANS-context but can be also formulated for LES. Thereby, it is assumed that the Reynolds stress $\left\langle U_i' U_j' \right\rangle$, turbulent kinetic energy k and turbulent dissipation rate ϵ_k correspond to their subgrid-scale counterparts τ_{ij}^{sgs}, k_{sgs}, $\epsilon_{k,sgs}$. This leads to

$$q_i^{sgs} = -C_\theta \tau_\theta \tau_{ij}^{sgs} \frac{\partial \widetilde{h}}{\partial x_j}, \tag{3.72}$$

where $\tau_\theta = \frac{k_{sgs}}{\epsilon_{sgs}}$ is a characteristic mechanical or thermal turbulence time scale and $C_\theta = 0.2$ represents a model coefficient.

The GGDH model gives reasonable approximations in free-shear regions, but underpredicts the stream-wise turbulent heat flux in wall-shear flows. To overcome this drawback, Abe and Suga [1] extended the classical GGDH model by using the quadratic product of the Reynolds stress tensor. In the LES context this model reads

$$q_i^{sgs} = -C_\theta \tau_\theta \left(\frac{\tau_{ik}^{sgs} \tau_{kj}^{sgs}}{k_{sgs}} \right) \frac{\partial \widetilde{h}}{\partial x_j}, \tag{3.73}$$

where $C_\theta = 0.3$.

A more complex extension of the GGDH was introduced by Younis, Speciale and Clark [255]. It is derived from the representation theorem based on rationally assumed functional relationships [255]. The final form of the model is given as

$$q_i^{sgs} = -\left(C_1 \frac{k_{sgs}^2}{\epsilon_{sgs}} \delta_{ij} + C_2 \frac{k_{sgs}}{\epsilon_{sgs}} \tau_{ij}^{sgs} + C_3 \frac{k_{sgs}^3}{\epsilon_{sgs}^2} \frac{\partial \widetilde{v}_i}{\partial x_j} + C_4 \frac{k_{sgs}^2}{\epsilon_{sgs}^3} \left(\tau_{ik}^{sgs} \frac{\partial \widetilde{v}_j}{\partial x_k} + \tau_{jk}^{sgs} \frac{\partial \widetilde{v}_i}{\partial x_k} \right) \right) \frac{\partial \widetilde{h}}{\partial x_j}, \tag{3.74}$$

where the first term on the right-hand side corresponds to the simple linear eddy diffusivity model, the second term is the GGDH model and the remaining higher order terms include the products of the gradients of the resolved temperature and velocity fields. The model coefficients are provided in [255] as $C_1 = -4.55 \times 10^{-2}$, $C_2 = 3.73 \times 10^{-1}$, $C_3 = -3.73 \times 10^{-3}$ and $C_4 = -2.35 \times 10^{-2}$.

Model by Peng and Davidson

The heat flux model of Peng and Davidson [184] is derived from considerations regarding the transport equation of the subgrid heat flux. Thereby, the subgrid heat flux can be interpreted as the amount of heat transfered from the resolved temperature scales to subgrid-scale thermal structures (*forward transfer*) and vice versa (*backward transfer*). In the transport equation of q_i^{sgs}, the production term $P_{\theta,i}$ actually represents the subgrid-scale heat flux dissipation. If $q_i^{sgs} > 0$, this dissipation indicates the heat flux exchange of forward ($P_{\theta,i} > 0$) and backward ($P_{\theta,i} < 0$) transfer. In the case $q_i^{sgs} < 0$, forward and backward transfer corresponds to $P_{\theta,i} < 0$ and $P_{\theta,i} > 0$, respectively [184]. This suggests that the transfer between the resolved and the subgrid scales is proportional to the production $q_i^{sgs} \propto P_{\theta,i}$. By means of dimensional analysis of q_i^{sgs} and $P_{\theta,i}$, it can be shown that

$$q_i^{sgs} = C_\theta \tau_\theta P_{\theta,i} = -C_\theta \tau_\theta \left(q_j^{sgs} \frac{\partial \widetilde{U}_i}{\partial x_j} + \tau_{ij}^{sgs} \frac{\partial \widetilde{h}}{\partial x_j} \right), \tag{3.75}$$

where C_θ is a scalar model parameter and τ_θ is an appropriate characteristic time scale. Equation 3.75 forms an implicit algebraic formulation for the subgrid-scale heat flux vector, which is an undesirable feature in an algebraic model. Therefore, Peng and Davidson neglected the implicit term. Furthermore, only the deviatoric subgrid part of the second term in equation 3.75 is taken into account, which is modeled based on the eddy diffusivity hypothesis and the Smagorinsky model. This yields a final formulation of the model as

$$q_i^{sgs} = -C_\theta \tau_\theta \tau_{\langle ij \rangle}^{sgs} \frac{\partial \widetilde{h}}{\partial x_j} = C_t \Delta^2 \left(\widetilde{D}_{ij} - \frac{1}{3} \widetilde{D}_{kk} \delta_{ij} \right) \frac{\partial \widetilde{h}}{\partial x_j}, \tag{3.76}$$

where the model parameter C_t is determined using a dynamic procedure.

Since the non-linear model of Peng and Davidson accounts for the interaction of the resolved temperature with the velocity fluctuations, it is expected that this model is able to predict the subgrid heat flux properly in flows where the resolved enthalpy gradient is perpendicular to the stream-wise direction.

Anisotropic model by Huai and Sadiki

In contrast to the model formulations discussed so far, the anisotropic model by Huai and Sadiki [90, 179] is based on the second law of thermodynamics in conjunction with the invariant theory. In this way, the irreversibility requirements of the second law of thermodynamics are automatically fulfilled. The model reads for non-rotating frame in its cubic form

$$q_i^{sgs} = -D_{ed} \frac{\partial \widetilde{h}}{\partial x_i} + D_{dev} \tau_\theta \tau_{\langle ij \rangle}^{sgs} \frac{\partial \widetilde{h}}{\partial x_j} + D_\lambda \left(\delta_{ij} \frac{\partial \widetilde{h}}{\partial x_k} \frac{\partial \widetilde{h}}{\partial x_k} \right) \frac{\partial \widetilde{h}}{\partial x_j}, \tag{3.77}$$

where $D(-)$ are the model coefficients and τ_θ is an appropriate characteristic time scale. In the final model formulation, the last term in equation 3.77 is neglected and the subgrid-scale tensor is modeled by means of the Smagorinsky model as

$$q_i^{sgs} = -\frac{\nu_{sgs}}{Pr_{sgs}} \frac{\partial \widetilde{h}}{\partial x_i} + D_{an} \Delta^2 \left(\widetilde{D}_{ij} - \frac{1}{3} \widetilde{D}_{kk} \delta_{ij} \right) \frac{\partial \widetilde{h}}{\partial x_j}, \tag{3.78}$$

where the turbulent Prandtl number Pr_{sgs} and the model coefficient D_{an} are determined using a Germano-type dynamic procedure. Similar to the model by Peng and Davidson, this formulation of the heat flux allows to predict flow situations properly where the resolved enthalpy gradient is not aligned with the heat flux vector.

Scale similarity models

In scale similarity models proposed in [18], it is assumed that the subgrid heat flux can be approximated by the heat flux evaluated on the basis of the smallest resolved scales. Thereby, a test filter approach is utilized which leads to

$$q_i^{sgs} = C_{SS}\left(\widehat{\widetilde{U}_i\widetilde{h}} - \widehat{\widetilde{U}}_i\widehat{\widetilde{h}}\right), \tag{3.79}$$

where C_{SS} denotes the model coefficient. A priori tests show good correlations between the scale similarity model and the real subgrid scale heat flux. However, as it is the case in scale similarity models for the subgrid-scale momentum transport, an additional diffusive term has to be added to the model in order to ensure sufficient energy dissipation.

Based on the scale similarity hypothesis, Jaberi and Colluci [97] modeled the heat flux as a combination of the eddy diffusivity and the scale similarity model as

$$q_i^{sgs} = -\frac{\nu_{sgs}}{Pr_{sgs}}\frac{\partial\widetilde{h}}{\partial x_i} + C_{SS}\left(\widehat{\widetilde{U}_i\widetilde{h}} - \widehat{\widetilde{U}}_i\widehat{\widetilde{h}}\right), \tag{3.80}$$

where the model coefficients C_{SS} and Pr_{sgs} are determined dynamically. Based on a priori and a posteriori test, they found that such mixed models provide reasonable results for reactive and non-reactive flows with turbulent heat transport.

3.3.3 A new anisotropic heat flux model

In analogy to the anisotropic heat flux model by Huai and Sadiki [90, 179], the explicit anisotropy resolving heat flux model proposed here, is based on the second law of thermodynamics in conjunction with the invariant theory. From this formalism, a general expression for the subgrid-scale heat flux vector in non-rotating observer system can be derived as

$$q_i^{sgs} = -\alpha_{ij}^{sgs}\frac{\partial\widetilde{h}}{\partial x_j} = \left(\beta_1\delta_{ij} + \beta_5\tau_{ij}^{sgs} + \beta_8\left(\frac{\partial\widetilde{h}}{\partial x_k}\frac{\partial\widetilde{h}}{\partial x_k}\right)\delta_{ij}\right)\frac{\partial\widetilde{h}}{\partial x_j}, \tag{3.81}$$

where the first term on the right-hand side represents the contribution by linear diffusion, the second term expresses the influence of the subgrid-scale flow fluctuations acting on the resolved enthalpy gradient and the last term is associated with production/dissipation of subgrid-scale variance.

The coefficients β_1, β_5 and β_8 are determined based on dimensional analysis, the inertial-convective subrange theory and scaling analysis. By means of dimensional analysis, equation 3.81 can be reformulated as

$$\begin{aligned} q_i^{sgs} = &\Bigg(- C_1\tau_\theta k_{sgs}\delta_{ij} - C_5\tau_\theta\frac{2}{3}k_{sgs}\delta_{ij} + C_5\tau_\theta 2\nu_{sgs}\left(\widetilde{D}_{ij} - \frac{1}{3}\widetilde{D}_{kk}\delta_{ij}\right) \\ &- C_8\tau_\theta\frac{k_{sgs}^2}{\epsilon_{\theta_{sgs}}\epsilon_{k_{sgs}}}\delta_{ij}\left(\frac{\partial\widetilde{h}}{\partial x_k}\frac{\partial\widetilde{h}}{\partial x_k}\right)\Bigg)\frac{\partial\widetilde{h}}{\partial x_j}, \end{aligned} \tag{3.82}$$

where $\tau_\theta = \sqrt{\frac{\theta_{sgs}k_{sgs}}{\epsilon_{\theta_{sgs}}\epsilon_{k_{sgs}}}}$ is a mixed subgrid-scale characteristic time scale. At this stage, it is obvious that transport equations of k_{sgs}, $\epsilon_{k_{sgs}}$, θ_{sgs} and $\epsilon_{\theta_{sgs}}$ are required to close this model. However, by applying the inertial-convective subrange theory as described in

section 3.1.3 and combining all isotropic terms on the right-hand side, equation 3.82 can be rewritten in a fully algebraic form as

$$q_i^{sgs} = -\frac{1}{Pr^{1/4}}\frac{\nu_{sgs}}{Pr_{sgs}}\frac{\partial \widetilde{h}}{\partial x_j} + C_\theta \frac{1}{Pr^{1/4}}\Delta^2 \left(\widetilde{D}_{ij} - \frac{1}{3}\widetilde{D}_{kk}\delta_{ij}\right)\frac{\partial \widetilde{h}}{\partial x_j}, \tag{3.83}$$

where Pr is the molecular Prandtl number that accounts for the effects of variable molecular fluid properties. Based on the inertial-convective subrange theory, the subgrid-scale Prandtl number is selected as $Pr_{sgs} = 0.42$ in the present model. The coefficient C_θ is determined in analogy to the generalized diffusion hypothesis and by using the inertial-convective subrange theory as $C_\theta = 0.081$.

Finally, in order to obtain the correct asymptotic behavior of $q_i^{sgs} \sim \mathcal{O}\left(y^3\right)$ in the vicinity of the wall, a damping factor f_q is added to the second term on the right-hand side of equation 3.83. This leads to the final formulation of the present explicit anisotropy resolving algebraic heat flux model as

$$q_i^{sgs} = -\frac{1}{Pr^{1/4}}\frac{\nu_{sgs}}{Pr_{sgs}}\frac{\partial \widetilde{h}}{\partial x_j} + C_\theta \frac{1}{Pr^{1/4}}\Delta^2 \left(\widetilde{D}_{ij} - \frac{1}{3}\widetilde{D}_{kk}\delta_{ij}\right) f_q \frac{\partial \widetilde{h}}{\partial x_j}, \tag{3.84}$$

whereby f_q is defined as

$$f_q = min\left[\frac{C_\epsilon^{1/2}\nu_{sgs}}{C_k^{3/2}\Delta^2\sqrt{2\overline{S}_{ij}\overline{S}_{ij}}}, 1\right], \tag{3.85}$$

which accounts for shear damping effects in the near-wall region. From scaling analysis, it appears that $f_q \sim \mathcal{O}\left(y^3\right)$ leads to the correct asymptotic behavior of the $q_i^{sgs} \sim \mathcal{O}\left(y^3\right)$ for $y \to 0$ in the case $\nu_{sgs} \sim \mathcal{O}\left(y^3\right)$. The coefficients of the model are given as $Pr_{sgs} = 0.42$, $C_\theta = 0.081$, $C_k = 0.094$ and $C_\epsilon = 1.048$.

3.4 Subgrid-scale modeling of entropy production

Now dealing with the entropy balance equation in which flow and heat transport processes contribute to the entropy production, it turns out in the LES framework that appropriate closure approaches are of profound importance, since entropy generation is directly linked to the dissipation of energy and therefore predominantly a subgrid-scale process. In this respect, it is worth mentioning that closure models for the entropy production rates for classical LES are actually not available in the literature. To close this gap, a set of closure models for zero- and first order LES modeling approaches is provided next. The reliability of these subgrid-scale models is evaluated in section 9.3.

In the case of non-reacting and single component fluid flow with Fourier heat conduction, the filtered second law of thermodynamics can be expressed in the form of the filtered imbalance of entropy given as

$$\frac{\partial \overline{\rho}\widetilde{s}}{\partial t} + \frac{\partial}{\partial x_j}\left(\overline{\rho}\widetilde{U_j s}\right) + \frac{\partial}{\partial x_j}\overline{\left(\frac{q_j}{T}\right)} = \overline{\Pi}_v + \overline{\Pi}_q \geq 0, \tag{3.86}$$

where $\widetilde{s}$ is the filtered entropy density, $\overline{\Pi}_v$ the filtered entropy production rate by viscous dissipation and $\overline{\Pi}_q$ the filtered entropy production rate by heat transport. The last two terms can be formulated for a Navier-Stokes-Fourier fluid as

$$\overline{\Pi}_v = \overline{\frac{\mu}{T}\left(\frac{\partial U_i}{\partial x_j} + \frac{\partial U_j}{\partial x_i} - \frac{2}{3}\frac{\partial U_k}{\partial x_k}\delta_{ij}\right)\frac{\partial U_i}{\partial x_j}}, \tag{3.87}$$

$$\overline{\Pi}_q = \overline{\frac{\lambda}{T^2}\frac{\partial T}{\partial x_j}\frac{\partial T}{\partial x_j}}, \tag{3.88}$$

which are unclosed terms that can not be directly calculated by the resolved velocity and temperature fields.

Assuming that the mean of the filtered entropy production rates by viscous dissipation $\left\langle\overline{\Pi}_v\right\rangle$ is approximately same as the mean of unfiltered entropy production rate $\langle\Pi_v\rangle$ leads to

$$\begin{aligned}\left\langle\overline{\Pi}_v\right\rangle \approx \langle\Pi_v\rangle = &\underbrace{\left\langle\frac{\overline{\mu}}{\widetilde{T}}\left(\frac{\partial\widetilde{U}_i}{\partial x_j}+\frac{\partial\widetilde{U}_j}{\partial x_i}-\frac{2}{3}\frac{\partial\widetilde{U}_k}{\partial x_k}\delta_{ij}\right)\frac{\partial\widetilde{U}_i}{\partial x_j}\right\rangle}_{\langle\Pi_v^{res}\rangle}\\ &+\underbrace{\left(\left\langle\overline{\Pi}_v\right\rangle-\left\langle\frac{\overline{\mu}}{\widetilde{T}}\left(\frac{\partial\widetilde{U}_i}{\partial x_j}+\frac{\partial\widetilde{U}_j}{\partial x_i}-\frac{2}{3}\frac{\partial\widetilde{U}_k}{\partial x_k}\delta_{ij}\right)\frac{\partial\widetilde{U}_i}{\partial x_j}\right\rangle\right)}_{\left\langle\Pi_v^{sgs}\right\rangle}\end{aligned} \tag{3.89}$$

and similar for the entropy production rate by heat transport

$$\left\langle\overline{\Pi}_q\right\rangle \approx \langle\Pi_q\rangle = \underbrace{\left\langle\frac{\overline{\lambda}}{\widetilde{T}^2}\frac{\partial\widetilde{T}}{\partial x_j}\frac{\partial\widetilde{T}}{\partial x_j}\right\rangle}_{\langle\Pi_q^{res}\rangle}+\underbrace{\left(\langle\overline{\pi}_\theta\rangle-\left\langle\frac{\overline{\lambda}}{\widetilde{T}^2}\frac{\partial\widetilde{T}}{\partial x_j}\frac{\partial\widetilde{T}}{\partial x_j}\right\rangle\right)}_{\langle\Pi_q^{sgs}\rangle}, \tag{3.90}$$

where $\langle.\rangle$ denotes temporal or spatial averaging. In order to close equations 3.89 and 3.90 the averaged unresolved terms of the entropy production, $\langle\Pi_v^{sgs}\rangle$ and $\langle\Pi_q^{sgs}\rangle$, have to be modeled, while the resolved entropy production terms, $\langle\Pi_v^{res}\rangle$ and $\left\langle\Pi_q^{res}\right\rangle$, can be directly calculated from the resolved velocity and temperature fields.

By the analogy of turbulent dissipation and entropy production, the unresolved terms $\langle\Pi_v^{sgs}\rangle$ and $\langle\Pi_q^{sgs}\rangle$ can be approximated as

$$\langle\Pi_v^{sgs}\rangle \approx \frac{\langle\overline{\rho}\rangle}{\left\langle\widetilde{T}\right\rangle}\left\langle\epsilon_{k_{sgs}}\right\rangle \quad \text{and} \quad \left\langle\Pi_q^{sgs}\right\rangle \approx \frac{\langle\overline{\rho}\rangle\langle\overline{c}_p\rangle}{\left\langle\widetilde{T}\right\rangle^2}\left\langle\epsilon_{\theta_{sgs}}\right\rangle, \tag{3.91}$$

where expressions for the dissipation rate of the subgrid-scale turbulent kinetic energy $\left\langle\epsilon_{k_{sgs}}\right\rangle$ and temperature variance $\left\langle\epsilon_{\theta_{sgs}}\right\rangle$ need to be defined. Both quantities can be either obtained by solving additional transport equations or by means of the inertial-convective subrange theory. For the latter case, the expressions 3.23 and 3.27 derived in section 3.1.3 can be utilized. For the mean subgrid entropy production rates, this leads to

$$\begin{aligned}\langle\Pi_v^{sgs}\rangle &\approx \frac{\langle\overline{\rho}\rangle}{\left\langle\widetilde{T}\right\rangle}\left(\frac{2}{3C_K}\right)^{3/2}\frac{\pi}{\Delta}\langle k_{sgs}\rangle^{3/2}\\ &\approx \frac{\langle\overline{\rho}\rangle}{\left\langle\widetilde{T}\right\rangle}\frac{1}{\Delta^4 C_S^4}\langle\nu_{sgs}\rangle^3\end{aligned} \tag{3.92}$$

and

$$\left\langle \Pi_q^{sgs} \right\rangle \approx \frac{\langle \overline{\rho} \rangle \langle \overline{c}_p \rangle}{\left\langle \widetilde{T} \right\rangle^2} \frac{2\pi}{3C_{OC}} \left(\frac{2}{3C_K} \right)^{1/2} \frac{\langle \theta_{sgs} \rangle \langle k_{sgs} \rangle^{1/2}}{\Delta} \langle Pr \rangle^{1/2}$$
$$\approx \frac{\langle \overline{\rho} \rangle \langle \overline{c}_p \rangle}{\left\langle \widetilde{T} \right\rangle^2} \frac{2}{3C_{OC}\pi^{4/3}C_S^{4/3}} \langle \nu_{sgs} \rangle \left\langle \frac{\partial \widetilde{T}}{\partial x_j} \frac{\partial \widetilde{T}}{\partial x_j} \right\rangle \langle Pr \rangle^{-1} . \tag{3.93}$$

The first expressions in equations 3.92 and 3.93 are suitable for first-order modeling approaches, while the second expressions can be used in the case of zero-order modeling. It is important to mention that the relations 3.92 and 3.93 hold only true for mean values of Π_v^{sgs} and Π_q^{sgs}. However, using the Steiner translation theorem, quadratic mean values among other moments can be formulated as

$$\langle QQ \rangle = \langle Q \rangle \langle Q \rangle + \left\langle Q'Q' \right\rangle , \tag{3.94}$$

where Q is an arbitrary statistic. Then, by neglecting the fluctuation part in equation 3.94, the expressions for the entropy production rates can be formulated for instantaneous values of Π_v^{sgs} and Π_q^{sgs} as

$$\Pi_v^{sgs} \approx \frac{\overline{\rho}}{\widetilde{T}} \left(\frac{2}{3C_K} \right)^{3/2} \frac{\pi}{\Delta} k_{sgs}^{3/2}$$
$$\approx \frac{\overline{\rho}}{\widetilde{T}} \frac{1}{\Delta^4 C_S^4} \nu_{sgs}^3 \tag{3.95}$$

and

$$\Pi_q^{sgs} \approx \frac{\overline{\rho}\ \overline{c}_p}{\widetilde{T}^2} \frac{2\pi}{3C_{OC}} \left(\frac{2}{3C_K} \right)^{1/2} \frac{\theta_{sgs} k_{sgs}^{1/2}}{\Delta} Pr^{1/2}$$
$$\approx \frac{\overline{\rho}\ \overline{c}_p}{\widetilde{T}^2} \frac{2}{3C_{OC}\pi^{4/3}C_S^{4/3}} \nu_{sgs} \frac{\partial \widetilde{T}}{\partial x_j} \frac{\partial \widetilde{T}}{\partial x_j} Pr^{-1}, \tag{3.96}$$

while the averaging of these equations should be performed in the same manner as equations 3.92 and 3.93.

PART II: DEVELOPMENT OF NUMERICAL TREATMENT

Chapter 4

Numerical Methods

In spite of decades of research, only very few analytical solutions of heat and fluid flow problems are known, all of them are restricted to simple flow configurations such as heated laminar boundary layer flows over flat plates, Couette flows or potential flows. In general, it is difficult or even impossible to obtain analytical solutions for turbulent heat and fluid flow in complex geometries. In such cases, numerical simulations can be employed that allow to produce an approximate solution of the balance laws at some pre-determined locations in space and time with a given discretization error. In this respect, the solution domain and the time are divided into a finite number of discrete regions and time intervals, respectively. Then, the partial differential equations representing these balance laws can be discretized and converted into a corresponding set of algebraic equations that can be solved numerically. Additionally, in the case of numerical simulations of fluid flow, nonlinearities in the balance laws and the pressure-velocity coupling require some special attention.

This chapter presents the second-order finite volume method (FVM) discretization procedure and the pressure-velocity couplings applied to solve turbulent heat and fluid flow problems in the present work. At first, for the convenience of the reader, the discretization procedure employed in the open source C++ library OpenFOAM, which is used in this study, are briefly summarized. Then, the pressure-correction methods to solve turbulent heat and fluid flow with constant and variable physical properties are discussed. These pressure-correction methods are added to the OpenFOAM framework as part of this project in order to improve the numerical stability and the computational efficiency compared to the solution procedure available in the standard OpenFOAM framework. The resulting improvement will be discussed in the subsequent chapter.

4.1 Discretization procedure

Generally, in the case of FVM and other discretization procedures like finite element or finite difference methods, the discretization process can be divided into two steps: (1) the spatial and temporal discretization of the solution domain, and (2) the discretization of the spatial and temporal terms in the balance laws [86]. The discretization practice utilized in the present work is briefly outlined in the following, which is based on the discretization procedure as it is implemented in the OpenFOAM framework [101, 76].

4.1.1 Discretization of the solution domain

The discretization of the solution domain in FVM consists in setting up a numerical grid, by which the continuum space and the time domain are replaced by a finite number of

grid cells and time intervals [86], respectively.

Since unsteady flows are parabolic in time, the solution at any time instant is influenced only by the conditions at previous time. The solution can be obtained by starting with a given initial condition and marching forward at successive time steps, corresponding to an extrapolation in time. Thus, time is an one-way coordinate [181] and only the time step that will be used during the calculation has to be prescribed in the case of temporal discretization of the time domain. The size of the time steps is generally non-equidistant and may change during a numerical simulation, often based on conditions calculated during the simulation, e.g. depending on the Courant-Friedrichs-Lewy (CFL) condition [48].

The spatial discretization is somehow more difficult. Herein, the space domain is subdivided into a finite number of discrete regions called control volumes (CV) that completely fill and bound the solution domain [101]. In the finite volume framework of OpenFOAM, solution variables such as velocity or pressure are colocated, which means that they are specified at the same set of discrete locations, more precisely at the cell centroids of the CV's [77]. This allows an arbitrary topology of CV's, e.g. tetrahedrons, prisms, pyramids or general polyhedrons, which has significant advantages in the discretization of complex solution domains.

A typical CV including the grid nomenclature used in the OpenFOAM framework is depicted in figure 4.1, where P is the cell centroid of a particular CV, N the cell centroid of a neighboring CV and d_i the vector between the two cell centroids.

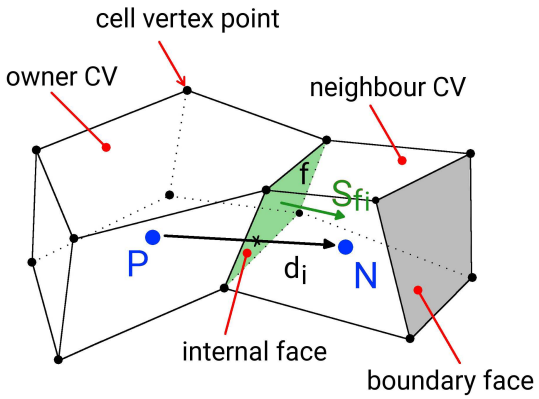

Figure 4.1: Schematic of a typical control volume including the grid nomenclature in OpenFOAM.

A CV is bounded by a set of flat faces f, that can be internal faces connecting two CV's or boundary faces of the solution domain. All CV's are stored in a list of face numbers. Faces consist of a specific number of cell vertex points and are defined by a list of vertex numbers. The vertex points are stored in a list of point coordinate vectors. Each face has a surface normal vector S_{fi} that points outwards from the CV with the lower label index. Thereby, the CV with the lower label index is called the "owner" of the face f and its label is stored in a "owner" list, while the relations to the neighboring CV's are stored in a "neighbour" list. This data structure allows to define an arbitrarily unstructured grid geometry for the FVM discretization procedure of the balance equations.

4.1.2 Spatial discretization

The FVM requires that the balance principles for basic quantities, such as mass, momentum and energy, are satisfied over any group of CV's and consequently over the whole

calculation domain [181, 208]. This leads to the integral form of the general balance equation (see equation 2.3 with $\psi = \rho\phi$) over an arbitrary control volume V_P with the centroid P as:

$$\underbrace{\frac{\partial}{\partial t}\int_{V_P} \rho\phi \; dV_P}_{\text{time derivative}} + \underbrace{\int_S \rho\phi U_i n_i \; dS}_{\text{convection}} - \underbrace{\int_S \varphi_i n_i \; dS}_{\text{diffusion}} = \underbrace{\int_{V_P} (Z + \Pi) \, dV_P}_{\text{sources}}, \tag{4.1}$$

where the terms from left to right represents the time derivative, convection, diffusion and sources of ϕ. In order to solve this equation by FVM, a series of volume and surface integrals have to be approximated by means of numerical integration. Additionally, in the case of unsteady problems, the time derivative has to be approximated which is the topic of the subsequent paragraph.

Assuming that the value of the quantity ϕ at the centroid P represents an appropriate average value over the entire CV, then it is possible to apply the midpoint rule to approximate the volume integral of ϕ over the control volume P as:

$$\int_{V_P} \rho\phi \; dV_P \approx \rho_P \phi_P \int_{V_P} dV_P = \rho_P \phi_P V_P, \tag{4.2}$$

where ϕ_P denotes the value of ϕ at the centroid P of the control volume V_P. This approximation is of second-order accuracy.

Since the CV is bounded by a series of flat faces, the surface integrals in equation 4.1 can be split into the sum of the integrals over all faces. Then, by assuming a linear variation of ϕ over the CV, the following expression for the surface integral is obtained (here written for a diffusive flux term)

$$\begin{aligned} \int_S \varphi_i n_i \; dS &= \sum_f \left(\int_f \varphi_i n_i dS \right) \\ &\approx \sum_f \varphi_{fi} S_{fi}, \end{aligned} \tag{4.3}$$

where φ_{fi} is the value of φ_i at the cell-face center of face f and S_{fi} is the surface area vector of f. Similar to volume integrals, this approximation is also of second-order accuracy.

Due to the data structure of OpenFOAM described above, the sum over the faces in equation 4.3 has to be split into the sum of "owned" and "neighboring" faces as

$$\sum_f \varphi_{fi} S_{fi} = \sum_{owner} \varphi_{fi} S_{fi} - \sum_{neighbor} \varphi_{fi} S_{fi}, \tag{4.4}$$

which guarantees global conservation. This summation over cell faces holds true for all surface integrals and is therefore omitted in the rest of the text for the sake of clarity.

In the next step it is necessary to approximate the function values and derivatives of ϕ at the cell-face centers by interpolation of variable values at the centroid P and neighboring points in order to approximate convective and diffusive fluxes, respectively. Additionally, the source terms on the right hand side of equations 4.1 have to be discretized. Several approximation schemes are available in OpenFOAM. In the following section, only the approximation methods which are applied in the present work are outlined.

Approximation of convective fluxes

The surface integral of the convection term in the general balance equation is approximated in accordance to equation 4.3 as

$$\int_S \rho\phi U_i n_i \, dS \approx \sum_f (\rho U_i)_f \, \phi_f S_{fi} = \sum_f F_f \phi_f, \tag{4.5}$$

where F_f represents the mass flux through the surface f, that is determined by linear interpolation. The surface field ϕ_f is evaluated in this work either by means of central differencing (CD) or special blended differencing (BD) interpolation schemes.

Regarding CD interpolation, the face value ϕ_f is linearly interpolated from the centroid value of P and the neighboring centroid value N. It follows that [76]

$$\phi_f = \frac{\overline{fN}}{\overline{PN}}\phi_P + \left(1 - \frac{\overline{fN}}{\overline{PN}}\right)\phi_N, \tag{4.6}$$

where $\overline{fN}$ is the distance between f and the centroid N, and $\overline{PN}$ is the distance between the centroids P and N. This interpolation scheme is unbounded and of second order accuracy.

The principle idea of BD schemes is to combine a CD approximation with an upwind differencing (UD) scheme of first order to preserve boundedness of the solution and in this respect to damp unphysical oscillations for convection dominated flows. It is a linear combination of CD and UD and reads

$$\phi_f = (\phi_f)_{UD} + \gamma \left((\phi_f)_{CD} - (\phi_f)_{UD}\right), \tag{4.7}$$

where $(\phi_f)_{CD}$ is the cell-face center value determined by a CD approximation and $(\phi_f)_{UD}$ is the cell-face center value calculated by means of upwind differencing as

$$(\phi_f)_{UD} = \begin{cases} \phi_P \text{ if } F_f \geq 0 \\ \phi_N \text{ if } F_f < 0 \end{cases}. \tag{4.8}$$

The blending factor γ in equation 4.7 can be a constant parameter or a function of the local flow conditions. The latter include so-called flux-limited schemes, some of which satisfy the total variation diminishing (TVD) criterion.

Regarding LES of convection dominated turbulent flows, the so-called "filteredLinear3V" flux-limited scheme of OpenFOAM is applied in the case ϕ_{fi} is a vector field. Thereby, the limiter function reads

$$\gamma = max\left(min\left(\alpha, 1\right), 0\right), \tag{4.9}$$

where α is given as

$$\alpha = 1 - \beta \frac{\left[(\phi_{Ni} - \phi_{Pi})\left(d_j \frac{\partial \phi_{Ni}}{\partial x_j}\right) - (\phi_{Ni} - \phi_{Pi})^2\right]\left[(\phi_{Ni} - \phi_{Pi})\left(d_j \frac{\partial \phi_{Pi}}{\partial x_j}\right) - (\phi_{Ni} - \phi_{Pi})^2\right]}{2\left[(\phi_{Nk} - \phi_{Pk})\left(d_l \frac{\partial \phi_{Nk}}{\partial x_l}\right) + (\phi_{Nk} - \phi_{Pk})\left(d_l \frac{\partial \phi_{Pk}}{\partial x_l}\right)\right]^2}, \tag{4.10}$$

with the scaling coefficient β for the gradient ratio that is selected as $\beta = 0.1$ in the present work corresponding to a limit of at most 10% upwind differencing.

In the case ϕ_f is a scalar, a minmod flux-limited scheme suggested by Roe [197] is applied in the case of supercritical fluid flow in order to assure boundedness of scalar quantities. Thereby, the limiter function equals equation 4.9 with α defined as

$$\alpha = 2\frac{d_i \frac{\partial \phi}{\partial x_i}}{\phi_N - \phi_P} - 1. \tag{4.11}$$

Here the gradient of ϕ is computed depending on the mass flux F_f as :

$$\frac{\partial \phi}{\partial x_i} = \begin{cases} \left(\frac{\partial \phi}{\partial x_i}\right)_P & \text{if } F_f \geq 0 \\ \left(\frac{\partial \phi}{\partial x_i}\right)_N & \text{if } F_f < 0 \end{cases} . \tag{4.12}$$

Regarding constant density flows, the so-called "filteredLinear" flux-limited scheme of OpenFOAM is applied in case ϕ is a scalar. This numerical scheme is similar to the "filteredLinear3V" flux-limited scheme described above.

Approximation of diffusive fluxes

Similar to the convection term, the diffusive flux is discretized as

$$\begin{aligned} \int_S \varphi_i n_i \, dS &= \int_S \rho\Gamma \frac{\partial \phi}{\partial x_i} n_i \, dS \\ &\approx \sum_f (\rho\Gamma)_f \left(\frac{\partial \phi}{\partial x_i}\right)_f S_{fi}, \end{aligned} \tag{4.13}$$

where Γ is the diffusion coefficient of ϕ. In the next step, it is necessary to determine the values of the normal derivative of ϕ at the CV faces by means of centroid values [208].

Regarding orthogonal numerical grids, where d_i and S_{fi} are parallel (see figure 4.1), the normal derivative of ϕ at the CV faces is evaluated according to

$$\left(\frac{\partial \phi}{\partial x_i}\right)_f S_{fi} = |S_{fi}| \frac{\phi_N - \phi_P}{|d_i|}, \tag{4.14}$$

where $|S_{fi}|$ is the magnitude value of the surface normal vector. In respect to general polyhedrons or non-orthogonal grids, d_i and S_{fi} are not necessarily aligned. Hence, an additional correction term has to be included. By means of the decomposition

$$S_{fi} = \Delta_{fi} + k_{fi}, \tag{4.15}$$

where Δ_{fi} is a parallel vector to d_i, the normal derivative of ϕ at the CV faces can be written as

$$\left(\frac{\partial \phi}{\partial x_i}\right)_f S_{fi} = \underbrace{|\Delta_{fi}| \frac{\phi_N - \phi_P}{|d_i|}}_{orthogonal} + \underbrace{k_{fi} \left(\frac{\partial \phi}{\partial x_i}\right)_f}_{non-orthogonal} . \tag{4.16}$$

Thereby, the surface gradient in the non-orthogonal part is interpolated using the cell-centered gradients of P and N by means of central differencing

$$\left(\frac{\partial \phi}{\partial x_i}\right)_f = \frac{\overline{fN}}{\overline{PN}} \left(\frac{\partial \phi}{\partial x_i}\right)_P + \left(1 - \frac{\overline{fN}}{\overline{PN}}\right) \left(\frac{\partial \phi}{\partial x_i}\right)_N , \tag{4.17}$$

and Δ_{fi} is calculated in this work based on the "over-relaxed" correction approach [101] as

$$\Delta_{fi} = \frac{d_i}{d_j S_{fj}} \left| S_{fk} \right|^2 . \tag{4.18}$$

The non-orthogonal vector k_{fi} is obtained from equation 4.15. Notice that the non-orthogonal term in equation 4.16 vanishes in the case of orthogonal grids, leading to the formulation 4.14 for the normal derivate of ϕ at the CV faces.

Approximation of source terms

Generally the source terms Z and Π in equation 4.1 may be a nonlinear function of the dependent variable ϕ. However, the nominally linear FVM framework applied in this work allows formally at best a linear dependence of a source term on the dependent variable. Therefore, in the case a source term (e.g. the supply term Z) is a nonlinear function of ϕ, it must be linearized as

$$Z_P(\phi) = Z_P^c + Z_P^p \phi_P, \tag{4.19}$$

where Z_P^c represents the constant part of $Z_P(\phi)$ and Z_P^p is the coefficient of ϕ_P [181]. Thus, from equation 4.2, the volume integral of the source terms is then calculated as

$$\int_{V_P} Z_P(\phi) \, dV_P = Z_P^c V_P + Z_P^p \phi_P V_P. \tag{4.20}$$

In the continuing solution procedure, the nonlinearity of the source terms and other nonlinearities (e.g. nonlinear in the momentum convection term or nonlinear dependency of physical properties) are handled by iteration. Thereby, the converged solution of the linearized equations represents the solution of the nonlinear equations (apart from the discretization error), even though it is obtained by solving solely linear equations [181]. The approximation of the source term integral is then consistent with the present second-order FVM approach.

4.1.3 Temporal discretization

So far, only spatial terms in the general balance equation 4.1 have been discretized. By using equations 4.2, 4.5, 4.13, 4.20, and assuming that the control volumes are temporally constant, the semi-discretized form of the general balance equation can now be written as

$$\begin{aligned} \left(\frac{\partial \rho_P \phi_P}{\partial t} \right)_P &= \frac{1}{V_P} \left[- \sum_f F_f \phi_f + \sum_f (\rho \Gamma)_f \left(\frac{\partial \phi}{\partial x_i} \right)_f S_{fi} + \left(Z_P^c + Z_P^p \phi_P + \Pi_P^c + \Pi_P^p \phi_P \right) V_P \right] \\ &= \mathfrak{R}(\phi), \end{aligned} \tag{4.21}$$

where $\mathfrak{R}(\phi)$ has been introduce to express the right hand side resulting from the spatial discretization. Since ϕ_f and $\left(\frac{\partial \phi}{\partial x_i} \right)_f$ are approximated with cell values of ϕ_P and ϕ_N, equation 4.21 represents an algebraic equation in terms of the discrete cell center variables for each CV. Globally, e.g. for all CV's, this produces a system of ordinary differential equations for the unknown function $\phi_P^i = \phi_P^i(t)$ for $i = 1, ..., N$, where N is the number of CVs [208].

In the next step, the time derivative term along with the corresponding right hand side term $\mathfrak{R}(\phi)$ must be approximated in order to determine the value of ϕ_P for a new time-level. For this purpose different time integration methods are available that are generally categorized as explicit and implicit methods. In the case of explicit methods,

the right hand side is only approximated by means of previous time levels, which means that the new value of ϕ_P can be calculated directly without solving a system of linear equations. For implicit methods the discretization of the right hand side depends also on the new, unknown time level. Thus, a system of linear equations has to be solved to obtain the new value of ϕ_P, which results in higher computational cost than explicit methods. However, implicit methods have the advantage as they are not restricted to small Courant-Friedrichs-Lewy (CFL) number to ensure numerical stability. Therefore, implicit methods allow larger time steps during simulations, which is highly desirable in the case of solving steady-state problems. However, in case of DNS or LES, in particular if high frequencies need to be resolved, the computational cost due to the complexity of the algorithms typically outweigh any advantages gained due to larger time steps [46]. Consequently, explicit methods are often applied in DNS or LES.

In the standard OpenFOAM framework only implicit time schemes are available, namely the Euler implicit, Crank-Nicolson and a second-order backward-differencing method. In the present work, an implicit backward-differencing scheme with second-order accuracy is primarily used in the case of heat transport and fluid flow with variable physical properties due to the relatively low computational cost of this scheme and at the same time high numerical stability. The high numerical stability is particularly important for flows at supercritical thermodynamic conditions, where transport and thermodynamic properties can vary significantly, leading to numerical instabilities. Regarding turbulent flows with constant physical properties and passive heat transfer an explicit time scheme, namely a three-stages explicit Runge-Kutta scheme of second-order accuracy [248] is applied, which was added to the OpenFOAM framework as part of this work. A detailed description of both, the implicit time integration methods of OpenFOAM and the explicit three-stages Runge-Kutta scheme, is given below, where the quantities

$$\psi^{n+1} \equiv \psi\left(t + \Delta t\right), \qquad \psi^{n} \equiv \psi(t), \qquad \psi^{n-1} \equiv \psi\left(t - \Delta t\right), \tag{4.22}$$

denote the values of $\psi = \rho\phi$ at different time levels.

Euler implicit method

Approximating the time derivative at the new time level by a first-order backward-differencing formula results in the implicit Euler method [208]

$$\frac{\psi^{n+1} - \psi^{n}}{\Delta t} = \mathfrak{R}\left(\psi^{n+1}\right). \tag{4.23}$$

Equation 4.23 is a first-order approximation that produces a system of ordinary differential equations that must be solved for ψ^{n+1}.

Backward-differencing formulas, such as equation 4.23, can be derived with arbitrary order of accuracy by using a corresponding number of previous time levels. The second-order backward-differencing approximation available in the standard OpenFOAM framework is one of them, which is described next.

Second-order Implicit backward-differencing method

In this implicit time integration scheme, the unknown value ψ^{n+1} is approximated by the parabola at the time levels $t + \Delta t$, t and $t - \Delta t$ as [208]

$$\frac{3\psi^{n+1} - 4\psi^{n} + \psi^{n-1}}{2\Delta t} = \mathfrak{R}\left(\psi^{n+1}\right), \tag{4.24}$$

which gives a second-order approximation. As in the case of implicit Euler method, the second-order implicit backward-differencing scheme produces a system of ordinary differential equations that must be solved for ψ^{n+1}.

Notice that the implicit backward-differencing approximation in equation 4.24 requires the value of ψ^{n-1} at the time level $t - \Delta t$, which is generally not known in the very first time step of a simulation. In the implementation of OpenFOAM this value is calculated using the implicit Euler method. Therefore, the present second-order implicit backward-differencing scheme is formally a first-order approximation when dealing with initial value problems and becomes only second-order accurate after the first time step.

Implicit Crank-Nicolson method

In the case of the implicit Crank-Nicolson method, the time derivative is approximated by means of the trapezoidal rule as

$$\frac{\psi^{n+1} - \psi^n}{\Delta t} = \frac{1}{2}\left[\mathfrak{R}\left(\psi^{n+1}\right) + \mathfrak{R}\left(\psi^n\right)\right], \tag{4.25}$$

which corresponds to a central differencing approximation of the time derivative at the time level $t + 1/2\Delta t$ with second-order accuracy [208]. Similar to the Euler implicit and second-order implicit backward-differencing methods, the implicit Crank-Nicolson method contains the value of ψ at the time level $t+\Delta t$ in the right-hand side and produces therefore a system of ordinary differential equations that must be solved for ψ^{n+1}.

As pointed out in [86, 208] and elsewhere, the Crank-Nicolson method is quite sensitive to nonlinearities and may exhibit stability problems for cases where the problem solution is spatially not "smooth". This aspect is particularly important for flows at supercritical thermodynamic conditions, where transport and thermodynamic properties can vary significantly, leading to numerical instabilities. The Crank-Nicolson method is therefore not used for supercritical flows in the present work, even though it is the most accurate implicit time integration method available in OpenFOAM. Instead, the second-order implicit backward-differencing method is applied in such cases.

Second-order three-stage explicit Runge-Kutta scheme

Regarding explicit time discretization of the transient term in equation 4.21, a Runge-Kutta method of second-order accuracy is applied in the case of turbulent flows with constant physical properties. In contrast to classical second-order Runge-Kutta methods with two stages, an additional stage has been introduced in order to improve the numerical stability of the procedure [125]. It is a low storage scheme that requires only two storage locations, one at the current time step ψ^n and another one at a new Runge-Kutta stage $\psi^{RK,i}$ [248]. The overall procedure reads

$$\begin{aligned}
&\text{stage 1:} \qquad \psi^{RK,1} = \psi^n + \frac{1}{3}\Delta t\ \mathfrak{R}\left(\psi^n\right), \\
&\text{stage 2:} \qquad \psi^{RK,2} = \psi^n + \frac{1}{2}\Delta t\ \mathfrak{R}\left(\psi^{RK,1}\right), \\
&\text{stage 3:} \qquad \psi^{RK,3} = \psi^n + \Delta t\ \mathfrak{R}\left(\psi^{RK,2}\right),
\end{aligned} \tag{4.26}$$

which can be written in its general form as:

$$\psi^{RK,i} = \psi^n + \beta_{RK,i}\Delta t\ \mathfrak{R}\left(\psi^{RK,i-1}\right), \qquad i \in 1, 2, 3, \tag{4.27}$$

where

$$\beta_{RK,1} = \frac{1}{3}, \qquad \beta_{RK,2} = \frac{1}{2}, \qquad \beta_{RK,3} = 1, \tag{4.28}$$

and $\psi^{RK,0} = \psi^n$ and $\psi^{RK,3} = \psi^{n+1}$ [124].

As evaluated in [124], this numerical scheme has a diffusion limit of $0 \leq \Gamma \Delta t / (\Delta x)^2 \leq 0.63$ and a convection limit of $u\Delta t/\Delta x \leq 1.73$.

4.1.4 Treatment of initial and boundary conditions

Finally, in order to obtain an unique solution of the discretized general balance equation, initial and boundary conditions of the variable ϕ have to be prescribed.

In this work, only stationary heat transfer and fluid flow processes are considered. Thereby, the initial field of ϕ is usually interpolated from a preceding simulation if available or by a synthetic generated field, e.g. a synthetic isotropic turbulent flow field. Furthermore, in order to avoid uncertainties caused by the initial transient, suitable start-up times of the simulations are selected to ensure stationarity of the initial condition.

The physical boundary conditions utilized in this study include walls, inflows, outflows, non-adiabatic walls, periodic boundaries, etc.. All of them can be represented with a set of Dirichlet, Neumann or periodic conditions. The numerical treatment of these basic boundary types in the OpenFOAM framework is outlined below. To clarify the nomenclature used, figure 4.2 depicts an arbitrary CV with a cell face f_b that comprises a part of an external boundary. The cell face center of the boundary face f_b is denoted as b and d_i is the vector that connects the cell centroid P with the cell face center b, while the vector d_{ni} is the component of d_i normal to the surface f_b. The remaining nomenclature is similar to that in sections 4.1.1 and 4.1.2.

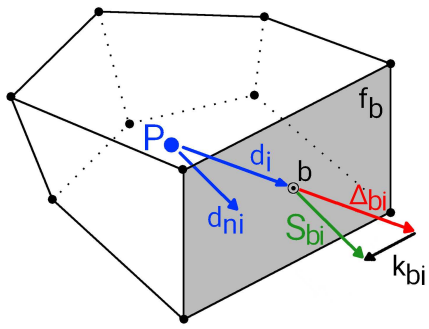

Figure 4.2: Representation of an arbitrary control volume with a cell face f_b that comprises a part of an external boundary.

Dirichlet boundary conditions

The Dirichlet boundary condition specifies the value of ϕ at the cell face center b to be g_b [101]. This has to be taken into account for the discretization procedures of convective and diffusive fluxes along the boundaries.

Convective fluxes are approximated according to equation 4.5 as

$$\int_S \rho\phi U_i n_i \, dS \approx \sum_f F_f \phi_f, \tag{4.29}$$

where the term for the boundary face f_b becomes $F_b\phi_P$, with F_b the specified flux across the boundary face f_b.

The FVM approximation of diffusive fluxes as defined in equation 4.12 reads

$$\int_S \varphi_i n_i \, dS \approx \sum_f (\rho\Gamma)_f \left(\frac{\partial\phi}{\partial x_i}\right)_f S_{fi},$$

where the face normal gradient of ϕ at the cell face center b has to be calculated. In line with the non-orthogonal correction procedure described in section 4.1.2, this is achieved as

$$\left(\frac{\partial\phi}{\partial x_i}\right)_b S_{bi} = |\Delta_{bi}| \frac{\phi_b - \phi_P}{|d_i|} + k_{bi} \left(\frac{\partial\phi}{\partial x_i}\right)_P, \tag{4.30}$$

where the decomposition of S_{bi} is same as that in equation 4.14.

Neumann boundary conditions

The Neumann type boundary condition specifies the gradient of ϕ normal to the boundary face f_b as

$$n_{bi} \left(\frac{\partial\phi}{\partial x_i}\right)_b = b_b, \tag{4.31}$$

where b_b is a prescribed function on the boundary and n_{bi} the normal vector at b.

In the case of convective fluxes, the cell face center value ϕ_b has to be calculated by means of the centroid value ϕ_P. Including the non-orthogonal correction, ϕ_b is approximated as

$$\begin{aligned} \phi_b &= \phi_P + d_{ni} \left(\frac{\partial\phi}{\partial x_i}\right)_b \\ &= \phi_P + |n_{bi} (d_j n_{bj})| \, b_b. \end{aligned} \tag{4.32}$$

Since the flux vector is prescribed in the case of Neumann boundary conditions, the diffusive term at the boundary face f_b simply becomes

$$(\rho\Gamma)_f \left(\frac{\partial\phi}{\partial x_i}\right)_f S_{fi} = (\rho\Gamma)_b \, |S_{bi}| \, b_b. \tag{4.33}$$

Periodic boundary conditions

Periodic boundaries are used to approximate large (infinite) solution domains with homogeneous directions by using only a small portion of the domain. This is achieved by means of an one-to-one mapping between the coupled boundaries. Since the coupled boundaries are directly linked in the system matrix, no special discretization practices are required to account for this boundary type [55].

4.2 Solution procedures for heat and fluid flow

The FVM framework of OpenFOAM presented above is employed in this study to solve incompressible turbulent fluid flow with heat transport using DNS and LES. Thereby, a major problem in the solution of incompressible flows consists in the linear dependence of velocity on pressure and vice-versa in the balance equations (inter-equation coupling), which requires a special numerical treatment [101].

In the case of constant density flows with passive heat transport, a low-dissipative projection method proposed by [43] is employed to establish the pressure-velocity coupling. This segregated approach is applied with the three-stages explicit Runge-Kutta scheme of second-order accuracy for time integration as described in section 4.1.3. Regarding incompressible turbulent fluid flow with heat transport and variable properties, a low Mach-number approach is employed, suitable for flows under incompressible conditions ($Ma < 0.3$). Thereby, a merged PISO[96]-SIMPLE[180] algorithm is used for the pressure-velocity coupling along with a second-order implicit backward-differencing scheme for time integration. Both solution procedures are added to the OpenFOAM framework as part of this project and are outlined in the following.

4.2.1 Turbulent flows with constant physical properties

For a turbulent Navier-Stokes-Fourier fluid flow with passive heat transport, no external body forces and constant physical properties, the employed balance equations of mass, momentum and internal energy are formulated as

$$\frac{\partial \overline{U}_i}{\partial x_i} = 0, \tag{4.34}$$

$$\frac{\partial \overline{U}_i}{\partial t} = -\frac{\partial}{\partial x_j}\left(\overline{U}_i \overline{U}_j\right) - \frac{\partial \overline{P}}{\partial x_i} + \frac{\partial}{\partial x_j}\left(\nu\left(\frac{\partial \overline{U_i}}{\partial x_j} + \frac{\partial \overline{U_j}}{\partial x_i}\right)\right) - \frac{\partial \tau^{sgs}_{\langle ij \rangle}}{\partial x_j}, \tag{4.35}$$

$$\frac{\partial \overline{T}}{\partial t} = -\frac{\partial}{\partial x_j}\left(\overline{U}_j \overline{T}\right) + \frac{\partial}{\partial x_i}\left(\frac{\nu}{Pr}\frac{\partial \overline{T}}{\partial x_i}\right) - \frac{\partial q^{sgs}_i}{\partial x_i}, \tag{4.36}$$

where P is the kinematic pressure, T the temperature, $\tau^{sgs}_{\langle ij \rangle}$ the deviatoric part of the subgrid-scale stress tensor and q^{sgs}_i the subgrid-scale heat flux vector. In the context of LES, $\overline{(.)}$ represents filtered variables, $(.)^{sgs}$ denotes subgrid-scale quantities and $\overline{P}$ is the modified pressure, which includes the isotropic part of the subgrid-scale tensor. Regarding DNS, all subgrid-scale quantities vanish and variables are fully resolved. Notice that the viscous dissipation and pressure dilation terms in the present formulation of the energy equation 4.38 are neglected.

The balance equations 4.34, 4.35 and 4.36 are numerically solved using a projection method proposed in [43], which is combined with the three-stage explicit Runge-Kutta scheme of second-order accuracy for time integration. Thereby, the solution procedure, which is calculated for each Runge-Kutta stage, can be summarized in four steps:

1. An intermediate velocity $\overline{U}^{*,k}_i$ is computed explicitly for the Runge-Kutta step k using the momentum equation, whereby the pressure term is omitted:

$$\overline{U}^{*,k}_i = \overline{U}^{n}_i + \beta_k \Delta t \, \mathfrak{R}^{*}_U\left(\overline{U}^{*,k-1}_i\right). \tag{4.37}$$

   Here Δt is the time increment, $\overline{U}^{n}_i$ the velocity from the previous time step, β_k the step size of the Runge-Kutta stage k and $\mathfrak{R}^{*}_U(.)$ is the discretized right-hand side term of the momentum equation excluding the pressure gradient. Thereby, the subgrid-scale stress tensor from the previous Runge-Kutta stage is used.

2. The pressure is calculated in such a way that the velocity field satisfies the divergence free condition. It follows for the pressure Poisson equation that:

$$\sum_f \left(\frac{\partial \overline{P}^{k}}{\partial x_i}\right)_f S_{fi} = \frac{1}{\beta_k \Delta t} \sum_f \overline{U}^{*,k}_{fi} S_{fi}, \tag{4.38}$$

where the surface gradient of $\overline{P}^k$ and the function value of $\overline{U}_{fi}^{*,k}$ at the cell-face centers are approximated with the procedures described in section 4.1.

3. Thereafter, the intermediate velocity field is corrected to obtain the value of the velocity at stage k using the updated pressure gradient interpolated to the cell centroid as:

$$\overline{U}_i^k = \overline{U}_i^{*,k} - \beta_k \Delta t \left(\frac{\partial \overline{P}^k}{\partial x_i} \right)_p . \tag{4.39}$$

Then the temperature field at stage k is approximated as

$$\overline{T}^k = \overline{T}^n + \beta_k \Delta t \; \mathfrak{R}_T \left(\overline{T}^{k-1} \right), \tag{4.40}$$

where the value of q_i^{sgs} and the corrected velocity $\overline{U}_i^{k-1}$ from the previous Runge-Kutta step are used to calculate the discretized right-hand term of the energy equation.

4. In the last step, turbulent quantities are updated for the next Runge-Kutta step in the case of LES.

In contrast to other velocity-pressure coupling methods such as pressure implicit with splitting of operator (PISO) [96] or semi-implicit method for pressure-linked equations (SIMPLE) [180], no additional corrector loop is required, which significantly speeds up calculation. Furthermore, it was shown in [240], that the projection method is less dissipative than the standards methods provided in OpenFOAM. The resulting improvement will be discussed in detail in section 5.3.

Notice that in the case of coarse grids and diffusion dominated flows, the time step size may be restricted by a high diffusion number rather than by the CFL number. In such cases the temperature equation is treated in an implicit matter by using the implicit temporal time integration schemes presented in section 4.1.3 to overcome this issue.

4.2.2 Turbulent flows with variable physical properties

In the case of incompressible Newtonian fluid flow with variable physical properties and Fourier heat transport, the employed balance equations of mass, momentum and sensible enthalpy are formulated as

$$\frac{\partial \overline{\rho}}{\partial t} = -\frac{\partial}{\partial x_i} \left(\overline{\rho} \widetilde{U}_i \right), \tag{4.41}$$

$$\frac{\partial \overline{\rho} \widetilde{U}_i}{\partial t} = -\frac{\partial}{\partial x_j} \left(\overline{\rho} \widetilde{U}_i \widetilde{U}_j \right) - \frac{\partial \overline{P}}{\partial x_i} + \frac{\partial}{\partial x_j} \left(\overline{\mu} \left(\frac{\partial \widetilde{U}_i}{\partial x_j} + \frac{\partial \widetilde{U}_j}{\partial x_i} - \frac{2}{3} \frac{\partial \widetilde{U}_k}{\partial x_k} \delta_{ij} \right) \right) - \frac{\partial \overline{\rho} \tau_{\langle ij \rangle}^{sgs}}{\partial x_j} + \overline{\rho} g_i, \tag{4.42}$$

$$\frac{\partial \overline{\rho} \widetilde{h}}{\partial t} = -\frac{\partial}{\partial x_j} \left(\overline{\rho} \widetilde{U}_j \widetilde{h} \right) + \frac{\partial}{\partial x_i} \left(\frac{\overline{\lambda}}{\overline{c}_p} \frac{\partial \widetilde{h}}{\partial x_i} \right) - \frac{\partial \overline{\rho} q_i^{sgs}}{\partial x_i}, \tag{4.43}$$

where P is the pressure, h the sensible enthalpy, $\tau_{\langle ij \rangle}^{sgs}$ the deviatoric part of the subgrid-scale stress tensor and q_i^{sgs} the subgrid-scale heat flux tensor. In the context of LES, $\widetilde{(.)}$ are Favre-filtered variables, $(.)^{sgs}$ denotes subgrid-scale quantities and $\overline{P}$ is the modified pressure, which includes the isotropic part of the subgrid-scale stress tensor. Regarding DNS, all subgrid-scale quantities vanish and variables are fully resolved. Notice that

the pressure-dilatation and viscous dissipation terms in the enthalpy equation are usually assumed to be small in incompressible flows [186]. It is therefore neglected in this work.

The set of balance equations 4.41, 4.42 and 4.43, are numerically solved using a low-Mach number approach suitable for flows under incompressible conditions ($Ma < 0.3$) and with variable properties. In this approach, the pressure P is divided into a thermodynamic p_{th} and a mechanical p_{dyn} part. The density variations caused by the mechanical part are neglected. In this way, in contrast to a fully compressible formulation, pressure and density are formally decoupled by defining the density and all other physical properties through constitutive equations expressed in terms of local temperature T and constant thermodynamic pressure p^{th}. Only the mechanical pressure appears in the momentum equation. In this way, acoustic and compressibility effects are neglected [12].

Similar to the pressure-based compressible approach available in the standard OpenFOAM framework, the pressure Poisson equation for the low Mach-number approach is derived from the discretized form of the momentum equation. Using the FVM procedure described previously and an implicit time integration scheme, the discretized momentum equation for a cell P may be written in matrix form as [101]

$$A_P \widetilde{U}_{Pi}^{n+1} = H_{U_i} - \left(\frac{\partial \overline{p}_{dyn}^{n+1}}{\partial x_i} \right)_P \qquad \text{with} \qquad H_{U_i} = -\sum_N \left(A_N \widetilde{U}_{Ni}^{n+1} \right) + S_{U_i} \tag{4.44}$$

where both sides are divided by the cell volume. A_P are the matrix coefficients of $\widetilde{U}_{Pi}$ that consists of the coefficients from the convective, diffusive and temporal terms. The vector H_{U_i} combines the neighbor matrix coefficients multiplied by their velocities and all other terms apart from the pressure gradient (see section 3.8.1 in [101]). By substituting equation 4.44 into the the continuity equation, the following Poisson equation for the mechanical pressure is obtained

$$\sum_f S_{fi} \left[\left(\rho^{n+1} A_P^{-1} \right)_f \left(\frac{\partial \overline{p}_{dyn}^{n+1}}{\partial x_i} \right)_f \right] = \frac{\partial \rho^{n+1}}{\partial t} + \sum_f S_{fi} \left(\rho^{n+1} H_{U_i}^{n+1} A_P^{-1} \right)_f . \tag{4.45}$$

The solution of the pressure Poisson equation 4.45 allows to correct the velocity in an explicit manner as

$$\widetilde{U}_{Pi} = H_{U_i}^{n+1} A_P^{-1} + A_P^{-1} \left(\frac{\partial \overline{p}_{dyn}^{n+1}}{\partial x_i} \right)_P , \tag{4.46}$$

where the pressure gradient is interpolated to the cell centers.

In the present low Mach-number approach, a merged PISO[96]-SIMPLE[180] algorithm is used for the coupling of the mechanical pressure and velocity. A schematic representation of the solution algorithm is depicted in figure 4.3. One iteration within a time step of the segregated approach can be summarized as follows:

1. First, the continuity equation is solved with face fluxes from the previous time step. This stage is called density predictor and gives an approximation of the new density field to an intermediate fractional time.

2. Then, the discretized momentum equation (equation 4.44) is solved using the most updated density and pressure fields from the previous iteration step. This stage is called momentum predictor and gives an approximation of the new velocity field to an intermediate fractional time and an update of the operator H_{Ui}. Thereby, the non-linear momentum convection term is linearized by using the mass flux from the previous iteration.

3. Next, the enthalpy equation is solved and the temperature is iteratively determined. In the case of tabulated thermodynamic properties, no iterative procedure is applied, instead the temperature is directly obtained by interpolation from a thermodynamic table using the value of the computed enthalpy.

4. Subsequently, the thermodynamic and transport properties are updated by means of the actual temperature field and the thermodynamic pressure.

5. Thereafter, the constant coefficient pressure Poisson equation is solved (equation 4.45) and the velocity and mass flux components are corrected in such a way that they are divergence free (equation 4.46).

6. Finally, turbulent quantities are updated in the last step.

This completes one iteration step of the segregated approach. However, due to the non-linearity of the momentum equation and the coupling between velocity and pressure, one iteration step has to be repeated using outer iteration loops (PISO- and SIMPLE-loop) for each time step until a prescribed accuracy is reached. Thereby, the matrix coefficients, source terms and thermodynamic properties are updated after each outer iteration. Notice, that during each inner loop, in which the linear equation system is iteratively solved (e.g. solution of the momentum predictor), the matrix coefficients, thermodynamic properties and source terms remain constant.

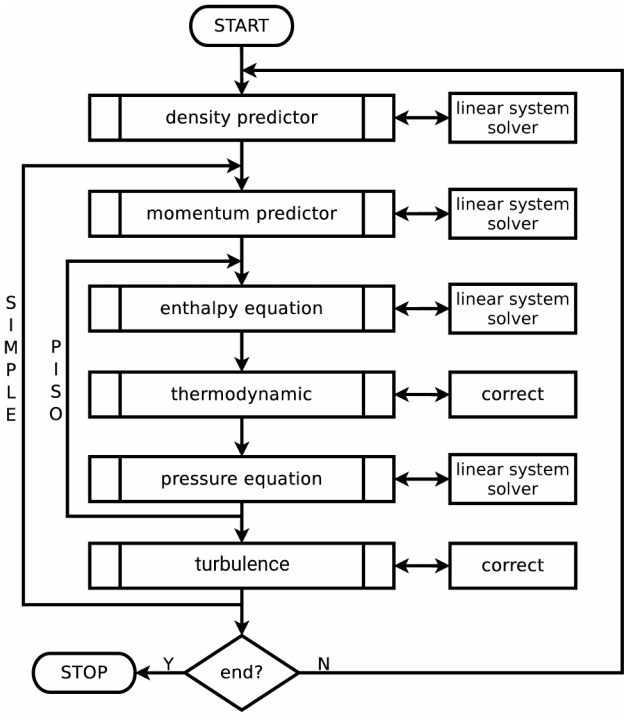

Figure 4.3: Flowchart of the low Mach-number merged PISO[96]-SIMPLE[180] solution algorithm.

As it can be seen in figure 4.3, two different outer iteration loops are available in the merged PISO-SIMPLE algorithm, namely, a PISO- and a SIMPLE-loop. The SIMPLE-loop repeats the solution procedure beginning from the momentum equation. Therefore, this outer loop also iterates over the momentum convection term taking its non-linearity into account. The PISO-loop repeats the solution procedure from the enthalpy equation.

It takes only into account the correction due to the change in the pressure gradient and thermo-physical properties, but not the correction of the non-linear momentum convection term. However, due to small time steps, the non-linear coupling is usually less important than the pressure-velocity and thermodynamic coupling in the case of DNS and LES. Therefore, the number of PISO-loops usually outweighs the number of SIMPLE-loops in the practical application of this solution procedure.

In contrast to the standard solution procedure for turbulent flows with variable physical properties and arbitrary Mach-numbers available in the OpenFOAM framework, the low Mach-number approach provides a significantly improved numerical stability, especially in cases where physical properties vary strongly. Moreover, no wave transmissive boundary conditions are required in the low Mach-number approach, which reduces the complexity of a simulation. An evidence of the improved numerical stability is provided later in section 5.3.

Chapter 5

Code Verification

In this chapter the implementations of the solution procedures for turbulent heat transport and fluid flow with constant and variable physical properties are verified. Herein, the term code verification describes the process of demonstrating that the discretized balance equations, as implemented in the source code, are solved consistently to the respective order-of-accuracy of the discretization method [205]. Therefore, it is most likely that a verified code is free of programming errors that affects the theoretical order-of-accuracy of the numerical algorithm [216]. Hence, code verification is an essential step in the development of reliable simulation software, also in this work.

Generally, several test approaches for code verification are reported in the literature including physical trend tests, symmetry tests, code-to-code comparison, approaches based on exact analytical solutions and methods using manufactured solutions. These tests are usually combined with a particular test acceptance criteria such as expert judgment, percentage error, consistency and/or order-of-accuracy [205]. However, as pointed out in [205] and elsewhere, only the Method of Exact Solutions (MES) and the Method of Manufactured Solutions (MMS) combined with the order-of-accuracy acceptance criteria allow to test the code capability in full generality.

Typically, in the MES code verification procedure, the generated numerical discrete solution is compared with published exact solution from the literature. If the code passes the selected acceptance criterion, it is considered adequately verified [205]. However, it is very difficult to find exact solutions to a set of balance equations, especially in the case of equations involving non-linearities and variable physical properties. This limitation often impedes the application of MES code verification procedure, likewise in the case of numerical approaches to solve turbulent heat and fluid flow problems.

In contrast to MES, the MMS verification procedure allows a more comprehensive alternative which is also applicable to more complex problems. In brief, a manufactured solution is an exact solution to a set of partial differential equations that has been constructed by solving the problem backwards [205]. This means that the analyst first selects a sufficiently differentiable function $\phi(x,t)$ to describe the desired evolution of the dependent variables in space and time. This solution does not necessarily fulfill the original set of partial differential equations. Therefore, a corresponding set of source terms are manufactured by applying the set of partial differential equations to $\phi(x,t)$ and added to the source code in order to balance the system [216]. The resulting set of modified partial differential equations, which include the additional source terms, are then solved for different spatial and/or temporal resolutions. Finally, the order-of-accuracy in space and time is quantified and verified for the numerical approach by comparing the obtained discrete solution with the exact manufactured solution. In this way, the MMS procedure allows

a rigorous code verification in full generality. Further information about the concept and procedure of MMS can be found in [205, 216, 166].

It is worth mentioning that a manufactured solution is not necessarily completely related to the physical problem of interest. It may represent some relevant features of the physical problem like strong variation of physical properties or steep velocity gradients, however it is mostly a generic test approach to demonstrate that the discretized balance equations are solved consistently to the respective order-of-accuracy of the discretization method. Thus, aspects like the numerical stability, efficiency or parallel scaling characteristics of a numerical approach as well as the validity of the physical modeling are generally not established in a MMS verification analysis. The numerical stability, efficiency and parallel scaling are usually addressed in numerical fluid dynamics by means of benchmark test cases like the well-known viscous Taylor-Green vortex flow [225], the transport of a sharp density step by pure convection or natural convection in a square cavity [54]. The validity is mostly the topic of case specific validation studies. Beside code verification, all these aspects should be addressed when developing reliable numerical simulation software.

In this work, the method of manufactured solutions is utilized to demonstrate that the solution procedure to solve turbulent heat transport and fluid flow, as added to the standard OpenFOAM source code, are solved consistently to the theoretical order-of-accuracy of the discretization method. In the following, first the outcome of the verification study for the solution procedure for thermo-fluid flows with constant physical properties are presented. Then, the implementation of the solution procedure for heat transport and fluid flow with variable properties is verified. The last part of this chapter deals with a demonstration of the efficiency, robustness and parallel scaling of the two approaches in comparison with the standard methods available in the OpenFOAM framework. The validation of the present numerical approaches is presented in the subsequent chapter.

5.1 Solution procedure for constant density flows

The code verification of the numerical procedure to solve thermo-fluid flows with constant physical properties consists of two parts. First, the spatial accuracy of the numerical approach is quantified by means of a steady-state three-dimensional manufactured solution. Then, the temporal accuracy of the explicit Runge-Kutta time integration scheme is assessed using a time-dependent manufactured solution.

Spatial accuracy

A steady-state, three-dimensional manufactured solution is selected to quantify the spatial accuracy of the numerical approach. Thereby, the velocity field resembles a Taylor-Green vortex [225], which leads to the following smoothly varying solutions for the velocity, pressure and temperature fields

$$\begin{aligned}
U_x &= -cos\left(2\pi x\right) \cdot sin\left(2\pi y\right) \cdot sin\left(2\pi z\right), \\
U_y &= 0.5 \cdot sin\left(2\pi x\right) \cdot cos\left(2\pi y\right) \cdot sin\left(2\pi z\right), \\
U_z &= 0.5 \cdot sin\left(2\pi x\right) \cdot cos\left(2\pi y\right) \cdot sin\left(2\pi z\right), \\
p &= \left(\frac{1}{3}x^3 - \frac{1}{2}x^2\right) \cdot \left(\frac{1}{3}y^3 - \frac{1}{2}y^2\right) \cdot \left(\frac{1}{3}z^3 - \frac{1}{2}z^2\right), \\
T &= 20 \cdot \left(sin\left(\pi x\right) + sin\left(\pi y\right) + sin\left(\pi z\right) + 273\right),
\end{aligned} \tag{5.1}$$

where x, y and z are the coordinates in space. The solution domain for the verification study is selected as $[0,1] \times [0,1] \times [0,1]$ for x, y, z. A representation of the manufactured

solution in the computational domain is depicted in figure 5.1, where (a) shows iso-surfaces of the velocity magnitude, (b) the distribution of the kinematic pressure, and (c) the variation of temperature.

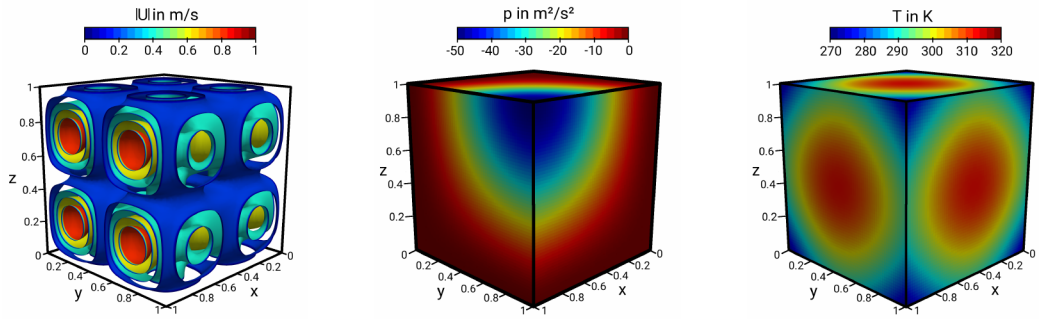

(a) (b) (c)

Figure 5.1: Representation of the manufactured solution. (a) iso-surfaces of velocity magnitude, (b) distribution of kinematic pressure, (c) variation of temperature.

The solution is applied to the governing equations in section 4.2.1 leading to non-zero source terms in the momentum and energy equations, which are implemented into the source code (not described here). No source term appears in the continuity equation since the manufactured solution satisfies the divergence free condition, which is advantageous due to the importance of mass conservation in the solution algorithm but not mandatory in the MMS verification procedure. The kinematic viscosity is set to one to balance the order of magnitude of convection and diffusion terms equally in the momentum equation. Four hexahedral numerical grids with equidistant cells are employed in the verification study with 512, 4096, 32768 and 262144 control volumes. Regarding the temperature and velocity at the boundaries, Dirichlet conditions are utilized, while a Neumann condition is used for the kinematic pressure. The numerical simulations are initialized with the exact solution and solved iteratively with a convergence criterion selected close to machine accuracy.

In order to quantify the global discretization error, which is required to determine the order-of-accuracy of the solution algorithm, the mean absolute error (MAE) is utilized. It is defined as

$$MAE = \frac{\sum_{i=1}^{n} |\phi_i^{num} - \phi_i^{ref}| \alpha_n}{n}, \tag{5.2}$$

where ϕ_i^{num} is the discrete solution at the cell i, ϕ_i^{ref} is the reference value from the manufactured solution at the same locations in space and time, n is the number of grid cells and α_n is a local measure of volume, which is constant in the case of uniform numerical grids and can be set to one. From equation 5.2 it follows that if $|\phi_i^{num} - \phi_i^{ref}| \alpha_n = O(h^p)$, then the MAE is of the order $O(h^p)$ and therefore the order of the numerical discretization approach.

Figure 5.2 shows a logarithmic scaled graph of the observed MAE's as a function of the number of control volumes. Results are shown for the magnitude velocity, kinematic pressure and temperature. Dashed lines represent the theoretical order-of-accuracy of the numerical approach.

As it is apparent in figure 5.2, the MAE drops by a factor of four with each halving of the grid cell size, thus matching the theoretical second-order slope and verifying that the numerical approach is of second-order accuracy in space. This holds true for the

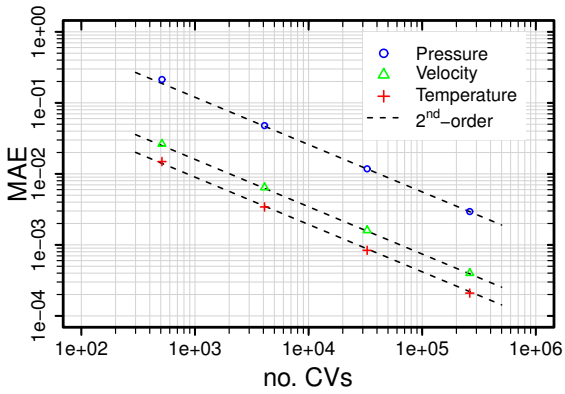

Figure 5.2: Mean absolute error (MAE) as a function of mesh size for the magnitude velocity, kinematic pressure and temperature.

magnitude velocity, kinematic pressure and temperature. Moreover, the manufactured solution is recovered as the grid size approaches to zero. This confirms that the balance equations are solved consistently.

Temporal accuracy

A time-dependent manufactured solution is selected to assess the temporal accuracy of the explicit three-stage Runge-Kutta scheme for time integration. It reads

$$U_x = U_z = sin\,(20\pi t)\,, \quad U_y = -cos\,(20\pi t)\,, \quad p = const., \quad T = sin\,(20\pi t)\,, \tag{5.3}$$

where t is the time. Notice that a temporal analysis of the pressure is not considered as no time derivative of p occurs in the balance equations. The time-dependent manufactured solutions are provided in figure 5.3.

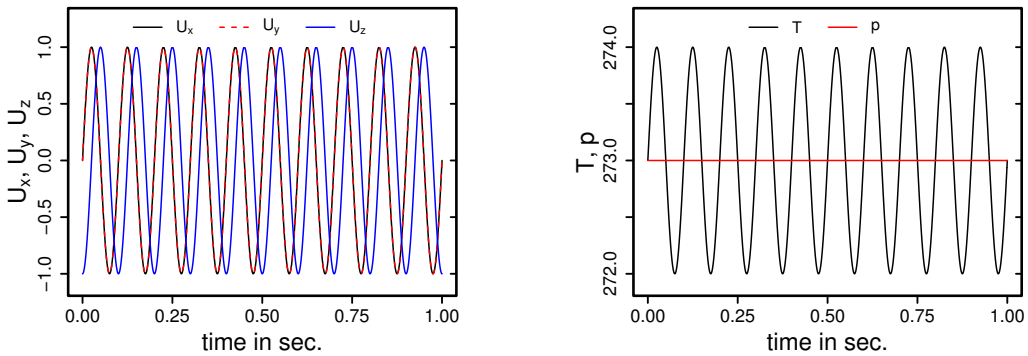

(a) (b)

Figure 5.3: The applied manufactured solution in the solution domain. (a) evolution of velocity components, (b) evolution of temperature and pressure.

Similar to the verification of the spatial accuracy, the solution is applied to the governing equations leading to non-zero source terms in the momentum and energy equations. No source term appears in the continuity equation. For this analysis, the time step is gradually increased from $\Delta t = 2 \cdot 10^{-3} s$ to $\Delta t = 2.5 \cdot 10^{-2} s$ by a factor of two and the time solution domain is selected as $[0, 1]$. The spatial domain is taken from the steady-state

three-dimensional manufactured solution with 512 control volumes and Dirichlet boundary conditions for all dependent variables.

Figure 5.4 shows a logarithmic scaled graph of the observed MAE's as a function of the time step size for the velocity magnitude and the temperature.

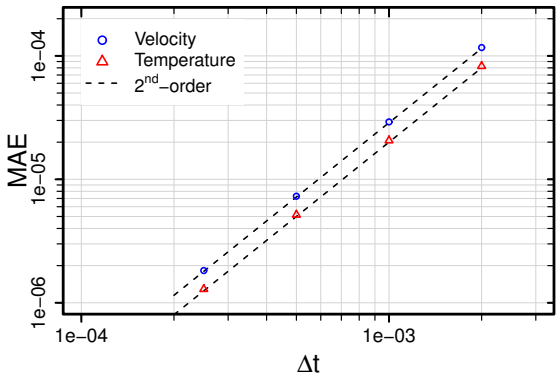

Figure 5.4: Mean absolute error (MAE) as a function of time step size for the magnitude velocity and temperature.

As it can be clearly observed in figure 5.4, the global errors decrease by a factor of four with each halving of the time step, thus matching the theoretical second-order slope, suggesting that the numerical approach is of second-order accuracy in time. This can be observed for both, velocity and temperature.

Based on the findings in the spatial and temporal verification studies it can be concluded that the numerical solution procedure to solve heat and fluid flow with constant physical properties is adequately verified. It is therefore most likely that the numerical algorithm is free of programming errors that affect the order-of-accuracy and can therefore be used for further benchmark and validation studies.

5.2 Solution procedure for variable density flows

A time-dependent, one-dimensional manufactured solution is selected to verify the numerical procedure for thermo-fluid flows with variable physical properties as presented in section 4.2.2. The manufactured solution used for this purpose is taken from [216]. As already mentioned above, a manufactured solution is not necessarily related to a physical problem, however, the manufactured solution utilized here mimics a binary mixing of two miscible fluids with large density ratio. It therefore represents some relevant flow features of variable-density flows with strong density variation typically of those encountered in flows under supercritical conditions. Hence, it may also give some insights into the behavior of the numerical solution procedure, when applied to such flow situations of interest. The relating solutions are given as

$$
\begin{aligned}
U_x &= 2k_2 exp\left(-k_1 t\right) \frac{\rho_0 - \rho_1}{\rho} \left(\frac{\hat{u}x}{\hat{u}^2 + 1} + \frac{\left(k_1/k_2 - 1\right)\left(arctan\left(\hat{u}\right) - \pi/4\right)}{\omega_0 exp\left(-k_2 t\right)} \right), \\
h &= \frac{exp\left(-k_1 t\right) - cosh\left(\omega_0 x exp\left(-k_2 t\right)\right)}{exp\left(-k_1 t\right)\left(1 - \rho_0/\rho_1\right) - cosh\left(\omega_0 x exp\left(-k_2 t\right)\right)}, \\
\rho &= \left(\frac{h}{\rho_1} + \frac{1-h}{\rho_0} \right)^{-1},
\end{aligned}
\tag{5.4}
$$

where $\hat{u} = exp\,(\omega_0 x exp\,(-k_2 t))$ and $\omega_0 = 50$, $k_1 = 4$, $k_2 = 2$, $\rho_0 = 10$, $\rho_1 = 1$ are constant parameters. x is the spatial coordinate and t the time. In this manufactured solution, the sensible enthalpy h ranges from 0 to 1, similar to a mixture fraction variable. The solution domain for the verification study is selected as $0 \leq x \leq 1$ and $0 \leq t \leq 0.1$.

The solution is applied to the governing equations of turbulent heat and fluid flow with variable physical properties (see section 4.2.2) with $\mu = \frac{\overline{\lambda}}{\overline{c}_p} = 0.03$ and $\overline{\rho} g_i = 0$, leading to a non-zero source term $S_h \neq 0$ in the enthalpy equation. No source term appears in the continuity equation since the manufactured solution satisfies mass conservation ($S_\rho = 0$). Furthermore, as pointed out in [216], no source term is specified in the momentum equation. Instead the pressure gradient is allowed to compensate the momentum transport in order to satisfy the momentum equation with a zero source term $S_u = 0$. The spatio-temporal evolution of the manufactured solution is depicted in figure 5.5, where the distribution of the velocity, the sensible enthalpy, the density and the distribution of S_h for different time instances are shown.

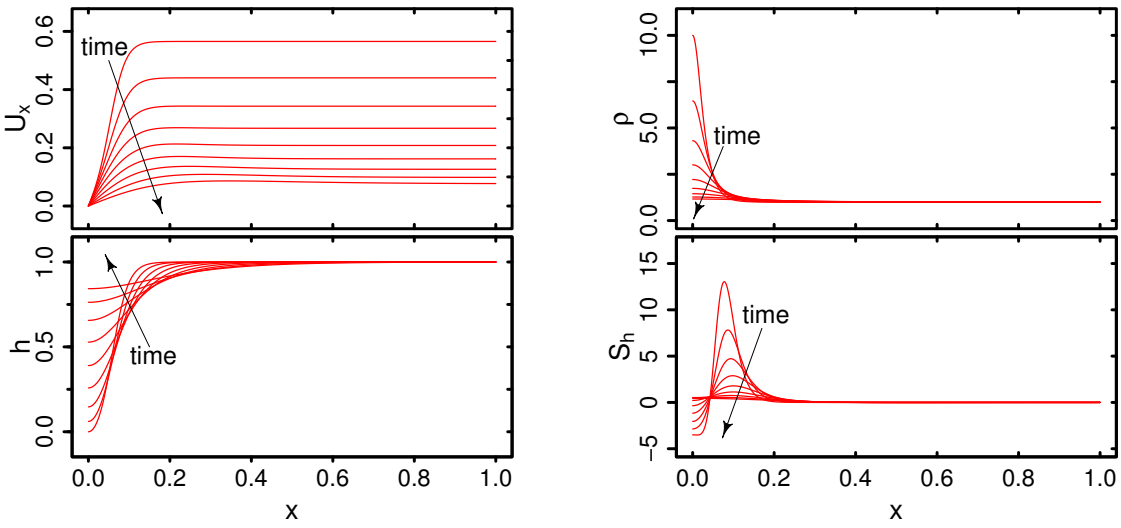

Figure 5.5: Spatio-temporal evolution of the time-dependent, one-dimensional manufactured solution.

A spatial grid-refinement study has been carried out to assess the convergence rate of the spatial accuracy of the low Mach-number solution procedure. For this purpose, a set of eight numerical grids with equidistant cells are employed consisting of 16, 32, 64, 128, 256, 512, 1024 and 2048 control volumes, respectively. Thereby, a small time step of $\Delta t = 1 \cdot 10^{-5} s$ is used in order to minimize the error contribution from the temporal discretization. A separate temporal-refinement study has been conducted using the second-order implicit backward differencing scheme and the implicit method of Crank-Nicolson for time integration, respectively. The numerical grid with 2048 control volumes is selected in this study to ensure a small spatial error and the time step is gradually increased from $\Delta t = 1.953125 \cdot 10^{-4} s$ up to $\Delta t = 0.05 s$ by a factor of two leading to a CFL-number range from $CFL = 0.1$ to $CFL = 50$. Dirichlet boundary conditions are imposed for the velocity and enthalpy at $x = 0$, while a zero Neumann condition is set for the mechanical pressure. At $x = 1$, Dirichlet conditions are employed for the mechanical pressure and the sensible enthalpy, and a zero Neumann condition is set for the velocity. All simulations are initialized with the exact manufactured solution and solved iteratively with a small convergence criterion.

Regarding the analysis of the spatial accuracy, figure 5.6 shows a logarithmic scaled graph of the observed MAE's for the velocity and sensible enthalpy as a function of the number of control volumes. Dashed lines represents the expected second-order convergence rate of the numerical procedure.

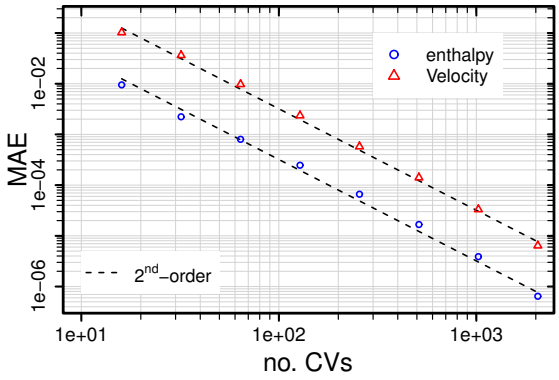

Figure 5.6: Mean absolute errors of velocity and enthalpy as a function of mesh size.

As it can be clearly observed in figure 5.6, the MAE drops by a factor of four with each halving of the grid size, thus verifying the theoretical second-order accuracy in space. This holds true for both, sensible enthalpy and velocity, which confirms that the discretized balance equations, as implemented in the source code, are solved consistently to the respective order-of-accuracy of the spatial discretization method.

Next, results of the temporal-refinement study are provided in figure 5.7. The dashed lines represents a convergence rate of second-order accuracy and dotted lines a first-order accuracy convergence rate.

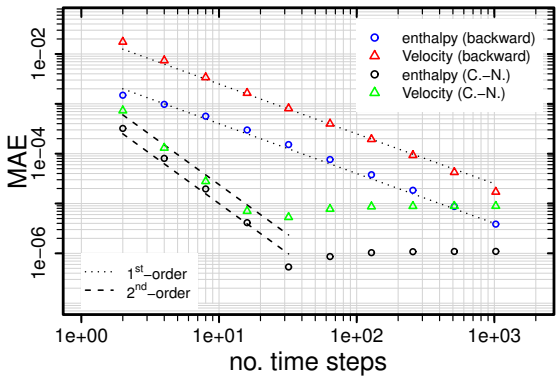

Figure 5.7: MAE for the velocity and enthalpy in respect to time step size. Comparison of the backward and Crank-Nicholson methods of OpenFOAM. (grid size: 2048 CVs)

Apparently in figure 5.7, the MAE of the implicit Crank-Nicolson method drops by a factor of four with each halving of the time step size, suggesting a time integration of second-order accuracy. However, it can be clearly seen that the error reduction stagnates for small time steps. This is due to the error contribution from the spatial discretization. Thereby, in the case of small time step sizes, the error contribution from the spatial discretization exceeds the temporal error contribution. Consequently, the MAE converge towards the spatial error, which is consistent with the findings in figure 5.6 and confirms that the implementation of this time integration scheme is second-order accurate.

In the case of the second-oder implicit backward-differencing scheme, the MAE drops only by a factor of two with each halving of the time step size, corresponding to a first-order time integration for more or less all time step sizes under consideration. As already mentioned above, the implicit backward-differencing approximation in equation 4.24 requires the value of the dependent variables at the time level $t - \Delta t$, which is generally not known in the first time step of a simulation. In the implementation of OpenFOAM this value is calculated using the implicit Euler method with first-order accuracy. Therefore, the present second-order implicit backward-differencing scheme is formally a first-order approximation when dealing with initial value problems (see figure 5.7). However, it becomes second-order accurate after the first time step or in cases in which the value of the dependent variables at the time level $t - \Delta t$ are known. This is usually the case in stationary heat and fluid flow problems, exclusively analyzed in this work. The second-order implicit backward-differencing scheme is therefore used in the present work due to the relatively low computational cost of this scheme and at the same time high numerical stability, even though it is formally a first-order time integration scheme.

Based on the findings in the verification study, it can be concluded that the numerical solution procedure to solve heat and fluid flow with variable physical properties is adequately verified. It is therefore most likely that the numerical algorithm is free of programming errors that affect the order of accuracy and, consequently, can be used for further benchmark and validation studies.

5.3 Efficiency, robustness and parallel scaling

In order to demonstrate the efficiency and robustness of the numerical solution procedures applied in the present study to solve fluid flow with constant and variable properties, two different benchmark problems are selected. The first test problem is the viscous Taylor-Green vortex flow at $Re = 1600$, which is used to study the dissipation characteristics and the computational cost of the solution procedure for fluid flow with constant physical properties. Thereby, results are compared with the standard solution procedure for constant density flows available in the OpenFOAM framework, called pisoFOAM. The second test problem is an one-dimensional convected density step, which is selected to demonstrate the numerical stability improvements by means of the low Mach-number approach in comparison to the standard all Mach-number approach available in OpenFOAM, called rhoPimpleFoam. Finally, the parallel scaling characteristic of both solution procedures are addressed at the end of this section to complete the code verification and performance analysis.

Viscous Taylor-Green vortex flow at $Re = 1600$

The viscous Taylor-Green vortex flow at $Re = 1600$ is aimed to study the dissipation characteristic and the computational cost of the solution procedure for fluid flow with constant physical properties as presented in section 4.2.1. It is defined by the simple

initial conditions [234]

$$
\begin{aligned}
U_x &= V_0 sin\left(\frac{x}{L}\right) \cdot cos\left(\frac{y}{L}\right) \cdot cos\left(\frac{z}{L}\right), \\
U_y &= -V_0 cos\left(\frac{x}{L}\right) \cdot sin\left(\frac{y}{L}\right) \cdot cos\left(\frac{z}{L}\right), \\
U_z &= 0, \\
p &= p_0 + \frac{\rho_0 V_0^2}{16}\left(cos\left(\frac{2x}{L}\right) + cos\left(\frac{2y}{L}\right)\right)\left(cos\left(\frac{2z}{L}\right) + 2\right),
\end{aligned} \tag{5.5}
$$

in a periodic cube with side length $-\pi L \leq x, y, z \leq \pi L$. The simulation parameters are $V_0 = 1$, $\rho_0 = 1$, $L = 1$, $p_0 = 0$ and $\mu = 6.25 \cdot 10^{-4}$, leading to an initial Reynolds number of $Re = \rho_0 \cdot V_0 \cdot L/\mu = 1600$.

The initial flow field (see equation 5.5) becomes first turbulent followed by an unsteady decay. Thereby, the large initial scales cascade into small-scale vortical structures similar to decaying homogeneous turbulence. An illustration of this characteristic transition process is depicted in figure 5.8, which shows iso-surfaces of the Q-criterion, colored by the kinetic energy at different characteristic convective time instants $t_c = L/V_0$.

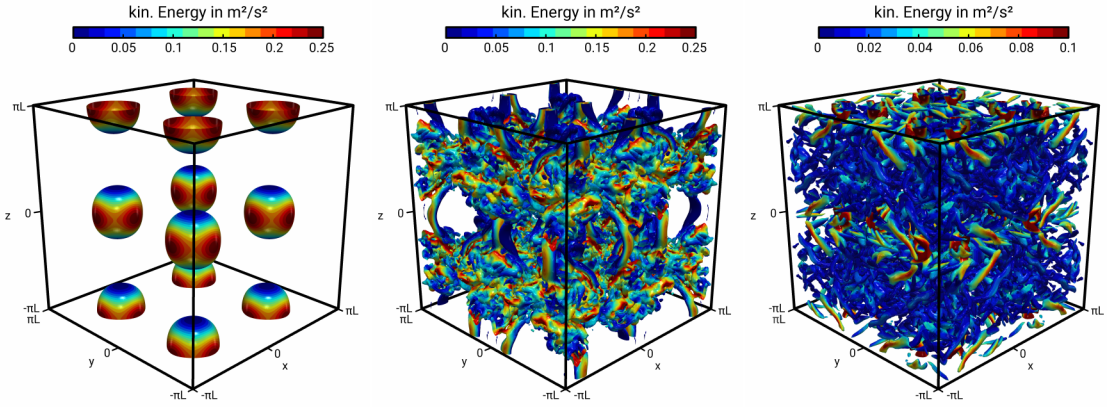

(a) $t/t_c = 0$ (b) $t/t_c = 10$ (c) $t/t_c = 20$

Figure 5.8: Iso-surfaces of the Q-criterion at $Q = 0.5$, colored by the instantaneous kinetic energy at different times for the viscous Taylor-Green vortex flow at $Re = 1600$. Results are obtained with the projection method combined with the three-stage explicit Runge-Kutta time integration with 128^3 control volumes.

Three hexahedral numerical grids with equidistant cells are employed consisting of 32^3, 64^3 and 128^3 control volumes. Thereby, the finest grid resolution with the second-order approach has 256^3 degrees of freedom, which is required to fully resolve the Taylor-Green vortex up to $t/t_c = 20$ [234]. Two numerical solution procedures, the standard OpenFOAM PISO approach applied with the second-order backward-differencing time integration scheme and the projection method applied with the three-stages explicit Runge-Kutta time integration of second-order (see section 4.2.1) are utilized in the performance study in order to compare the dissipation characteristics of both solution procedures. Thereby, all numerical simulations are solved with the same numerical setup and convergence criteria. For comparison, the grid-converged DNS dataset of [234] obtained on a numerical grid with 512^3 cells and a dealiased pseudo-spectral code are utilized.

Figure 5.9 shows the evolution of (a) the kinetic energy and (b) the dissipation rate of the kinetic energy ($dE/dt = -\epsilon$) integrated over the solution domain as a function of time.

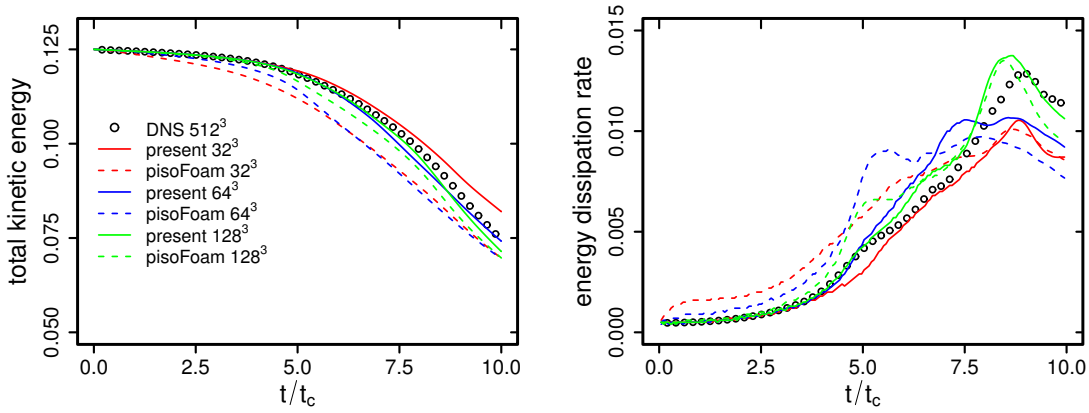

Figure 5.9: Comparison of the present solution procedure with the standard OpenFOAM PISO approach. (a) evolution of the kinetic energy and (b) dissipation rate of the kinetic energy integrated over the solution domain as a function of time. Reference DNS dataset of [234] with 512^3 grid cells.

It can be observed in figure 5.9, as expected the projection method applied with the second-order explicit Runge-Kutta time integration scheme compares much better against the DNS reference than the standard OpenFOAM PISO approach. This holds true for both, the evolution of kinetic energy and the corresponding dissipation rate for all grid resolutions under consideration. To note that the standard OpenFOAM PISO approach has dissipated a significant portion of kinetic energy within the first five characteristic convective time scales, especially in the case of coarse grid resolution, even though turbulent scales are relatively large in this time interval. In contrast, the present projection method almost fully conserves the kinetic energy for all grid sizes under consideration. Therefore, it can be concluded that the projection method applied with the second-order explicit Runge-Kutta time integration scheme has a relatively low level of numerical dissipation. Moreover, it was observed that the computational cost of the present approach is about $25\% - 50\%$ lower than the standard OpenFOAM PISO approach. The projection method applied with the three-stages explicit Runge-Kutta time integration is therefore used in the present work to solve heat and fluid flow with constant physical properties instead of the standard OpenFOAM PISO approach.

One-dimensional convected density step

The numerical configuration with an infinitively sharp density step by pure convection is often employed to study the stability of numerical schemes, see e.g. [124, 191]. This generic benchmark test case is therefore used in the present work to demonstrate the improvements in the numerical stability of the low Mach-number solution procedure in comparison to the standard all Mach-number approach available in the OpenFOAM framework (rhoPimpleFoam), especially to handle flow situations with strongly varying physical properties. Such flow conditions are often encountered in supercritical flows where pseudo-boiling takes place. It is therefore of profound importance for the present work, that the proposed numerical solution procedure is able to handle such flow conditions.

The numerical setup is depicted in figure 5.10 with simulation parameters summarized in table 5.1.

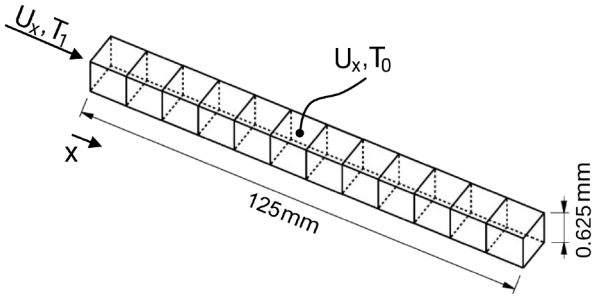

Figure 5.10: Computational domain of the one-dimensional convected density step.

Property	Value
no. CV's	200
U_x	1m/s
T_0	3000K
T_1	300K
ρ_1/ρ_0	10
μ	$1.8 \cdot 10^{-5}\ Pa \cdot s$
λ/c_p	$0\ m^2/s$
q_i^{sgs}, τ_{ij}^{sgs}	0

Table 5.1: Simulation parameters of the convected density step.

The solution domain is initialized with air of constant temperature $T_0 = 3000K$ and velocity $U_x = 1m/s$. At time $t = 0$, air with the same velocity but lower temperature ($T_1 = 300K$) enters the domain with a sudden change in density ($\rho_1/\rho_0 = 10$). The thermal diffusivity is set to zero in the test case. Thus, the exact solution of the problem resembles the transport of an infinitely sharp density step by pure convection.

The predicted evolution of the density step and the corresponding velocity at several time instants are shown in figure 5.11, where (a) depicts the results obtained by the low Mach-number approach and (b) presents the predictions of the all Mach-number approach available in the standard OpenFOAM framework. Red dashed lines denote the exact solution for the convection of an infinitely sharp density step.

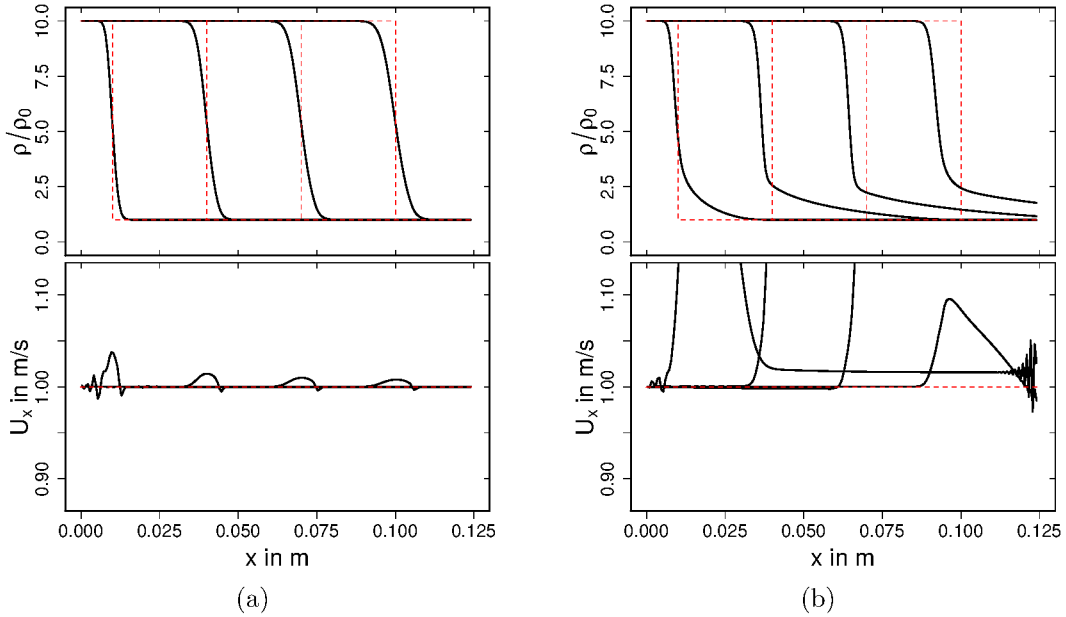

Figure 5.11: Temporal evolution of the transport of an infinitely sharp density step by pure convection. (a) results from the low Mach-number approach; (b) prediction of the all Mach-number approach available in the standard OpenFOAM framework.

Comparing the temporal evolution of density, it appears that the results obtained by the low Mach-number approach are very close to the exact solution, except the unavoidable flattening of the very sharp step because of limitations in the spatial resolution. In contrast, the all Mach-number approach available in the standard OpenFOAM framework is not able to predict the density profiles properly. Two issues within the standard OpenFOAM approach are clearly visible. First, the position of the step is significantly delayed compared to the exact solution. Secondly, predicted density profiles tend to smear out towards the region of lower density. The reason for such an unphysical behavior becomes clearer by examining the evolution of the predicted velocity. Here, the exact solution would be a constant velocity of $U_x = 1m/s$. However, due to the numerical diffusion an additional momentum flux is numerically introduced, which must be balance by the pressure correction in order to satisfy mass conservation [124]. This artificial momentum flux leads to unphysical velocities, which should decay since the density step becomes increasingly resolved during the simulation. As it can be seen in figure 5.11 (a), the low Mach-number approach converges towards the exact solution during the simulation, with maximal velocity deviation of $\sim 5\%$ in the first time steps. It provides therefore an acceptable solution for such flow conditions. In contrast, predicted velocities by the standard OpenFOAM all Mach number approach deviate significantly from the exact solution. Especially in the first time steps, the velocity overshoots more than 30%. Furthermore, the error in the velocity field does not decrease during the simulation.

The one-dimensional convected density step benchmark test case clearly demonstrates the improvements in the numerical stability of the low Mach-number solution procedure in comparison to the standard all Mach-number approach available in the OpenFOAM framework to handle flow situations with strongly varying physical properties. From this it is obvious that the low Mach-number approach as described in section 4.2.2 is utilized in the further studies to solve DNS and LES of sub- and supercritical flows with heat transfer.

Parallel scaling

Despite the improvements in the efficiency of the numerical solution algorithms, the numerical simulations of DNS and LES of sub- and supercritical flows carried out in the present study are still very demanding with respect to computing power and memory capacity. Consequently, parallel computing is exploited to further reduce the required computing time significantly. In this respect, it is important to verify the parallel scaling of the added solution procedures to solve heat transport and fluid flow with constant and variable physical properties within the OpenFOAM framework.

As described in [76], OpenFOAM employs domain decomposition and can be applied with several MPI libraries, such as those optimized for particular hardware platforms used in high performance computers (e.g. IBM or Cray). Scaling of the current solution procedures up to 480 CPUs have been evaluated on the Lichtenberg High Performance Computer (HHLR) at the Technische Universität Darmstadt for the phase 2 infrastructure. Thereby, scaling of the code was measured using 2 million control volumes applying strong scaling test, which means that the code performance was evaluated for a constant problem size and increasing number of cores. A problem size of 2 million control volume is selected since it represents a typical number of control volumes of LES in the present study. The obtained results from the scaling test for both solution procedures with constant and variable physical properties are depicted in figure 5.12. Thereby, the relative computing time is normalized based on the value for 15 CPUs.

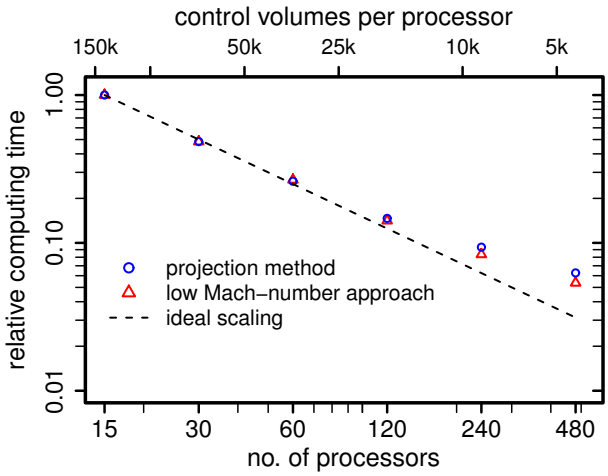

Figure 5.12: Computational speed-up for both solution procedures on the Lichtenberg high performance computer of the Technische Universität Darmstadt. (normalized to 15 processors).

As it can be seen in figure 5.12, both solution procedures exhibit a nearly ideal scaling up to 15000 control volumes per processor, which corresponds to a total number of 120 processors for a grid size of 2 million control volumes. Notice that the maximal reasonable number of processors depends on the total number of control volumes and the respective hardware used. However, it turned out that the code is able to exploit the full capacity of the Lichtenberg high performance computer, when using $\sim$ 15000 control volumes per processor. This also holds true for grid sizes larger than 2 million cells.

Chapter 6

Code Validation

In this chapter the validity of the numerical methods and LES modeling approaches as described and verified in the previous chapters are established. In brief, the term validation describes the process of quantifying the physics modeling accuracy of the computational simulation by comparing with experimental data [167]. It therefore provides evidence of how accurately the computational model simulates the real world and addresses the question whether or not the computational method satisfies the acceptable accuracy criteria requirements.

Generally, in code validation studies, the ability of a numerical model to simulate a real world physical process or a set of processes is quantitatively determined. In this context, the real world is traditionally restricted to be only measured quantities in a physical experiment [5]. This assumes that (1) the validation experiments are executed correctly and (2) presupposes that appropriate experimental data for validation purpose are available. However, it is worth mentioning that both is often not the case. The limitations of present measurement techniques, especially in turbulent near-wall flows and fluid flow with variable physical properties where steep gradients, small turbulent flow scales and extreme thermodynamic operating conditions make reliable measurements very difficult. Besides, several experiments are not well designed to provide true validation data, which means that they do not measure all the relevant physical data as well as initial and boundary conditions that are required to perform a meaningful code and model validation study.

Even though, the code validation process is usually restricted to a comparison with experimental data, in the present work highly accurate numerical solutions from DNS studies are also considered in order to validate the code and the utilized models, in case reliable experimental data is not available. In this way the reference DNS can be seen as a numerical experiment without any physical modeling error, although this is not true in most cases.

The present code and model validation study is divided into three parts. First, the validity of the solution procedure for flows with constant physical properties is established by means of DNS of passive heat transport in a turbulent channel flow at $Re_\tau = 180$. Then, DNS of a strongly heated turbulent air flow in a vertical pipe at $Re_\tau = 180$ were conducted in order to validate the solution procedure for flows with variable physical properties. Finally, LES of a turbulent heated annulus flow of CO_2 at supercritical pressure and at $Re_b = 8900$ were carried out to assess the prediction accuracy of the low-Mach number approach under supercritical thermodynamic conditions.

6.1 DNS of turbulent channel flow with passive heat transport

In order to establish the validity of the solution procedure for flows with constant physical properties, a DNS of fully developed turbulent channel flow with heated walls has been carried out at a Reynolds number of $Re_\tau = 180$ based on the friction velocity and with a molecular Prandtl number of $Pr = 0.71$. Thereby, buoyancy effects are not taken into account, and the temperature is treated as a passive scalar. This configuration is selected since it features a wall-bounded turbulent flow with heat transfer as encountered in various engineering applications like plate heat exchangers or other cooling/heating devices, where the change in physical properties can be often neglected. To compare the present DNS results, laser-Doppler measurements of Niederschulte et al. [165] and reference DNS data of Kawamura et al. [109] are utilized.

6.1.1 Numerical setup

A schematic of the flow domain is provided in figure 6.1, where: (a) depicts an isometric view of the channel configuration; (b) the view along the z-axis (flow direction); and (c) the view along the x-axis (front view). δ denotes half the height of the channel. Notice that only the heat transport within the flow field region is numerically investigated, while the heat conduction inside the solid wall is not considered.

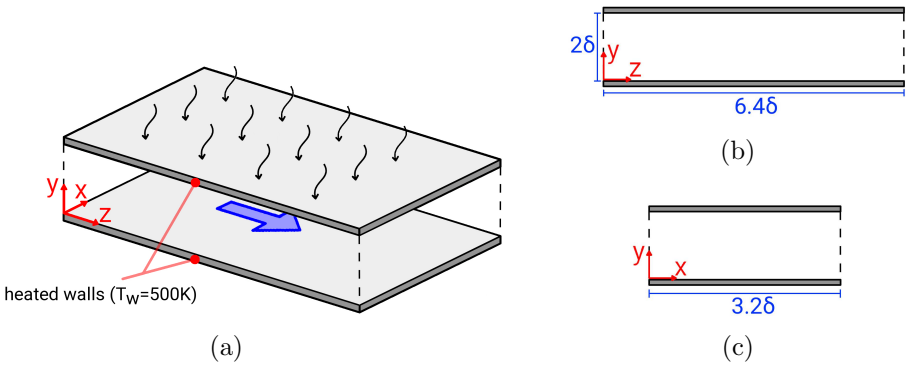

Figure 6.1: Schematic of the flow domain. (a) isometric view; (b) view along z-axis; (c) view along x-axis. δ denotes half the height of the channel.

In line with the reference DNS of [109], the computational domain has a length of 6.4δ and an extent in the span-wise direction of 3.2δ. Thereby, the numerical grid equals the grid used in [109] with $128 \times 66 \times 128$ grid points in span-wise, wall-normal and stream-wise directions, respectively. The near-wall region is refined in order to fully resolve the small flow structures in the vicinity of the solid wall.

An isotropic turbulent velocity field is used to initialize the channel flow simulation. Therefore, a random velocity field Ω is generated in a channel with equally spaced grid, which has a zero mean velocity by construction. In order to fulfill the continuity equation in Fourier space, the random field is cross-multiplied with the wavenumber vector $\vec{\kappa}$ and re-scaled. In the next step, the autocorrelation spectrum

$$E\left(\vec{\kappa}\right) = E_a \left(\frac{|\vec{\kappa}|}{\kappa_0}\right)^4 e^{-2(|\vec{\kappa}|/\kappa_0)^2}, \tag{6.1}$$

similar to that found in [256], is imposed on each component of the random velocity field. Subsequently the resulting random flow field $\vec{U}^*$ is multiplied with a random phase n and inverse Fourier transformation $\mathfrak{F}(\kappa)^{-1}$ is carried out leading to an initial fluctuation field of

$$\vec{u}' = \mathfrak{F}(\kappa)^{-1}\left[cos(2\pi n)\cdot\vec{U}^* + i\cdot sin(2\pi n)\cdot\vec{U}^*\right], \tag{6.2}$$

where i is the imaginary unit. Afterwards, $\vec{u}'$ is linearly interpolated onto the non-equidistant grid and is set to zero at the channel wall. Finally, in order to ensure fully developed flow, a cyclic time of ten flow through the domain is used before averaging is started.

Periodic boundary conditions are applied in the stream-wise and span-wise directions for the velocity and temperature. At the channel walls, no-slip condition is set for the velocity and a zero Neumann conditions for the kinematic pressure. For temperature, a constant wall temperature of $T_w = 500K$ is imposed. The pressure and temperature gradient, which drive the heat and fluid flow, are adjusted dynamically to maintain a constant mass flux and mean mixed temperature, respectively. For this purpose, a source term is added to the momentum and energy equations (see [121]).

6.1.2 Results

Figure 6.3 shows the predicted mean and rms values of the velocity as a function of the non-dimensional wall distance y^+. For comparison, laser-Doppler measurements of Niederschulte et al. [165] and reference DNS data of Kawamura et al. [109] are utilized.

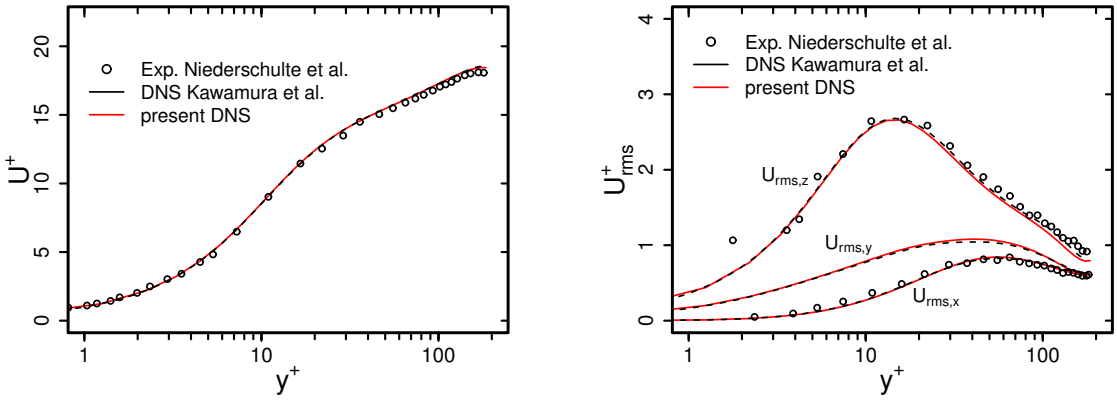

Figure 6.2: Mean (a) and rms (b) velocities as a function of the non-dimensional wall distance y^+. Comparison of simulation results with measurements of [165] and DNS data of [109].

Apparently in figure 6.2, predicted mean and rms velocities agree quite well with both the reference DNS dataset and measurements. The characteristic viscous sublayer region ($y^+ < 5$), the buffer layer region ($5 < y^+ < 30$) as well as the log-law region ($y^+ > 30$) are well retrieved, which holds true for mean and rms velocities.

Predicted non-dimensional mean and rms temperature profiles are shown in figure 6.3 (a) and (b), respectively. The non-dimensional temperature is defined as $\theta^+ = (T_w - T)/T_\tau$, where $T_\tau = q_w/(\rho c_p u_\tau)$ is the friction temperature and $q_w = 1180K/m$ is the heat flux from both walls. Notice that results of mean and rms temperatures are only compared with the DNS dataset of [109] since no experimental data is available.

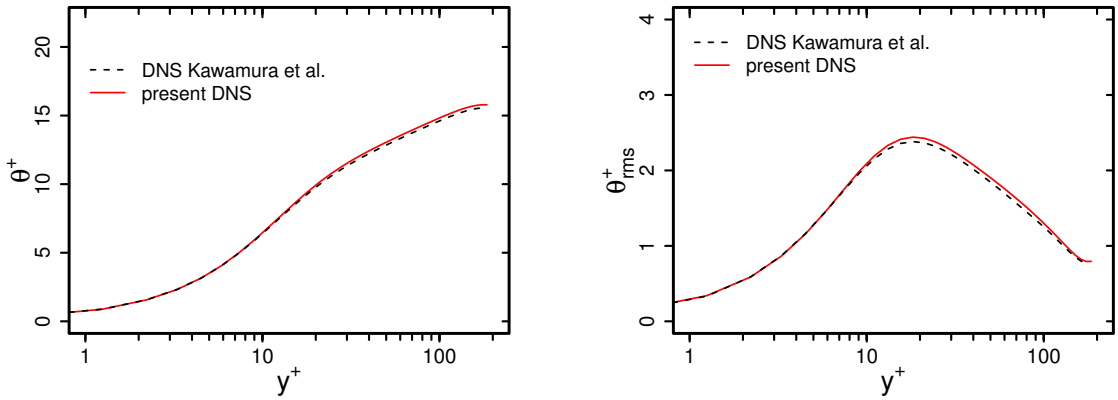

Figure 6.3: Non-dimensional mean (a) and rms (b) temperatures as a function of the non-dimensional wall distance y^+. Comparison of simulation results with reference data of [109].

Similar to first and second order statistical moments of the velocity field, predicted profiles of non-dimensional mean and rms temperatures are very close to the reference DNS dataset. The logarithmic, the wake and the near-wall region as well as the characteristic peak of temperature variance in the vicinity of the wall at $y^+ \sim 20$ are well retrieved by the present numerical approach.

Finally, the prediction accuracy of turbulent thermo-fluid processes are analyzed by means of the evolution of turbulent kinetic energy and temperature variance in figure 6.4. Thereby, the budget terms of the turbulent kinetic energy are normalized by ν/u_τ^4 and budget terms of temperature variance by $\nu/\left(u_\tau^2 T_\tau^2\right)$. The predictions are only compared with the DNS of [109] since reliable experimental data is not available in literature.

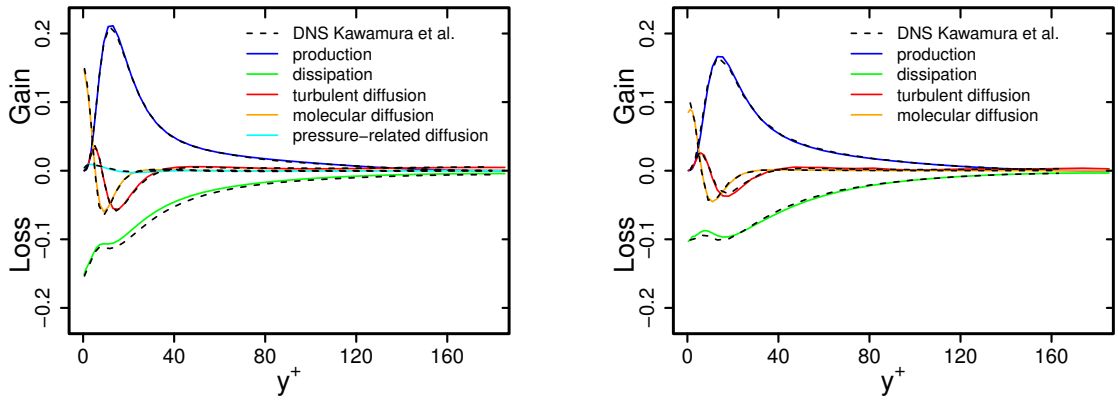

Figure 6.4: Normalized budget terms of turbulent kinetic energy (a) and temperature variance (b). Comparison of simulation results from the present DNS with reference data of [109].

The predicted balances of budget terms of turbulent kinetic energy and temperature variance are very close to the reference DNS data. Furthermore, it can be seen that turbulent thermo-fluid processes within the heated channel flow are dominated by near-wall effects rather than free-stream turbulence, which are well captured by the present numerical method. This establishes the validity of the present DNS results and confirms that the numerical methods applied are appropriate to describe heat and fluid flow statistics

along with thermo-fluid processes for wall-bounded turbulent flows with constant physical properties and can therefore be used for further investigation studies.

6.2 DNS of strongly heated turbulent air flow in a vertical pipe

In various engineering applications with heat transfer, strong temperature differences occur, e.g. in exhaust gas systems or gas turbine engines. In such cases, thermodynamic and transport properties change strongly and a numerical approach based on constant thermo-physical properties is no longer justifiable. Regarding flows with negligible compressibility effects ($Ma < 0.3$) a low-Mach number approach as described in section 4.2.2 can be applied. The validity of the present low-Mach number approach is established in this section. For this purpose, DNS of a strongly heated turbulent air flow in a vertical pipe with constant wall heat flux have been carried out and simulation results are compared with measurements of [214] and DNS data of [14].

6.2.1 Numerical setup

A schematic of the strongly heated vertical pipe flow configuration is shown in figure 6.5, where (a) depicts an isometric view; (b) the view along the flow direction; and (c) the view along the radial direction. D denotes the diameter of the pipe.

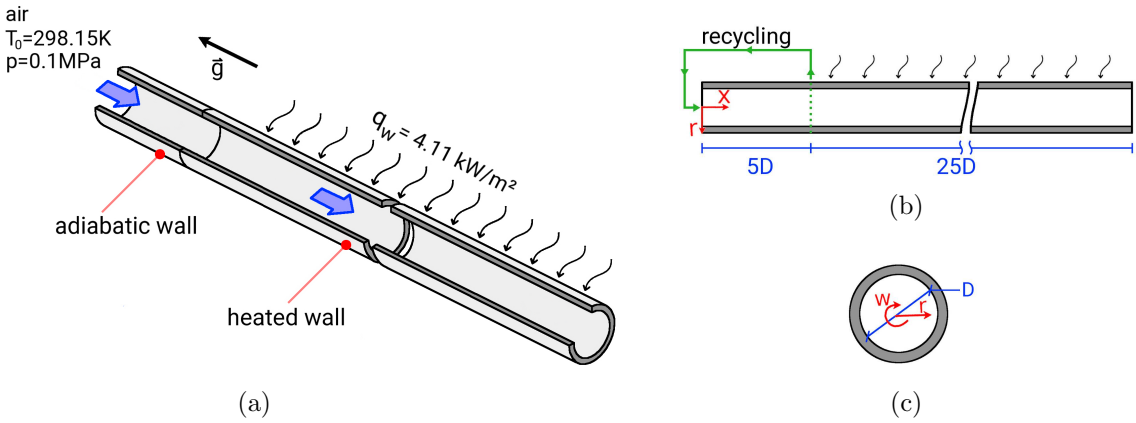

Figure 6.5: Schematic of the heated pipe flow domain. (a) isometric view; (b) view along x-axis; (c) view along r-axis. D denotes the inner diameter of the pipe.

In the test section, fully developed turbulent flow of dry air ($Re = 6000$, $T_0 = 298.15K$, $p = 0.1MPa$) enters a DN-25 pipe ($D = 0.0272m$, $L = 30D$) and is heated up after an entrance length of $5D$. The heated pipe region has a length of $25D$ with a constant wall heat flux of $q_w = 4.11kW/m^2$. In line with the DNS study of [14], air is treated in the current DNS study as an ideal gas using the ideal gas equation. Other thermo-physical properties are obtained by means of power laws in the temperature as described in [14].

A block-structured numerical grid is used to discretize the pipe flow domain. It consists of approximately 28 million control volumes, equivalent to $74 \times 234 \times 1600$ grid points in radial r, circumferential ω and axial x directions, respectively. The near-wall region is refined in order to fully resolve the small turbulence scales in the vicinity of the wall.

At the pipe wall, a no-slip condition is set for the velocity and a zero Neumann conditions for the pressure. In the case of temperature, a constant wall heat flux of

$q_w = \frac{\lambda}{c_p}\frac{\partial h}{\partial r}\big|_{r=R} = 4.11 kW/m^2$ is imposed at the heated wall while a zero temperature gradient condition is set at the adiabatic wall. In order to obtain realistic inflow turbulence, the velocity field is extracted for each time step at the $x = 5D$ plane downstream of the inlet and used to prescribe the velocity field at the inflow plane. At the outlet, a convective boundary condition is used for the velocity to maintain the overall mass conservation, while the pressure is set to a constant value.

In order to avoid uncertainties caused by the initial solution, a fully developed turbulent temperature and velocity fields are generated by means of a separate LES, which is interpolated on the numerical grid of the DNS. Afterwards, one flow through the domain is solved before averaging of the DNS results is started.

6.2.2 Results

A comparison of predicted mean temperature and velocity profiles with hot wire measurements of [214] and DNS results of [14] is depicted in figure 6.7 (a) and (b), respectively. Thereby, the temperature T is normalized by the inflow temperature T_0 and the velocity by the local bulk velocity U_b.

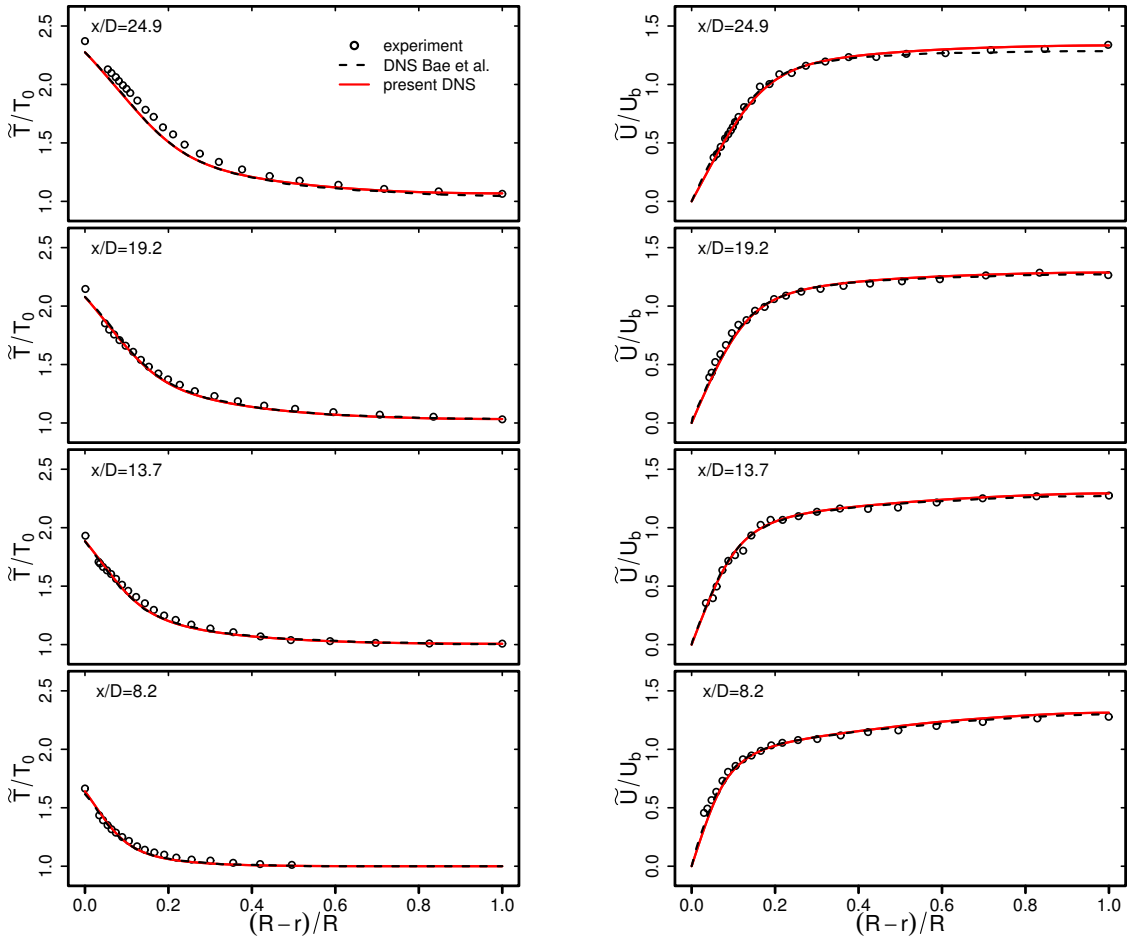

Figure 6.6: Comparison of radial mean temperature and velocity profiles with hot wire measurements of [214] and DNS results of [14] at x/D=8.2, 13.7, 19.2, 24.9.

The mean temperature and velocity profiles agree well with the hot wire measurements and also with the reference DNS dataset. This holds true for all axial locations and over

the entire radius, which confirms that the present approach is able to provide reliable predictions for the configuration of strongly heated pipe flow.

Further validation of the present DNS results regarding the prediction of turbulent kinetic energy and axial heat fluxes is given in figure 6.7 (a) and (b), respectively. The turbulent kinetic energy is non-dimensionalized by means of the local fluid density at the wall ρ_w and the local friction velocity u_τ, and the turbulent axial heat flux by the wall heat flux q_w. Results are exclusively compared with DNS data since no experimental data is available.

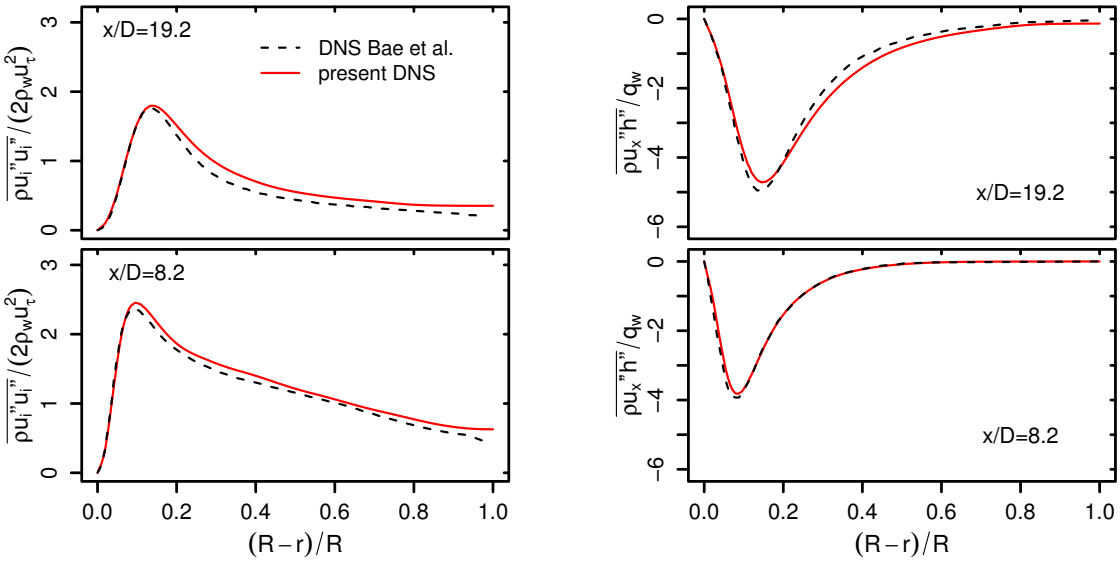

Figure 6.7: Comparison of turbulent kinetic energy and axial turbulent heat fluxes with DNS results of [14] at x/D=8.2, 13.7, 19.2, 24.9.

Similar to mean statistics, turbulent kinetic energy and axial turbulent heat flux agree well with the reference DNS data, also close to heated walls. Therefore, it can be concluded that the numerical methods applied are appropriate to describe turbulent wall-bounded flows with heat transport and variable thermo-physical properties in order to use for further investigations.

6.3 LES of heated carbon dioxide flow in an annulus at supercritical pressure

In this section, the low-Mach number approach is evaluated for wall-bounded flows at supercritical thermodynamic conditions. For this purpose, LES of heated carbon dioxide flow at supercritical pressure in an annulus at $Re_b = 8900$ (based on bulk velocity and hydraulic diameter) has been carried out. Since experimental data are not available for this specific flow configuration, simulation results are solely compared with the DNS dataset of [15, 13].

This annulus flow configuration is especially selected since it features very complex turbulent heat transport phenomena along with pseudo-boiling effects which are relevant in particular to supercritical carbon dioxide heat pumps, supercritical water-cooled nuclear reactors and other heating/energy applications with working fluids under supercritical thermodynamic conditions.

6.3.1 Numerical setup

An illustration of the heated supercritical annulus flow configuration is presented in figure 6.8, where (a) depicts an isometric view of half the annulus geometry; (b) the view along the flow direction x; and (c) the view along the radial direction r. δ denotes the channel half width of the concentric annulus, which is selected as $\delta = 0.5mm$ according to the DNS study of [15].

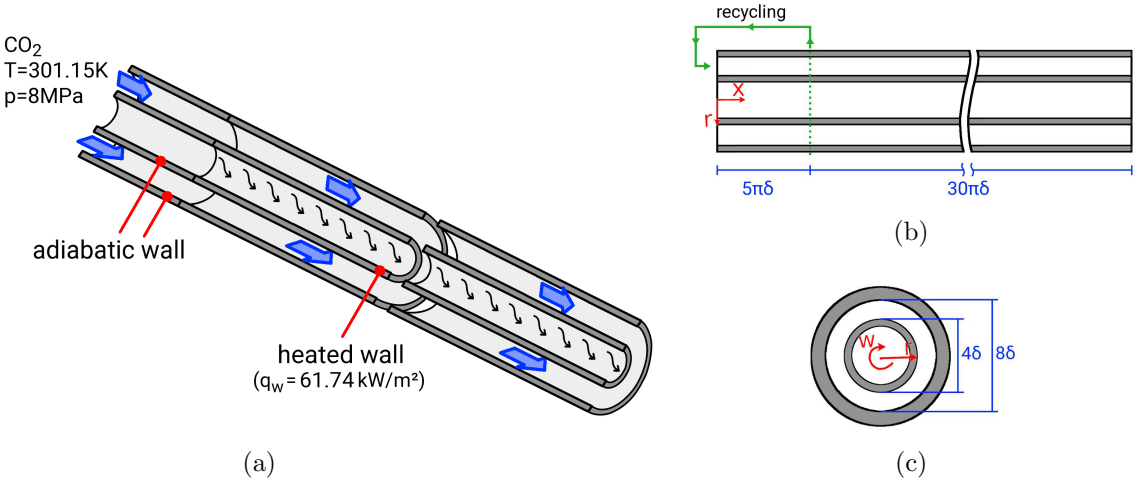

Figure 6.8: Schematic of the turbulent heated annulus flow at supercritical pressure. (a) isometric view; (b) view along x-axis; (c) view along r-axis. δ denotes the channel half width selected as $\delta = 0.5mm$.

In this test case, a fully-developed stream of carbon dioxide at supercritical pressure ($T = 301.15K < T_c$, $p = p_{ref} = 8MPa > p_c$, $Re_b = 8900$) flows inside a concentric annulus with an inner-to-outer wall radius ratio of $r_i/r_o = 0.5$ and an hydraulic diameter of $D_h = 4\delta = 2mm$. After an entrance length of $5\pi\delta$ with adiabatic walls, the stream of carbon dioxide is heated up at the inner side of the concentric annulus with a constant wall heat flux of $q_w = 61.74kW/m^2$. Due to the resulting temperature conditions $T_\infty < T_c < T_w$, carbon dioxide cross its critical temperature within the thin boundary layer of the turbulent annulus flow and pseudo-boiling takes place. Thereby the density among other thermo-physical properties undergo a transition from a liquid-like to a vapor-like character while the fluid is subject to a strong acceleration in flow direction at the same time.

The computational domain applied in the LES study has a total length of $35\pi\delta$ and a height of 2δ. In accordance with the DNS of [15], only one quarter sector of the fully cross section is considered. In order to perform a grid sensitivity analysis of the LES, three different block-structured numerical grids with 851760, 1752408 and 3412578 control volumes are employed in the validation study. The numerical grids are refined in the near wall regions to ensure that the small turbulence scales and steep gradients of thermodynamic properties in the vicinity of the wall are fully resolved.

For the subgrid-scale modeling of the momentum transport, the WALE model is employed with a classical constant of $C_W = 0.5$. For the subgrid-scale heat flux, the eddy diffusivity model is utilized. Thereby, a turbulent Prandtl number of $Pr_{sgs} = 1$ is selected in the present study.

In line with the reference DNS study of [15], a look-up table method is employed to compute the thermodynamic and fluid transport properties of carbon dioxide during

the simulation. The thermodynamic database is generated by the computer program PROPATH Ver.13.1 [80]. Thereby, the tabulated thermodynamic and fluid transport properties are interpolated with a linear interpolation by using the local temperature T and the constant reference pressure p^{th}, e.g. for the molecular viscosity $\mu = \mu(T, p^{th})$. A comparison of the generated thermodynamic table by means of PROPATH Ver.13.1 with reference data from NIST [134] is provided in figure 6.9.

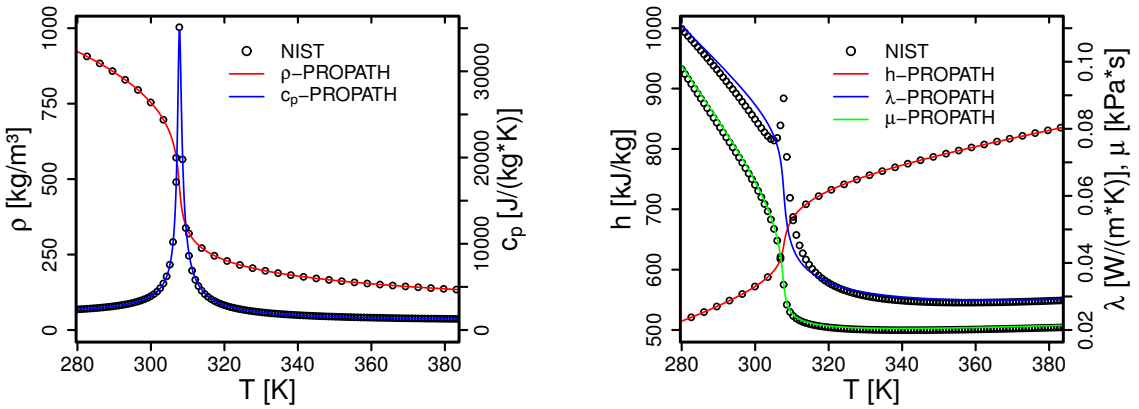

Figure 6.9: Comparison of the generated thermodynamic database from PROPATH [80] with reference data from NIST [134]. (a) mass density ρ and isobaric heat capacity c_p; (b) specific sensible enthalpy h, thermal conductivity λ and molecular viscosity μ.

Apparently in figure 6.9, values of mass density, isobaric heat capacity and specific enthalpy generated by means of PROPATH are in excellent agreement with the reference dataset from NIST. However, discrepancies appear in the case of predicted transport properties especially in the case of thermal conductivity. These discrepancies are most notable where the thermo-physical properties undergo a transition from vapor- to liquid-like character ($300K < T < 315K$) as well as at the region of dense fluid properties ($T < 300K$). Notwithstanding these discrepancies, the PROPATH database is used in the present validation study for the sake of consistency with the reference DNS study of [15].

Regarding the boundary conditions, no-slip condition is set at the walls for each velocity component and a zero Neumann condition for the mechanical pressure. At the heated wall, a constant heat flux conditions is imposed as $q_w = \frac{\lambda}{c_p}\frac{\partial h}{\partial r}\big|_{r=2\delta} = 61.74 kW/m^2$ and a zero temperature gradient condition is specified at the unheated walls. In order to obtain realistic inflow turbulence, the velocity field is extracted for each time step at the $x = 5\pi\delta$ plane downstream of the inlet and used to prescribe the velocity field at the inflow plane. At the outlet, a convective boundary condition is utilized for the velocity to maintain the overall mass conservation, while the kinematic pressure is set to a constant value. Periodic boundary conditions are used in the circumferential direction.

In order to avoid uncertainties caused by the initial solution, three flows through the domain are simulated before averaging is started. In addition, results from the coarse grid are used to initialize the velocity and enthalpy fields of the subsequent finer grids.

6.3.2 Results

To start with the features of the flow field, figure 6.10 shows the evolution of (a) mean axial velocity and (b) turbulent kinetic energy profiles at various locations of the heated wall region ($x/\delta = 25, 45, 65, 85$) and at the isothermal inflow region ($x/\delta = 0$). Mean velocity profiles are normalized using the local bulk velocity U_b while profiles of the turbulent

kinetic energy are normalized by means of the density ρ_0 and velocity U_0 at the inflow. The DNS data of [15, 13] are utilized to evaluate the LES results.

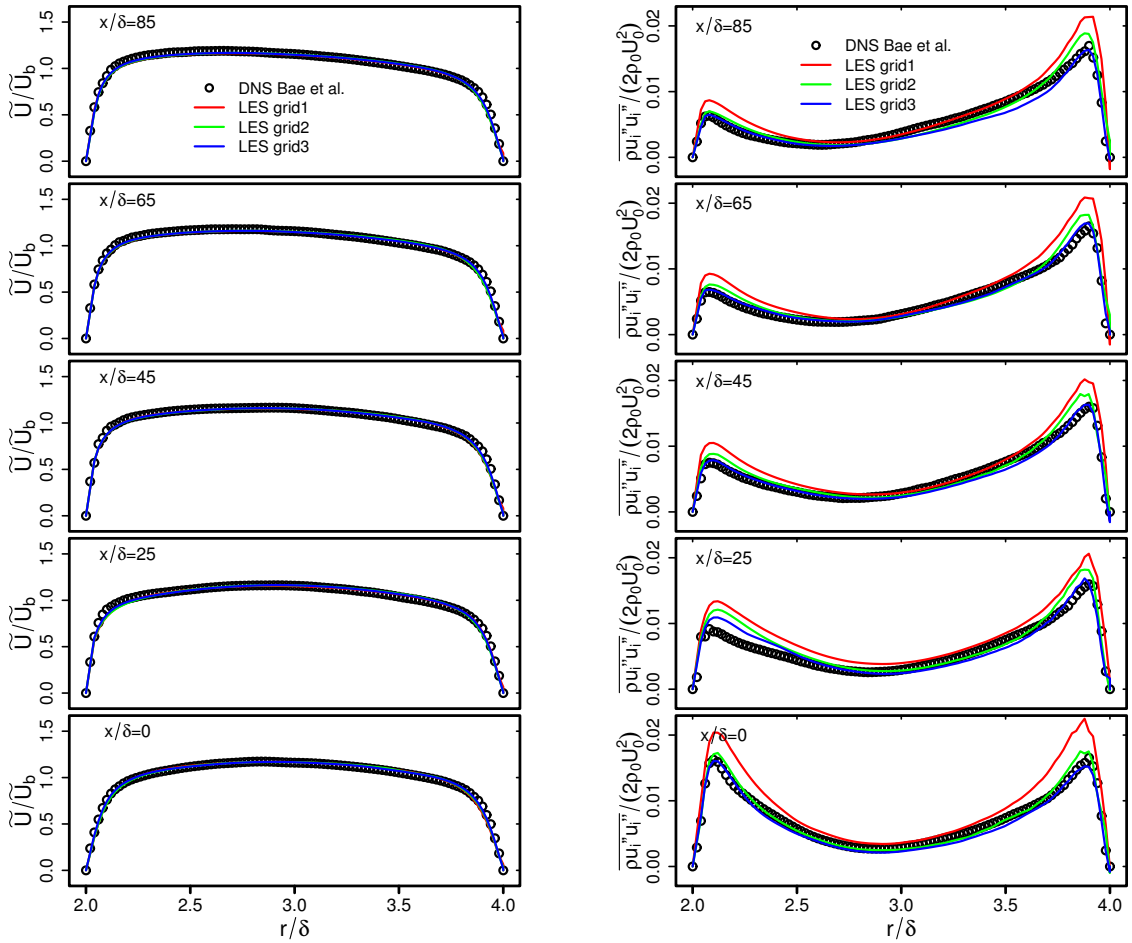

Figure 6.10: Predicted radial profiles of (a) mean axial velocity and (b) turbulent kinetic energy at $x/\delta = 0, 25, 45, 65, 85$. Comparison of LES results with DNS data of [15, 13]. Results are normalized by means of local bulk velocity U_b and values of density ρ_0 and velocity U_0 at the inflow.

Regarding mean velocity profiles, it can be clearly observed in figure 6.10 (a), that the flow is locally accelerated near the heated wall, due to thermal expansion caused by pseudo-boiling effects. This leads to asymmetric velocity profiles as the flow progresses downstream. Thereby, peak values of turbulent kinetic energy in the vicinity of the heated wall are damped (see figure 6.10 (b)). Both, asymmetric velocity profiles and damping of turbulent kinetic energy in the vicinity of the heated wall are well retrieved by the LES. This behavior is observed almost for all grid resolutions under consideration.

Next, the stream-wise turbulent heat fluxes obtained from the LES simulations are compared with DNS results at stream-wise locations $x/\delta = 20$ and $x/\delta = 60$ in figure 6.11 (a) and (b), respectively. The turbulent axial heat fluxes are non-dimensionalized by the wall heat flux q_w.

As expected, axial turbulent heat flux is very high at the heated wall, peaks in its vicinity and decreases rapidly away from it. Thereby, peak values of $\overline{\rho u_x'' h''}$ increase downstream. The physics of turbulent heat transfer are well retrieved by the LES. The observed results are very close to the DNS data with slight influence of the spatial resolution.

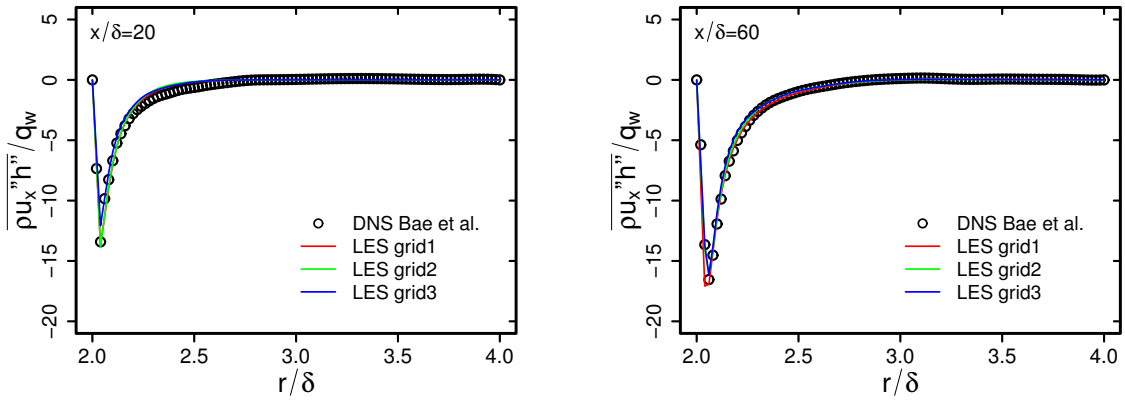

Figure 6.11: Comparison of axial turbulent heat fluxes with DNS results of [15, 13] at $x/\delta = 20$ and $x/\delta = 60$. Values are normalized by the constant wall heat flux q_w.

Finally, the distributions of predicted local Nusselt numbers and wall temperature along the heated inner wall of the annulus flow are compared with DNS in figure 6.12 (a) and (b), respectively. Thereby the local Nusselt number is calculated as $Nu = h_i D_h/\lambda_0$, where h_i is the convective heat transfer coefficient at the heated wall [15].

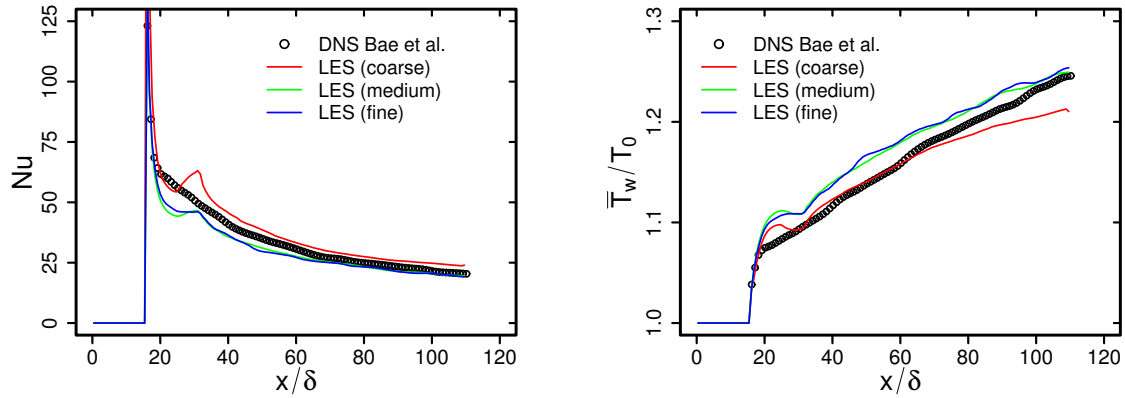

Figure 6.12: Distributions of local Nusselt number (left) and wall temperature (right) along the heated inner wall. Comparison of LES predictions with DNS data of [15, 13].

As it can be seen in figure 6.12, the distributions of local Nusselt number and wall temperature show similar trend to the reference DNS dataset. However, discrepancies in the Nusselt number and wall temperature occur in the range of $20 < x/\delta < 60$, which can be attributed to the limitations of spatial resolution. Nevertheless, the overall physics are well reproduced by the LES. Thus, it can be concluded that the numerical methods and models applied to describe turbulent wall-bounded flows with heat transport and variable thermo-physical properties under supercritical thermodynamic conditions are appropriate, suggesting its applicability for further numerical investigations.

PART III: IRREVERSIBILITY ANALYSIS USING DNS

Chapter 7

Irreversibilities in a 45°-inclined impingement jet on a heated plate

The numerical methods to predict turbulent heat transport with constant physical properties as presented and validated in part II of this thesis are utilized now to investigate near-wall thermal transport processes and entropy production mechanisms in a subcritical 45°-inclined impinging jet on a heated solid surface using DNS. This specific configuration is selected since it features very interesting heat and fluid flow properties and is of practical relevance in cooling arrangements for gas turbines or electronic components. It allows to reduce the size of such heat transfer equipments.

The objectives of the DNS study are to analyze the complex mechanisms of turbulent heat transport in the vicinity of an inclined impinged wall and to determine the causes of irreversibilities that are responsible for the reduction of performance of impingement cooling applications. In this respect a comprehensive experimental and numerical database including entropy production rates for validation purpose were made available by the author in [E4], [E7]. In the following sections, the main findings of this numerical investigations are outlined.

7.1 Description of the test case

A schematic of the inclined impinging jet configuration is provided in figure 7.1, where (a) depicts an isometric view; (b) the view along the y-axis; and (c) the top view, including a detailed view of the turbulence generating grid after the contraction nozzle.

In the test bench, dry air ($T_0 = 290K$, $p = 1atm$) enters a settling chamber and streams through honeycombs followed by two screens in order to homogenize the flow. Then, the homogeneous flow is accelerated by means of a contraction and, before exiting, encounters a perforated plate that serves as a turbulence generating grid. Finally, the generated turbulent air stream ($Re = 5000$ based on the nozzle exit diameter, turbulence intensity $\sim 10\%$) leaves the nozzle and impinges on a 45°-inclined heated wall, which has a constant wall temperature of $T_W = 330K$. At the impinged wall, the main flow is divided into two opposed jet streams directed outward along the solid wall and heated up.

In order to validate the DNS results, measurements of the flow field using planar two-component particle image velocimetry (PIV) have been carried out. For this purpose, a frequency double-pulsed neodymium yttrium vanadate laser ($Nd : YVO_4$, $\lambda = 532nm$, 4.0 mJ/pulse, pulse separation $100\mu s$, Edgewave IS 4II-DE (EdgeWave GmbH, Würselen, Germany)) was applied to illuminate aluminum oxide particle ($d \sim 1\mu m$) that were seeded into the flow. Mie-scattering from the particles was recorded with a digital complementary

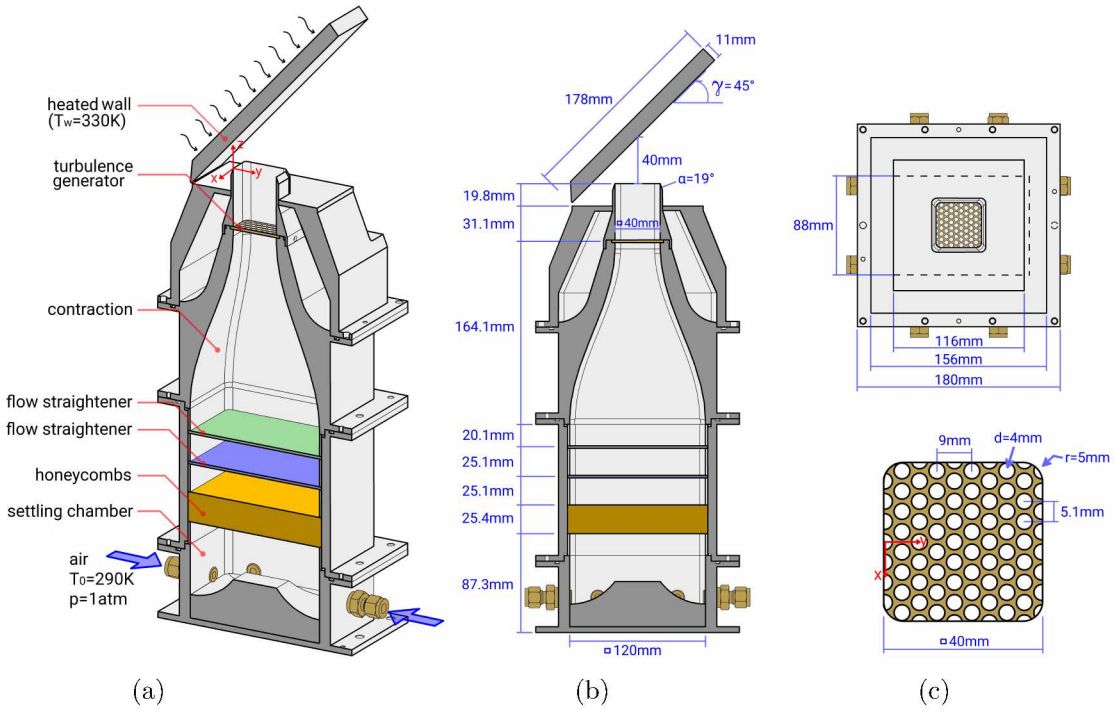

Figure 7.1: Schematic view of the inclined impinging jet. (a) isometric view; (b) view along the y-axis; (c) top view and detailed view of the turbulence grid.

metal-oxide-semiconductor (CMOS) camera (Phantom v711) and a 180mm f/3.5 macro camera lens. A repetition rate of 20Hz was used to ensure statistically independent samples. 3000 PIV images were recorded to obtain reliable statistical results. All PIV images were processed with LaVision DaVis 8.2.1 software. Interrogation windows of 24×24 $pixels^2$ and 75% overlap are used resulting in a vector spacing of $\sim 200\mu m$. Three different impingement angles of 0°, 45° and 90° are experimentally investigated, while only the 45°-configuration is computed in the DNS. Detailed information on the test bench and the experimental study can be found in [E4], [E7].

The operating conditions of the non-isothermal inclined impinging jet configuration under investigation are summarized in Table 7.1.

Property	Description	Value
γ	inclination angle of the plate	45°
D	nozzle exit diameter	40 mm
H	jet-to-plate distance	40 mm
U_{inlet}	velocity at the contraction entrance	0.214 m/s
T_{inlet}	temperature at the contraction entrance	290 K
T_{wall}	wall temperature of the heated surface	330 K
p	ambient pressure	1.01325 bar
Re_D	Reynolds-number based on nozzle exit diameter	5000
Pr	molecular Prandtl number	0.71

Table 7.1: Operating condtions of the inclined impinging jet configuration.

7.2 Numerical setup

A schematic of the the flow region and the computational domain used in the numerical study are depicted in figure 7.2.

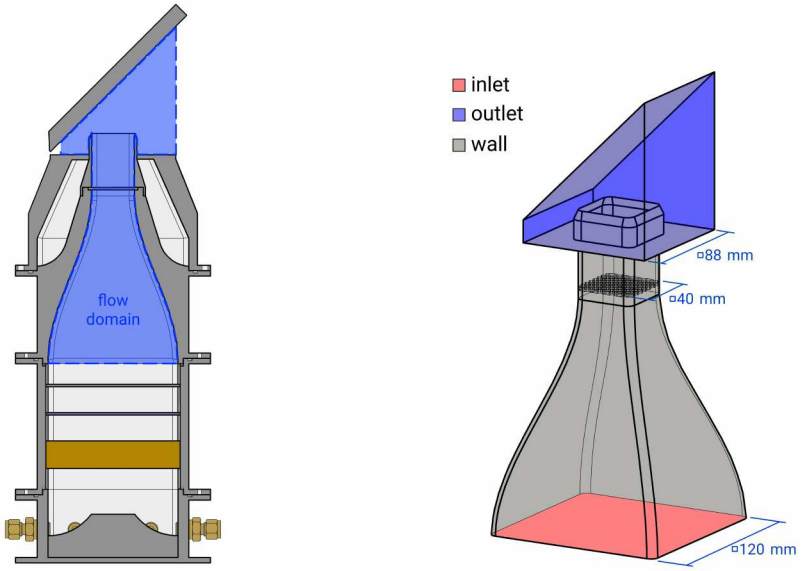

(a) (b)

Figure 7.2: Flow region (a) and computational domain (b) of the 45°-inclined impinging jet DNS study.

As it is visible in figure 7.2 (a), only the flow after the second flow straightener is simulated in the present DNS study. Thereby, the three-dimensional computational domain consists of the contraction section, the turbulence generating grid and the jet impinging region located downstream of the nozzle exit. At the contraction inlet, an uniform velocity field is imposed and no-slip conditions are utilized at the walls. Regarding the outflows, a velocity inlet/outlet boundary condition is used to allow entrainment of air from the surrounding. Thereby, the incoming fluid velocity is obtained by the internal cell value, while zero Neumann conditions are applied in the case of outflow. In contrast to the experimental setup, the small enclosed corner at the lower-left hand side of the plate (see figure 7.2 (a)) is omitted in the numerical study. Here, an outflow condition is applied in order to allow unrestricted fluid flow outwards the domain along the impinged wall. As it was shown in [E4] by comparison with experimental data, this boundary condition has no influence on the region of interest around the stagnation point.

A block-structured, three-dimensional grid is employed in the present study. It consists of approximately 109 million control volumes and is refined around the perforated plate and towards the walls ($y^+ < 1$) in order to ensure that the near-wall region is fully resolved in the DNS study. Furthermore, considering the commonly used DNS spatial resolution criterion [79], the ratio of local mesh size and Kolmogorov length scale is below $\Delta/\eta_K < 2.1$ in almost the entire domain (see [E4]), which ensures sufficient spatial resolution apart of solid walls. In addition, the validity of computed flow statistics was established by means of comparison with experimental data in [E4].

To avoid uncertainties caused by the initial solution, a fully developed turbulent velocity field is generated by means of a separate LES, which is interpolated onto the numerical grid of the DNS. Afterwards, two flow through times (after the turbulence generating grid)

are solved before sampling is started. In the case of LES, the same computational domain and boundary conditions are used as in the DNS study, while a numerical grid of approximately 6 million cells is utilized. Closure is obtained using the WALE subgrid scale model by [163]. Furthermore, an universal equilibrium stress model based on the wall function of [223] is applied at the walls in the LES.

7.3 Results

At first, the achieved numerical results of the turbulent flow field are examined and compared with the PIV-measurements. Subsequently, thermal properties in the vicinity of the wall are discussed. Finally, generation of entropy is analyzed to identify and quantify the causes of irreversibilities evolving in such thermal devices.

Results are presented at the mid-plane section ($x/D = 0$) for the wall-normal traverses ($\zeta/D = -0.5, -0.15, 0, 0.25, 0.5, 1$). The corresponding sampling locations are depicted in figure 7.3. Notice that an additional coordinate system is introduced with η representing the wall-normal direction and ζ denoting the direction along the wall. The origin of the additional coordinate system is located at the stagnation point.

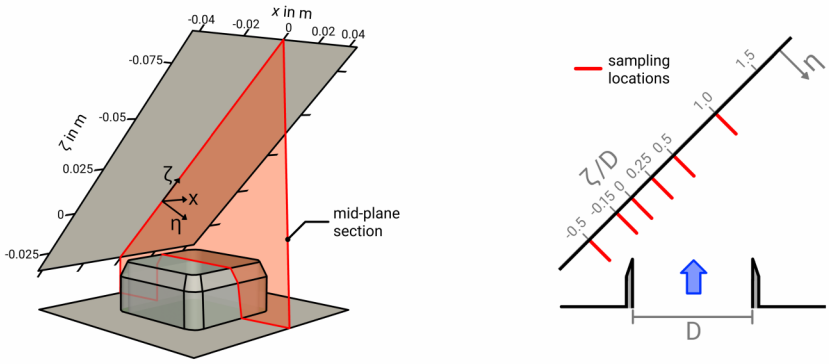

Figure 7.3: Region of interest including coordinate system and sampling locations at $\zeta/D = -0.5, -0.15, 0, 0.25, 0.5, 1$.

7.3.1 Turbulent fluid flow properties

In order to obtain a global perception of the general flow features of the inclined impinging jet flow, figure 7.4 shows: (a) a contour plot of the time-averaged magnitude velocity $|\overline{U}|$; (b) iso-surfaces of the Q-criterion colored by the instantaneous magnitude velocity; and (c) instantaneous values of the vorticity magnitude $|\omega|$ in the vicinity of the heated wall.

As pictured in figure 7.4, five main regions with distinctive flow features can be distinguished in the inclined impinging jet configuration. First the stagnation region (I), which is located half a diameter away from the geometric center of the jet origin. Here, the fluid is subject to a strong acceleration and stretching, leading to thin streak flow structures that are orientated in flow direction. Secondly, the wall jet region in main flow direction (II), where the flow is predominantly parallel to the wall and turbulence structures are considerably larger and toroidally organized. Thirdly, the shear layer on the side away from the impinging wall (III), which is triggered by the interaction of the jet with the ambient fluid. Thereby, large coherent roll-up vortices are created by the induced shearing and subsequently carried along with the flow. Fourth, the opposed wall-jet region (IV), where streamline curvature is high and turbulence structures interact with the shear layer

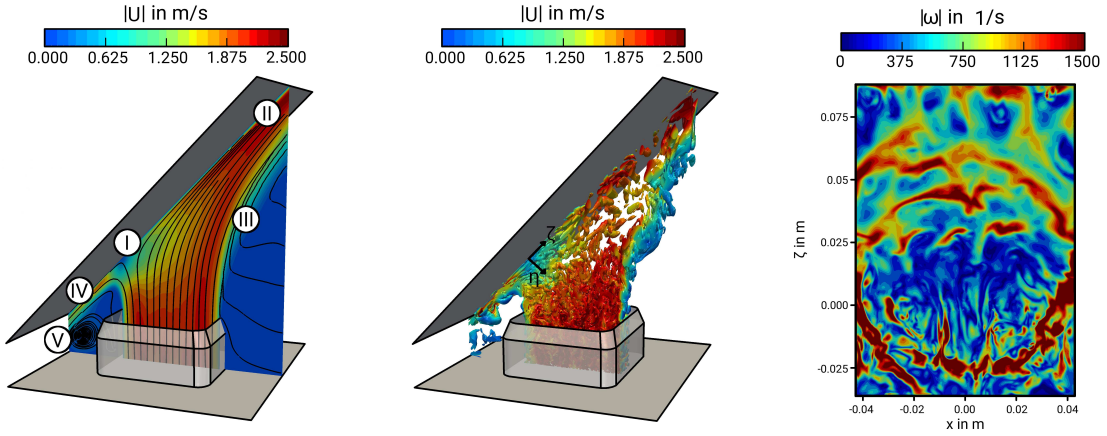

(a) (b) (c)

Figure 7.4: Instances of: (a) time-averaged velocity magnitude $|\overline{v}|$ at the mid-plane section; (b) iso-surfaces of the Q-criterion colored by the instantaneous velocity magnitude; and (c) instantaneous values of the vorticity magnitude $|\omega|$ in the vicinity of the impinged wall.

of the main jet. Finally, the recirculation zone (V), which is enclosed by the compression side of the impinged plate, the nozzle wall and the lower confined surface. At this region, the flow is predominantly laminar. The resulting instances of the large-scale structures on the impinged wall are shown in figure 7.4 (c). Here, it can be seen as well that coherent fluid flow structures are extremely elongated at the stagnation region. Thereby, vorticity appears small at the stagnation region with isolated stretched nests of concentrated vorticity that are orientated in the flow direction. Further downstream, vorticity becomes circumferentially interconnected resulting in large ring structures of strong flow circulation that serve as precursors of large coherent turbulent eddies in the near wall region.

The mean and rms velocity components in wall-parallel direction are now analyzed in figure 7.5. For comparison, the PIV measurements are also depicted.

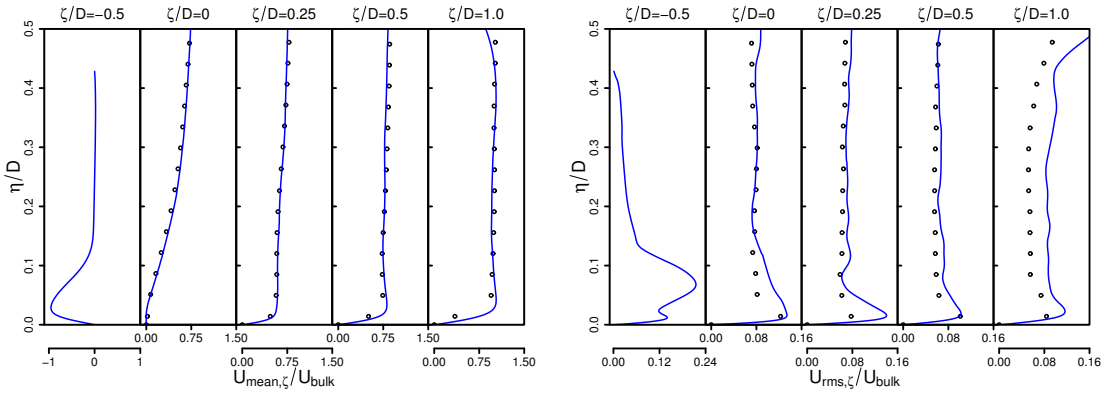

(a) (b)

Figure 7.5: Mean (a) and rms (b) velocity wall-parallel components in wall-normal direction. Comparison of DNS results (—) with PIV measurements (•).

Figure 7.5 (a) reveals clearly that the jet is separated into a primary stream in the flow direction and a smaller secondary one in the opposite direction, leading to two distinctive wall-jets. This characteristic flow pattern can be observed in both, the experimental

investigation and the DNS study. Furthermore, measurements and numerical results are very close to each other, which confirms the validity of DNS results in terms of mean flow. Regarding rms velocities shown in figure 7.5 (b), it can be seen that the most vigorous turbulent activity appears in the vicinity of the wall, associated with high rms velocities that decline with increasing wall distance and remain approximately constant for $\eta/D > 0.2$. Further, it is visible that rms velocities of the experiment and DNS differ in the near-wall region and close to the boundary of the PIV window ($\zeta/D = 1$). As reported in the experimental study [E4], these discrepancies are caused by reflections of the laser light from the solid wall and low particle seeding density at the boundary of the PIV window. This is usually negligible in measurements of mean velocities, however, it can have a significant influence on the measurement accuracy of rms velocities. Nevertheless, deviations are fairly small and it can be concluded that the present DNS is appropriate to describe the turbulent flow field within the impinging jet configuration.

7.3.2 Near-wall thermal characteristics

After determining the general flow features of the impinging jet, near-wall thermal characteristics are analyzed now. At first, the achieved results of mean and rms temperatures in the vicinity of the wall are presented and discussed. Then budget terms of the turbulent kinetic energy and temperature variance are examined to identify and quantify turbulent transport phenomena that are not directly described by means of first and second order moments. Subsequently, heat fluxes within the thermal boundary layer are investigated, and deviations from isotropic behavior are pointed out. Finally, Nusselt numbers are provided to complement the analysis of the near wall thermal characteristics.

First and second order thermal moments

Figure 7.6 (a) shows the normalized mean and rms temperature ($\overline{\Theta}$ and Θ_{RMS}) profiles along the wall normal direction η/D, where the non-dimensional temperature is defined as $\Theta = (T - T_{inlet})/\,(T_{wall} - T_{inlet})$. The corresponding thermal boundary layer thickness δ_Θ and the evolution of peak values of turbulent kinetic energy k and Θ_{RMS} along the wall parallel direction ζ/D are depicted in figure 7.6 (b), where δ_Θ is defined as the distance to the wall where $\Theta = 0.05$.

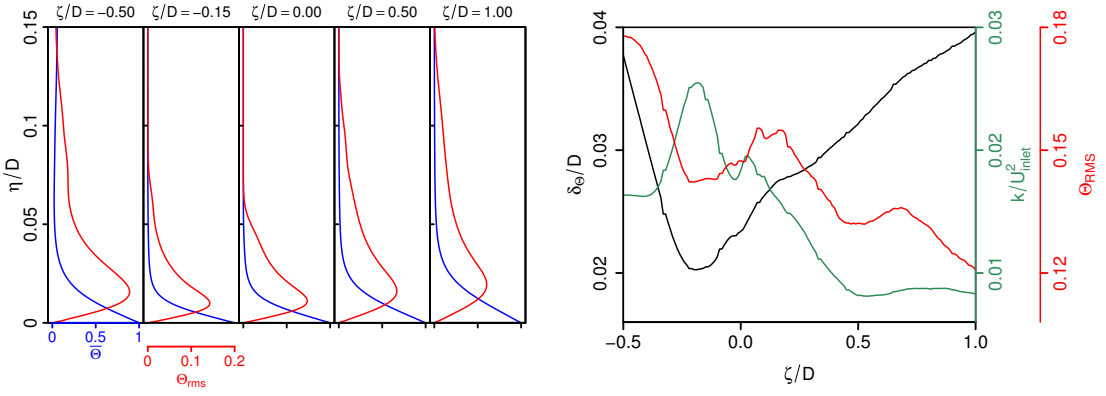

(a) (b)

Figure 7.6: Mean $\overline{\Theta}$ (—) and rms temperature Θ_{RMS} (—) with respect to the wall distance (a); thermal boundary layer thickness δ_Θ (—), peak values of turbulent kinetic energy k (—) and rms temperature Θ_{RMS} (—) along the wall parallel direction ζ/D (b).

As expected, mean temperatures are high at the wall and decrease rapidly with increasing distance to the wall (see blue lines in figure 7.6 (a)). Surprisingly, steepest wall-normal temperature gradients associated with intense heat transfer occur at $\zeta/D = -0.15$ and not directly at the stagnation point, as is usually the case in jets impinging normally on a heated surface (for a comparison, see, e.g., [83]). Away from $\zeta/D = -0.15$, temperature profiles enlarge, while at the same time, gradients tend to smear out. Regarding temperature fluctuations (red lines in figure 7.6 (a)), high values of Θ_{RMS} are concentrated in the near-wall region with strong peaks situated close to the wall, closest at $\zeta/D = -0.15$. In line with the mean temperature, profiles of Θ_{RMS} spread away from $\zeta/D = -0.15$, while peak values become shifted away from the wall. The peculiar behavior of this location for the thermal transport within the 45°-inclined impinging jet configuration becomes clearer by examining the variations of thermal boundary layer thickness δ_Θ and the evolution of peak values of k and Θ_{RMS} along the wall parallel direction in figure 7.6 (b). Here, it can be seen that the minimum of δ_Θ appears not directly at the stagnation point as is usually the case in jets impinging normally on a heated surface. Instead, the minimum of δ_Θ is slightly shifted towards the compression side at $\zeta/D \approx -0.15$ and increases rapidly away from it. Thereby, it is interesting to observe that the minimum of δ_Θ coincides with the peak value of k and with a local minimum of Θ_{RMS}. Obviously, turbulence-induced mixing among other thermo-fluid processes enhances the heat transfer at $\zeta/D \approx -0.15$, resulting in a thinning of the thermal boundary layer, which is significantly thinner than at the stagnation point where k exhibits a local minimum.

Turbulent thermal processes

After examining mean and temperature variances, turbulent thermal transport phenomena close to the impinged wall are investigated next. For this purpose, the evolution of turbulent kinetic energy $k = 1/2 \langle U_i' U_i' \rangle$ and temperature variance $\theta = 1/2 \langle T' T' \rangle$ are analyzed, that read in the case of constant density fluid flow with convective passive heat transfer [189]:

$$\frac{\partial k}{\partial t} + \langle U_i \rangle \frac{\partial k}{\partial x_i} = \underbrace{- \left\langle U_i' U_j' \right\rangle \frac{\partial \langle U_i \rangle}{\partial x_i}}_{P_k} \underbrace{- 2\nu \left\langle D_{ij}' D_{ij}' \right\rangle}_{\epsilon_k} \underbrace{- 2 \frac{\partial}{\partial x_j} \left\langle U_j' p' \right\rangle}_{\Pi_{tke}} + \underbrace{2\nu \frac{\partial}{\partial x_j} \left\langle U_i' D_{ij}' \right\rangle}_{D_{tke}} \underbrace{- \frac{\partial}{\partial x_j} \left\langle \frac{1}{2} U_i' U_i' U_j' \right\rangle}_{T_{tke}}, \tag{7.1}$$

$$\frac{\partial \theta}{\partial t} + \langle U_i \rangle \frac{\partial \theta}{\partial x_i} = \underbrace{- \left\langle U_i' T' \right\rangle \frac{\partial \langle T \rangle}{\partial x_i}}_{P_\theta} \underbrace{- \frac{\nu}{Pr} \left\langle \frac{\partial T'}{\partial x_i} \frac{\partial T'}{\partial x_i} \right\rangle}_{\epsilon_\theta} + \underbrace{\frac{1}{2} \frac{\nu}{Pr} \frac{\partial^2 \left\langle T'^2 \right\rangle}{\partial x_i^2}}_{D_\theta} - \underbrace{\frac{\partial}{\partial x_i} \left(\left\langle \frac{1}{2} U_i' T'^2 \right\rangle \right)}_{T_\theta}. \tag{7.2}$$

The first and second terms on the left-hand side denote the local change and mean-flow convection of k and θ, respectively; P_* represents the production, ϵ_* the dissipation, D_* the molecular diffusion and T_* the turbulent diffusion of k and θ. Π_{tke} is the pressure-related diffusion term, which appears only in the evolution equation of k. Figure 7.7 shows

profiles of the normalized budget terms of k and θ at the stagnation point ($\zeta/D = 0$) and at the location with smallest thermal boundary layer thickness ($\zeta/D = -0.15$). The budget terms of temperature variance are normalized by $U_{inlet} \cdot (T_{wall} - T_{inlet})^2 / D$ and the budget terms of the turbulent kinetic energy by U_{inlet}^3 / D.

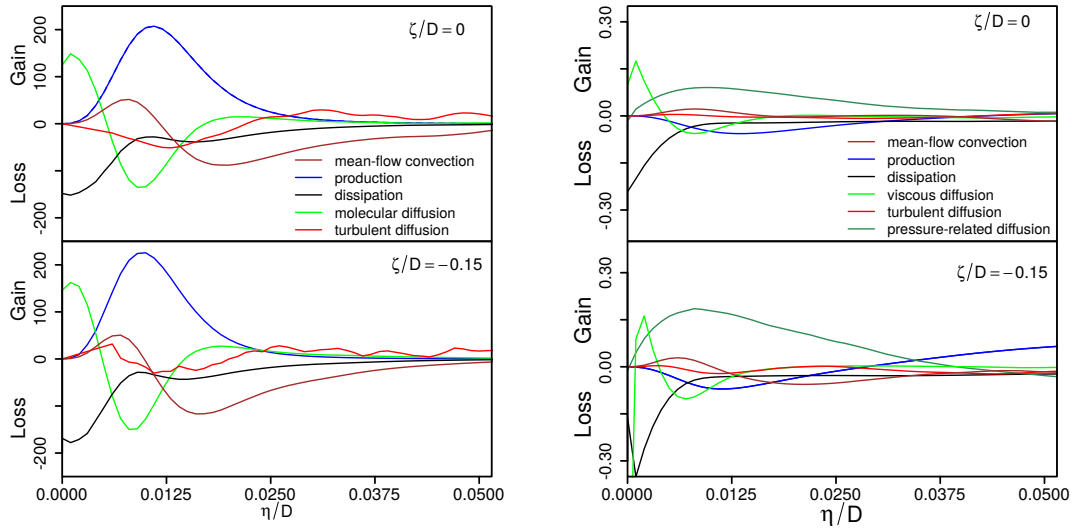

(a) (b)

Figure 7.7: Normalized budget terms of θ (a) and k (b) along the wall-normal direction at $\zeta/D = 0$ and $\zeta/D = -0.15$.

Regarding budget terms of θ as shown in figure 7.7 (a), the production, dissipation, molecular diffusion and mean-flow convection are the dominant terms, while turbulent diffusion is relatively small. At the edge of the thermal boundary layer ($\eta/D = \delta_\Theta/D \approx 0.02$), negative mean-flow convection dominates and transports excess temperature variance towards the wall. Closer to the wall, the production term exhibits a strong peak situated approximately at half the thermal boundary layer thickness, where Θ_{RMS} is maximal as well. Thereby, mean-flow convection becomes positive, and the production is predominantly balanced by negative molecular diffusion and not by dissipation as is usually the case in turbulent heat transfer in channel flows or round jets (see, e.g., [109, 178]). Immediately adjacent to the wall, production, turbulent diffusion and mean-flow convection vanish, and only molecular diffusion contributes to balance the high dissipation term. A comparison of budget terms of temperature variance at $\zeta/D = 0.0$ and $\zeta/D = -0.15$ shows that the contributions of mean-flow convection and molecular diffusion are slightly higher at $\zeta/D = -0.15$, which allows one to explain the smaller temperature variance in this region. However, both balances of the contributions are quite similar, and consequently, the overall physics of turbulent thermal transport behave similar in both regions.

In contrast to the budget of temperature variance, the balances of the turbulent kinetic energy in figure 7.7 (b) differ significantly from each other. At both $\zeta/D = 0$ and $\zeta/D = -0.15$, the production is negative in the vicinity of the wall, which is balanced by pressure-related diffusion of k rather than viscous dissipation. Thereby, it can be seen that pressure-related diffusion and mean-flow convection are considerably higher at $\zeta/D = -0.015$. It is therefore most likely that the vigorous turbulent activity at $\zeta/D = -0.15$ is predominantly caused by pressure-related diffusion and mean-flow convection processes. Another noticeable difference is the high amount of production outside the boundary layer ($\eta/D > 0.03$) only apparent at $\zeta/D = -0.15$, which suggests that

turbulence is to some extent also induced by the free-stream.

Heat transport

Next, turbulent heat fluxes $\langle U_i'\Theta'\rangle$ and mean temperature gradients $\nabla_i\Theta$ in the vicinity of the impinged wall are examined. Profiles of wall-parallel and wall-normal components of $\langle U_i'\Theta'\rangle$ and $\nabla_i\Theta$ are plotted in figure 7.8.

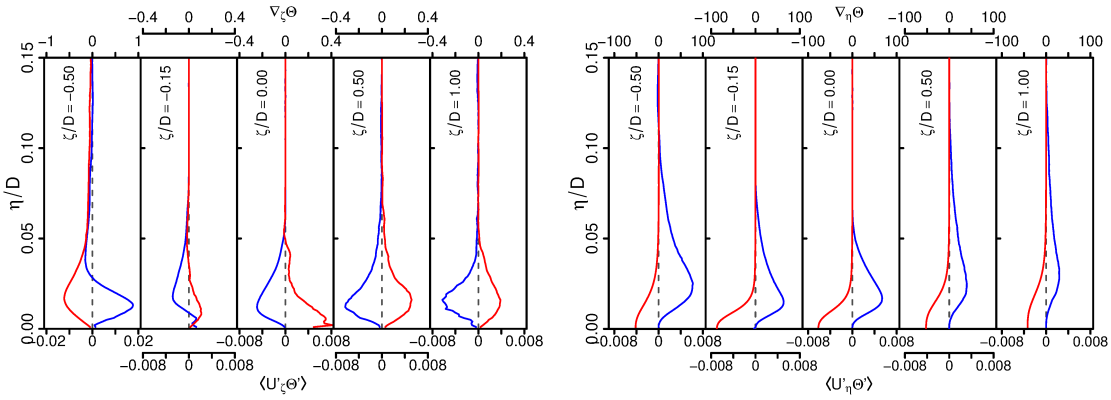

(a) (b)

Figure 7.8: Wall-parallel (a) and wall-normal (b) components of the turbulent heat flux vector and mean temperature gradient at different wall-normal traverses. (—): mean temperature gradient $\nabla_i\Theta$; (—): turbulent heat flux vector $\langle U_i'\Theta'\rangle$.

Concerning turbulent heat fluxes, values of $\langle U_\zeta'\Theta'\rangle$ and $\langle U_\eta'\Theta'\rangle$ are large at the opposed wall-jet region ($\zeta/D = -0.5$) and considerably smaller away from it. Thereby, values of wall-normal gradients $\nabla_\eta\Theta$ are significantly larger than wall-parallel ones $\nabla_\zeta\Theta$, even though the corresponding heat flux components are of the same order of magnitude. This is most notable at $\zeta/D = -0.15$ and at the stagnation point ($\zeta/D = 0$). Therefore, heat transport in the inclined impinging jet configuration is primarily directed normal to the wall and only qualitatively aligned with mean temperature gradients. This is in good agreement with observations in fully-developed jets impinging normally on a heated surface (see, e.g., [83]), which also holds true for impinging flows that impinge at a particular angle of 45°. In addition, it is interesting to observe that close to the wall at $\zeta/D = -0.15$ and in the free-stream at $\zeta/D = -0.5$, heat is transported counter the gradient from low to high temperature regions. As pointed out by Schumann [212], the reason for such a paradoxical behavior arises in flows if the dissipation of temperature fluctuations is too small to balance diffusional sources, while turbulence intensity is large and θ is small. Both, low dissipation of temperature fluctuations, as well as vigorous turbulent intensity and small values of θ are observed in the present study in regions where counter gradient heat flux takes place (see figures 7.6 and 7.7).

The observation that wall-normal temperature gradients are several times larger than wall-parallel ones and the occurrence of counter gradient heat flux within the inclined impinging jet configuration warrants a closer examination of turbulent heat fluxes. With regard to turbulent heat flux modeling in RANS and LES of jet impingement heat transfer, most often, linear eddy diffusivity models are applied in the literature (see, e.g., [100, 25, 60, 83]), similar to those described in section 3.2.1. The applicability of such models is examined in figure 7.9 (a) within the thermal boundary layer of the impinging jet ($0 < \eta/\delta_\Theta < 1$). Exemplarily, results are depicted at both the wall-jet region ($\zeta/D = -0.5$),

the location of minimal boundary layer thickness ($\zeta/D = -0.15$), the stagnation point ($\zeta/D = 0$) and at the boundary layer region ($\zeta/D = 1$). Thereby, the deviation from isotropic heat flux is represented by plotting $\left\langle U'_\zeta \Theta' \right\rangle \cdot \langle \nabla_\eta \Theta \rangle$ against $\langle U'_\eta \Theta' \rangle \cdot \langle \nabla_\zeta \Theta \rangle$. Both quantities are equal in the case of isotropic heat flux, which is illustrated by a black dashed line in the graph. Regions where heat is transported counter the gradient from low to high temperature regions are highlighted in gray. Notice that for the sake of visibility, the scaling of both axes in figure 7.9 (a) are not equal. The black dashed line of isotropic state is therefore not a diagonal line in this graph.

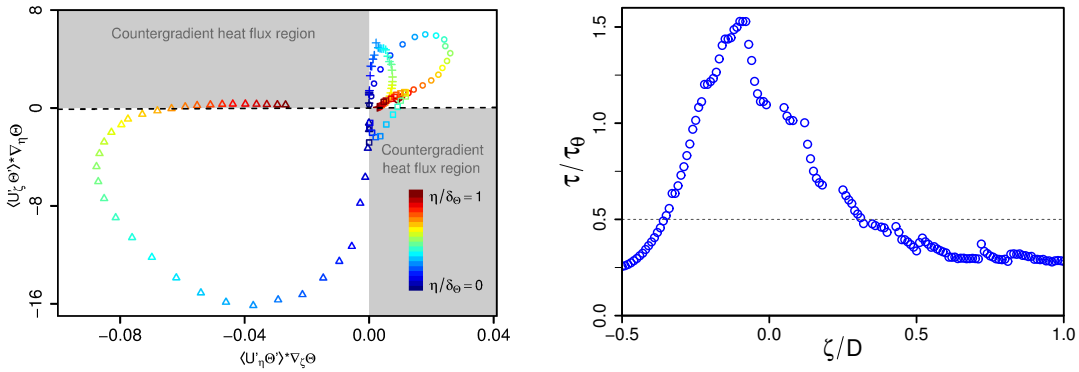

(a) (b)

Figure 7.9: (a) Anisotropy map of heat fluxes. △: $\zeta/D = -0.5$, □: $\zeta/D = -0.15$, ○: $\zeta/D = 0$, +: $\zeta/D = 1$. The dashed line represents the isotropic state where $\left\langle U'_\zeta \Theta' \right\rangle \cdot \langle \nabla_\eta \Theta \rangle = \langle U'_\eta \Theta' \rangle \cdot \langle \nabla_\zeta \Theta \rangle$. (b) The ratio of mechanical ($\tau = k/\epsilon_k$) and thermal ($\tau_\theta = \theta/\epsilon_\theta$) time scales along the wall-parallel direction at a wall distance of $\eta = 0.5 \cdot \delta_\Theta$.

It can be clearly seen in figure 7.9 (a) that heat fluxes are predominantly isotropic very close to the wall, become considerably anisotropic with increasing wall distance and finally return back to the isotropic state for $\eta/\delta_\Theta > 0.8$. This holds more or less for all regions under consideration. Additionally, it can be observed that heat fluxes behave most anisotropically at the wall-jet region, while they turn back to the isotropic state with increasing ζ/D, but do not reach fully-isotropic behavior. Further, it appears that counter gradient heat flux takes place close to the wall at $\zeta/D = -0.15$, as well as in the free-stream at $\zeta/D = -0.5$, which is in line with the observations in figure 7.9 (a). Both counter gradient heat flux and the inherently anisotropic nature of heat fluxes within the thermal boundary layer of the inclined impinging jet suggest that tensorial heat diffusivity models such as the explicit anisotropy resolving heat flux model proposed in section 3.3.3 might be suitable for such kind of flows.

To complete the discussion of turbulent heat transport modeling within the inclined impinging jet configuration, figure 7.9 (b) shows the ratio of mechanical ($\tau = k/\epsilon_k$) and thermal time scales ($\tau_\theta = \theta/\epsilon_\theta$) along the wall-parallel direction at a wall distance of $\eta = 0.5 \cdot \delta_\Theta$. This characteristic time-scale ratio is of particular importance for the heat transport description and is usually close to 0.5 in equilibrium thermal boundary layers (see, e.g., [24]). Clearly, from figure 7.9 (b), τ/τ_θ varies strongly along ζ/D and deviates considerably from the equilibrium value of $\tau/\tau_\theta = 0.5$. In particular, at $\zeta/D = -0.15$, the time-scale ratio exceeded 1.5, indicating strong non-equilibrium effects in heat and fluid flow transport. This is in good agreement with the earlier observation above that dissipation is relatively small and diffusion processes dominate the turbulent heat transport

at $\zeta/D = -0.15$.

Wall heat transfer

Finally, heat transfer from the target plate to the fluid is examined by means of the local Nusselt number, defined as:

$$Nu = \frac{h_t D}{\lambda} = \frac{\frac{\partial T}{\partial \eta}\big|_{\eta=0} D}{T_w - T_{inlet}}, \tag{7.3}$$

where h_t is the heat transfer coefficient and λ the thermal conductivity. Figure 7.10 shows the instantaneous (a) and time-averaged (b) local Nusselt Number at the impinged wall.

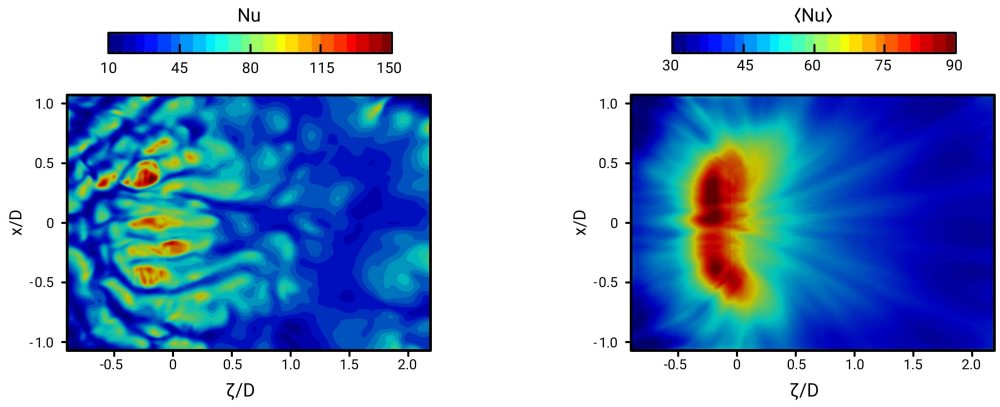

(a) (b)

Figure 7.10: (a) Instantaneous and (b) time-averaged instances of the Nusselt number at the impinging wall.

Similar to fully-developed jets impinging normally on a heated surface (see, e.g. [83]), high values of instantaneous Nusselt numbers associated with large-scale eddy structures are concentrated around the stagnation point. However, as might be seen in figure 7.10 (a), peak values are not directly situated at the stagnation point. Instead, it appears that they are slightly shifted towards the opposed wall-jet region ($\zeta/D \approx -0.15$). A similar pattern is found for mean Nu numbers in figure 7.10 (b). Thereby, the highest values of Nu appear at $\zeta/D \approx -0.15$ in the range of $-0.2 < x/D < 0.2$. Away from this region, Nu numbers decrease rapidly. This is in good agreement with the finding above, pointing out that the wall-normal temperature gradients are very steep at $\zeta/D \approx -0.15$ associated with high heat transfer. Notice that in figure 7.10 (b) the striped pattern in mean Nusselt numbers results from small jets generated in the turbulence generating grid inside the nozzle.

7.3.3 Entropy generation mechanisms

It is evident from the observations above that the inclined impinging jet configuration features very complex heat and fluid flow properties, especially in the vicinity of the impinged wall. The entropy generation mechanisms within the evolving transport and energy conversion processes are examined next in order to identify and quantify sources of irreversibilities that are responsible for the efficiency reduction in such applications. To display these sources of irreversibilities, the second law of thermodynamics is applied in the form of local entropy imbalance at the continuum mechanical level as described in section

2.1. Thereby, the entropy production rates related to viscous dissipation Π_v and due to heat transport Π_q in the entropy imbalance are investigated since both terms represent irreversibilities evolving in thermo-viscous fluid flows.

In the case of turbulent heat and fluid flow problems, it is useful to split Π_v and Π_q into time-mean and fluctuation parts, which allows to distinguish between entropy production by mean and turbulent quantities. This leads to

$$\begin{aligned}\langle \Pi_v \rangle = & \underbrace{\frac{\langle \mu \rangle}{\langle T \rangle}\left(\frac{\partial \langle U_i \rangle}{\partial x_j}+\frac{\partial \langle U_j \rangle}{\partial x_i}\right)\frac{\partial \langle U_i \rangle}{\partial x_j}}_{\langle \Pi_v^m \rangle} \\ & + \underbrace{\left(\left\langle \frac{\mu}{T}\left(\frac{\partial U_i}{\partial x_j}+\frac{\partial U_j}{\partial x_i}\right)\frac{\partial U_i}{\partial x_j}\right\rangle - \frac{\langle \mu \rangle}{\langle T \rangle}\left(\frac{\partial \langle U_i \rangle}{\partial x_j}+\frac{\partial \langle U_j \rangle}{\partial x_i}\right)\frac{\partial \langle U_i \rangle}{\partial x_j}\right)}_{\langle \Pi_v^t \rangle}\end{aligned} \tag{7.4}$$

for the entropy production due to viscous dissipation. A Similar expression can be derived for the Π_q as:

$$\langle \Pi_q \rangle = \underbrace{\frac{\langle \lambda \rangle}{\langle T \rangle^2}\frac{\partial \langle T \rangle}{\partial x_j}\frac{\partial \langle T \rangle}{\partial x_j}}_{\langle \Pi_q^m \rangle} + \underbrace{\left(\left\langle \frac{\lambda}{T^2}\frac{\partial T}{\partial x_j}\frac{\partial T}{\partial x_j}\right\rangle - \frac{\langle \lambda \rangle}{\langle T \rangle^2}\frac{\partial \langle T \rangle}{\partial x_j}\frac{\partial \langle T \rangle}{\partial x_j}\right)}_{\langle \Pi_q^t \rangle}. \tag{7.5}$$

Here, the terms $\langle \Pi_v^m \rangle$ and $\langle \Pi_q^m \rangle$ represent entropy production due to mean gradients, while $\langle \Pi_v^t \rangle$ and $\langle \Pi_q^t \rangle$ are due to fluctuating gradients.

Starting with the analysis of instantaneous entropy generation, figure 7.11 depicts snapshots of entropy production rates related to (a) viscous dissipation and (b) heat conduction. In order to visualize the wide range of entropy generating scales evolving in the 45°-inclined impinging jet configuration, a logarithmic color range is used.

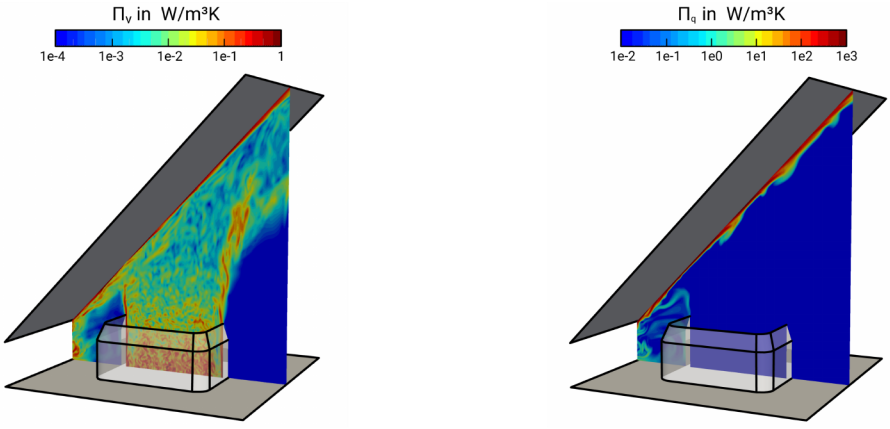

(a) (b)

Figure 7.11: Snapshot of instantaneous entropy generation rate by (a) viscous dissipation and (b) by heat transport at the mid-plane section of the inclined impinging jet.

Focusing on the instantaneous entropy generation rate by viscous dissipation (see figure 7.11 (a)), it appears that the entropy is predominantly produced downstream the perforated plate located inside the nozzle, at the jet's shear layer and especially in the vicinity of the impinged wall due to a large contribution of shear-induced turbulence mixing in these regions. Thereby, large coherent streaks with high values of Π_v are generated at

the mixing layers that are carried along by the flow and dissolve while they cascade into smaller ones. At the jet's core, the entropy production is small and decreases in the main flow direction. In contrast, entropy production rates by heat conduction are primarily concentrated at the impinged wall; see figure 7.11 (b). This seems reasonable because of the extreme non-uniformity of the temperature field resulting in steep gradients in this region. Apart from the wall, entropy is also produced at the recirculation zone on the compression side of the impinging jet due to heat transport, where hot fluid is separated from the heated wall and transported back to the jets' shear layer, inducing temperature gradients. By comparing figures 7.11 (a),(b), it is apparent that scales of Π_q are considerably larger than those of Π_v. This makes clear that irreversibilities evolving in such impinging cooling arrangements occur at different scales, predominantly on large scales in the case of heat transport and over a wide range of scales in the case of viscous dissipation.

From a qualitative point of view, it appears especially that the heated wall acts as a strong source of irreversibility within impinging cooling arrangements for both entropy production due to viscous dissipation and heat conduction. This observation is quantified next by means of time-averaged rates of entropy production in the vicinity of the impinged wall. Figure 7.12 (a) shows the time-averaged rates of entropy production by viscous dissipation $\langle \Pi_v \rangle$ and by heat transport $\langle \Pi_q \rangle$ as a function of non-dimensional wall distance η/D. Variations of the entropy production boundary layer thicknesses δ_{Π_v} and δ_{Π_q} are depicted in figure 7.12 (b), where δ_{Π_v} is defined as the distance to the wall where $\langle \Pi_v \rangle = 0.05 \cdot \langle \Pi_v \rangle \big|_{\eta/D=0}$ and δ_{Π_q} the distance to the wall where $\langle \Pi_q \rangle = 0.05 \cdot \langle \Pi_q \rangle \big|_{\eta/D=0}$. Notice that values δ_{Π_v} at the immediate vicinity of the stagnation point are omitted because $\langle \Pi_v \rangle$ is inherently very small in this region.

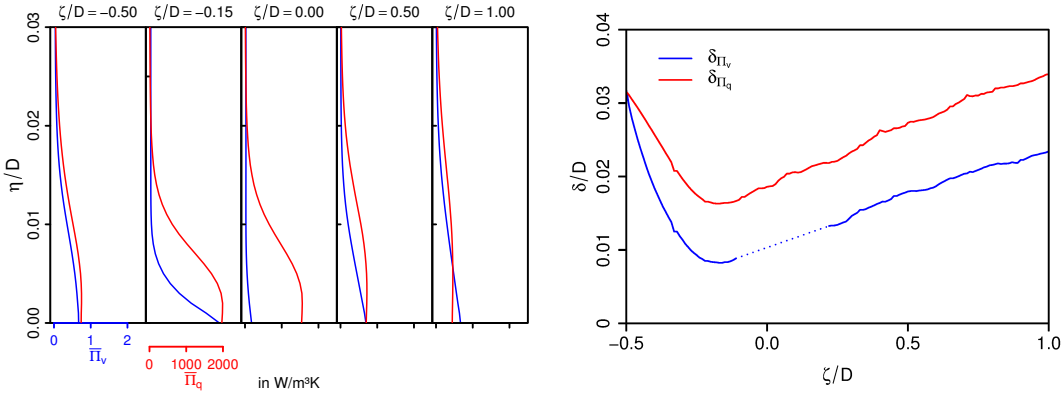

(a) (b)

Figure 7.12: (a) Profiles of time-averaged entropy production rates due to viscous dissipation $\langle \Pi_v \rangle$ and to heat conduction $\langle \Pi_q \rangle$ as a function of non-dimensional wall distance η/D; (b) boundary layer thickness of $\langle \Pi_v \rangle$ and $\langle \Pi_q \rangle$.

Both $\langle \Pi_v \rangle$ and $\langle \Pi_q \rangle$ are high in the vicinity of the wall and decrease rapidly away from it. In line with the observation made that thermal and fluid flow transport processes are predominantly limited to the near-wall region, it turns out clearly that these transport processes are essentially irreversible, especially at $\zeta/D = -0.15$. This holds more or less for the entire range from $\zeta/d = -0.5$ up to $\zeta/d = 1$, excluding the stagnation point. Here, values of $\langle \Pi_v \rangle$ are relatively small because of the absence of shearing, while at the same time, the heat transfer along with $\langle \Pi_q \rangle$ is intense. Obviously, irreversible fluid flow transport processes hardly have any influence on the heat transport at the stagnation

point, in contrast to the near-wall region elsewhere. In addition, it is interesting to notice (figure 7.12 (b)) that irreversible fluid flow transport processes occur much closer to the wall than irreversible heat transport processes ($\delta_{\Pi_v}/\delta_{\Pi_q}$ ranging from 0.5–0.9). This may be related to the small molecular Prandtl number in the present study ($Pr = 0.7$), which implies that the thermal diffusivity process dominates the momentum diffusivity, yielding a smaller momentum boundary layer thickness and consequently a smaller boundary layer thickness of $\langle \Pi_v \rangle$ compared with δ_{Π_q}.

To complete the analysis of irreversible processes for the 45°-inclined impinging jet configuration, time-mean and turbulent parts of entropy production rates due to viscous dissipation ($\langle \Pi_v^m \rangle$ and $\langle \Pi_v^t \rangle$) and related to heat conduction ($\langle \Pi_q^m \rangle$ and $\langle \Pi_q^t \rangle$) are depicted in figure 7.13. Results are exclusively shown for the stagnation point ($\zeta/D = 0$) and at $\zeta/D = -0.15$, in which a semi-logarithmic scale is used in order to distinguish between high entropy production rates at the near-wall region and low values in the free-stream. In addition, estimations for the turbulent parts of entropy production rates based on the turbulence dissipation rates are plotted in figure 7.13 (dashed red lines). Such estimations are commonly applied in second law analyses within the RANS context (see, e.g. [116]) and also applied in the present work in the context of LES (see section 3.4). They read:

$$\left\langle \Pi_v^{t,*} \right\rangle = \frac{\langle \rho \rangle}{\langle T \rangle} \epsilon_k \quad \text{and} \quad \left\langle \Pi_q^{t,*} \right\rangle = \frac{\langle \rho \rangle \langle c_p \rangle}{\langle T \rangle^2} \epsilon_\theta, \tag{7.6}$$

where ϵ_k is the dissipation rate of the turbulence kinetic energy, ϵ_θ the dissipation rate of the temperature variance and c_p the isobaric heat capacity. In these formulations, it is assumed that temperature fluctuations in the denominator, $1/T$ and $1/T^2$, respectively, are negligible [116].

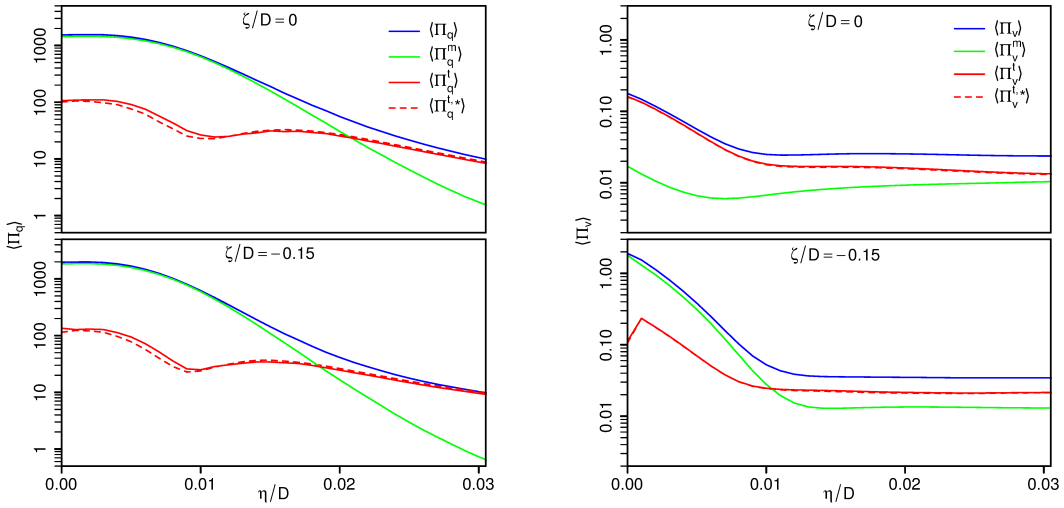

(a) (b)

Figure 7.13: Profiles of mean, turbulent and total entropy production rates due to (a) viscous dissipation and (b) heat conduction at $\zeta/D = 0$ and $\zeta/D = -0.15$. Dashed lines represent turbulent parts of entropy production rates estimated by means of turbulent dissipation rates.

As it is apparent from figure 7.13, the entropy generation in the vicinity of the wall is predominantly caused by mean gradients rather than by turbulence processes, except in the case of entropy production by viscous dissipation at the stagnation point. Here,

entropy production by fluid flow processes is predominantly caused by turbulence. Further away from the wall, $\langle \Pi_v^m \rangle$ and $\left\langle \Pi_q^m \right\rangle$ decrease, and the entropy production related to fluctuating gradients ($\left\langle \Pi_v^t \right\rangle$ and $\left\langle \Pi_q^t \right\rangle$) predominates at both locations. By comparing entropy production rates at $\zeta/D = 0$ and $\zeta/D = -0.15$, the contributions of entropy generated by heat conduction are very similar at both locations. This holds true for $\langle \Pi_v \rangle$, excluding $\langle \Pi_v^m \rangle$, which is considerably larger at $\zeta/D = -0.15$ compared to the value at the stagnation point. Regarding the turbulent part of entropy production rates estimated by means of turbulence dissipation rates, $\left\langle \Pi_v^{t,*} \right\rangle$ and $\left\langle \Pi_q^{t,*} \right\rangle$ in figure 7.13, it can be clearly seen that the predictions obtained by the estimations (see equation (7.6)) are very close to the profiles calculated directly from Equations (7.4)–(7.5), respectively. This confirms that the formulations in equation (7.6) are appropriate to describe the entropy generation due to fluctuating gradients, at least for the 45°-inclined impinging jet configuration. However, it should be noted here that the prediction accuracy of the estimation (equation 7.6) strongly depends on an accurate description of ϵ_k and ϵ_θ in both the RANS and LES context, particularly in the vicinity of the wall.

7.4 Conclusion

DNS of turbulent fluid flow with convective heat transport in a turbulent jet impinging on a 45°-inclined heated plate at $Re = 5000$ has been conducted in order to investigate heat and fluid flow transport phenomena along with entropy generation mechanisms within this configuration. Thereby, a comprehensive dataset has been generated including statistical moments of the temperature and flow field, budget terms in the turbulent kinetic energy and temperature variance equations, turbulent heat fluxes, mechanical and thermal time scales, local Nusselt numbers and local entropy production rates related to both viscous dissipation and heat transport. Such a dataset is difficult to obtain experimentally, especially in the vicinity of the wall, and will be used in the present work for evaluation purposes of near-wall modeling approaches and entropy production analysis in the context of LES (see section 10.2).

Some important observations from this DNS study concerning impingement cooling, thermal processes, causes of irreversibilities and modeling strategies regarding LES and RANS can be outlined as following:

(1) Examining the turbulent flow field, it appears that the 45°-inclined impinging jet configuration features very complex fluid flow phenomena with strong flow/wall interaction processes. Thereby, different characteristic flow regimes can be distinguished: (I) a stagnation region that is shifted half a diameter away from the geometric center of the jet origin; (II) two opposed wall-jet regions with strong streamline curvature; (III) a shear layer region, that is triggered by the interaction of the jet with the ambient fluid; (IV) a recirculation zone where the flow is predominantly laminar.

(2) In terms of near-wall thermal statistics within the 45°-inclined impinging jet configuration, it turned out that the peak heat transfer does not appear directly at the stagnation point as it is usually the case in jets impinging normally on a heated surface. Instead, the highest Nusselt numbers, the thermal boundary layer thickness minimum and the largest wall-normal heat transport are slightly shifted towards the compression side of the inclined jet ($\zeta/D = -0.15$). Thereby, turbulent intensity is high, while temperature variance exhibits a local minimum at this location.

(3) Based on the analysis of the budget contributions of different terms in the temperature variance and turbulence kinetic energy equations, it appears that turbulent thermal and fluid flow transport processes around the stagnation point of the inclined impinging jet are considerably different from those found in other wall-bounded flows. Dissipation is relatively small, while molecular and pressure-related diffusion dominate. In the case of turbulent kinetic energy, the production term is prevailing negative.

(4) It is observed that heat is transported counter to the gradient from low to high temperature regions at the location of maximal heat transfer ($\zeta/D = -0.15$). The reason for such a paradoxical behavior is that dissipation of temperature fluctuations is too small to balance diffusional sources (see also [212]).

(5) Regarding turbulent heat transport, it turned out that fluxes are predominantly isotropic very close to the wall, become highly anisotropic with increasing wall distance and finally return to the isotropic state at the edge of the thermal boundary layer. Furthermore, the heat fluxes behave most anisotropically on the compression side. Both, the counter gradient heat flux and the inherently anisotropic nature of heat fluxes in the thermal boundary layer of the inclined impinging jet suggest that tensorial heat diffusivity models might be appropriate for such kinds of thermo-viscous flows.

(6) The ratio of mechanical τ and thermal time scales τ_θ deviates considerably from the equilibrium value of $\tau/\tau_\theta = 0.5$ in the thermal boundary layer of the inclined impinging jet. In particular around the stagnation point, the time-scale ratio exceeded 1.5, indicating strong non-equilibrium effects in heat and fluid flow transport.

(7) Especially the heated wall acts as a strong source of irreversibility in the case of impinging cooling arrangements. This holds for both entropy production due to viscous dissipation and heat conduction. Thereby, the entropy production contribution of mean gradients dominates that of the fluctuating gradients. This suggests that the design of the impinged plate (surface roughness, corrugation, chevron angle, etc.) as well as the inclination angle are particularly important for efficient use of energy in such thermal arrangements that may exhibit intensification of turbulence in the vicinity of the wall.

(8) Regarding the conceptional engineering design of such thermal devices, this study confirms that the estimation of the turbulent part of the entropy production based on turbulence dissipation rates in non-reacting, non-isothermal fluid flows represents a reliable approximation for second law analysis, likewise in the context of computationally less expensive simulation techniques like RANS and/or LES.

Chapter 8

Entropy generation in a round jet at supercritical conditions

Today, there is a great interest in processes occurring under supercritical thermodynamic conditions, like in propulsion applications including rocket engines, gas turbines or diesel engines [115, 152, 4]. In this context, a clear trend to operate at higher combustion chamber pressure is observed in order to favor the production of higher specific energy conversion rates along with the improvement of thermodynamic performance. This is mainly achieved at pressures exceeding the critical pressure.

Under subcritical conditions, the injected fuel disintegrates due to the action of surface tension, which induces ligament formation, atomization and evaporating droplet with sharp interfaces. Once supercritical condition is reached, the breakup is replaced by mixing, including turbulent mixing and diffusion, as surface tension vanishes. Thereby, the fluid properties differ significantly from that of a perfect gas, and distinct liquid and gas phases do not exists. Instead, when crossing the so-called pseudo-critical temperature, thermodynamic and fluid transport properties undergo a transition from liquid-like to vapor-like character and the isothermal vaporization is replaced by a continuous non-equilibrium process. High pressure real fluid effects merely distribute the latent heat over a finite temperature interval, and the thermal energy supplied is used to increase the temperature and overcome molecular forces simultaneously [16].

Within this narrow thermodynamic condition range, where the transport and thermodynamic properties vary significantly, the changes of the entropy generation rate are large - due to the irreversibility of thermo-fluid processes evolving - which is known as a natural consequence of the properties of the material. The consideration of the second law of thermodynamics along with the entropy generation appears therefore useful in order to delineate favorable locations of handling while determining the causes of irreversibilities in supercritical injection processes.

This chapter deals with the analysis of a supercritical injection process based on DNS technique and the second law of thermodynamics. For this purpose, DNS of a fully-developed turbulent jet of cryogenic nitrogen injected into a warm nitrogen environment has been conducted. The DNS study mimics the experiment by Mayer et al. [149] in terms of geometry, thermodynamics, and hydrodynamics but at a reduced jet Reynolds number of $Re = 5300$. Thereby, the selected operating conditions are particularly relevant to injection processes in liquid rocket engines. The objectives of the DNS study are: (1) to investigate the heat and fluid flow mechanisms that dominate the mixture formation, (2) to gain further insight into the complex physics of fuel disintegration processes under supercritical conditions, and (3) to examine the entropy production rates in this super-

critical flow in order to identify the causes of irreversibilities and to display advantageous locations of handling along with the process regimes favorable to mixing. In this respect, a comprehensive DNS database of turbulence statistics and entropy production rates were provided by the author in [E2], [E3], that is difficult to obtain experimentally at such extreme thermodynamic conditions. The main findings of these studies are presented in the following section.

8.1 Description of the test case

In accordance with the experimental study of Mayer et al. [149] (Case 3), a cryogenic round nitrogen jet injected into a cylindrical chamber is examined. A schematic view of the experimental high-pressure test chamber is depicted in figure 8.1.

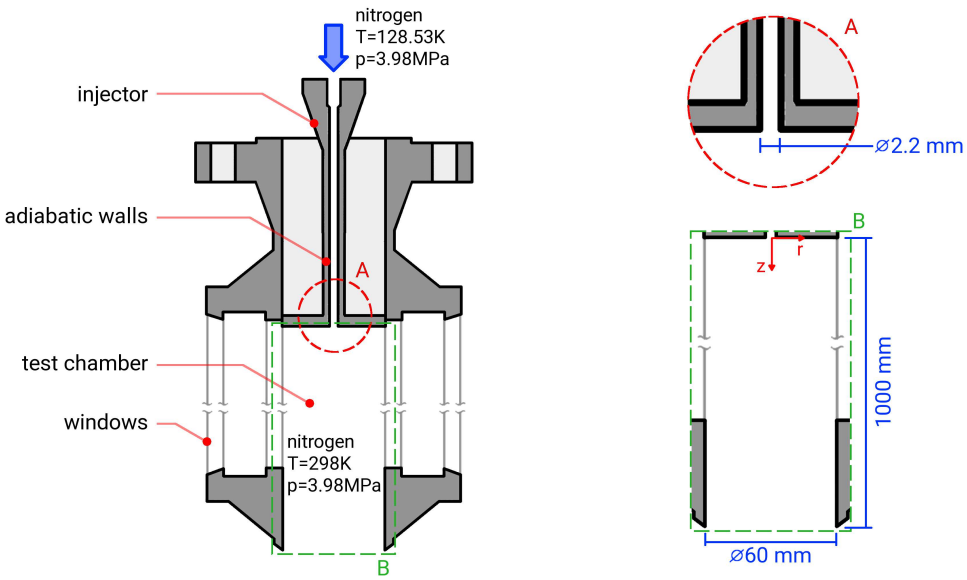

Figure 8.1: Schematic view of the experimental high-pressure test chamber and the injection tube outlet.

The test chamber has a length of 1000mm, a diameter of 60mm and is initially filled with warm nitrogen at supercritical pressure ($p_\infty = 3.98MPa$, $T_\infty = 298K$). The cryogenic nitrogen ($T_{inj} = 123.53K$, $p_{inj} = p_\infty = 3.98MPa$) is injected from a long pipe with a diameter of $D = 2.2mm$ into the test chamber. Thereby, the incoming jet flow is assumed to be fully-developed at a jet Reynolds number of $Re = 1.62 \times 10^5$. In contrast to the experiment, a smaller inlet velocity is selected in the DNS study ($U_{inj} = 0.151m/s$) leading to a reduced jet Reynolds number of $Re = 5300$, whereas the geometry of the configuration and the thermodynamic operating conditions are similar of the experimental investigation.

The density profiles along the jet axis and at several radial location were measured by means of 2-D Raman imaging in [149]. Measurements of the velocity or temperature fields are not available for this configuration. Moreover, due to the different Reynolds numbers in the experiment and the numerical study, the available experimental data are only used for qualitative comparison.

The thermodynamic and flow conditions of the supercritical nitrogen jet simulation are summarized in table 8.1.

Property	Description	Value
U_{inj}	jet injection velocity	$0.151 m/s$
T_{inj}	jet injection temperature	$128.53 K$
T_∞	chamber temperature	$298 K$
p_∞	chamber pressure	$3.98 MPa$
Re_{inj}	jet Reynolds number	5300

Table 8.1: Operating and flow conditions of the DNS study of cryogenic nitrogen injection.

8.2 Numerical setup

Computational domain and numerical grid

Only a small portion of the experimental chamber, corresponding to the region of interest, is simulated in the DNS study. The computational domain consists of an injection part with a length of $2D$ and a portion of the chamber with a length of $32D$. To capture the spreading of the jet, the extent of the chamber part is increased gradually from $5D$ at the injection region up to $18D$ at the outflow. A representation of the three-dimensional numerical grid is depicted in figure 8.2.

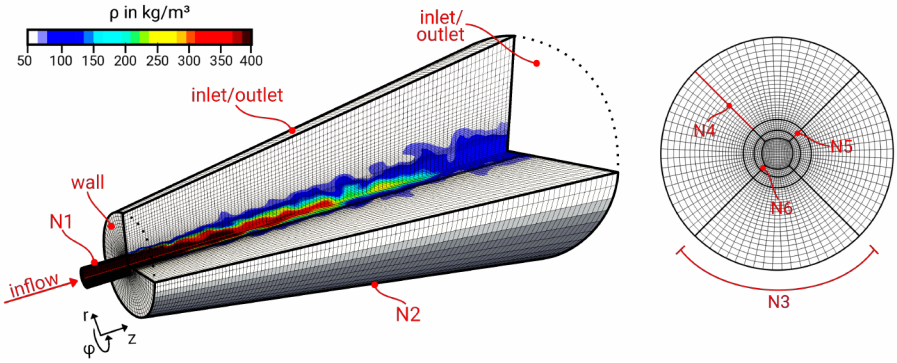

Figure 8.2: Computational domain and numerical grid of the direct numerical simulation of nitrogen injection at supercritical conditions. The number of grid points are given as $N1 = 138$, $N2 = 689$, $N3 = 86$, $N4 = 80$, $N5 = 504$, $N6 = 46$.

A block-structured, three-dimensional numerical grid is employed in the present study. It consists of approximately 48 million cells and is refined around the injection region and throughout the jet's core. As it is shown in [E4], the selected spatial resolution resolution enables grid-independent turbulence statistics, which ensures that the quantities of interest depend only on the physics and are no more affected by the numerical approaches used. Furthermore, considering the commonly used DNS spatial resolution criterion [79], the ratio of local mesh size and Kolmogorov length scale is below $\Delta/\eta_K < \pi$ in the entire domain (see [E4]).

Initial and boundary conditions

Realistic inflow turbulence is generated by a separate DNS of a fully developed turbulent pipe flow at $Re = 5300$. Thereby, slices of the instantaneous velocity field are extracted from the middle section of the pipe domain for each time step and stored in a database. These data are utilized as realistic turbulent inflow conditions of the jet simulation. At

the outflows, a velocity inlet/outlet boundary condition is imposed to allow entrainment of fluid from the surroundings. Thereby, the incoming fluid velocity is obtained by the internal cell value, while a zero Neumann condition is applied in the case of outflow. At the walls, the no-slip condition is applied. In the case of temperature boundaries, a Dirichlet condition is set for the inlet, while zero Neumann conditions are imposed at the outflows and at the walls.

Regarding the separate DNS of turbulent pipe flow, the pipe diameter, bulk velocity and Reynolds number are equal to the cryogenic jet simulation. Periodic boundary conditions are applied in stream-wise direction and the pressure gradient, that drives the flow, is adjusted dynamically to maintain a constant mass flux. A computational domain with a length of $L = 14D$ is used in order to resolve the maximum wavelengths of turbulent motion [E8]. The numerical grid consists of approximately 22 million control volumes with a non-dimensional grid spacing of $r^+_{wall} \times \Delta^+\omega \times \Delta^+ z = 0.7 \times 5.2 \times 3.3$. Notice that the spatial resolution of the pipe equals the resolution of the jet nozzle section. Figure 8.3 shows the predicted mean and rms velocities in respect to the non-dimensional wall distance r^+. For comparison, the DNS dataset of Ahn et al. [3] is utilized.

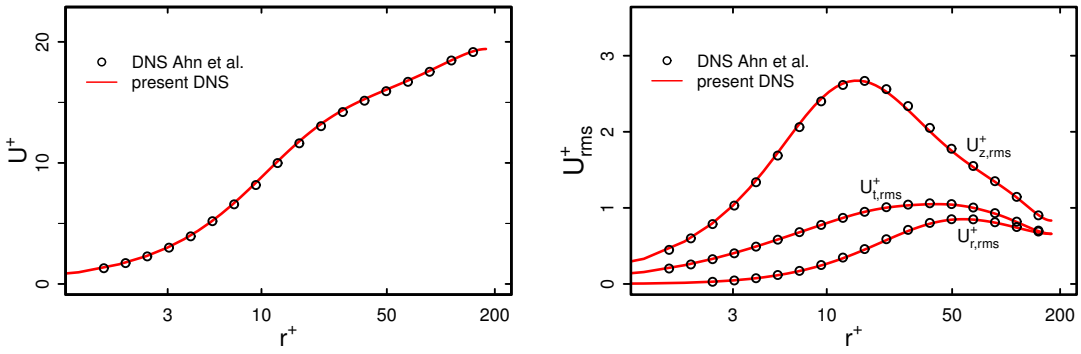

(a) (b)

Figure 8.3: Comparison of predicted mean (a) and rms (b) velocities of the turbulent pipe flow at $Re = 5300$ with reference data of [3].

As it can be clearly seen in figure 8.3, predicted mean and rms velocities are in excellent agreement with the reference DNS dataset, indicating appropriate spatial resolution. Therefore, accurate inflow conditions can be assumed for the present simulation of cryogenic nitrogen injection. Notice that the recorded length of the inflow dataset and the duration time of the jet simulation are identical.

In order to avoid uncertainties caused by the initial solution, the start-up phase of the jet simulation has to be long enough to ensure fully developed turbulent flow. Similar to the start-up phase used in [245], sampling is started after two convective time scales, which is defined as $t_c = 2 \cdot L/U_{inj}$.

Thermodynamic and transport models

To account for the non-ideal gas behavior at supercritical conditions, the Peng-Robinson equation of state (PR-EoS) [183] in conjunction with the generalized volume translation method of Abudour et al. [2] is employed in this study, here denoted as PRC-EoS. Non-ideal correction of the sensible enthalpy and isobaric heat capacity are expressed in terms of departure functions derived from the PR-EoS, whereas quantities for the hypothetical ideal gas state are calculated using seven-coefficient NASA polynomials [35]. Regarding

transport properties, the correlations of Chung et al. [44], applicable for dilute and dense fluids, are applied for the calculation of the molecular viscosity and thermal conductivity. A description of this modeling approach can be found in section 2.2.2.

Figure 8.4 shows profiles of mass density, isobaric heat capacity, molecular viscosity and thermal diffusivity of nitrogen at $p = 3.98MPa$ (critical pressure $p_c = 3.3958MPa$) predicted by the present modeling approach. For comparison, highly accurate reference data from the NIST chemistry webBook [134] and predictions of other commonly-used cubic equations of state, namely, the van der Waals equation (vdW-EoS) [232], the Peng-Robinson equation (PR-EoS) [183], the Redlich-Kwong equation (RK-EoS) [192], the Soave-Redlich-Kwong equation (SRK-EoS) [221] and the ideal gas law are also presented.

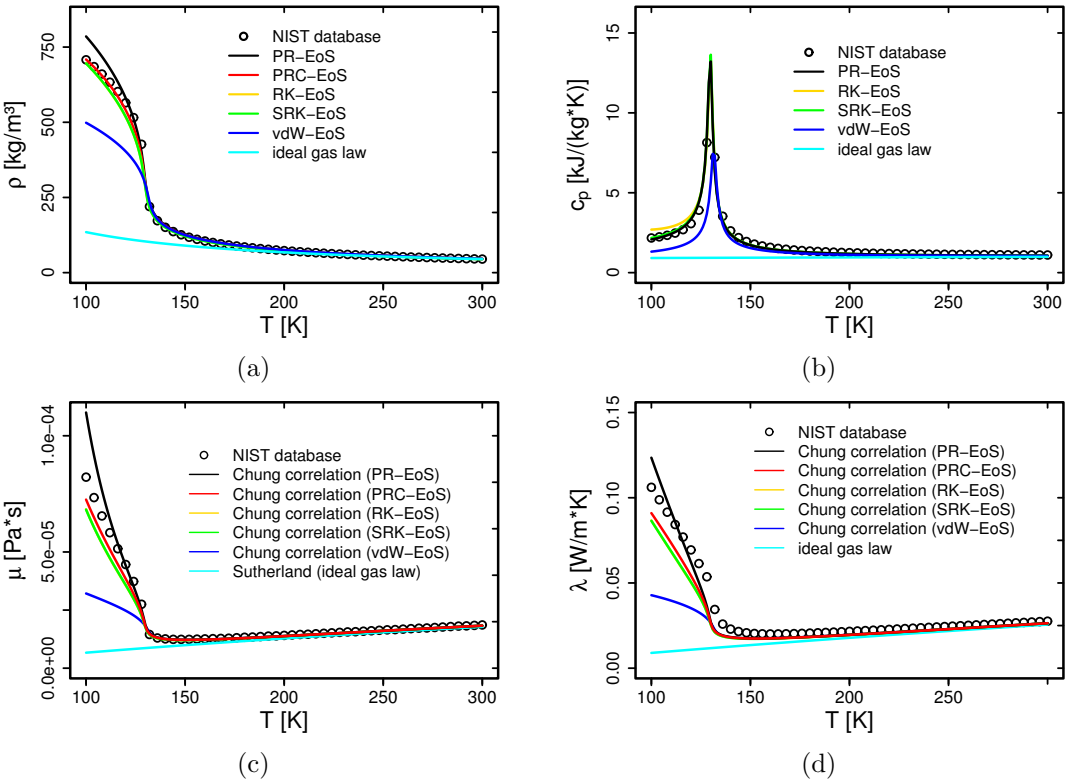

Figure 8.4: Predicted mass density (a), isobaric heat capacity (b), molecular viscosity (c) and thermal diffusivity (d) of nitrogen at $p = 3.98MPa$ with respect to temperature. Comparison of commonly-used equations of state (EoS) with reference data from [134]. PR, Peng-Robinson; PRC, corrected Peng-Robinson; RK, Redlich-Kwong; SRK, Soave-Redlich-Kwong; vdW, van der Waals.

In the range of the present operating conditions, the PRC-EoS, RK-EoS and SRK-EoS are well suited to predict the mass density of nitrogen, while the PR-EoS without volume translation, the vdW-EoS and the ideal gas law yield poor predictions at low temperatures. Regarding isobaric heat capacity, predictions of the PR-EoS, RK-EoS and SRK-EoS are in good agreement with the reference data. These EoS are able to capture the non-ideal behavior close to the critical temperature. In contrast the vdW-EoS and ideal gas law are not able to predict the sharp peak close to the critical temperature properly. Similar to the thermodynamic properties, the correlations of Chung et al. [44] combined with the PRC-EoS, RK-EoS and SRK-EoS are well suited to predict the molecular viscosity and

thermal diffusivity over the entire temperature range. Again, the vdW-EoS and ideal gas law yield poor predictions at low temperatures. In line with these results, the PRC-EoS combined with the correlations of Chung et al.[44] are used in the present DNS study, since this modeling approach provides the most accurate description of thermodynamic and transport properties of nitrogen under such extreme operating conditions from the models under consideration.

8.3 Results

In this section, the achieved results of the DNS of nitrogen injection at supercritical conditions are presented and discussed. First, general flow features of the jet and thermal transport properties are analyzed. Then, entropy production mechanisms evolving in the transport processes are investigated and the characteristic disintegration stages of the injection process are determined.

8.3.1 Turbulent fluid flow properties

Figure 8.5 displays the instantaneous velocity magnitude, temperature, density gradient magnitude and molecular Prandtl number fields at mid-plane section of the jet at $2.5t_c$ (convective time scales) after start of injection. Results are shown for the evolution of the jet up to $z/D = 20$ in the ambient nitrogen. Red isolines in figure 8.5 (c) denote the mean density between the incoming and ambient nitrogen associated with the interface between the liquid-like and gas-like nitrogen.

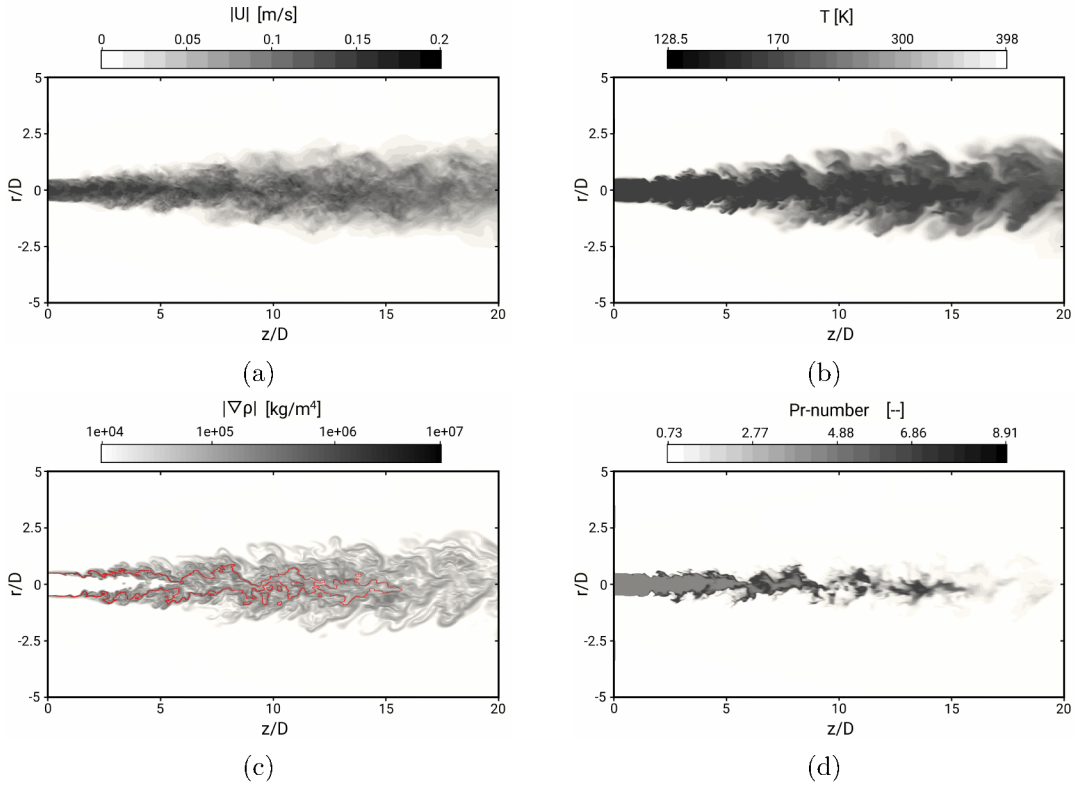

Figure 8.5: Snapshot of the velocity magnitude (a), temperature (b), density gradient magnitude (c) and molecular Pr-number (d) at $2.5t_c$ after start of injection. Red isolines in (c) refer to the mean density between incoming and ambient nitrogen.

As the turbulent jet streams into the ambient nitrogen, the magnitude velocity decreases with increasing axial distance and the jet spreads in radial direction. In terms of the temperature field, it varies from low values at the core of the jet to large values in the ambient nitrogen, whereby no truly sharp interface can be observed. Close to the inlet ($z/D < 2$), the jet surface is almost unaffected by the surrounding. Further downstream, finger-like objects are formed due to stretching of the inner core by the shear layer of the jet. These temperature structures are carried away with the flow and dissolve further downstream, which leads to a disintegration of the jet. Similar dynamics of supercritical jets were also observed in experimental investigations [41, 175]. Regarding the density, sharp gradients occur at the interface between the liquid-like cold jet and the warm gas-like surrounding. Thereby, dense pockets of liquid-like nitrogen are separated from the jet core and tend to persist for a significant length downstream. This formation of dense pockets cannot be ascribed to phase separation, due to the absence of surface tension at supercritical conditions. It is rather associated with poor thermal diffusivity and high isobaric heat capacity at the interface between the cold liquid-like jet and the warm gas-like ambient nitrogen resulting in high Pr-numbers (see figure 8.5 (d)). Thereby, the molecular Pr-numbers are approximately ten times higher at the jet interface than at the ambient nitrogen.

Regarding pseudo-boiling effects, figure 8.6 displays the isobaric heat capacity at four different cross sections (z/D=1, 5, 10, 15) at $2.5t_c$ after the injection. Thereby, pseudo-boiling is characterized by a maximum in specific heat capacity at supercritical pressure. Red isolines denote the mean density between the inlet and ambient nitrogen, associated with the interface of liquid-like and gas-like nitrogen.

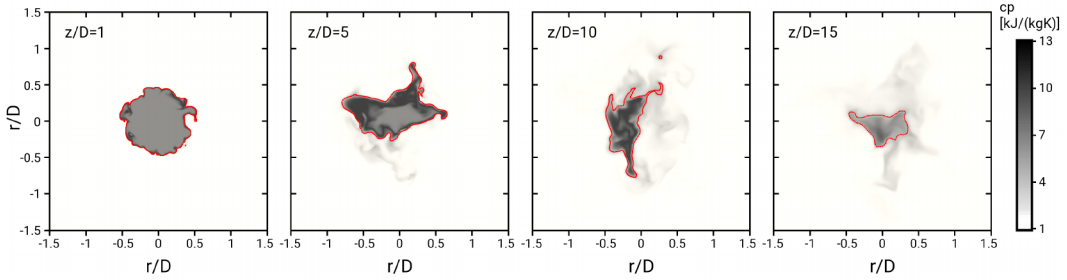

Figure 8.6: Isobaric heat capacity at four different cross sections, z/D = 1, 5, 10, 15 at $2.5t_c$ after the injection. Red isolines refer to the mean density between inlet and ambient nitrogen.

Close to the injection (z/D=1), the jet is fairly circular with high heat capacities at the jet interface. Further downstream, the jet becomes stretched and the heat capacity tends to smear out. For ($z/D \leq 10$), the heat capacity is approximately four times higher at the pseudo-boiling surface than that of the liquid-like jet and more than ten times higher than that of the surrounding nitrogen. In this region, supplied thermal energy from the ambient nitrogen is primarily used to overcome intermolecular attraction, associated with a sharp change in the density. Thereby, a supercritical state transition takes place and the fluid absorbs heat without significantly raising the temperature. Further downstream ($z/D > 10$), the pseudo-boiling surface is smeared out, and the temperature begins to increase slightly.

Regarding the self-similarity of supercritical jets, figure 8.7 shows the variation of the averaged axial velocity along the centerline and as a function of radial distance. Here, $r_{U,1/2}$ denotes the jet's half-width defined such that $\widetilde{U}(z/D, r_{U,1/2}) = 0.5 \cdot \widetilde{U}_c$, where $\widetilde{U}_c$

is the local value at the jet axis and $\widetilde{(.)}$ are Favre-averaged quantities. For comparison, experimental data from an isothermal, subcritical round jet of Wyngnanski and Fiedler [250] are utilized.

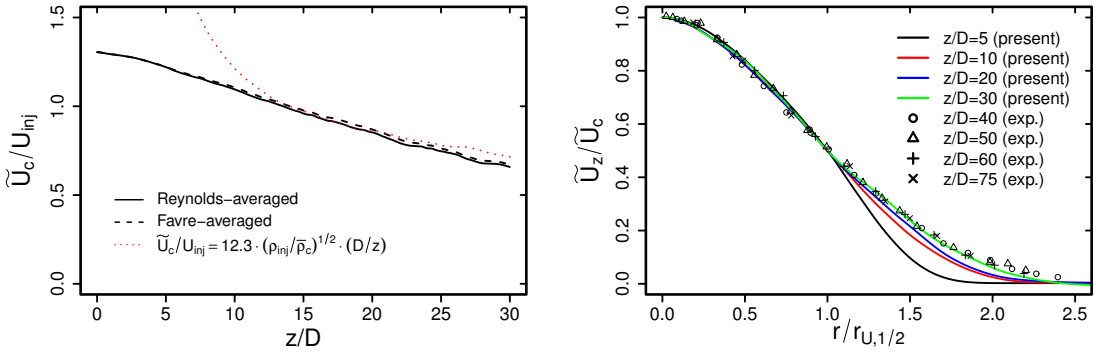

(a) (b)

Figure 8.7: Variation of mean axial velocity along the centerline (a) and against radial distance (b). Comparison with measurements from a subcritical round jet of Wyngnanski and Fiedler [250].

With increasing axial distance, the axial velocity decays gradually and the jet spreads in radial direction (see figure 8.7 (a)). In the case of variable density jet flow, dimensional analysis and conservation of momentum imply that beyond the developing region $\widetilde{U}_c/U_{inj} = B_U \cdot (\rho_{inj}/\overline{\rho}_c)^{1/2} \cdot D/z$, where B_U is an empirical constant. In the present study, $B_U = 12.3$, which is approximately twice the velocity decay rate of subcritical jets. Regarding normalized mean axial velocity plotted against $r/r_{U,1/2}$, profiles collapse onto a single curve for $z/D \geq 20$ and become self-similar. Thereby, the shape of the profiles are in excellent agreement with that of isothermal, subcritical round jets. A similar behavior can be observed for the variation of mass density along the centerline and against radial direction as depicted in figure 8.8. Here, $r_{\rho,1/2}$ is defined such that $\overline{\rho}(z/D, r_{\rho,1/2}) = 0.5 * (\overline{\rho}_c + \rho_\infty)$, where $\overline{(.)}$ denotes time-averaged values. For comparison, the measurements of the supercritical nitrogen jet of Mayer et al. [149] are selected.

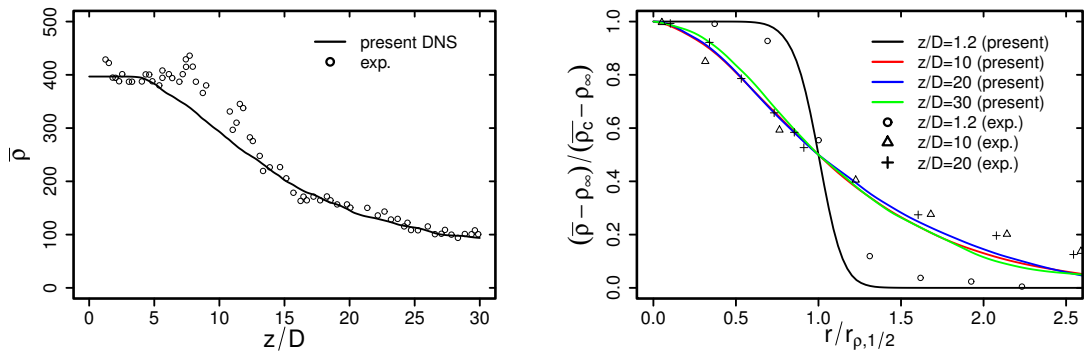

(a) (b)

Figure 8.8: Predicted mean density along the centerline (a) and against radial distance (b). Comparison with measurements of a supercritical round jet of Mayer et al. (2003) [149].

Close to the injection, density remains approximately constant, decreases rapidly while the jet disintegrates ($5 < z/D < 15$) and subsequently tends to the value of ambient density. In comparison to the measurements of Mayer et al. (2003) [149], the present results agree quite well, even though the Re-number is significantly higher in the experiment. However, it can be seen that the jet breaks up slightly earlier even though a reduced Reynolds number normally leads to later transition of the jet. In accordance to the axial velocity, density profiles plotted against $r/r_{\rho,1/2}$ collapse onto a single curve beyond $z/D \approx 20$ and become self-similar as well. Thereby, shapes of the profiles are slightly steeper than the experimental ones.

Finally, the self-similarity of fluctuating quantities in supercritical jets is analyzed in figure 8.9, which displays profiles of the rms velocity and rms density along the jet's axis and also in radial direction.

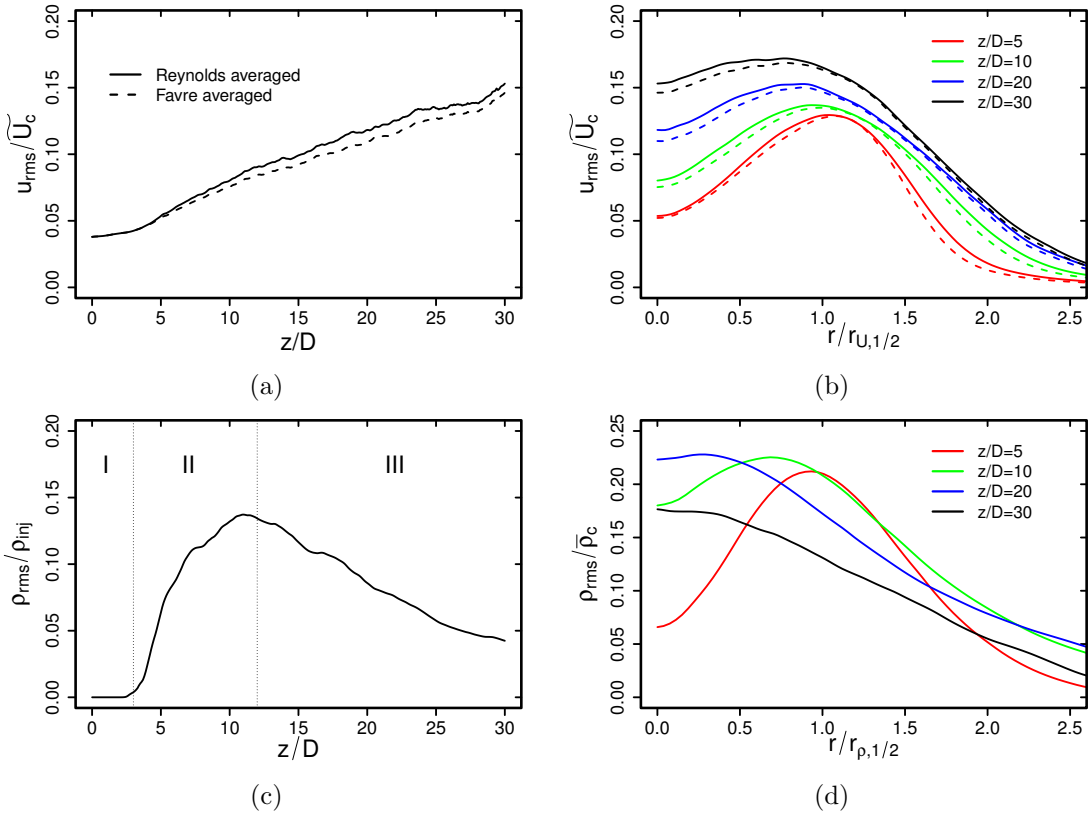

Figure 8.9: Variation of root-mean-square velocity and density fluctuations along the centerline (a),(c) and against radial distance (b),(d).

In the case of rms velocity along the centerline, $u_{rms}/\widetilde{U_c}$ remains approximately constant for $z/D < 5$ and increases while the jet breaks up. In contrast to subcritical jets, in which the rms velocity is about 25% of the mean after the developing region [178], $u_{rms}/\widetilde{U_c}$ is clearly reduced and does not reach a constant value. Similarly, profiles of $u_{rms}/\widetilde{U_c}$ plotted against $r/r_{U,1/2}$ rise with increasing axial distance and do not collapse. Thus, in contrast to subcritical jets [245], the Reynolds stresses are not self-similar up to $z/D = 30$ in supercritical jets.

Similar to velocity fluctuations, rms density profiles are not self-similar up to $z/D = 30$. Instead, three characteristic stages of the disintegration process can be observed considering the variation of rms density along the centerline of the jet (see figure 8.9 (c)).

First, in the potential core region (stage I), mean density remains constant and density fluctuations are zero. Then, dense pockets of liquid-like nitrogen are separated from the core and persist for a significant length downstream (see red isolines in figure 8.5 (c)), which causes a strong decrease of mean density and high density fluctuations (stage II). Finally, the liquid-like pockets break up and smear out. Thereby, density fluctuations decrease and tend asymptotically to zero (stage III).

8.3.2 Thermal transport properties

It appears that the turbulent flow properties of the supercritical jet differ significantly from those found in subcritical, isothermal jets. Deviations from subcritical jets arise primarily from thermodynamic and thermal effects rather than turbulence dynamics phenomena. This warrants a closer examination of the thermal transport and its contribution to the mixture formation in supercritical jets. For this purpose, figure 8.10 shows the variations of the mean and rms temperature along the jet's centerline.

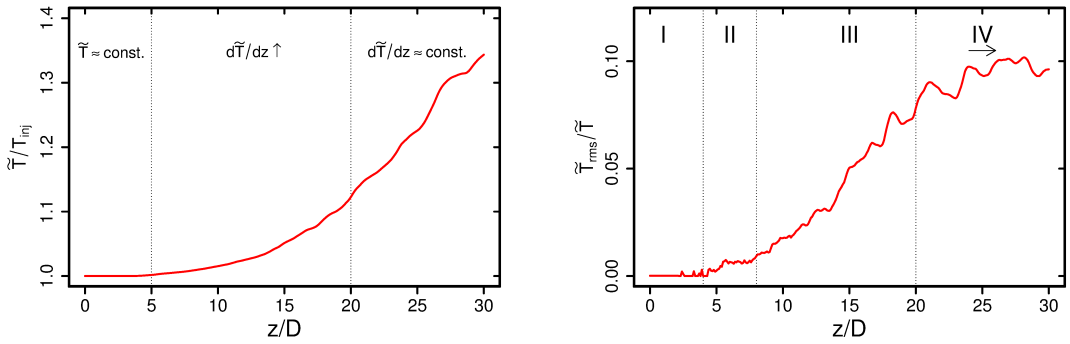

(a) (b)

Figure 8.10: Variation of mean (a) and rms (b) temperature along the jet's centerline.

Close to the inflow, the temperature remains constant, rises slowly while the jet breaks up and increases approximately linearly further downstream. The reason for such a behavior becomes clearer by examining the corresponding rms temperatures along the centerline. Thereby, in contrast to the rms density (see figure 8.9 (c)), four mixing stages might be distinguished. In the first stage (I), temperature fluctuations are zero, and the liquid-like core is nearly unaffected by the surroundings. Then, in the second stage (II), instabilities occur, and dense pockets of liquid-like nitrogen are separated from the core. Thereby, temperature fluctuations increase slightly. The third stage (III) is dictated by supercritical state transition. Supplied thermal energy from the ambient nitrogen is primarily used to overcome intermolecular forces, and the fluid absorbs heat without significantly increasing the temperature, while temperature fluctuations increase rapidly. In the last stage (IV), turbulent mixing dominates, and temperature increases rapidly, while normalized temperature fluctuations remain approximately constant. As will be shown in the next section, each of these disintegration stages has its own driving forces and can be distinguished much better by means of entropy generation analysis.

After analyzing the thermal mixing phenomena of supercritical disintegration processes, the turbulent heat fluxes and temperature scales are examined in order to assess appropriate heat flux modeling approaches in the context of RANS and LES for supercritical flows. In this respect, it is well known that in the case of subcritical homogeneous shear flows, the direction of the heat flux can be different to that of the corresponding

mean gradient (see, e.g. [224]), which is in contradiction to the linear eddy diffusivity hypothesis. This behavior is analyzed for the supercritical jet in figure 8.11. Thereby, the deviation from isotropic behavior is visualized by plotting $\widetilde{u_z''\Theta''} \cdot \nabla_r \widetilde{\Theta}$ against $\widetilde{u_r''\Theta''} \cdot \nabla_z \widetilde{\Theta}$. These two quantities have to be equal in the case of isotropic heat flux which is represented by a dashed line. Gray shaded areas highlight regions where heat is transported counter the temperature gradient.

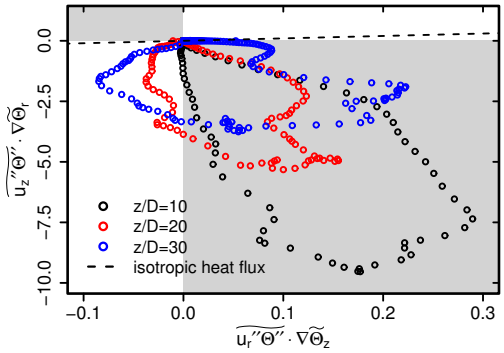

Figure 8.11: Anisotropy map of heat fluxes in the supercritical jet. Dashed line represents the isotropic state where $\widetilde{u_z''\Theta''} \cdot \nabla_r \widetilde{\Theta} = \widetilde{u_r''\Theta''} \cdot \nabla_z \widetilde{\Theta}$.

As it can be clearly seen in figure 8.11, heat fluxes are significantly anisotropic, especially close to the region where the jet breaks up ($z/D = 10$). Thereby, it is interesting to observe that heat fluxes are returning to the isotropic state with increasing axial distance, however they do not reach a fully-isotropic state up to $z/D = 30$. Furthermore, it can be seen, that in some regions of the jet, heat is transported counter the mean temperature gradient, which is predominantly caused by the dilatation of the jet in radial and axial direction because of pseudo-boiling effects. This suggests that anisotropic heat flux models may be appropriate for such kind of flows at supercritical conditions, in particular in the context of RANS.

Finally, temperature scales within the supercritical disintegration process are analyzed. As already mentioned above, values of the molecular Prandtl number are high at the interface between the cold liquid-like jet and the warm gas-like ambient nitrogen ($Pr \approx 10$). Therefore, it is expected to observe different physical regimes associated with different scalar dynamics in the temperature variance spectra of supercritical jets. This is analyzed in figure 8.12, which presents temporal autospectra of the temperature at different axial locations. The spectra are normalized using local values of the jet half-width of the temperature $r_{T,1/2}$, the variance of the temperature $\widetilde{T'^2}$ and the centerline velocity $\widetilde{U}_c$. The quantity f represents the frequency.

At $z/D = 10$, where the jet breaks up and the fluid has an almost liquid-like character, three physical regimes emerge in the temperature mixing spectrum. First the universal inertial convective range, which refers to the range of scales where direct effects of thermal diffusivity are negligible. Thus, the spectrum exhibits a $-5/3$ slope. Second is the viscous convective subrange, where temperature fluctuations are anisotropic and smoothed out by thermal diffusivity leading to a f^{-1} dependency. This regime is less pronounced for the present supercritical jet in comparison to the other physical regimes. Third is the dissipation range, where viscous forces dominate and the spectrum exhibits a f^{-7} dependency. Further downstream ($z/D > 10$), where the fluid resembles a subcritical gas, all normalized mixing spectra tend towards a $-5/3$ slope for higher frequencies, collapse onto a single curve and become self-similar. In this region, no viscous convective subrange occurs and

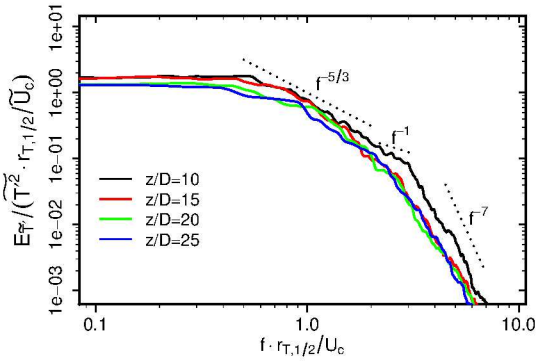

Figure 8.12: Normalized autospectra of the temperature at $z/D = 10$, 15, 20 and 25.

mixing spectra resemble turbulent kinetic energy spectra as they appear in turbulent jets of subcritical gases.

8.3.3 Entropy production mechanisms

To complete the picture of disintegration processes under supercritical conditions, entropy generation mechanisms are analyzed next in order to identify the causes of irreversibilities in such processes. Figure 8.13 depicts instantaneous entropy production rates by heat transport Π_q and viscous dissipation Π_v at the mid-plane section of the jet.

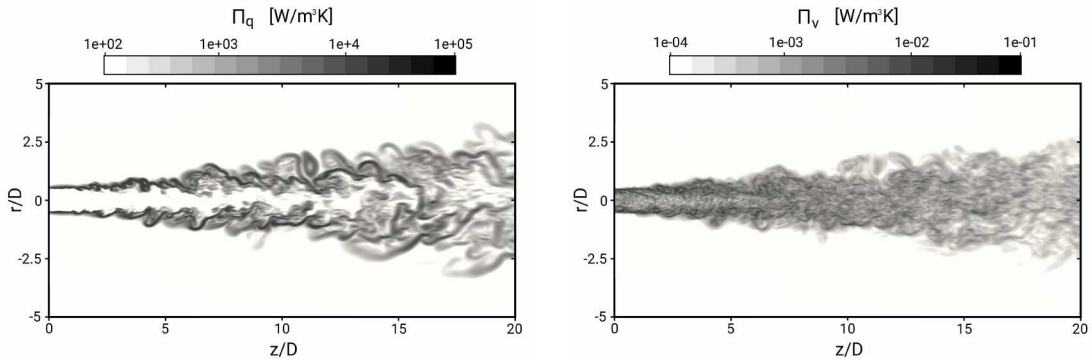

(a) (b)

Figure 8.13: Snapshots of entropy generation rate by heat transport (a) and viscous dissipation (b).

Due to the extreme operating conditions, it appears that entropy is primarily produced by heat transport Π_q including supercritical state transition, while the contribution of viscous dissipation Π_v appears negligibly small. Regarding entropy generation by heat transport as shown in figure 8.13 (a), streaks with high values of Π_q are generated at the mixing layer between the liquid-like cold jet and gas-like surrounding fluid. Similar to the temperature field, these streaks are carried along by the flow and dissolve further downstream. Furthermore, it can be seen that Π_q is small at the jet's core - due to the absence of temperature gradients - and high at the mixing layer. This seems to be reasonable because of the extreme non-uniformity of the temperature field resulting in steep gradients in the mixing layer. In contrast, irreversibilities caused by viscous dissipation are distributed uniformly throughout the jet, and turbulent structures of Π_v appear to be smaller (see figure 8.13 (b)). As expected, the highest values of Π_v occur at

the shear layer due to a large contribution of turbulent mixing and steep velocity gradients. Further downstream, irreversibilities caused by viscous dissipation decrease slightly, and turbulent structures of Π_v becomes larger.

Next, entropy production rates along the centerline of the jet are examined in order to characterize the disintegration process under supercritical conditions and to identify the causes or irreversibilities that are responsible for the jet break up. This is done in Figure 8.14, which displays the Favre-averaged terms of the entropy production by heat transport $\widetilde{\Pi}_q$ and by viscous dissipation $\widetilde{\Pi}_v$, respectively.

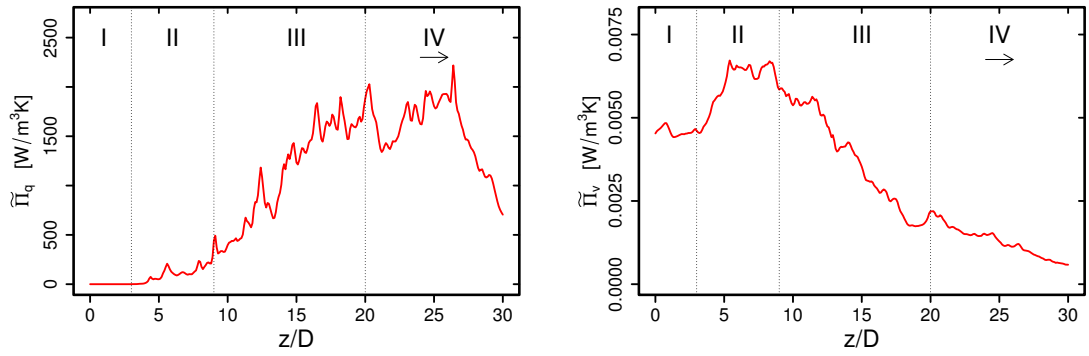

Figure 8.14: Time-averaged entropy production rates by heat transfer (a) and viscous dissipation (b) along the centerline of the jet.

In line with the variation of the rms temperature along the centerline shown in figure 8.10 (b), four main stages associated with the disintegration process are obvious from the consideration of entropy production rates. First, close to the injector outlet (I), $\widetilde{\Pi}_q$ is zero due to the absence of temperature gradients, while $\widetilde{\Pi}_v$ is high as a result of the evolving turbulent mixing. In the next stage (II), dense pockets of liquid-like nitrogen are separated from the jet core, inducing additional shearing and temperature gradients. Thus, both entropy production terms increase. In the subsequent stage (III), dense pockets further break up, and pseudo-boiling takes place. Thereby, absorbed heat is primarily used to overcome intermolecular attraction, which leads to a rapid increase of $\widetilde{\Pi}_q$, while at the same time, shearing is reduced and $\widetilde{\Pi}_v$ decreases. In the last stage (IV), most of the liquid-like nitrogen seems to be pseudo-evaporated, and the entropy generation is dominated by turbulent mixing processes. Thereby, $\widetilde{\Pi}_q$ decreases rapidly while $\widetilde{\Pi}_v$ declines slowly.

It appears that the disintegration process under supercritical conditions consists of four characteristic stages and is driven by heat transport phenomena. Furthermore, it is important to identify different scales, which influence the process. For this purpose, figure 8.15 presents normalized mixing autospectra of entropy production rates by heat transfer and by viscous dissipation. Fixed probes at $z/D = 5$, 15 and 25 are selected, corresponding to the disintegration stages (II), (III) and (IV).

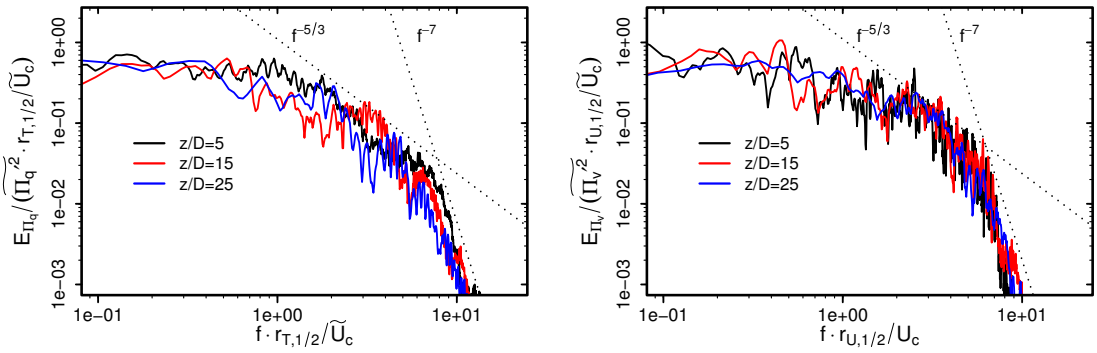

(a) (b)

Figure 8.15: Normalized autospectra of entropy generation rates by heat transport (a) and viscous dissipation (b) at $z/D = 5$, 15 and 25.

As it can be seen in figure 8.15, normalized spectra of entropy production by heat transport and by viscous dissipation exhibit a well-developed inertial and dissipation range and collapse onto a single curve at different axial locations. Thus, entropy production spectra are self-similar in supercritical jets. By comparing both spectra, it appears that more of the variance is expressed in higher frequencies in the case of mixing spectra of $\widetilde{\Pi}_v$, while large scales dominate in the mixing spectra of $\widetilde{\Pi}_q$.

8.4 Conclusion

DNS of a turbulent round jet of cryogenic nitrogen were conducted, which mimics the fuel injection process in liquid rocket engines. Real fluid equation of state, realistic inflow turbulence and generalized transport property models were included and evaluated. Using the second law of thermodynamics, an entropy production analysis has been performed, which allows to elucidate several distinctive features of the disintegration process and causes of irreversibilities.

Some important observations from this study concerning the self-similarity of supercritical jets, the disintegration process at supercritical thermodynamic conditions, modeling strategies in the context of RANS and LES, and causes of irreversibilities in such applications can be outlined as following:

(1) Examining turbulent flow statistics within the supercritical jet, it appears that the mean velocity and mean density are self-similar beyond $z/D = 20$. In contrast to subcritical jets, normalized Reynolds stresses and density fluctuations are clearly reduced and do not collapse on a single curve up to $z/D = 30$.

(2) Turbulent heat fluxes are highly anisotropic in supercritical jets, especially close to the injection. Further downstream, heat fluxes become less anisotropic, but do not reach full isotropy. Furthermore, it is observed that heat is transported counter the mean temperature gradient in some regions of the jet. Both, anisotropic heat fluxes and counter gradient diffusion suggest that anisotropic heat flux models may be appropriate for such applications in the context of RANS and LES.

(3) It is shown that the temperature variance spectrum in supercritical injection processes exhibits an additional viscous-convective subrange resulting from high Prandtl numbers in the liquid-like jet close to the injection region. From this it is evident

that the scalar dynamics of small temperature scales is less universal in supercritical injection processes than in subcritical gas injection.

(4) Regarding causes of irreversibilities, it turned out that the jet disintegration process under supercritical conditions is driven predominantly by heat transport and thermodynamic effects rather than by turbulent flow dynamics. Especially the contribution resulting from the state transition process appears dominant. Furthermore, entropy generation mechanisms in supercritical disintegration processes occur on different scales. While this takes place predominantly on large scales in the case of entropy production by heat transport, it evolves over a wide range of scales in the case of viscous dissipation.

(5) Finally, based on second law analysis, the jet disintegration process under supercritical conditions can be divided into four main stages:

I. Liquid-like core stage:
Within this first disintegration stage, the liquid-like core of the jet is almost unaffected by its surrounding. Thereby, the mean temperature along the centerline remains constant, rms temperature values are zero and the entropy production is small.

II. Separation stage:
Dense pockets of liquid-like fluid are separated from the core, inducing additional shearing and temperature gradients. At this stage, both entropy production rates increase along the centerline.

III. Pseudo-boiling stage:
Dense pockets tend to smear out and pseudo-boiling takes place. Absorbed heat is primarily used to overcome intermolecular cohesion. Accordingly, shearing is reduced and entropy production by heat transport increases strongly.

IV. Turbulent mixing stage:
Most of the liquid-like nitrogen is pseudo-evaporated and turbulent mixing dominates. While temperature increases, the entropy production rates decrease.

Depending on the operating and flow conditions, some of these stages may be more dominant than the others.

PART IV: PREDICTION OF IRREVERSIBILITIES USING LES

Chapter 9

Evaluation of the LES subgrid-scale modeling approaches

In this chapter, the subgrid-scale modeling approaches for momentum transport, heat transport and entropy production rates as described in chapter 3 are evaluated. This is achieved by a systematic comparison of LES predictions with DNS results using error analysis and by providing an estimation of the computational expenses of the subgrid-scale models. For the sake of clarity, the methods and error metrics used in the present assessment studies are briefly described below (see [E8] for further information). Then, the results of the evaluation studies are presented.

In order to evaluate numerical simulation results, the prediction accuracy need to be quantified by the estimation of the error measure of the simulation results [154, 239]. It is defined as the deviation of the predicted statistics Q_x^{sim} and the corresponding statistic observed by the reference Q_x^{ref} interpolated at position x. In contrast to other LES assessment studies [75, 88, 155, 239], the error measures used in the present work are normalized by the difference $d(.)$ between the maximal and minimal value of the reference data Q^{ref}, corresponding to the interval of interest. This leads to a normalized error measure as:

$$e_x \equiv \frac{Q_x^{sim} - Q_x^{ref}}{d(Q^{ref})}, \tag{9.1}$$

which is a non-dimensional metric and therefore well suited to compare the prediction accuracy for different statistical quantities. Contrary to the relative error often used for evaluating simulation results, equation 9.1 never gives infinite values except in the irrelevant case where all reference data are equal. Alternatively, the error can be normalized using another characteristic quantity that has to be non-zero, e.g., mean or median value, which might be advantageous in cases of wide spreading reference data.

In the case of LES, discrepancies between the reference data and calculated flow properties arise from inaccuracies of the physical subgrid-scale modeling e_x^{mod}, the numerical error e_x^{num}, the sampling error e_x^{rand}, the influence of the initial conditions e_x^{init}, the discrepancies in the boundary conditions e_x^{bc} and the error of the reference data e_x^{ref}. It follows that

$$e_x = f\left(e_x^{mod}, e_x^{num}, e_x^{rand}, e_x^{init}, e_x^{bc}, e_x^{ref}\right). \tag{9.2}$$

In order to determine the accuracy of a subgrid-scale model, the error contributions e_x^{num}, e_x^{rand}, e_x^{init}, e_x^{bc}, e_x^{ref} have to be much smaller than the inaccuracies of the physical modeling.

By means of explicit filtering, when the filter width and the grid spacing are independent, the modeling and the numerical error can be determined separately, such that a grid-independent solution can be reached [31]. In the context of implicit filtering as used

in this work, these two errors interact and are difficult to estimate separately as addressed in [239, 138, 38]. Therefore, in the present assessment framework the modeling and the numerical errors are combined to build e_x^{LES}, which allows to characterize the prediction accuracy of the entire LES method.

In order to obtain a global error metric of a predicted statistic Q^{sim} , the normalized mean absolute error (nMAE) is introduced as

$$nMAE_Q = \frac{\frac{1}{n}\sum_{i=1}^{n} |Q_i^{sim} - Q_i^{ref}|}{d\,(Q^{ref})}, \tag{9.3}$$

where i is the location and n the number of spatial points. Following the criteria of appropriate global metrics [166], the nMAE is non-dimensional, non-negative, symmetric and fulfills the triangle inequality. Furthermore, it can be used for datasets which have mean or median of zero (e.g. periodic data). Notice that it is very important to choose an appropriate number of spatial points within a representative region of interest when using a global error metric like the nMAE.

The framework used in the present assessment studies is intended to allow control of the trade-offs between accuracy, uncertainties and computational costs as function of the degree of fidelity expected. In this respect it is also important to address the required computational cost of a subgrid-scale model as well as the scaling of each model with regard to the spatial resolution. The relative computational cost of a subgrid-scale model $CPUh^*$ can be defined as the ratio of the CPU time spent for the calculation of the subgrid-scale model $CPUh^{sgs}$ and the total computation time of the simulation $CPUh^{tot}$. It follows that

$$CPUh^* = \frac{CPUh^{sgs}}{CPUh^{tot}}. \tag{9.4}$$

Notice that the relative computational cost depends generally not only on the subgrid-scale model, but also on the selected test case, the particular code implementation and the solution procedures applied.

9.1 Evaluation of LES subgrid-scale models for the momentum transport

In order to assess the prediction accuracy, physical consistency and computational cost of the subgrid-scale models for the momentum transport, a fully developed turbulent pipe flow test case at $Re_\tau = 180$ is considered. Seven subgrid-scale models are evaluated, namely the Smagorinsky model [220] with van Driest wall damping [233], the one-equation subgrid-scale kinetic energy model [254] with van Driest wall damping, the wall-adapting local eddy-viscosity (WALE) model [163], the SIGMA model [164], the localized dynamic Smagorinsky model [71], the localized dynamic one-equation subgrid-scale kinetic energy model [151] and the new σ-k_{sgs}-transport equation model as described in chapter 3. Thereby, classical model coefficients from the literature [220, 254, 163, 164] are employed.

9.1.1 Numerical setup

In the numerical pipe flow configuration, a computational domain length of $L = 14D$, a non-dimensional averaging time of $t_{av}^+ = tu_\tau^2/\nu = 1.5e4$ and a cyclic time of 500 integral time scales for the initial transient are selected. As pointed out by the author in [E8], this ensures that (1) the extend of the computational domain is sufficiently large to avoid any artificial constraints on the formation of fluid structures, (2) that computed turbulence

statistics are no more affected by the domain size, (3) that the sampling errors are smaller than 0.2% for mean and smaller than 0.4% for rms velocities when additional spatial averaging in azimuthal and flow directions is applied, and (4) guarantees statistical stationarity of mean and rms velocities before averaging is started. Detailed information about the quantification of each error contribution (e_x^{rand}, e_x^{init}, e_x^{bc} and e_x^{ref}) for the present pipe flow test case can be found in [E8].

A systematic grid-refinement study is conducted for five numerical grids with different spatial resolution to analyze the prediction accuracy and computational cost of the subgrid-scale models. A representation of the numerical grid is depicted in figure 9.1. Characteristic quantities of the numerical grids are summarized in table 9.1. Thereby, the numerical grid with the finest spatial resolution (grid 5) serves as a reference DNS in the present assessment study in consistence with the numerical approach applied in the LES studies. It has a ratio of mean grid width $\Delta = (\Delta_r \Delta_\omega \Delta_x)^{1/3}$ and Kolmogorov length scale η_K smaller than 1.5 in the entire domain, which ensures sufficient spatial resolution apart from the pipe wall [79]. In order to fully resolve the smallest scales in the near-wall region, the numerical grid is refined towards the wall whereby the non-dimensional cell size of the first cell at the wall is $\triangle^+ r_{wall} < 0.7$. Furthermore, it was shown in [E8] that the discrepancies between the present DNS results and the reference DNS data of [3] are $\sim 0.3\%$ for the mean and $\sim 0.7\%$ for the rms velocity components, which lies within the typical variability of reference DNS data from the literature ($\sim 2\%$) [E8].

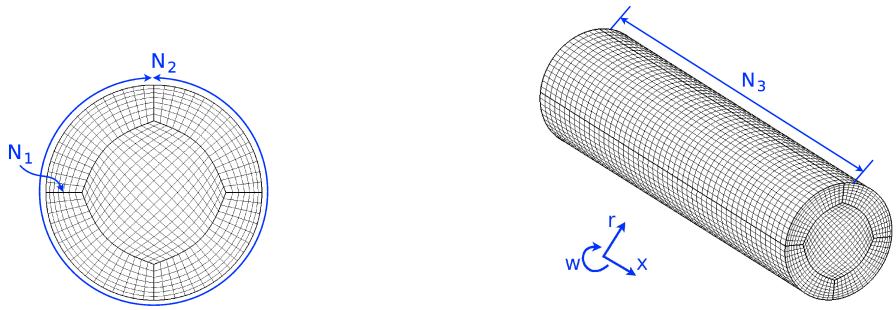

(a) (b)

Figure 9.1: Numerical grid of the pipe flow test case. (a) front view; (b) isometric view. $N_{1,2,3}$ represents the number of grid points.

	Grid 1	Grid 2	Grid 3	Grid 4	Grid 5 (DNS)
N	42900	145350	503100	1784640	21714100
N_1	8	11	16	24	46
N_2	45	69	105	161	341
N_3	101	151	226	339	965
$\triangle^+ r_{wall}$	1	0.9	0.9	0.7	0.7
$\triangle^+ \omega_{wall}$	25	17	11	7	3
$\triangle^+ x$	51	34	22	15	5

Table 9.1: Numerical resolution of the LES (grid 1-4) and DNS (grid 5) for the assessment study of subgrid-scale momentum transport models. N: total number of cells; $\triangle^+ r_{wall}$: non-dim. size of 1^{st} cell; $\triangle^+ \omega_{wall}$: non-dim. cell size; $\triangle^+ x$: non-dim. cell size.

An isotropic velocity field is used to initialize the pipe flow simulations. The initialization procedure is similar to the DNS of turbulent channel flow with passive heat transport described in section 6.1. At the inflow and outflow, periodic boundary conditions are applied in stream-wise direction for the pressure and velocity. In the case of pipe wall, no-slip condition is set for the velocity and a zero Neumann condition for the pressure. The additional pressure gradient, that drives the flow, is adjusted dynamically to maintain a constant mass flux. Therefore, the pressure is split into a periodic pressure and a non-periodic pressure part. A source term for the non-periodic pressure gradient is added to the momentum equation.

In the assessment study, various LES and one DNS were conducted using the standard solver pimpleFoam of the open source C++ library OpenFOAM 2.4.0, which is similar to the present low Mach-number formulation in the case of fluid flow with constant physical properties and without heat transfer. Important features of the numerical simulations, including the model coefficients used, are listed in table 9.2.

Case	Model	Grid no.
1, 2, 3, 4	Smagorinsky with van Driest [220] ($C_S = 0.18$)	1, 2, 3, 4
5, 6, 7, 8	One-equation with van Driest [254] ($C_k = 0.1$, $C_\epsilon = 1$)	1, 2, 3, 4
9, 10, 11, 12	WALE [163] ($C_W = 0.5$)	1, 2, 3, 4
13, 14, 15, 16	SIGMA [164] ($C_\sigma = 1.5$)	1, 2, 3, 4
17, 18, 19, 20	loc. dyn. Smagorinsky [71]	1, 2, 3, 4
21, 22, 23, 24	loc. dyn. one-equation [151]	1, 2, 3, 4
25, 26, 27, 28	present σ-k_{sgs}-equation model ($C_k = 0.1$, $C_\epsilon = 1$, $C_\sigma = 1.5$)	1, 2, 3, 4
29	No model (DNS)	5

Table 9.2: Summary of LES performed in the assessment study of subgrid-scale models for momentum transport. (see table 9.1 for "Grid no.")

9.1.2 Results

In the following, the evaluation of the physical behavior, the prediction accuracy and the computational cost of the LES models are analyzed. However, LES results of the Smagorinsky and one-equation models with van Driest wall damping using the two coarsest grids (cases 1, 2, 5, 6 in table 9.2) are excluded from the analysis, since both models overdiffuse the flow so that it was not possible to get a fully developed flow field with these two LES subgrid-scale models.

Near-wall physical consistency and comparison of statistical moments

Figure 9.2 shows the mean and rms velocity profiles predicted by the LES models in comparison with the generated DNS dataset. All velocity profiles are normalized by the friction velocity of the DNS. Results are exclusively shown for the one-equation model with van Driest wall damping, the SIGMA model, the localized dynamic one-equation model and the present σ-k_{sgs}-transport equation model, as representatives for different near-wall treatments. The results obtained using the other models with the same near-wall treatment are very similar and are therefore not shown here.

As expected, results from the LES become more accurate with increasing spatial resolution and collapse onto the DNS data in the case of highest resolution as apparent for all models under consideration. Regarding the axial mean velocity profiles, values are

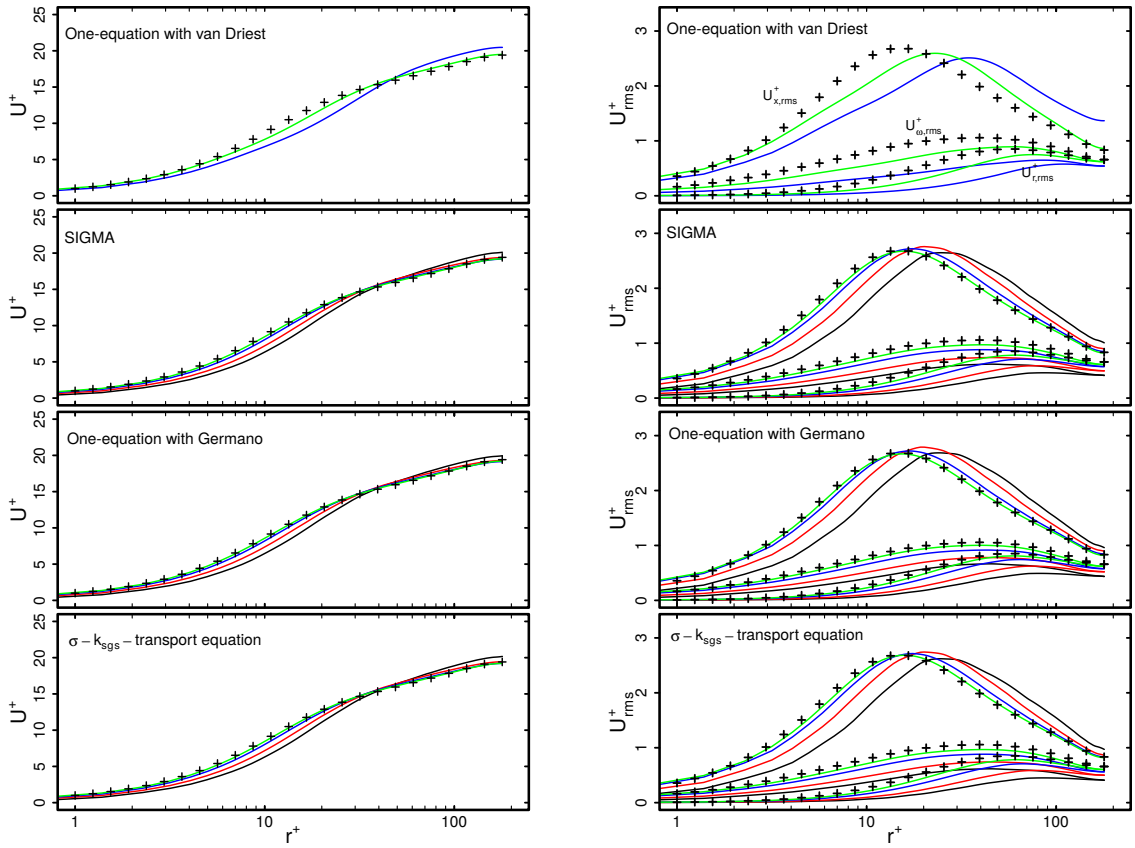

Figure 9.2: Predicted mean and rms velocities for different spatial resolutions. Grid no.1 (—), grid no. 2 (—), grid no. 3 (—), grid no.4 (—), DNS/grid no. 5 (+) (see table 9.1).

underestimated at the buffer layer region and near the wall ($r^+ \leq 30$). This tendency holds more or less for all models and spatial resolutions, but it is most notable for low mesh resolutions and for models using van Driest wall damping function. In the case of rms velocity profiles, results are apparently more affected by the spatial resolution. Peak values of the rms velocities are shifted towards the log-law region, especially in the case of models using van Driest wall damping and low spatial resolution. This non-physical behavior is less pronounced for the wall-adapting models (WALE, SIGMA), the dynamic models and the present σ-k_{sgs}-transport equation model, and results of these models are quite similar.

It appears that models using a van Driest wall damping function underestimate the axial mean velocity especially at the buffer layer and feature a non-physical shift in the peak values of the rms velocity components. One reason for such inconsistencies might be an inappropriate near-wall scaling of the eddy viscosity, which is analyzed in figure 9.3 for the one-equation model with van Driest wall damping, the SIGMA model, the localized dynamic one-equation model and the present σ-k_{sgs}-transport equation model. Dashed lines represent the correct near-wall scaling of the eddy viscosity ($\nu^{sgs} = O(r^3)$).

By examining the near-wall scaling of the predicted eddy viscosities in figure 9.3, it turns out that the wall-adapting models and the present σ-k_{sgs}-transport equation model are able to retrieve the theoretical asymptotic behavior near solid boundaries. Thereby, the scaling of the wall-adapting SIGMA model differs slightly from the ideal behavior very close to the wall, possibly due to limitations in the numerical accuracy by calculating the

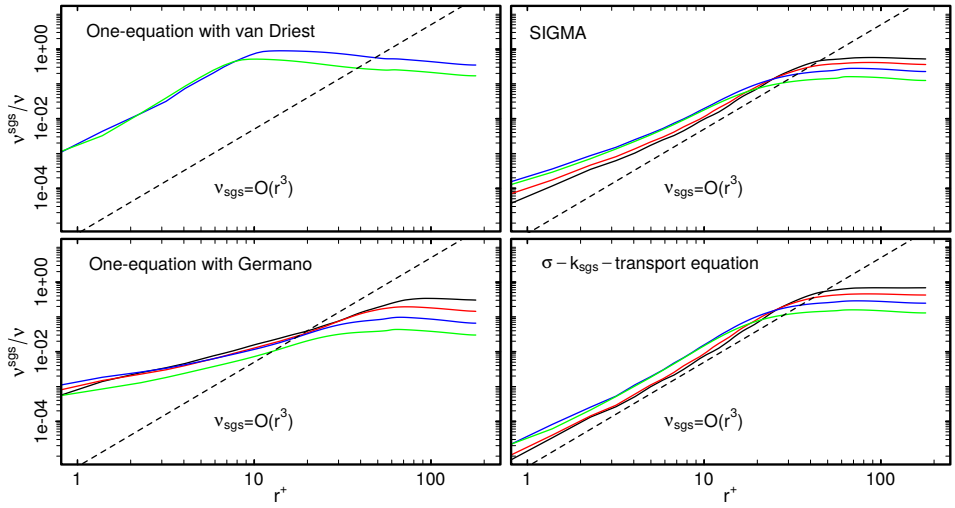

Figure 9.3: Near wall scaling of the eddy viscosity. Grid no.1 (—), grid no. 2 (—), grid no. 3 (—), grid no.4 (—) (see table 9.1). Dashed lines represent the proper near wall scaling of the eddy viscosity ($\nu^{sgs} = O(r^3)$).

singular values. In contrast, the scaling of the σ-k_{sgs}-transport equation model is very close to the theoretical asymptotic behavior even at the immediate vicinity of the wall. The near-wall scaling is also well reproduced by models using van Driest wall damping function. However, a non-physical amount of eddy viscosity is produced at the buffer layer and near the wall, which seems to be responsible for the shift in the rms velocity profiles, since the ratio ν_{sgs}/ν does not differ significantly from the wall-adapting models or the σ-k_{sgs}-transport equation model in the remaining region. Considering the localized dynamic Smagorinsky and one-equation models, both LES subgrid-scale models overdiffuse the near-wall region and are unable to reproduce the proper asymptotic behavior near the wall. As mentioned in [164] and elsewhere, the proper asymptotic behavior can be only obtained in such models when the dynamic procedure is applied over homogeneous planes parallel to the walls, which is not feasible in complex geometries, and therefore not applied in the present work. Although the scaling is wrong in the case of dynamic models, the ratio of ν_{sgs}/ν is quite small close to the wall, which might have therefore a minor contribution to the overall prediction accuracy of such models.

Error characteristics and prediction accuracy

The apparent performance of the subgrid-scale models established by comparison with the generated DNS dataset is now quantified by means of an error analysis. For this purpose, figure 9.4 shows the normalized relative error of the mean and rms velocities with respect to the non-dimensional wall distance r^+. Results are exemplarily shown for grid 3 (see table 9.1). Similar error characteristic are also obtained for the other spatial resolutions.

As revealed in figure 9.4, deviations are small in the viscous sublayer ($r^+ \leq 5$), increase rapidly with increasing wall distance, reach a maximum at the buffer layer ($5 < r^+ < 30$) and finally decrease in the outer region ($r^+ > 50$). This trend in the error characteristics is similar for all models and also for both statistics, mean and rms velocities. Furthermore, it can be seen that deviations are considerably higher in the case of models using a van Driest wall damping function, especially at the buffer layer and near the wall. In contrast, discrepancies in statistics predicted by wall-adapting models, dynamic models and the σ-k_{sgs}-transport equation model are significantly smaller and comparable. Thereby, results

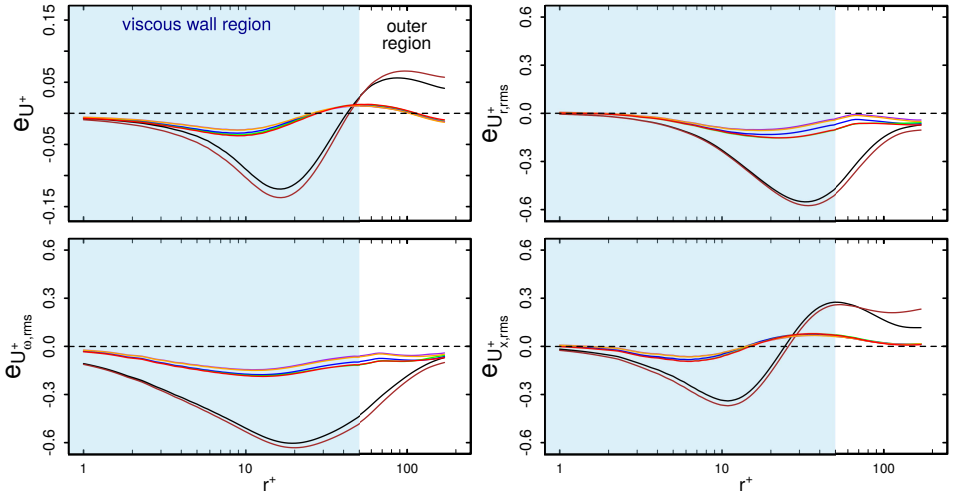

Figure 9.4: Normalized error of the predicted mean and rms velocities evaluated on grid no. 3 of table 9.1). Smagorinsky with van Driest damping (—), one-equation with van Driest damping (—), WALE (—), SIGMA (—), Smagorinsky with Germano (—), one-equation with Germano (—), σ-k_{sgs}-equation (—).

of the dynamic models are slightly more accurate, even though these models do not exhibit the correct near-wall behavior of the eddy viscosity.

After analyzing the error characteristics of the subgrid-scale models for a given spatial resolution and for different flow regimes, the overall prediction accuracy of the models with respect to the spatial resolution is further examined. For this purpose, the nMAEs of mean and rms velocities are calculated (equation 9.3). Thereby, locations at which the nMAEs are computed are logarithmically distributed along the pipe radius in order to obtain approximately and equal number of sampling points in each flow regime. Results with respect to the spatial averaged ratio of Kolmogorov length scale η and grid width Δ_{grid} are depicted in figure 9.5. Thereby, η is computed for each location using the local turbulent kinetic energy dissipation rate from the DNS.

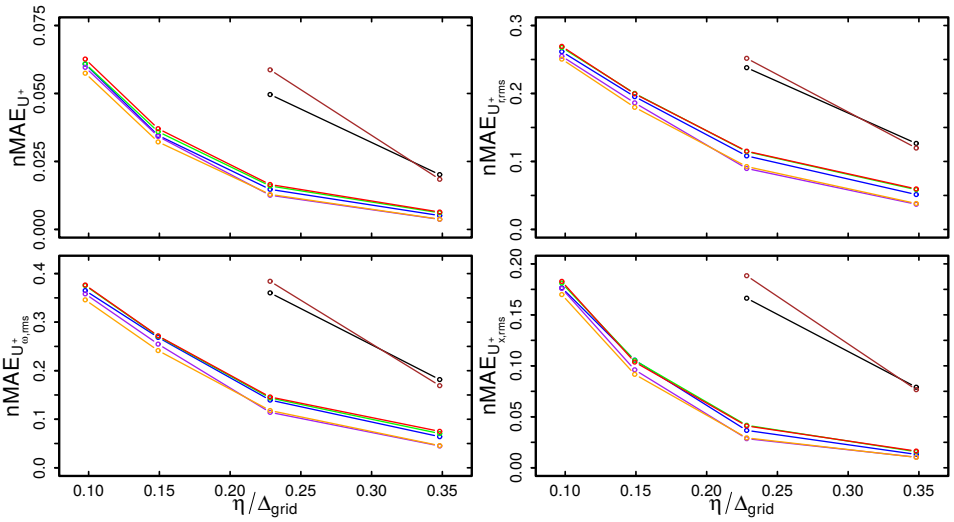

Figure 9.5: Normalized mean absolute error (nMAE) of predicted mean and rms velocities with respect to spatial resolution. (see figure 9.4 for legend).

As expected, the nMAEs decrease with increasing spatial resolution ($\eta/\Delta_{grid} \uparrow$). Especially for the wall-adapting models, dynamic models and the present σ-k_{sgs}-equation model, a lower spatial resolution is required to achieve an acceptable accuracy, reflecting a smaller modeling error of such subgrid-scale models in comparison with models using van Driest wall damping. The prediction accuracy of these models are quite similar. However, as it is visible in figure 9.5, the localized dynamic one-equation model is the most accurate for both, mean and rms velocity components over the entire resolution range for the selected test case.

Estimation of computational cost

One of the key objectives for developing LES is to establish it as an numerical model-based engineering design tool. This is possible if it is able to provide predictions using economically computational cost. Therefore, it is of practical interest to address the required computational cost of a subgrid-scale model to achieve results with an acceptable accuracy. For this purpose, figure 9.6 shows the required relative computational cost for each subgrid-scale model as a function of normalized spatial resolution. Here, $\overline{\Delta}_{grid}$ represents the spatially averaged grid size and D is the diameter of the pipe. For the estimation of the relative computational cost $CPUh^*$, only one CPU-core is used and the maximal CFL-number is set to one.

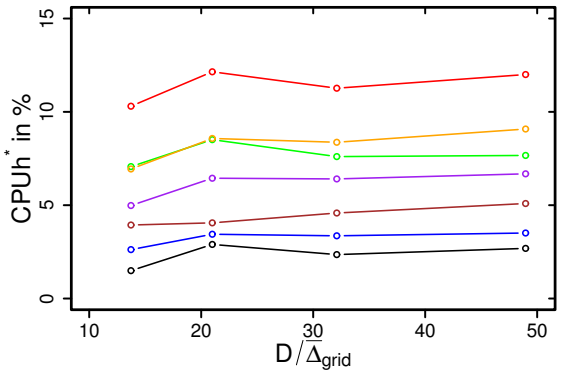

Figure 9.6: Ratio of the CPU time spent for the calculation of each subgrid-scale model and the total computation time as a function of the normalized spatial resolution. Smagorinsky with van Driest damping (—), one-equation with van Driest damping (—), WALE (—), SIGMA (—), Smagorinsky with Germano (—), one-equation with Germano (—), σ-k_{sgs}-equation (—).

As it might be expected, the Smagorinsky model with van Driest wall damping and the WALE model have the lowest relative computational cost $CPUh^* \sim 3\%$, whereas the one-equation model with Germano procedure, the SIGMA and especially the present σ-k_{sgs}-equation model are the most expensive ones with $CPUh^* \sim 10\%$. The high computational cost of the one-equation model with Germano procedure is quite obvious due to the additional effort spent for solving the transport equation of k^{sgs} along with the effort to automatically adapt the model coefficients. Surprisingly, the computational cost is high for the SIGMA model, which is purely algebraic and does not use any dynamic procedure. It appears that the calculation of the SIGMA model operator is computationally intensive since the three singular values of the velocity gradient tensor have to be computed for each control volume and each time step. This is also the reason for the relatively high computational expense of the σ-k_{sgs}-equation model, since the SIGMA model operator

has to be calculated along with an additional transport equation of k^{sgs}. Nevertheless, the CPU time spent for the calculation of all subgrid-scale models under consideration is quite small compared to the total computation time of the simulation. It can be therefore concluded that the computational cost plays a minor role for such relatively simple subgrid-scale models.

9.1.3 Conclusion

A fully developed turbulent pipe flow at $Re_\tau = 180$ is considered to assess the prediction accuracy, physical consistency and computational cost of seven subgrid-scale models for momentum transport. Thereby it turned out that wall-adapting models, localized dynamic models and the present σ-k_{sgs}-equation model reproduce the physics of the flow field more reliably while revealing a superior prediction accuracy than models using a van Driest wall damping approach. Especially at the viscous wall region ($r^+ \leq 50$), wall-adapting models, dynamic models and the σ-k_{sgs}-equation model are more accurate. Regarding the near-wall scaling of the eddy viscosity, it is shown that only wall-adapting models and the σ-k_{sgs}-equation model are able to reproduce the theoretical asymptotic behavior at the wall correctly. Localized dynamic approaches and models using a van Driest wall damping function overdiffuse the near-wall region and consequently do not reproduce the theoretical asymptotic behavior at the wall correctly. Finally, by examining the computational cost of the subgrid-scale models it appears that the Smagorinsky model with van Driest wall damping and the WALE model have the lowest relative computational cost of $CPUh^* \sim 3\%$, whereas the one-equation model with Germano procedure, the SIGMA model and the present σ-k_{sgs}-equation model are the most expensive ones with $CPUh^* \sim 10\%$. Nevertheless, the CPU time spent for the calculation of all subgrid-scale models under consideration is quite small compared to the total computation time of the simulation. The computational cost plays therefore a minor role for such relatively simple subgrid-scale models.

Based on these findings, it is evident that localized dynamic models and models using a van Driest wall damping function are not used in this work for further investigations of irreversibilities in sub- and supercritical turbulent near-wall flows. In such flow configuration wall-adapting models and especially the σ-k_{sgs}-equation model are the models of choice due to their prediction accuracy and physical consistency.

9.2 Evaluation of LES subgrid-scale models for heat transport

In this section, the subgrid-scale modeling approaches of heat transport as described in chapter 3 are assessed. In line with the evaluation study of subgrid-scale models for momentum transport, this is achieved by a systematic comparison of LES predictions with DNS results using an error analysis and by providing an estimation of the computational expense of the subgrid-scale models. For this purpose, various LES of a fully developed turbulent channel flow with heated walls ($Re_\tau = 395$, $Pr = 0.71$) have been carried out to evaluate the prediction accuracy, physical consistency and computational cost of the different subgrid-scale heat flux models. These models are the commonly used eddy diffusivity model with constant turbulent Prandtl number Pr_{sgs}, the eddy diffusivity model using a dynamic procedure to calculate Pr_{sgs} [158] and the present explicit anisotropy resolving algebraic heat flux model as described in chapter 3. In order to quantify the

influence of the numerical approach on the LES predictions, simulations without any subgrid-scale model for the subgrid-scale heat flux were also carried out.

9.2.1 Numerical setup

Based on the DNS study of Kawamura et al. [109], the computational domain of the channel simulation has a length of 6.4δ and an extent in span-wise direction of 3.2δ, where δ is half the height of the channel. Notice that this domain size may not be large enough to ensure that turbulence structures and computed turbulence statistics are no more affected. Nevertheless, for the sake of consistency with the reference DNS database of Kawamura et al. [109], the same computational domain size is selected in the present evaluation study. A schematic of the computational domain is depicted in figure 9.7.

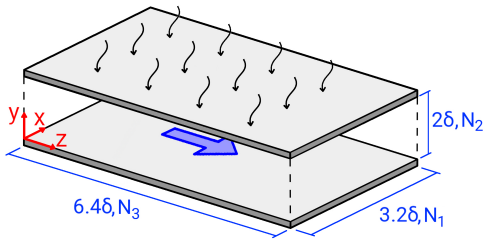

Figure 9.7: Computational domain for the LES study of heated channel flow at $Re_\tau = 395$. $N_{1,2,3}$ represents the number of grid points.

A systematic grid-refinement study consisting of four numerical grids with different spatial resolution has been conducted to analyze the prediction accuracy and computational cost of the subgrid-scale heat flux models. Characteristic quantities of the applied numerical grids are summarized in table 9.3.

	Grid 1	Grid 2	Grid 3	Grid 4
N	288000	576000	1013760	1958400
N_1	61	81	97	121
N_2	81	91	111	137
N_3	61	81	97	121
y^+_{wall}	1.3	0.8	0.7	0.7
$\triangle^+ x$	21.1	15.8	13.2	10.5
$\triangle^+ z$	42.1	31.6	26.3	21

Table 9.3: Numerical resolution of the LES for the assessment study of subgrid-scale heat transport models. N: total number of cells; y^+_{wall}: non-dim. size of 1^{st} cell at the wall; $\triangle^+ x$: non-dim. cell size in span-wise direction; $\triangle^+ z$: non-dim. cell size in flow direction.

An isotropic velocity field is utilized to initialize the channel flow simulations. The initialization method is exactly the same as that of the DNS of turbulent channel flow with passive heat transport as described in section 6.1. Periodic boundary conditions are applied in the stream-wise and span-wise directions for the velocity, pressure and temperature. At the channel walls, no-slip condition is set for the velocity and a zero Neumann condition is used for the kinematic pressure. Regarding the temperature, a constant wall temperature of $T_w = 500K$ is imposed. The pressure and temperature gradients, which drive the heat and fluid flow, are adjusted dynamically to maintain a

constant mass flux and mixed temperature, respectively. For this purpose, source terms are added to the momentum and energy equations.

The present low Mach-number approach is utilized in the LES studies, where the temperature equation is solved implicitly using the Crank-Nicholson method and the filtered-Linear scheme is used for all convective terms (see section 4). Notice that the filteredLinear scheme is less dissipative than most TVD schemes usually used to discretize the convective terms. For the sake of consistency with the reference DNS of Kawamura et al. [109], thermodynamic and transport properties are taken as constant values in the LES simulations. A summary of the LES study is given in table 9.4. Notice that in the case of subgrid-scale modeling of momentum transport, the σ-k_{sgs}-equation model is employed for all cases.

Case	Model	Grid no.
1, 2, 3, 4	eddy diffusivity model ($Pr_{sgs} = 0.7$)	1, 2, 3, 4
5, 6, 7, 8	eddy diffusivity model with dynamic Pr_{sgs}	1, 2, 3, 4
9, 10, 11, 12	present anisotropic heat flux model	1, 2, 3, 4
13, 14, 15, 16	no model	1, 2, 3, 4

Table 9.4: Summary of LES performed to assess the subgrid-scale models for heat transport. (see table 9.3 for "Grid no.")

9.2.2 Results

Before starting with the evaluation of the selected LES heat flux models, the predicted turbulent flow field by the LES is examined first to identify potential discrepancies, which might have some influence on the heat transport characteristics. Then, the physical behavior, the prediction accuracy and the computational cost of the selected LES heat flux models are analyzed and evaluated. The DNS database of Kawamura et al. [109] is utilized to compare the present LES results.

Comparison of the turbulent flow field

Figure 9.8 shows predicted mean and rms velocities as a function of the non-dimensional wall distance y^+ obtained with the different numerical grids from table 9.3. All velocity profiles are normalized by the friction velocity of the reference DNS.

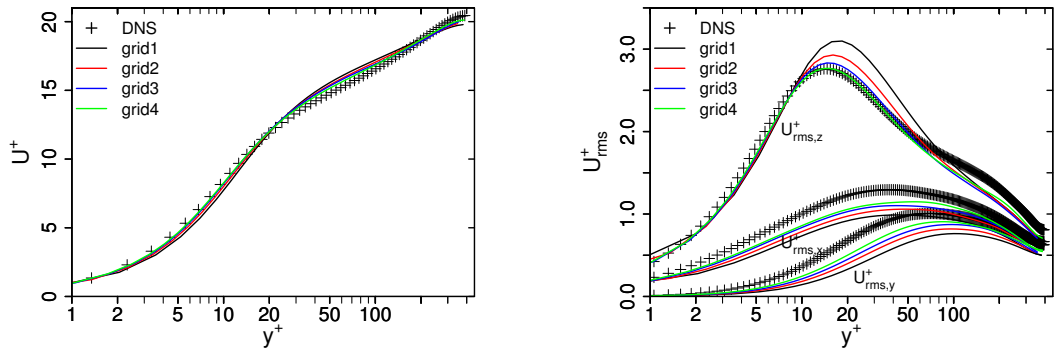

(a) (b)

Figure 9.8: Predicted mean (a) and rms (b) velocities as a function of non-dimensional wall distance y^+. Comparison of LES results with DNS data of [109].

As it is apparent in figure 9.8 (a), predicted mean velocities are very close to the reference DNS data of [109]. Fluctuations are slightly more affected by the spatial resolution (see figure 9.8 (b)), especially in the case of axial rms velocities that are overestimated in the buffer layer region. Nevertheless, the overall physics of the turbulent flow field is well reproduced by the LES, even with the coarsest numerical grid under consideration. It is therefore most likely that discrepancies in the predicted flow field have only a minor influence on thermal properties.

Physical consistency and comparison of thermal statistical moments

Figure 9.9 shows non-dimensional mean and rms temperatures profiles predicted by the different heat flux models and the no model approach in comparison with the reference DNS data. The non-dimensional temperature is defined as $\Theta^+ = (T_w - T)/T_\tau$, where $T_\tau = q_w/(\rho c_p u_\tau)$ is the friction temperature taken from the reference DNS.

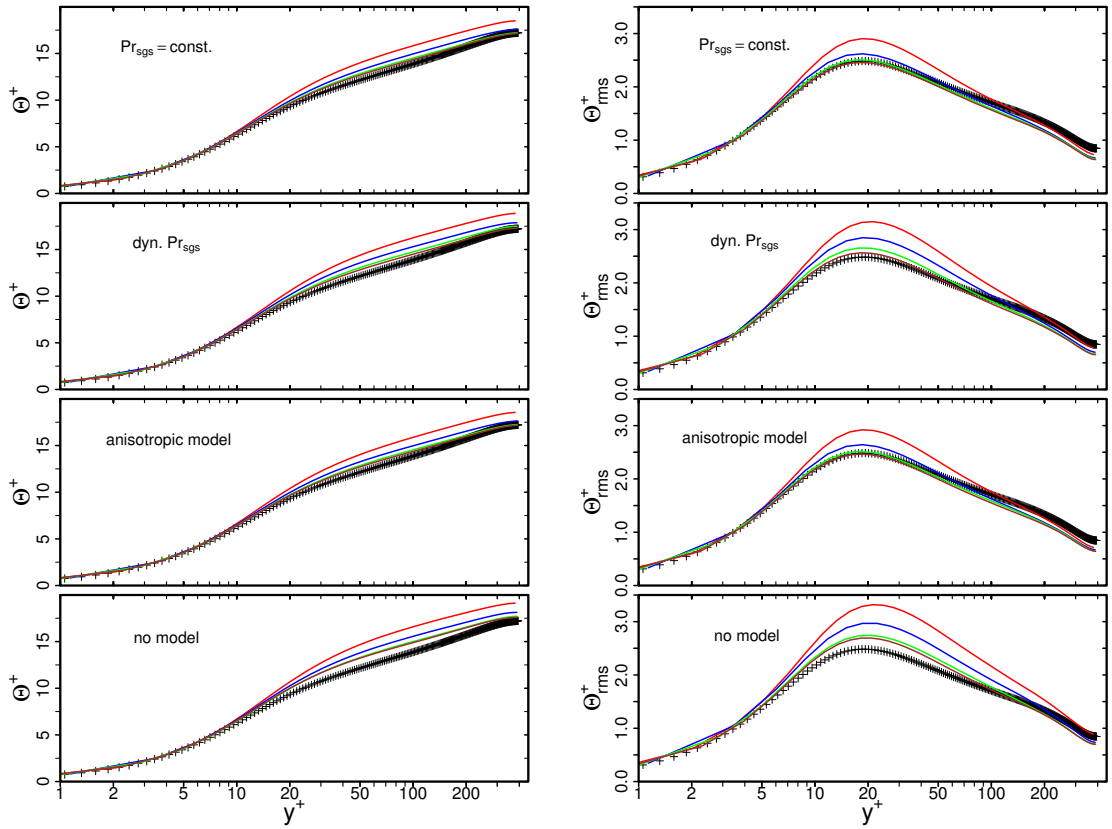

(a) (b)

Figure 9.9: Predicted non-dimensional mean and rms temperature profiles for different spatial resolutions. Grid no.1 (—), grid no. 2 (—), grid no. 3 (—), grid no.4 (—) (see table 9.3). Comparison with reference DNS data (+) of Kawamura et al. [109].

As it is expected, with increasing spatial resolution, results from the LES become more accurate for all heat flux models under consideration and also for the no model approach. Regarding mean temperature profiles shown in figure 9.9 (a), predicted values are overestimated at the buffer layer and log-law region. This tendency holds true for all models and spatial resolutions, whereby differences in the predictions of the different heat flux models are fairly small. However, it can be clearly seen that deviations from DNS

are highest in the case of the no model approach. Regarding rms temperature profiles as depicted in figure 9.9 (b), LES results are apparently more affected by the spatial resolution and the subgrid-scale modeling. Here, it can be observed that predictions of the peak value at the buffer layer region ($10 < y^+ < 40$) are too high, in particular for low mesh resolutions and especially in the case of the no model approach. Best agreement is achieved in the case of the anisotropic and the eddy diffusivity model with constant Pr_{sgs}. Therefore, it can be concluded that the subgrid-scale heat flux modeling has a minor influence on first order thermal statistics but significantly improves second order thermal statistics, while the diffusivity of the numerical approach seems almost negligible, at least for the selected turbulent heated channel flow test case at $Re_\tau = 395$ and $Pr = 0.71$.

Next, the physical consistency of the different subgrid-scale heat flux models is analyzed. For this purpose, figure 9.10 shows predicted wall-normal (a) and axial (b) turbulent heat fluxes as a function of non-dimensional wall distance in comparison with the reference DNS data. Solid lines denote resolved heat fluxes, while dashed lines represent subgrid-scale heat fluxes.

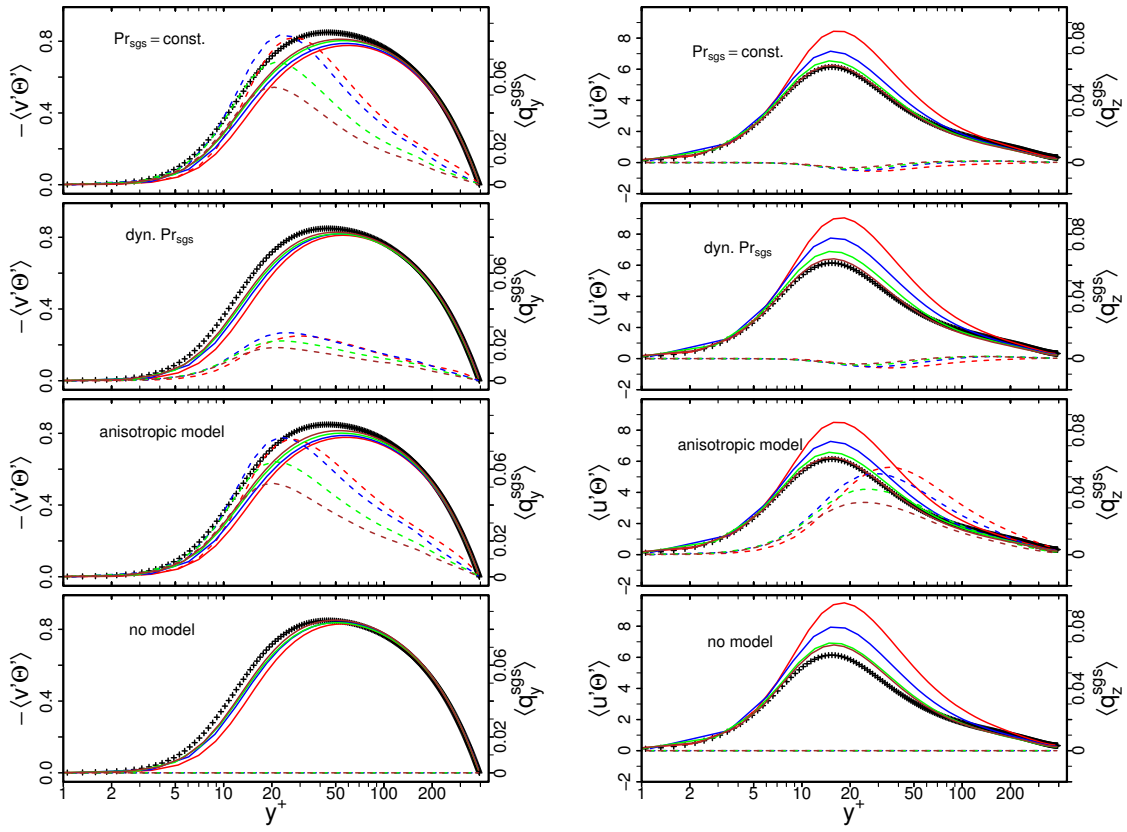

Figure 9.10: Predicted wall-normal (a) and axial (b) turbulent heat fluxes as a function of non-dimensional wall distance. Comparison with reference DNS data (+) of Kawamura et al. [109]. Solid lines represent resolved heat fluxes and dashed lines are subgrid-scale heat fluxes. (see figure 9.9 for legend).

Regarding the wall-normal heat flux in figure 9.10 (a), resolved fluxes are underestimated in the near-wall region but compare quite well in the log-law region. The contribution of the subgrid-scale wall-normal heat flux appears relative small in all LES heat flux models ($\sim 5 - 10\%$ of the resolved wall heat flux), but it is smallest in the case of

the eddy diffusivity model using the dynamic procedure to calculate Pr_{sgs}. Furthermore, resolved and subgrid-scale wall-normal heat fluxes are aligned, which indicates a consistent modeling of the wall-normal heat flux for all LES heat flux models under consideration. In contrast, resolved axial heat fluxes are significantly higher than DNS values, especially in the buffer layer region (see figure 9.10 (b)). Thereby, it is interesting to observe that resolved and subgrid-scale axial heat fluxes are only aligned in the case of the explicit anisotropy resolving heat flux model, reflecting the physical consistency of this model under these operating conditions. Considering the isotropic heat flux models, both, the standard and dynamic eddy diffusivity models are unable to reproduce the correct direction of the axial subgrid-scale heat flux. Although, the resolved and subgrid-scale axial heat fluxes are not aligned in the isotropic models, the contribution of the subgrid-scale modeling appears quite small, which might explain that the overall prediction accuracy of thermal statistics with such models is comparable to anisotropic models (for comparison see figure 9.9).

Error characteristics and prediction accuracy

It appears that deviations in predicted thermal statistics are quite small, even though subgrid-scale heat fluxes are only modeled consistently by the anisotropic subgrid-scale heat flux model. This is quantified now by means of an error analysis. For this purpose, figure 9.11 shows the normalized relative error of the mean and rms temperatures with respect to the non-dimensional wall distance y^+. Results are exemplarily shown for grid 2 (see table 9.3). Similar error characteristics are obtained for the other spatial resolutions.

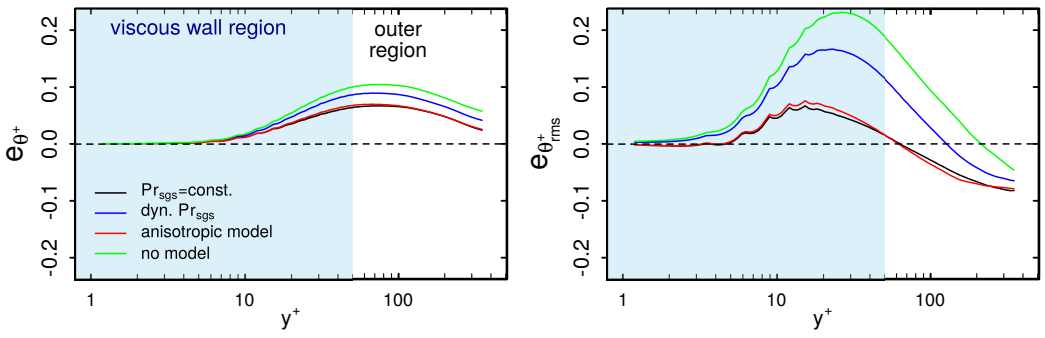

Figure 9.11: Normalized error of the predicted mean and rms temperatures evaluated on grid no. 2 of table 9.3).

It can be observed in figure 9.11, that errors are small in the near-wall region, increase rapidly in the buffer layer and finally decrease in the outer region. This trend in the error characteristics is similar for all LES heat flux models and also for both statistics, mean and rms temperatures. The error contributions of the approach with constant Pr_{sgs} and the anisotropic model are very similar and it can be clearly seen that both models are the most accurate ones. In contrast, the error contribution of the dynamic Pr_{sgs} approach and especially the no model approach are significantly higher, indicating a higher modeling error of both models.

After examining the error characteristics of the heat flux models for a given spatial resolution, the overall prediction accuracy of the models with respect to the spatial resolution is analyzed now. For this purpose, the nMAEs of the mean and rms temperatures are

calculated (see equation 9.3). Thereby, the locations at which the nMAEs are computed are logarithmically distributed along the channel hight in order to obtain approximately and equal number of sampling points in each flow regime. Results with respect to the spatial averaged ratio of Obukhov-Corrsin length scale η_{OC} and grid width Δ_{grid} are depicted in figure 9.12. The η_{OC} is estimated from the reference DNS of Kawamura et al. [109].

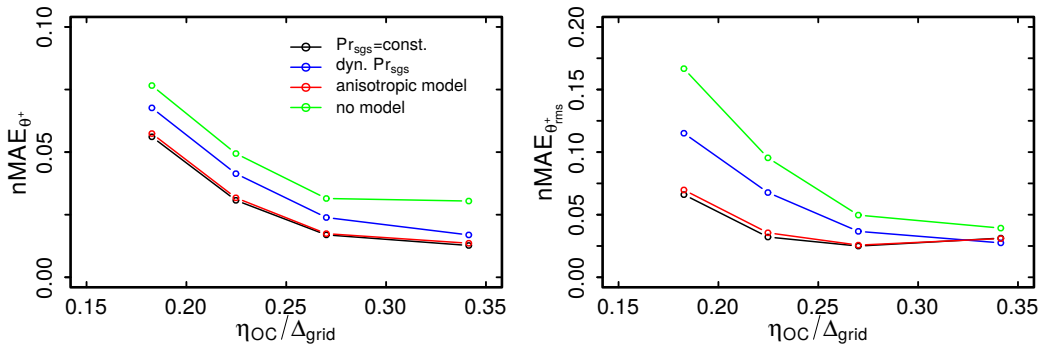

Figure 9.12: Normalized mean absolute error (nMAE) of predicted mean and rms velocities with respect to the spatial resolution.

As it is visible in figure 9.12, the nMAEs decrease with increasing spatial resolution ($\eta_{OC}/\Delta_{grid} \uparrow$). In particular the constant Pr_{sgs} approach and the anisotropic model have lowest values of nMAEs, reflecting a smaller modeling error in comparison to the other models under consideration. Unexpectedly, nMAEs of the eddy diffusivity model using a dynamic procedure to calculate Pr_{sgs} are significantly higher than the constant Pr_{sgs} approach. This may be attributed to additional numerical errors induced by the test filtering approach, where the anisotropy of the numerical grids is not considered in the present formulation of the test filter.

Estimation of computational cost

Finally, the required computational cost of the heat flux models to achieve an acceptable accuracy is assessed. Figure 9.13 shows the relative computational cost of each subgrid-scale model as a function of normalized spatial resolution.

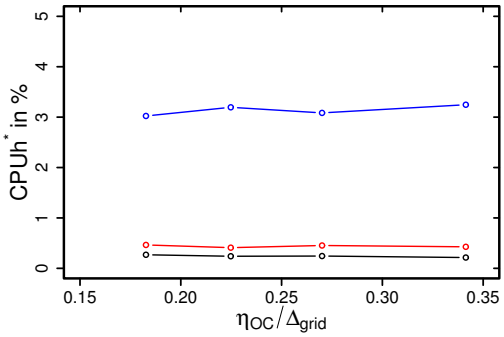

Figure 9.13: Ratio of the CPU time spent for the calculation of each subgrid-scale heat flux model and the total computation time as a function of the normalized spatial resolution. Eddy diffusivity model with constant Pr_{sgs} (—), eddy diffusivity model with dynamic procedure to calculate Pr_{sgs} (—), explicit anisotropy resolving heat flux models (—).

Apparently in figure 9.13, the eddy diffusivity model with constant Pr_{sgs} has the lowest relative computational cost ($CPUh^* \sim 0.25\%$), whereas the eddy diffusivity model using a dynamic procedure to calculate Pr_{sgs} is the most expensive one with $CPUh^* \sim 3\%$. The explicit anisotropy resolving heat flux model is also quite inexpensive ($CPUh^* \sim 0.5\%$) since it is fully algebraic and does not use any dynamic procedure. Moreover, the CPU time spent for the calculation of all heat flux models under consideration is fairly small compared to the total computation time of the simulation. It can be therefore concluded that the computational cost is not of great significance for such relatively simple subgrid-scale heat flux models.

9.2.3 Conclusion

Various LES of a fully developed turbulent channel flow with heated walls ($Re_\tau = 395$, $Pr = 0.71$) have been carried out to evaluate the prediction accuracy, physical consistency and computational cost of different subgrid-scale heat flux models. Thereby, it turns out that isotropic and anisotropic models are able to predict thermal statistics accurately within the channel flow test case, regardless a dynamic procedure is used or not. In contrast, only the explicit anisotropy resolving model is able to predict subgrid-scale heat fluxes consistently in the case of the axial heat flux. It is therefore used for further analysis of irreversibilities in sub- and supercritical turbulent near-wall flows. Finally, by examining the computational expense of the heat flux models it appears that all models under consideration are fairly inexpensive. Thus, the computational cost of such relative simple models is not significant in the context of LES.

9.3 Evaluation of subgrid-scale modeling of entropy production

In this last evaluation study, the reliability of the subgrid-scale modeling approach for entropy production rates as described in section 3.4 are assessed. In this respect it is worth mentioning that reference DNS data from the literature regarding entropy production rates in turbulent heated near-wall flows do not exist. Therefore, an additional DNS of a turbulent heated channel flow at $Re_\tau = 395$ and $Pr = 0.71$ has been performed in order to generate a reliable DNS database of entropy production rates for such flow configurations. The numerical test case is same as that of the DNS of Kawamura et al. [109] used in the evaluation study for the subgrid-scale heat flux models (see section 9.2.1). The numerical grid consists of 9879552 control volumes and is refined in the near-wall region to ensure a non-dimensional wall distance smaller than one ($y^+ < 1$). Furthermore, the ratio of Kolmogorov length scale and mean grid width η_K/Δ is smaller than 2.5 in the entire domain. Both, $y^+ < 1$ and $\eta_K/\Delta < 2.5$, confirm an appropriate spatial resolution of the present DNS. A comparison of fluid flow and thermal statistics from the present DNS with the reference dataset of Kawamura et al. [109] is shown in figure 9.14.

Mean and rms profiles of the velocity and temperature agree very well with the reference DNS data of [109]. This establishes the validity of the present DNS and confirms that the numerical method applied is appropriate to describe thermo-fluid processes inside the heated channel flow configuration. The generated dataset can be therefore used for the evaluation of the subgrid-scale modeling approach for entropy production rates.

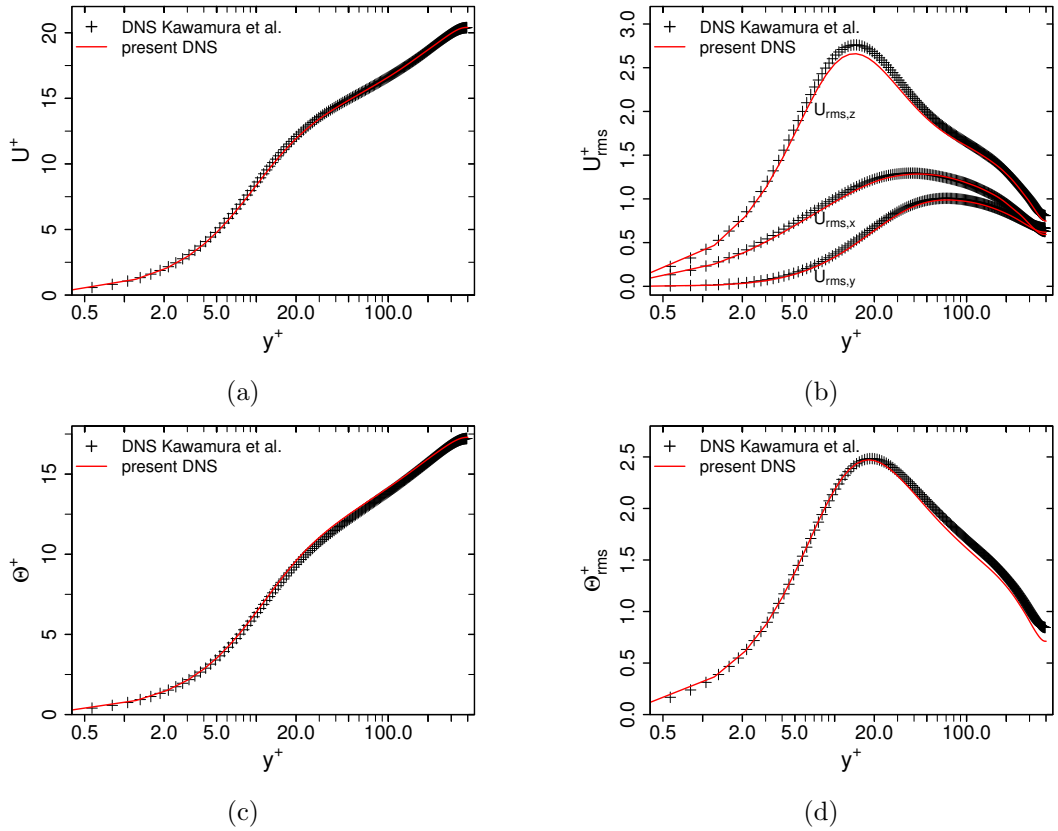

Figure 9.14: Mean (a), (c) and rms (b), (d) velocities and temperature as a function of the non-dimensional wall distance y^+. Comparison of results from the present DNS with the reference DNS dataset of Kawamura et al. [109].

9.3.1 Numerical setup

A systematic grid refinement study consisting of four numerical grids with different spatial resolutions has been conducted to analyze the reliability and prediction accuracy of the subgrid-scale modeling approach for entropy production rates in the context of LES. The same numerical grids employed in the evaluation study of the subgrid-scale heat flux models are also used here. Characteristic quantities of the numerical grids can be found in table 9.3.

Regarding subgrid-scale modeling of momentum and heat transport, the σ-k_{sgs}-equation model and the explicit anisotropy resolving heat flux model are applied. The remaining numerical procedure is the same as that of the evaluation study of subgrid-scale heat flux models (see section 9.2.1).

9.3.2 Results

Figure 9.15 shows LES predictions of time-averaged entropy production rates by viscous dissipation $\langle \Pi_v \rangle$ and by heat transport $\langle \Pi_q \rangle$ in comparison with the generated DNS dataset. Thereby, $\langle \Pi_v \rangle$ is normalized by $T_\tau \nu / (\rho u_\tau^4)$ and $\langle \Pi_q \rangle$ by $2\nu T_\tau^2 \lambda / (\rho c_p Pr)$, where $T_\tau = q_w / (\rho c_p u_\tau)$ is the friction temperature and q_w the heat flux from the walls. Dashed lines in figure 9.15 denote the resolved entropy production rates by the LES ($\langle \Pi_v^{res} \rangle$ and $\langle \Pi_q^{res} \rangle$), while solid lines represent the sum of the resolved part and the subgrid-scale contribution. Notice that the results are presented in a double logarithmic scaled graph

in order to visualize the large range of entropy production rates.

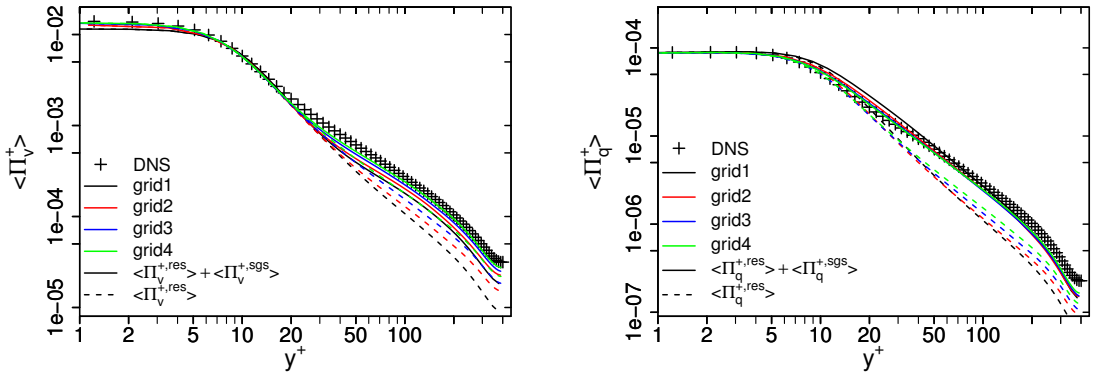

(a) (b)

Figure 9.15: Time-averaged entropy production rates by viscous dissipation (a) and heat transport (b). Comparison between DNS results and LES predictions.

Entropy generation rates are high at the viscous sublayer ($y^+ < 5$), decrease rapidly in the buffer layer ($y^+ < 30$) and they are low at the log-law region ($y^+ > 30$). This characteristic physical behavior of entropy generation in wall-bounded heated flows is well retrieved by the LES approach. Regarding the modeling of the subgrid-scale entropy production rates, it can be clearly seen that predictions of $\langle \Pi_v \rangle$ and $\langle \Pi_q \rangle$ including the subgrid scale contribution are more reliable than taking only the resolved part. Furthermore, the residual part is small in the near-wall region and increases significantly away from the wall. This seems reasonable since the near-wall region is fully-resolved in the LES simulations, thus subgrid-scale quantities vanish towards the wall. In the outer region ($y^+ > 40$) subgrid-scale entropy production rates are high, approximately of the same order than the resolved part. In this region, total entropy production rates are underestimated by the LES modeling approach, even when the residual contribution is added. Nevertheless, the overall agreement of LES predictions with the DNS data is fairly good.

Subsequently, the prediction accuracy of entropy production rates with and without adding the residual contribution is quantified by means of an error analysis in figure 9.16. Notice that in contrast to the error analyses conducted in the previous evaluation studies, the relative error is used instead of the normalized relative error due to the large range of entropy production rates within the heated channel flow.

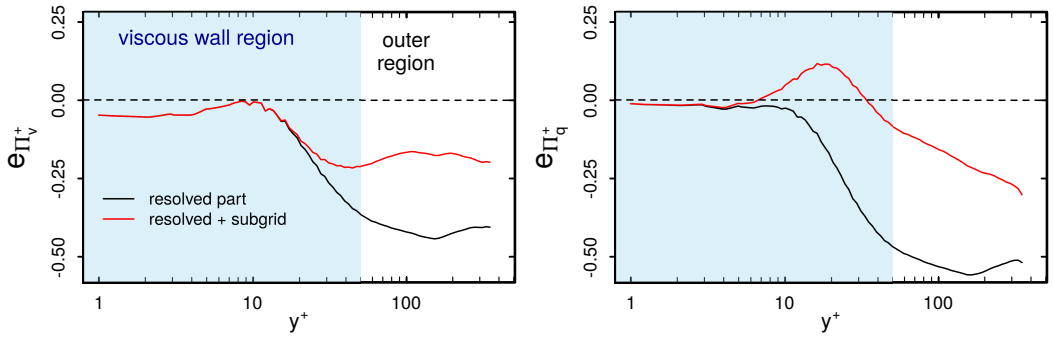

Figure 9.16: Relative error of resolved and total entropy production rates evaluated on grid no. 4 of table 9.3.

As it can be seen in figure 9.16, relative errors of predicted entropy production rates are small at the viscous wall region and increase in the outer region. Thereby, adding the subgrid-scale contribution significantly improves the prediction accuracy of entropy production rates. This holds true for both, $e_{\Pi_v^+}$ and $e_{\Pi_q^+}$, and confirms the reliability of the present modeling approach. It is important to mention in this context that the contribution of entropy production in the near wall region is significantly higher than away from the wall. Therefore, by using wall-resolved LES, subgrid-scale entropy production does not considerably contribute to the integral entropy production in case of fully developed turbulent heated channel flow. However, as it will be shown in chapter 10 for turbulent jet flow, subgrid-scale entropy production can have a significant contribution to the integral entropy production.

9.3.3 Conclusion

When dealing with entropy production analysis in the LES framework, it turned out that entropy generation is predominantly a subgrid-scale process and therefore accurate closure approaches are of profound importance. The formulations based on inertial and inertial-convective subrange scaling as suggested in section 3.4 proved to be a promising approach for entropy analysis in LES as testified by a comparison with generated DNS data of a turbulent heated channel flow at $Re_\tau = 395$ and $Pr = 0.71$.

Chapter 10

LES with second law analysis for sub- and supercritical flows

The numerical methods and modeling approaches developed and evaluated in the previous chapters are now utilized to perform entropy production analyses for sub- and supercritical flows using LES. First, entropy generation mechanisms in supercritical fuel disintegration processes at operating conditions relevant for liquid rocket engines are analyzed. LES combined with the second law of thermodynamics is used to identify causes of irreversibilities in such technical flow applications and distinctive features of the fuel disintegration process are then characterized. Thereby, the predictive capability of the LES framework in terms of entropy generation analysis for flows with complex thermodynamic properties is evaluated. The second part of this chapter deals with irreversibilities evolving in subcritical impingement cooling arrangements. Here, LES with second law analysis is applied to identify mechanisms and geometric designs that are responsible for thermodynamic losses. In this respect, entropy generation maps for different impingement angles and Reynolds numbers are provided. It is shown that LES combined with entropy generation analysis is a useful tool to identify desirable operating conditions and designs for the efficient use of energy in such thermal devices.

10.1 Entropy generation in supercritical fuel disintegration processes

The use of fuel-oxidizer mixtures under supercritical conditions has proved to be a valuable and viable option for applications where specific impulse is a determining parameter, like in the case of liquid rocket engines [175, 149, 41]. In this aspect, liquid-oxygen-gas-hydrogen (LOX-GH) mixture is commonly employed in liquid rocket engines due to the high specific impulse that it produces. In this respect, LOX-GH injection has been extensively investigated numerically and experimentally under operating pressure which exceeds the critical pressure of both substances, while the prevailed temperature is in a range that oxygen is injected in a liquid-like condition and hydrogen being in a gas-like phase. Despite intense research activities in the last decades, there are still many phenomena that are not completely understood. However, a good knowledge of the injection phenomena in the supercritical regime is essential in order to optimize the performance of combustion in liquid rocket engines.

As pointed out by Banuti et al. [17] and others, the bulk breakup process in supercritical fuel injection is essentially a pure fluid phenomenon dictated by the disintegration of the liquid-like potential core and subsequent pseudo-boiling of the cryogenic oxidizer.

This leads researchers to investigate injection processes of solely pure substances under supercritical conditions, since such simplification reduces the complexity of experimental and/or numerical studies compared to multi-component LOX-GH injection. This also allows to identify and characterize the bulk fuel breakup process within such applications. A prominent example of a pure substance injection experiment under operation conditions relevant for liquid rocket engines is the experimental investigation of Mayer et al. [149], in which a cryogenic nitrogen jet is injected into a warm ambient nitrogen environment at supercritical pressure. Axial and radial profiles of the density are provided that allow comparison with computational models and enables a characterization of the main features of the disintegration process under such extreme operating conditions. However, due to limitations in the present measurement techniques, several aspects of the fuel disintegration process remain still unclear, even for the injection of pure substances.

This section deals with the analysis of supercritical fuel injection processes based on LES combined with the second law of thermodynamics. For this purpose, LES has been conducted for a fully developed turbulent jet of cryogenic nitrogen injected into a warm nitrogen environment. The numerical study resembles the experiment by Mayer et al. [149] in terms of geometry, thermodynamics, and hydrodynamics, but at a reduced Reynolds number of $Re = 5300$. To appraise the LES results, the generated DNS database provided in chapter 8 is utilized. The objectives of this LES study are to contribute on the understanding of fuel disintegration process under supercritical conditions and to demonstrate the applicability of entropy generation analysis in terms of LES for flows with complex thermodynamic properties.

10.1.1 Numerical setup

Similar to the DNS study described in chapter 8, a round jet of cryogenic nitrogen injected into a warm nitrogen environment at supercritical pressure is examined in the LES study. A block-structured, three-dimensional grid consisting of an injection section with a length of $2D$ and a conical part of $32D$ is employed, where D is the injection diameter. To account for the spreading of the jet, the extent of the conical part is increased gradually from $5D$ at the injection up to $18D$ at the outlet. Three different numerical grids with moderate spatial resolutions of approximately 0.2, 0.5 and 1 million control volumes are considered in the present LES study. Figure 10.1 illustrates the numerical grid. Characteristic properties of the numerical grids are summarized in table 10.1.

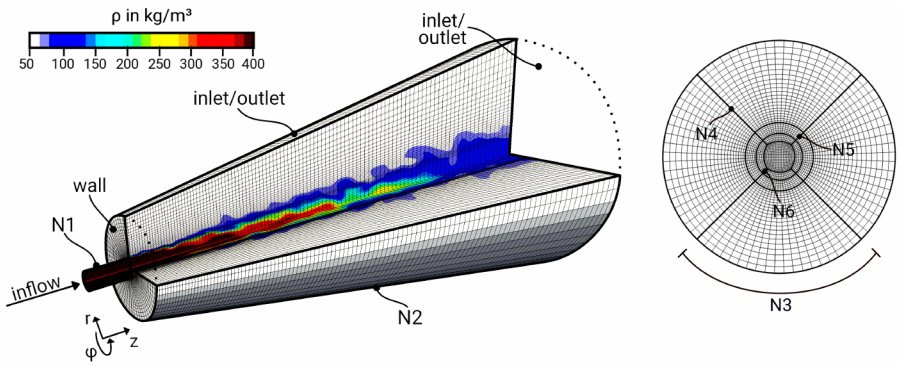

Figure 10.1: Computational domain and numerical grid of the LES of nitrogen injection at supercritical conditions. $N1$-$N6$ represents the number of grid points.

	N	$N1$	$N2$	$N3$	$N4$	$N5$	$N6$
Grid 1	218008	23	110	15	20	5	8
Grid 2	514292	30	143	20	26	5	9
Grid 3	1056768	38	179	25	33	5	13

Table 10.1: Numerical resolution of the LES studies of the cryogenic nitrogen injection. N: total number of cells; N_i: cells along i=1,2,3,...

The present low Mach number approach is utilized in the LES calculations. Thereby, the WALE model and the linear eddy diffusivity model with $Pr_{sgs} = 1$ is applied. Regarding inflow data and boundary conditions, the same approach as used in the DNS study is employed. Further details on the test case and numerical setup can be found in section 8.2.

10.1.2 Results

The evolution of injected cryogenic nitrogen into warm nitrogen environment under supercritical conditions is examined now using LES. Thereby, comparisons with the generated DNS database (see chapter 8) will be made in order to appraise the LES predictions along with the predictive capability of LES in the case of entropy production analysis. At first, turbulent flow and thermal properties related to the disintegration process are analyzed. Then, entropy generation within such supercritical injections are investigated.

Turbulent flow and thermal properties

Figure 10.2 depicts instantaneous fields of mass density (a) and compressibility factor (b) at mid-plane section of the supercritical jet. LES results of the finest grid resolution (grid 3 in table 10.1) are shown.

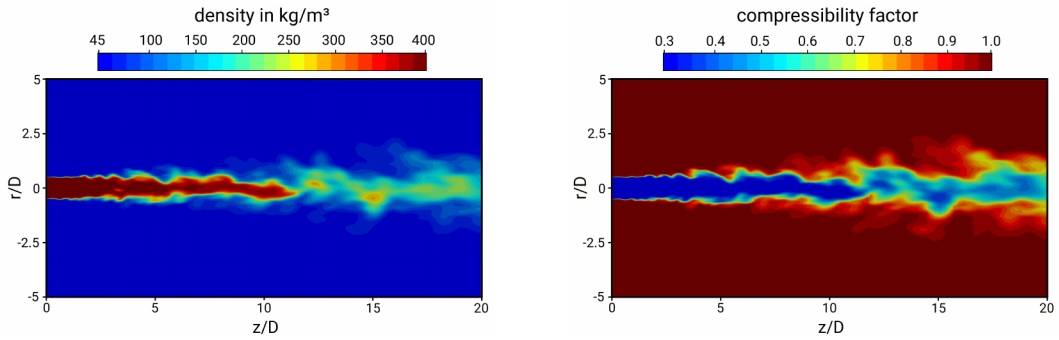

(a) (b)

Figure 10.2: Instantaneous fields of mass density (a) and compressibility factor (b) at mid-plane section of the jet. LES result using grid 3 (see table 10.1).

By examining the density variation within the supercritical injection process, it can be seen that the liquid-like core of the jet remains nearly unchanged up to $z/D \approx 5$. Then, instabilities occur and dense pockets of nitrogen are separated from the potential core. These dense pockets are carried away by the flow and dissolve downstream while pseudo-boiling and turbulent mixing takes place. Regarding real gas effects, values of the compressibility factor are small around the jet's core and approximately one in the

remaining part. This suggests that only the inner core of the jet is dominated by real gas effects, while the fluid in the outer region behaves similar to an ideal gas.

Figure 10.3 shows variations of the mean (a) and rms (b) density along the centerline in comparison with the experimental data of Mayer et al. [149] and the generated DNS dataset. In order to examine the grid sensibility of the LES, results are depicted for all three different spatial resolutions (see table 10.1).

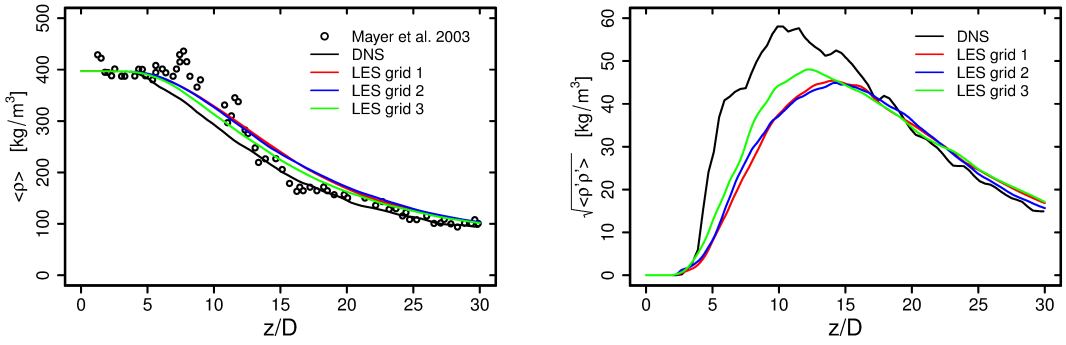

(a) (b)

Figure 10.3: Variation of mean (a) and rms density (b) along the centerline of the jet. Comparison of LES results with the present DNS and experimental data of Mayer et al. [149].

The density is nearly constant along the centerline up to $z/D < 5$, decreases rapidly while the jet breaks up and finally reaches approximately the value of gas-like state (see figure 10.3 (a)). LES results are fairly close to the DNS and experimental data, however it can be seen that the jet breakup is delayed in the case of LES compared to the DNS results. Regarding the variation of rms density along the centerline (see figure 10.3 (b)), results are more affected by the spatial resolution, in particular at the disintegration region ($5 < z/D < 15$), where the rms density is underestimated by the LES. Nevertheless, the characteristic fuel disintegration and mixing processes are clearly retrieved by the LES, even with the relatively moderate mesh size. The LES can be therefore used for further investigations of entropy generation mechanisms.

Entropy generation analysis

The entropy production mechanisms are now analyzed in order to identify causes of irreversibilities within the injection process and to assess the reliability of the present LES framework in terms of entropy generation analysis. For this purpose, figure 10.4 depicts instances of predicted Favre-averaged entropy production rates by viscous dissipation (a) and by heat transport (b) at mid-plane section of the jet. Here, the sum of resolved and subgrid-scale entropy production rates are shown.

Due to the extreme thermodynamic conditions, it appears that entropy is predominantly generated by heat transport including supercritical state transition rather than by viscous dissipation. Highest entropy production rates can be found at the mixing layer between the liquid-like cold jet and gas-like surrounding fluid. This seems reasonable because of the extreme non-uniformity of the velocity and temperature fields resulting in steep gradients, especially at the mixing layer. In contrast, entropy generation is small at the potential core of the jet, in particular for entropy production by heat transport due to the absence of temperature gradients. Both, intense entropy generation around the mixing

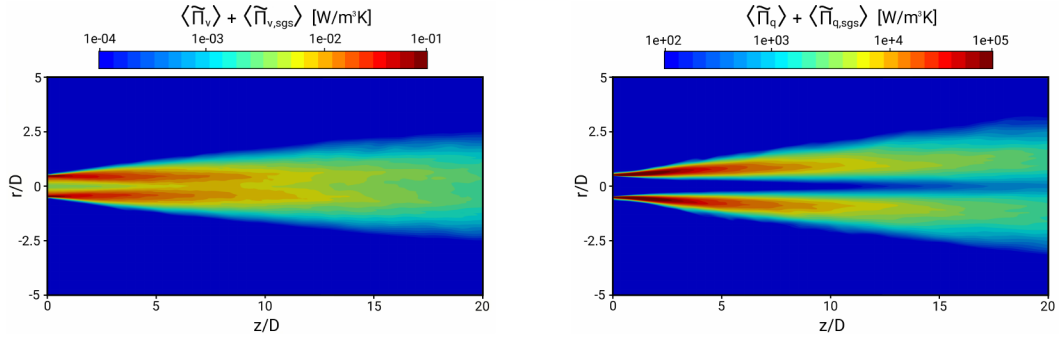

(a) (b)

Figure 10.4: LES results of entropy generation rates by viscous dissipation (a) and heat transport (b). Results are shown for the sum of resolved entropy production rates and subgrid contribution for "Grid 3" (see table 10.1).

layer and small production rates at the jets core are well reproduced by the LES (see the representative instantaneous DNS results in figure 8.13).

In order to characterize the supercritical disintegration process and to appraise the predictive capability of LES in terms of entropy generation analysis, entropy production rates along the centerline of the jet are examined in figure 10.5 compared to the generated DNS dataset. Dashed lines represent resolved entropy production rates, while solid lines are the sum of resolved and subgrid-scale contributions.

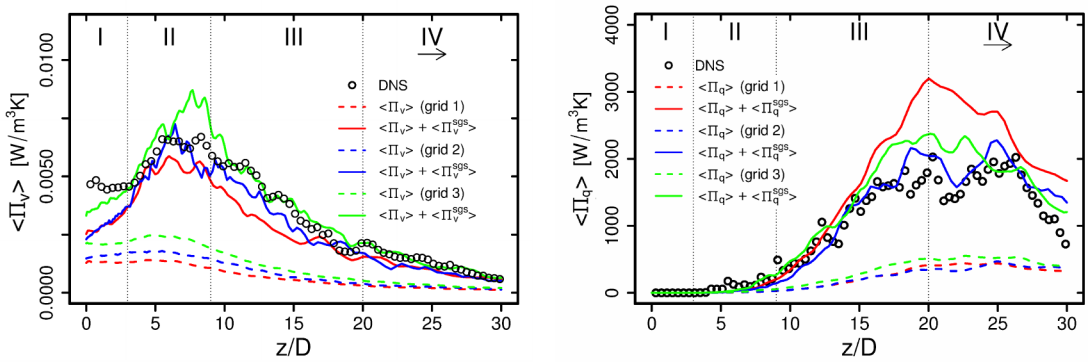

(a) (b)

Figure 10.5: Comparison of LES results with DNS data of entropy generation rate by viscous dissipation (a) and heat transport (b) along the centerline of the jet.

Four main stages are obvious from the observation of predicted entropy production rates in figure 10.5. According to the DNS findings, close to the injection (stage I), $\langle \Pi_q \rangle$ is zero due to the absence of temperature gradients, while values of $\langle \Pi_v \rangle$ are relatively high because of intense turbulent mixing. In stage II, pockets of liquid-like nitrogen are separated from the potential core. Thereby, additional shearing and temperature gradients are induced, consequently $\langle \Pi_v \rangle$ and $\langle \Pi_q \rangle$ increases. Then, in stage III, dense pockets of nitrogen smear out and supercritical state transition takes place. Thereby, most of the absorbed heat is used to overcome intermolecular attraction and $\langle \Pi_q \rangle$ increases rapidly, while at the same time shearing is reduced and $\langle \Pi_v \rangle$ decreases. Finally, in stage IV, most of the liquid-like nitrogen is pseudo-evaporated and the entropy generation is dominated by turbulent mixing. Thereby, $\langle \Pi_q \rangle$ decreases rapidly while $\langle \Pi_v \rangle$ declines slowly.

It can be seen in figure 10.5 that entropy generation is predominantly a subgrid-scale process, for which the resolved contribution is relatively small. Therefore, accurate closure approaches are of profound importance. Even though the amount of subgrid-scale modeling is high, results obtained by the closure approaches proposed in section 3.4 are very close to the generated DNS data. This holds true for both, entropy production by viscous dissipation and by heat transport. Therefore, it can be concluded that the formulations based on inertial-convective subrange scaling proved to be a promising approach for entropy production analysis in LES not only for simple flow configurations like turbulent channel flow (see section 9.3) but also for flows with complex thermodynamic properties like supercritical flows.

10.1.3 Conclusion

LES with second law analysis of cryogenic nitrogen injection under supercritical conditions at moderate Reynolds number has been conducted. Several distinctive features of the disintegration process has been identified and the predictive capability of LES in terms of entropy production analysis has been evaluated. Thereby, it turned out that:

(1) The compressibility factor are small around the jet's core and approximately one in the remaining part. This suggests that only the jet's core is dominated by real gas effects, while the fluid behaves similar to an ideal gas in the remaining part.

(2) By examining the entropy production, four main stages of the jet disintegration process have been clearly identified, namely the potential core, the shear-dominated process, the so-called pseudo-boiling stage and the turbulent mixing stage. This is in good agreement with the DNS findings in section 9.3.

(3) In dealing with entropy production analysis in the LES framework, it turned out that entropy generation is predominantly a subgrid-scale process and therefore accurate closure approaches are of profound importance. The formulations based on inertial-convective range scaling as proposed in section 3.4 proved to be a promising approach for entropy generation analysis in LES not only for simple flows but also for those with complex thermodynamic properties like supercritical flows as shown by comparison with DNS data.

10.2 Irreversibilities in subcritical impingement cooling arrangements

Impingement cooling has been widely used as means of heat transfer equipment in a variety of engineering application like cooling of gas turbine blades, electronic components or quenching of metals and glass, because it provides a very effective and flexible way to transfer thermal energy between a target surface and coolant fluid. Compared to conventional flow arrangements like free wall-parallel flows, impinging cooling enables up to threefold higher heat transfer coefficients at a given maximum flow speed [257]. Given their practical relevance, several jet geometries and flow conditions were examined, like nozzle shapes, Reynolds number effects, the influence of jet-to-plate spacing, jet impingement angle and many more. From the gained insights, various empirical correlations for the practical use of impinging flows were derived. Reviews of experimental studies, numerical modeling, general uses and performance of impinging jets can be found in [257, 258, 141, 98, 236].

Despite the significant progress towards a better understanding of the physics and applicability of impingement cooling, an optimal thermodynamic design of such thermal devices is difficult to find due to the large number of operating parameters. Furthermore, characterized by strong flow/wall interaction processes, impingement cooling features very complex heat and fluid flow dynamics with interlinked effects including stagnation points, shear flow boundary layers, strong streamline curvatures and anomalies in the distribution of Nusselt number. These complex thermal transport and fluid flow processes makes an analysis based on entropy production well suited to provide not only a deeper insight into the complex physical mechanisms of impingement cooling but also to localize possible irreversibilities within such thermal devices. An entropy production analysis can be therefore useful to identify favorable operating conditions and conceptual designs for the efficient use of energy in impingement cooling devices.

In the present study, LES combined with an entropy production analysis is used to investigate general heat and fluid flow features along with entropy generation mechanisms in a turbulent impinging jet on a heated solid surface at different inclination angles. The influence of the Reynolds number on the thermodynamic performance of the impinging cooling is also analyzed for jet Reynolds numbers of $Re = 5000$, $Re = 10000$ and $Re = 20000$. Based on the obtained results, some important aspects for the conceptual design of efficient impingement cooling arrangements are derived.

10.2.1 Numerical setup

A schematic of the impingement cooling arrangement investigated in the LES study is provided in figure 10.6, where (a) shows the three-dimensional computational domain, (b) a slice through the numerical grid at mid-plane section, and (c) a description of the coordinate system and the inclination angle α. Notice that the origin of the introduced coordinate system (ζ, η) is located at the stagnation point S of the jet (see figure 10.6 (c)). Thus, it is located directly at the geometric origin C of the jet in the case of an inclination of $\alpha = 90°$ and shifted approximately half a diameter away from the geometric origin C towards the compression side in the case of $\alpha = 45°$. The point N in figure 10.6 (c) represents the location where the Nusselt number is maximal.

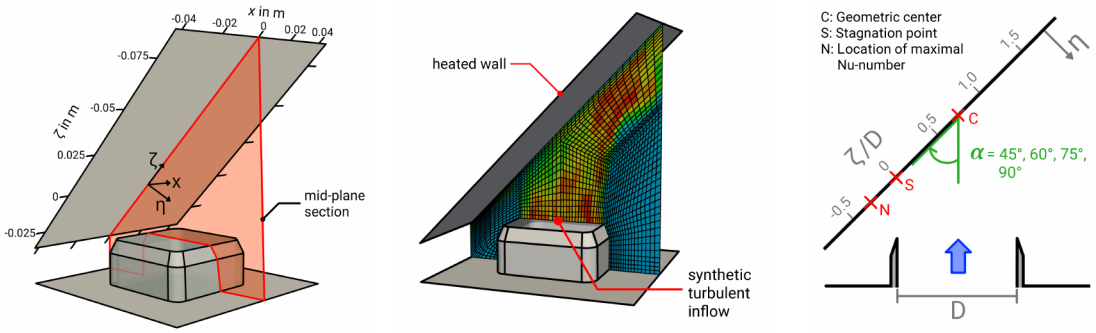

(a) (b) (c)

Figure 10.6: Computational domain (a), slice through the numerical grid at mid-plane section (b), and description of the coordinate system and inclination angle α (c) of the impinging cooling configuration. C: geometric center point of the jet; S: stagnation point; N: location of maximal Nusselt number.

In line with the DNS study described in chapter 7, a turbulent jet of dry air ($T_0 = 290K$, $p = 1atm$) leaves a square nozzle ($D = 40mm$) and impinges on a heated wall, which has

a constant wall temperature of $T_W = 330K$ and a jet-to-plate spacing of $H/D = 1$. At the impinged wall, the jet is divided into two opposed wall-jets directed outward along the solid wall and gets heated up. In contrast to the DNS study in which only an inclination angle of $\alpha = 45°$ and a Reynolds number of $Re = 5000$ is examined, different inclination angles ($\alpha = 45°, 60°, 75°, 90°$) and Reynolds numbers ($Re = 5000$, $Re = 10000$ and $Re = 20000$) are considered in the LES. Thereby, only the region after the nozzle exit section is simulated in the LES, while synthetic turbulent inflow conditions are employed at the nozzle exit section. These inflow data are generated by means of the digital filtering approach proposed by Klein et al. [114], while the mean velocity profile is taken from the DNS study. The other boundary conditions are similar to that used in the DNS study (see chapter 7).

The solution procedure for constant density flows as described in section 4.2.1 is applied in the LES calculations. Thereby, the σ-k_{sgs}-equation model and the explicit anisotropy resolving heat flux model are used for subgrid-scale closure (see sections 3.2.3 and 3.3.3). A summary of the parametric study is given in table 10.2. The quality of the numerical grids used in the LES study is judged by means of the ratio of subgrid-scale to total turbulent kinetic energy M in the entire domain. Furthermore, case 1-3 are used for a systematic grid variation study to determine the grid-sensitivity of the LES results for $\alpha = 45°$ and $Re = 5000$.

Case	α	Re	No. of cells	M
1	45°	5,000	1.0 million	0.06
2	45°	5,000	1.7 million	0.04
3	45°	5,000	3.1 million	0.03
4	60°	5,000	1.7 million	0.05
5	75°	5,000	1.7 million	0.04
6	90°	5,000	1.7 million	0.04
7	45°	10,000	3.0 million	0.04
8	60°	10,000	3.0 million	0.05
9	75°	10,000	3.0 million	0.04
10	90°	10,000	3.0 million	0.04
11	45°	20,000	4.8 million	0.05
12	60°	20,000	4.8 million	0.05
13	75°	20,000	4.8 million	0.04
14	90°	20,000	4.8 million	0.04

Table 10.2: Summary of the parametric study for the entropy production analysis in the impingement cooling device. α: inclination angle; Re: jet Reynolds number, M: subgrid-scale to total kinetic energy in the entire domain.

10.2.2 Results

In order to establish the validity of the simulations, LES predictions are first compared with the generated DNS dataset. Then, general heat and fluid flow features of the inclined impinging jet are analyzed with respect to different inclination angles and jet Reynolds numbers. Finally, the entropy generation in the impinging jet configurations is analyzed and the thermodynamic efficiency of the different arrangements are evaluated based on the method of entropy generation minimization [28].

Comparison with DNS data (cases 1-3)

Figure 10.7 shows the predicted LES mean velocity component in wall-parallel direction $\langle U_\zeta \rangle$ (a) and turbulent kinetic energy tke (b) in comparison with DNS as a function of the wall-normal direction η/D. All results are normalized by the jet's bulk velocity U_{bulk}.

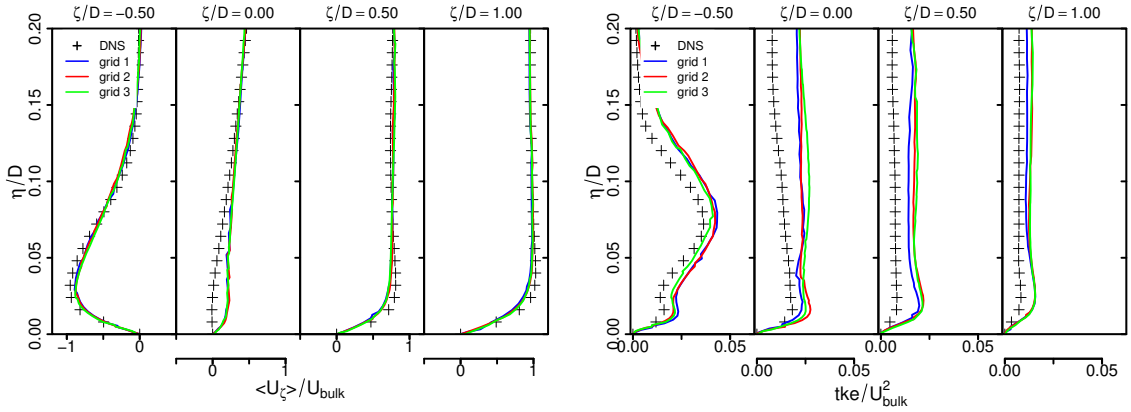

(a) (b)

Figure 10.7: Mean wall-normal velocity (a) and turbulent kinetic energy tke (b). Comparison of LES results and DNS data.

As it can be observed in figure 10.7 (a), predicted mean velocities agree well with the reference DNS with minor discrepancies at the stagnation region. Slight deviation from DNS for tke predictions can be observed, especially at the stagnation region (see figure 10.7 (b)). However, characteristic flow features of the 45°-inclined impinging jet are well reproduced by the LES. This holds true for all numerical grids under consideration and confirms that the numerical setup and spatial resolution are appropriate to describe the turbulent flow field of this configuration. A similar conclusion can be drawn for predicted mean and rms temperature profiles as depicted in figure 10.8. Here, LES predictions are very close to the reference DNS data, also at the stagnation region.

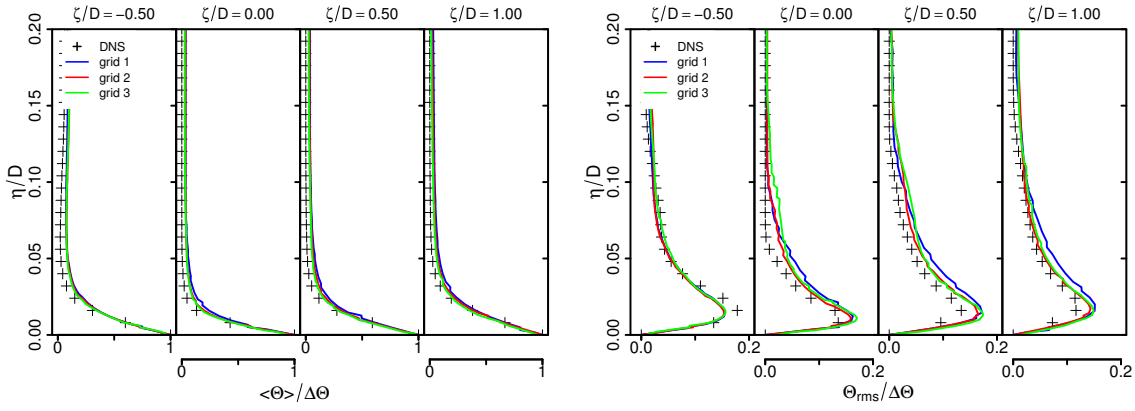

(a) (b)

Figure 10.8: Mean (a) and rms (b) temperature profiles in the near-wall region of the 45°-inclined impinging jet on a heated plate. Comparison of LES results and DNS data.

Finally, predicted time-averaged entropy production rates by viscous dissipation $\langle \Pi_v \rangle$ and heat transport $\langle \Pi_q \rangle$ are compared with the generated DNS dataset in figure 10.9.

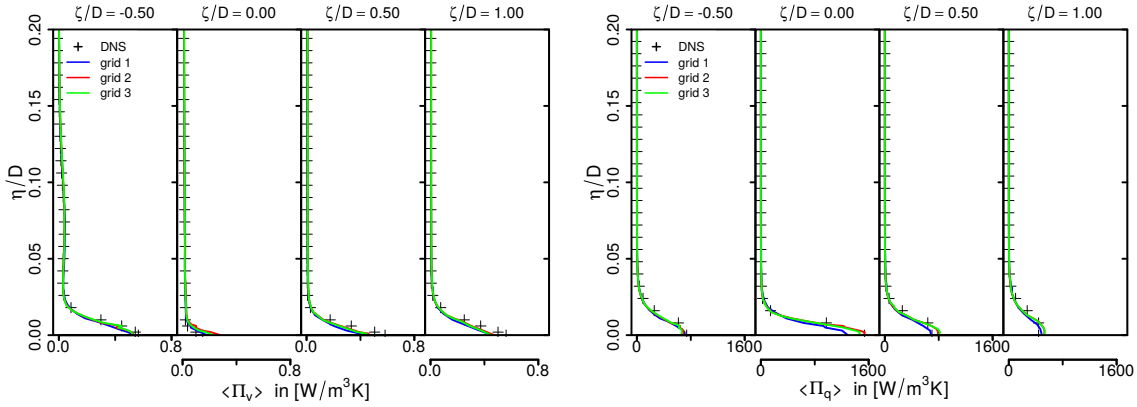

(a) (b)

Figure 10.9: Time-averaged entropy production rates by viscous dissipation (a) and heat transport (b). Comparison of LES predictions and DNS data.

Entropy production is high at the near-wall region and decreases rapidly away from the wall. Thereby, entropy is predominantly generated by heat transport rather than viscous dissipation, in particular at the stagnation region. This behavior is well reproduced by the LES, even for the coarsest grid. Furthermore, LES predictions are very close to the DNS data, which establishes the predictive capability of the present LES framework in terms of entropy production. It can be therefore used for further investigations of different inclination angles and Reynolds numbers in the inclined impinging jet configuration.

Influence of the Reynolds number and inclination angle (cases 3-10)

After establishing the validity of the LES, the influence of the inclination angle and Reynolds number on thermal and fluid flow properties is analyzed now. For this purpose, figure 10.10 shows the time-averaged velocity magnitude field at mid-plane section of the jet. Black solid lines represent streamlines of the mean flow field, S the stagnation point, N the location of maximum Nusselt number and C the geometric center of the jet. Results are exemplarily shown for a jet Reynolds number of $Re = 5000$ (cases 3-6).

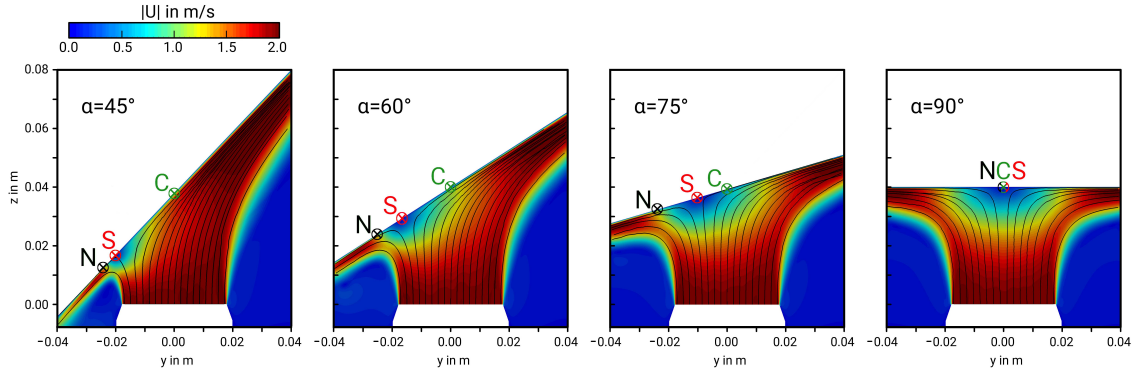

Figure 10.10: Mean velocity field at mid-plane section of the impinging jet for different inclination angles α. S: stagnation point; N: location of maximal Nusselt number; C: geometric center of the jet. (for $Re = 5000$).

It can be clearly seen in figure 10.10 that the stagnation point S becomes shifted towards the compression side with decreasing inclination angle α. Thereby, streamlines

are highly curved, especially at the location where the opposed wall-jets begin to form. In this respect, it is interesting to observe that the heat transfer is most intense at the opposed wall-jet region at the compression side, except in the case of $\alpha = 90°$. Here, the stagnation point S and the location of maximal heat transfer N coincide at the same point. These anomalies of the stagnation point and peak Nusselt number are quantified in figure 10.11, which depicts the displacement distance between the stagnation point and the geometric center of the jet $\overline{SC}$ (a), and between the stagnation point and the location of maximal Nusselt number $\overline{SN}$ (b) as a function of α and Re.

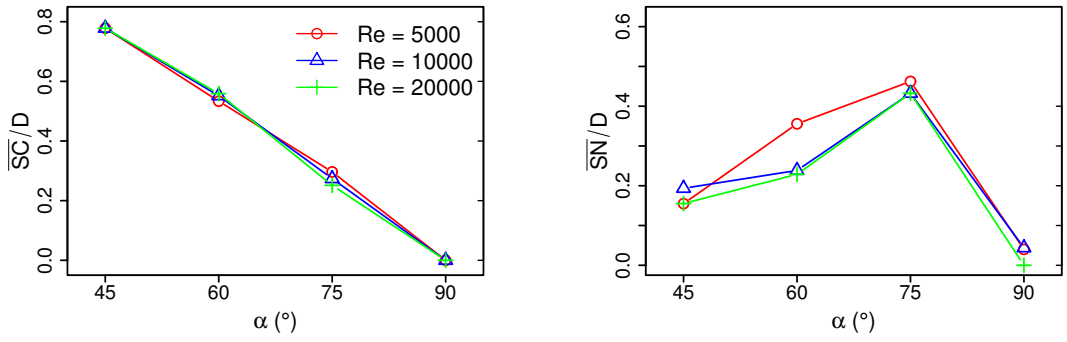

(a) (b)

Figure 10.11: Displacement distance between (a) stagnation point and geometric center of the jet $\overline{SC}$, and (b) between stagnation point and location of maximal Nusselt number $\overline{SN}$ as a function of inclination angle α for $Re = 5000$, $Re = 10000$ and $Re = 20000$.

As expected, $\overline{SC}$ decreases linearly with increasing inclination angle and is zero for $\alpha = 90°$. In contrast, the displacement $\overline{SN}$ is maximal for $\alpha = 75°$ and decreases with decreasing inclination angle. For $\alpha = 90°$, the maximal Nusselt number occurs exactly at the stagnation point. This characteristic behavior of $\overline{SC}$ and $\overline{SN}$ is independent of the Reynolds number and predominantly caused by geometric constraints rather than turbulence dynamics.

In order to quantify the interaction between the turbulent jet and the impinged wall, figure 10.12 shows mean and maximal wall shear stresses for different inclination angles and Reynolds numbers. Values are non-dimensionalized by the bulk velocity of the jet.

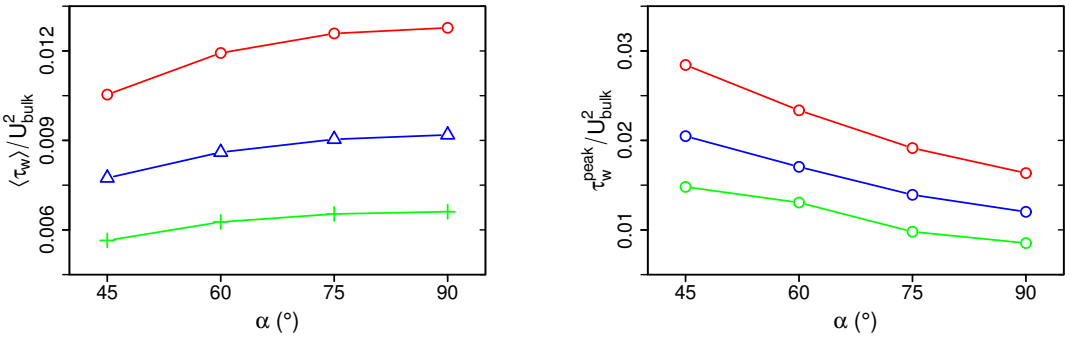

(a) (b)

Figure 10.12: Mean (a) and maximal (b) wall shear stresses at the impinged wall for different inclination angles and Reynolds numbers.

The mean wall shear stress $\langle \tau_w \rangle$ averaged over the impinged wall is highest in the 90°-configuration and decreases with decreasing inclination angle (see figure 10.12 (a)). In contrast, the peak value of τ_w appears highest in the 45°-configuration and decreases with increasing inclination α (see figure 10.12 (a)). The peak value in the wall shear stress is predominantly concentrated at the opposed wall-jet on the compression side of the impinged wall, where the flow direction changes suddenly and the fluid is subject to a strong acceleration in wall-parallel direction. Furthermore, in analogy to the skin-friction coefficient in pipe or channel flows, non-dimensional values of τ_w decrease with increasing Reynolds number, which holds true for mean and maximal values of τ_w. Thereby, non-dimensional values of τ_w are approximately five times higher in the impinging jet configuration than skin friction coefficients found in pipe or channel flows with similar Reynolds numbers (for comparison see [189]).

It appears that flow/wall interaction dynamics are strong in the inclined impinging jet configuration, in particular at the wall-jet region on the compression side of the impinged wall. The influence on the heat transfer is examined in figure 10.13, which depicts mean (a) and maximal (b) values of the Nusselt number at the impinged wall as a function of inclination angle α for $Re = 5000$, $Re = 10000$ and $Re = 20000$.

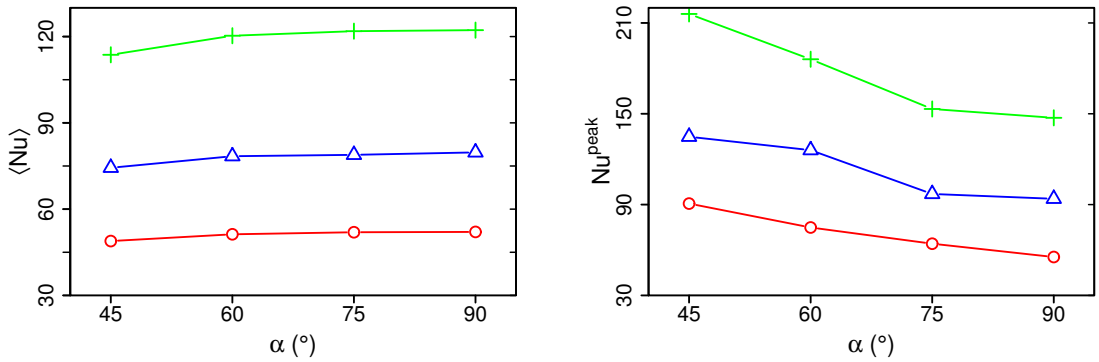

(a) (b)

Figure 10.13: Mean (a) and maximal (b) Nusselt numbers at the impinged wall for different inclination angles and Reynolds numbers.

In analogy to wall shear stresses, the mean Nusselt number averaged over the impinged wall decreases with decreasing inclination angle α (see figure 10.13 (a)), while the peak Nu number decreases with increasing α (see figure 10.13 (b)). Additionally, it can be seen that Nusselt numbers at $Re = 20000$ are significantly higher than values at $Re = 5000$. By using the empirical correlation of Dittus and Boetler for forced convection in turbulent pipe flow [95] ($Nu = 18.26$), it appears that the impinging jet configuration enables approximately three times higher Nusselt numbers for the same Reynolds number. This establishes the high efficiency of impinging cooling arrangement to transfer thermal energy between a heated surface and a coolant fluid.

Second law analysis (cases 3-10)

As an effective cooling device, the impingement cooling arrangement should provide a high heat transfer performance and small friction loss in order to use the available energy efficiently. However, the heat transfer enhancement in thermal devices is usually associated with an increase of friction loss, which is also the case in the impingement cooling

arrangements as determined before (compare figure 10.12 and 10.13). Therefore, to find an optimal trade-off between heat transfer enhancement and friction loss by selecting the best flow conditions and impingement configuration is a challenging task. In this respect, the significance of both, heat transfer enhancement and friction loss, can be evaluated by means of entropy generation of the respective impingement setup with smallest entropy generation in the thermodynamic optimal design.

For a proper evaluation of the different impingement setups, the external wall heat flux at the impinged wall and the heat transfer area should be fixed in the entropy generation analysis in order to obtain the general performance of the system independent of the boundary conditions. Instead of a fixed wall temperature, a constant heat flux of $\dot{q}_w = 1000W/m^2$ is used in the present study for all cases. This value is selected based on the averaged heat flux obtained in the DNS study for an inclination angle of 45°. The resulting time-averaged entropy generation maps related to viscous dissipation (a) and heat transport (b) are depicted in figure 10.14 for a jet Reynolds number of $Re = 5000$.

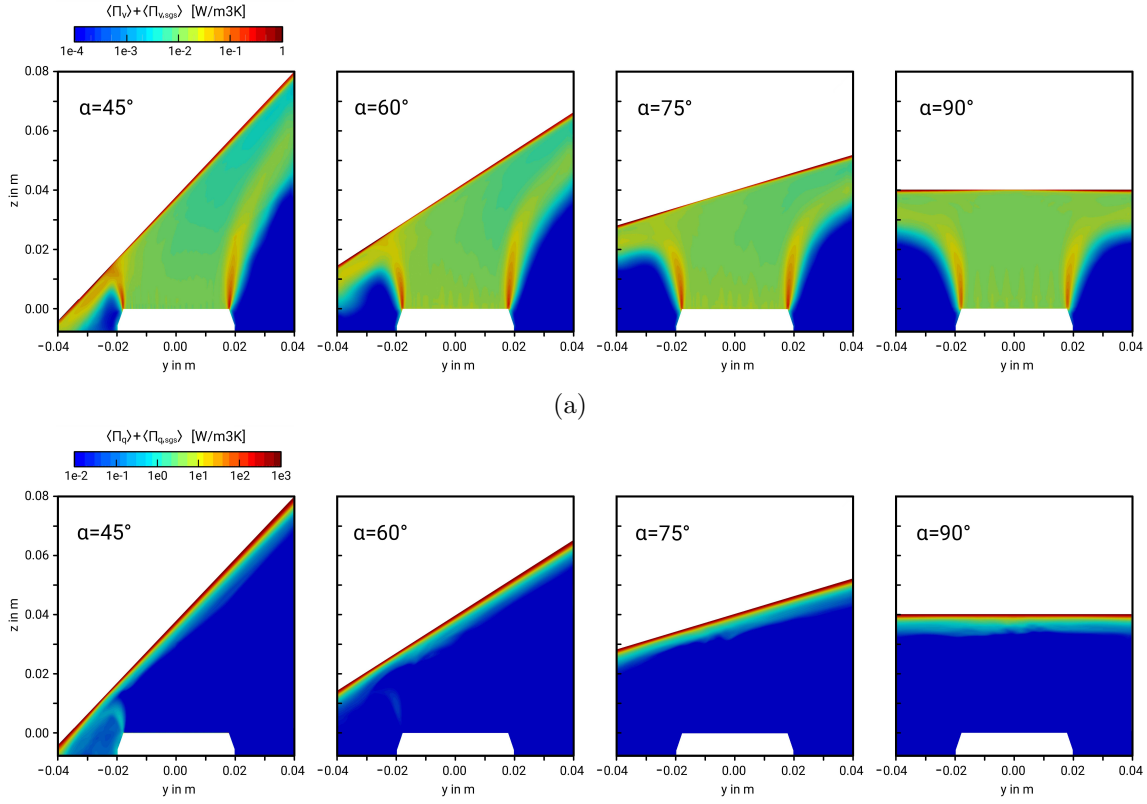

Figure 10.14: Predicted entropy generation maps related to viscous dissipation (a) and heat transport (b). Results are shown for the sum of resolved entropy production rates and subgrid contribution.

Regarding friction losses (see figure 10.14 (a)), entropy is primarily produced at the shear layer of the jet and in the vicinity of the impinged wall due to steep velocity gradients. Furthermore, entropy generation rates related to viscous dissipation are also high at the opposed wall-jet region on the compression side of the impinging jet. This can be attributed to the sudden change in the flow direction and the strong acceleration of the fluid in wall-parallel direction in this region, which lead to intense shearing and an increase

in the entropy production. In contrast, entropy generation related to heat transport is predominantly concentrated at the near-wall region (see figure 10.14 (b)), where temperature gradients are high. Moreover, by comparing figures 10.14 (a) and (b), it appears that entropy is predominantly generated by heat transport rather than viscous dissipation for the present impingement cooling setup.

Once the main sources of irreversibilities evolving in the impingement cooling arrangements have been identified, the amount of exergy loss is then quantify in order to identify the thermodynamic optimal impingement design. For this purpose, figure 10.15 shows the entropy generation numbers of friction loss N_v and heat transport N_q. They are defined as [28]

$$N_v = \frac{\int_V \left(\langle \Pi_v \rangle + \langle \Pi_v^{sgs} \rangle\right) dV}{\dot{Q}_w / T_0}, \tag{10.1}$$

$$N_q = \frac{\int_V \left(\langle \Pi_q \rangle + \langle \Pi_q^{sgs} \rangle\right) dV}{\dot{Q}_w / T_0}, \tag{10.2}$$

where V is the volume of the impingement cooling system, $\dot{Q}_w$ the thermal power introduced into the system and T_0 the inflow temperature of the jet. N_v and N_q represent essentially the ratio of the lost exergy divided by the total exergy introduced into the system [28].

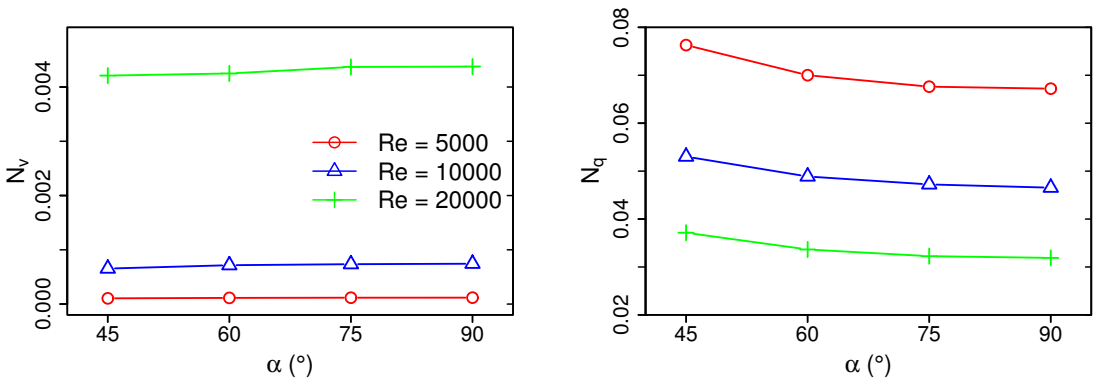

(a) (b)

Figure 10.15: Entropy generation numbers of friction loss (a) and heat transport (b) as a function of inclination angle α for $Re = 5000$, $Re = 10000$ and $Re = 20000$.

As it can be seen in figure 10.15 (a), friction losses increase slightly with increasing inclination angle α and are highest in the 90°-configuration. Friction losses are more significant for higher Reynolds number, which is approximately 40 times higher for $Re = 20000$ than in the case of $Re = 5000$. Nevertheless, the exergy loss caused by viscous dissipation appears relatively small compared to the loss by heat transport, which is about one order of magnitude larger for the selected operating conditions (see figure 10.15 (b)). Thereby, a minimum in N_q can be observed for the 90°-configuration, which is attributed to the higher heat transfer coefficients of this configuration (see figure 10.15 (a)) resulting in milder temperature gradients in the flow field. Furthermore, it can be clearly seen that increasing the Reynolds number enhances the heat transfer considerably without producing irreversibilites in the heat transport. Therefore, it can be concluded that a 90°-configuration is most effective in terms of heat transfer. Moreover, an increase in Reynolds number not only intensifies the heat transfer, but also increase friction losses.

Finally, the total thermodynamic efficiency of the different impingement setups is determined. For this purpose, the total entropy generation number is introduced, which is defined as the sum of exergy losses by viscous dissipation and heat transport $N_{tot} = N_q + N_v$. Figure 10.16 depicts the total exergy loss of the impingement cooling devices as a function of inclination angle and Reynolds number.

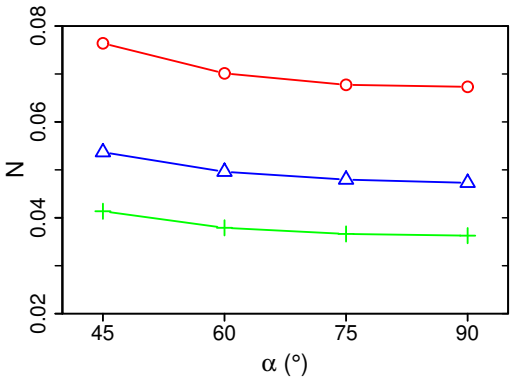

Figure 10.16: Total entropy generation number as a function of inclination angle α for $Re = 5000$, $Re = 10000$ and $Re = 20000$.

For the present operating conditions, figure 10.16 clearly shows that the $\alpha = 90°$ configuration is the thermodynamically optimal setup with the lowest value of N_{tot} of all configurations under consideration. Therefore, it allows the most efficient use of energy in the impingement cooling device. In this respect, it is further observed that the overall efficiency can be significantly improved by increasing the Reynolds number from $Re = 5000$ to $Re = 20000$. However, the analysis of the frictional exergy losses in figure 10.15 suggests that there is still scope for further improvement at higher Reynolds numbers.

10.2.3 Conclusion

LES with second law analysis is used to investigate general heat and fluid flow features along with entropy production mechanisms of a turbulent impingement cooling system. Based on this, the influences of impingement angle and Reynolds number on the thermodynamic performance of the system are analyzed.

Some important observations from this LES study concerning LES modeling of entropy generation, flow characteristics in impinging flows, causes of irreversibilities and optimal thermodynamic design of impingement cooling devices can be outlined as following:

(1) The present LES framework combined with the improved subgrid-scale models and entropy production closure formulations enables an accurate description of turbulent heat transfer and irreversibilities in impingement cooling devices (testified by comparison with DNS data).

(2) Examining general heat and fluid flow properties, it appears that the location of the stagnation point and maximal Nusselt number differs in the case of inclination angles except $\alpha = 90°$. Both are shifted towards the compression side of the impinging jet with decreasing inclination angle. Only in the case of $\alpha = 90°$, the stagnation point and the location of maximal heat transfer coincide at the same point.

(3) Impinging flows are characterized by strong flow/wall interaction processes. Thereby, wall shear stress averaged over the impinged wall are high in the 90°-configuration

and decreases with decreasing inclination angle α. In contrast, peak wall shear stress appears highest in the 45°-configuration and decreases with increasing α.

(4) In analogy to wall shear stresses, the mean Nusselt number averaged over the impinged wall decreases with decreasing inclination, while the peak Nu number increases with decreasing α. Highest mean Nusselt numbers are observed for an inclination angle of 90°, that are approximately three times higher than in pipe or channel flows with similar operating conditions.

(5) Entropy is primarily produced by heat transport processes rather than viscous dissipation in the present impingement cooling devices. In particular the impinged wall acts as a strong source of irreversibility.

(6) Regarding the optimal design of impingement cooling devices, this LES study suggests that an inclination angle of 90° allows the most efficient use of energy in such thermal devices. Furthermore, increasing the Reynolds number intensifies the heat transfer and increases the second law efficiency of the system. Thereby, the thermal efficiency enhancement can overwhelm the frictional exergy losses.

PART V: SUMMARY AND OUTLOOK

Chapter 11

Summary and outlook

With continually increasing computational resources, LES based numerical approaches are becoming more and more common in both academic research and industrial practice by demonstrating the capability and prediction accuracy of this technique for unsteady turbulent heat and fluid flow problems. LES provides inherent advantages compared to conventional Reynolds averaged approaches, especially in dealing with flows with large scale, unsteady characteristics. However, despite the great potential of LES, the extent of its usage for entropy generation analysis has been insignificant and unsatisfactory. This can be attributed mainly due to the challenges in modeling of the unresolved irreversibilities in the subgrid. From an engineering perspective, LES combined with second law analysis can be a very useful tool to identify advantageous operating conditions and designs for the efficient use of energy in many engineering and industrial applications. This motivates the present work, which is focused on the development of a reliable LES framework combined with the second law of thermodynamics that allows to characterize and optimize sub- and supercritical wall-bounded flow applications. This goal is progressively accomplished in a series of development stages.

In the very first stage, reliable numerical treatments have been developed to simulate turbulent heat and fluid flow as part of this project. It is based on the open source CFD code OpenFOAM with a second-order finite volume discretization procedure. Appropriate pressure-correction methods to solve incompressible flows with constant and variable physical properties have been added to the OpenFOAM framework and verified in full generality using the method of manufactured solutions. In this respect, it is shown that the source code is free of programming errors, which is an essential step in the development of reliable simulation software. Thereafter, benchmark test cases have been conducted to evaluate the applicability of the present numerical approach to handle turbulent flow situations with strongly varying physical properties as it is often encountered in supercritical flow applications. In contrast to the standard methods available in OpenFOAM, it turned out that the proposed numerical approach is able to handle such flow situations along with improvements in the computational efficiency and numerical stability. Finally, in order to establish the validity of the present numerical approach, several validation cases have been simulated, namely, a DNS study of a turbulent channel flow with passive heat transport, a DNS study of a strongly heated turbulent air flow in a vertical pipe, and a LES study of heated carbon dioxide flow in an annulus at supercritical conditions. Based on a comparison with experimental and DNS data from the literature, it turned out that the present numerical approach is well suited for DNS and LES of turbulent wall-bounded flows with heat transport under sub- and supercritical conditions.

The next development stage is dedicated towards the development of accurate and consistent closure models for the momentum transport, heat transport and entropy generation in the subgrid. In particular, a wall-adapting one-equation subgrid-scale kinetic energy model has been proposed, which provides the correct asymptotic behavior in the near-wall region without using any ad-hoc or dynamic procedure. Regarding the closure of the subgrid-scale heat flux, a thermodynamic consistent anisotropic heat flux model suitable for wall-bounded turbulent heat transport has been derived. It is based on the second law of thermodynamics in conjunction with the invariant theory, such that the irreversibility requirements of the second law are automatically fulfilled. Similar to the wall-adapting one-equation model, the proposed anisotropic heat flux model requires no ad-hoc or dynamic procedure to provide a proper near-wall behavior. Finally, based on the inertial-convective subrange theory, appropriate closure terms for the subgrid-scale entropy generation related to friction loss and heat transport have been provided. Since entropy generation is directly linked to the dissipation of energy and therefore predominantly a subgrid-scale process, such subgrid-scale closure model are essential for entropy generation analysis. The proposed subgrid-scale models are proven to be a promising approach for LES of wall-bounded turbulent heat and fluid flows as shown by a systematic comparison of LES predictions with DNS results of generic flow configurations.

In order to testify as an engineering tool, the proposed LES framework has to be evaluated for realistic flow situations with complex thermodynamic properties in the next stage. In this respect, it is worth mentioning that reliable reference data from the literature regarding entropy generation in complex flows were not available. Therefore, comprehensive DNS databases have been generated to close this gap in the literature and to allow an evaluation of the present approach under more complex flow situations. Two specific applications of practical relevance were selected in the DNS studies, namely, an impingement cooling device and supercritical injection of cryogenic nitrogen into warm nitrogen environment. Thereby, distinctive flow features of both applications have been analyzed and comprehensive databases of thermal and fluid flow properties as well as entropy generation have been provided. It is found in the DNS study of the impingement cooling that such flow arrangements feature very complex heat and fluid dynamics with strong flow/wall interaction processes, that are essentially irreversible. In particular the heated wall acts as a strong source of irreversibility and its design is especially important for efficient use of energy in such thermal devices. In the DNS study of supercritical nitrogen injection, entropy production analysis along the centerline of the jet allows to distinguish four characteristic stages of the disintegration process under supercritical conditions, namely, the potential core stage, a shear-dominated stage, a pseudo-boiling stage and a turbulent mixing stage.

Finally, in the last development stage, the LES framework has been utilized to characterize supercritical injection processes and to optimize impingement cooling devices under realistic operating and flow conditions. The objectives of the first LES study are to contribute to the understanding of fuel disintegration processes under supercritical conditions and to evaluate the predictive capability of the LES framework in terms of entropy generation analysis for flows with complex thermodynamic properties. For this purpose, LES of cryogenic nitrogen injection under supercritical conditions has been conducted and results have been compared with the generated DNS dataset. Within this LES study, the four characteristic stages of the disintegration process have been clearly identified and it turned out that the proposed closure models for subgrid-scale entropy production proved to be a reliable approach for entropy generation analysis in LES for flows with complex thermodynamic properties. The second LES study deals with the thermodynamic optimization of impingement cooling devices based on the concept of entropy generation minimization.

The influence of target plate inclination and Reynolds number on the thermodynamic performance of the impingement cooling have been addressed. In this parametric study, it is shown that an inclination angle of 90° (in respect to the jet's axis) allows the most efficient use of energy in such thermal devices. Furthermore, increasing the Reynolds number intensifies the heat transfer and further increases the second law efficiency of the system. Thereby, the thermal efficiency enhancement can overwhelm the frictional exergy losses.

It is evident from the present work that LES with second law analysis is a very valuable and viable tool for predictive engineering and design optimization of complex heat and fluid flow applications. However, entropy generation analysis based on LES is still in its early stage of development and the proposed methodology can be surely extended and improved in several ways. Some recommendations for future work are therefore outlined.

- It is well known that LES has shortcomings in dealing with near-wall dominated flows unless very fine grids are used in the vicinity of the wall. Due to limited computing power, it is common practice in LES to use near-wall modeling approaches, especially in the case of high Reynolds number flows. An extension of the present methodology regarding near-wall modeling is highly recommended in order to allow second law analysis for realistic engineering applications at high Reynolds numbers. However, it requires additional closure models for the unresolved entropy production in the near-wall region which is known to be a strong source of irreversibility and therefore very important in dealing with entropy generation analysis.

- Many engineering applications involve complex physical phenomena such as multi-component mixing, chemical reactions, multi-phase flow, radiation, magnetic effects, etc.. The integration of such potential sources of irreversibilities into the entropy generation analysis would be very useful in order to characterize and optimize such complex engineering application.

- Apart from the optimization and characterization tasks, entropy generation analysis can be also used for the physical evaluation of subgrid-scale models. In this way, the thermodynamic consistency of a modeling approach can be appraised and also the capability to predict the directionality of turbulent processes. Entropy generation analysis may be therefore an useful tool for model development and evaluation.

- Finally, in order to assess the strengths and weaknesses of the proposed LES framework for entropy generation analysis, it should be applied to complex engineering application such as internal combustion engine. This specific configuration features very complex heat and fluid flow phenomena, multiphase flow, chemical reactions, multi-component mixing and many more. Beginning with motored engine operation without fuel injection towards engine operating conditions including combustion and mixture preparation allows an evaluation of the LES framework with successively increasing complexity. This can be achieved by systematic comparison with experimental and/or DNS reference data, likewise from the institute of reactive flows and diagnostics at the University of Darmstadt in the context of "Darmstadt Engine Workshop".

Bibliography

[1] K. Abe and K. Suga. Towards the deveolpment of a reynolds-averaged algebraic turbulent scalar-flux model. *Int. J. Heat Fluid Fl.*, 22:19 – 29, 2001.

[2] A.M. Abudour, S.A. Mohammad, R.L. Robinson Jr, and K.A.M Gasem. Volume-translated peng-robinson equation of state for saturated and single-phase liquid densities. *Fluid Phase Equilibr.*, 335:74–87, 2012.

[3] J. Ahn, J.L. Lee, and H.J. Sung. Direct numerical simulations of fully developed turbulent pipe flows for re_τ=180, 544 and 934. *Int. J. Heat Fluid Fl.*, 44:222–228, 2013.

[4] Y. Ahn, S.J. Bae, M. Kim, S.K. Cho, S. Baik, J.I. Lee, and J.E. Cha. Review of supercritical co_2 power cycle technology and current status of research and development. *Nucl. Eng. Technol.*, 47:647–661, 2015.

[5] AIAA. Guide: Guide for the verifiction and validation of computational fluid dynamics simulations. Technical report, American Institute of Aeronautics and Astronautics, AIAA G-077-1998(2002), 2002.

[6] P. Aillaud, F. Duchaine, L.Y.M. Gicquel, and S. Didorally. Secondary peak in the nusselt number distribution of impinging jet flows: A phenomenological analysis. *Phys. Fluids*, 28:095110, 2016.

[7] P. Aillaud, L.Y.M. Gicquel, and F. Duchaine. Investigation of the concave curvature effect for an impinging jet flow. *Phys. Rev. Fluids*, 2:114608, 2017.

[8] Y.E. Akansu, M. Sarioglu, K. Kuvvet, and T. Yavuz. Flow field and heat transfer characteristics in an oblique slot jet impinging on a flat plate. *Int. Commun. Heat Mass Transf.*, 35:873 – 880, 2008.

[9] J. Altenbach and H. Altenbach. *Einführung in die Kontinuumsmechanik*. Teubner, 1994.

[10] R.J. Goldstein amd M.E. Franchett. Heat transfer from a flat surface to an oblique impinging jet. *J. Heat Transf.*, 110:84 – 90, 1988.

[11] J. Spurk an A. Nuri. *Strömungslehre: Einfürung in die Theorie der Strömungen*. Springer-Verlag Berlin Heidelberg New York, 2010.

[12] J.H. Bae and J.Y. Yoo. Direct numerical simulation of turbulent supercritical flows with heat transfer. *Phys. Fluids*, 17:105104, 2005.

[13] J.H. Bae, J.Y. Yoo, H. Choi, and D.M. McEligot. Influence of fluid-property variation on turbulent convective heat transfer in vertical annular channel flows. In *The* 11^{th} *International Topical Meeting on Nuclear Thermal-Hydraulics (NURETH-11), Popes' Palace Conference Center, Avignon, France, October 2-6*, 2005.

[14] J.H. Bae, J.Y. Yoo, H. Choi, and D.M. McEligot. Effects of large density variation on strongly heated internal air flows. *Phys. Fluids*, 18:075102, 2006.

[15] J.H. Bae, J.Y. Yoo, and D.M. McEligot. Direct numerical simulation of heated co_2 flows at supercritical pressure in a vertical annulus at re=8900. *Phys. Fluids*, 20:055108, 2008.

[16] D.T. Banuti. Crossing the widom-line - supercritical pseudo-boiling. *J. Supercrit. Fluid*, 98:12–16, 2015.

[17] D.T. Banuti, M. Raju, P.C. Ma, M. Ihme, and J.-P-Hickey. Seven questions about supercritical fluids - towards new fluid state diagram. *AIAA SciTech Forum.*, 2017.

[18] J. Bardina, J.H. Ferziger, and W.C. Reynolds. Improved turbulence models based on large eddy simulation of homogeneous, incompressible, turbulent flows. Technical report, NASA-NCC-2-15 Report No. TF-19, 1983.

[19] G.K. Batchelor. Diffusion in a field of homogeneous turbulence. *J. Sci. Res.*, 2:437 – 450, 1949.

[20] G.K. Batchelor. Small-scale variation of convected quantities like temperature in turbulent fluid. part 1. general discussion and the case of small conductivity. *J. Fluid Mech.*, 5:113 – 133, 1959.

[21] G.K. Batchelor. *An introduction to fluid dynamics*. Cambridge University Press, 2000.

[22] J.W. Baughn and S. Shimizu. Heat transfer measurements from a surface with uniform heat flux and an impinging jet. *J. Heat Transf.*, 111:1096 – 1098, 1989.

[23] F. Beaubert and S. Viazzo. Large eddy simulations of plane turbulent impinging jets at moderate reynolds numbers. *Int. J. Heat Fluid Flow*, 24:512 – 519, 2003.

[24] C. Béguier, I. Dekeyser, and B.E. Launder. Ratio of scalar and velocity dissipation time scales in shear flow turbulence. *Phys. Fluids*, 21:307 – 310, 1978.

[25] M. Behnia, S. Parneix, Y. Shabany, and P.A. Durbin. Numerical study of turbulent heat transfer in confined and unconfined impinging jets. *Int. J. Heat Fluid Flow*, 20:1–9, 1999.

[26] A. Bejan. Second law analysis in heat transfer. *energy*, 5:720 – 732, 1980.

[27] A. Bejan. *Entropy generation minimization: the method of thermodynamic optimization of finite-size systems and finite-time processes.* CRC Press: Boca Raton, FL, USA, 1 edition, 1995.

[28] A. Bejan. Method of entropy generation minimization, or modeling and optimization based on combined heat transfer and thermodynamics. *Rev. Gen. Therm.*, 35:637 – 646, 1996.

[29] L.H. Benedict and R.D. Gould. Towards better uncertainty estimates for turbulence statistics. *Exp. Fluids*, 22:129–136, 1996.

[30] J.P. Boris, F.F. Grinstein, E.S. Oran, and R.L. Kolbe. New insights into large eddy simulation. *Fluid Dyn. Res.*, 10:199 – 228, 1992.

[31] S.T. Bose, P. Moin, and D. You. Grid-independent large-eddy simulation using explicit filtering. *Phys. Fluids*, 22, 2010.

[32] J.-P. Bouchez and R.J. Goldstein. Impingement cooling from a circular jet in a cross flow. *Int. J. Heat Mass Transf.*, 18:719 – 730, 1975.

[33] M. Bovo and B. Rojo. Single pulse jet impingement on inclined surface, heat transfer and flow flied. In *Proceedings of the 11th International Conference on Engines & Vehicles, Napoli, Italy, 15–19 September*, 2013.

[34] L.A. Brignoni and S.V. Garimella. Effects of nozzle-inlet chamfering on pressure drop and heat transfer in confined air jet impingement. *Int. J. Heat Mass Transf.*, 43:1133 – 1139, 2000.

[35] A. Burcat and B. Ruscic. Third millennium ideal gas and condensed phase thermochemical database for combustion with updates from active thermochemical tables. Technical report, Report No. TAE 960, 2005.

[36] S. Candel, G. Herding, R. Syder, P. Scouflaire, C. Rolon, L. Vingert, M. Habiballah, F. Grisch, M. Péalat, P. Bouchardy, D. Stepowski, A. Cessou, and P. Colin. Experimental investigation of shear coaxial cryogenic jet flames. *J. Propul. Power*, 14:826 – 834, 1998.

[37] I. Celik, M. Klein, and J. Janicka. Assessment measures for engineering les applications. *J. Fluids Eng.*, 13:031102, 2009.

[38] I.B. Celik, Z.N. Cehreli, and I. Yavuz. Index of resolution quality for large eddy simulations. *J. Fluids Eng.*, 127:949 – 958, 2005.

[39] S. Chapman and T.G. Cowling. *The mathematical theory of non-uniform gases*. Cambridge, New York, 1 edition, 1939.

[40] B. Chehroudi. Recent experimental efforts on high-pressure supercritical injection for liquid rockets and their implications. *Int. J. Aerospace Eng.*, page 121802, 2012.

[41] B. Chehroudi, D. Talley, and A. Coy. Visual characteristics and initial growth rates of round cyogenic jets at subcritical and supercritical pressures. *Phys. Fluids*, 14(2):850, 2002.

[42] K. Choo, T.Y. Kang, and S.J. Kim. The effect of inclination on impinging jets at small nozzle-to-plate spacing. *Int. J. Heat Mass Transf.*, 18:3327 – 3334, 2012.

[43] A.J. Chorin. Numerical solution of the navier-stokes equations. *Math. Comput.*, 22:745 – 762, 1968.

[44] T.-H. Chung, M. Ajlan, L.L. Lee, and K.E. Starling. Generalized multiparameter correlation for nonpolar and polar fluid transport properties. *Ind. Eng. Chem. Fundamen.*, 27:671–679, 1988.

[45] Y.M. Chung and K.H. Luo. Unsteady heat transfer analysis of an impinging jet. *J. Heat Transf.*, 124:1039 – 1048, 2002.

[46] G.N. Coleman and R.D. Sandberg. A primer on direct numerical simulation of turbulence - methods, procedures and guidelines. Technical report, Technical Report AFM-09/01a, 2010.

[47] S. Corrsin. On the spectrum of isotropic temperature fluctuations in an isotropic turbulence. *J. Appl. Phys.*, 22:469 – 473, 1951.

[48] R. Courant, K. Friedrichs, and H. Lewy. Über die partiellen differenzengleichungen der mathematischen physik. *Math. Ann.*, 20:32 – 74, 1928.

[49] T. Cziesla, G. Biswas, H. Chattopadhyay, and N.K. Mitra. Large-eddy simulation of flow and heat transfer in an impinging slot jet. *Int. J. Heat Fluid Flow*, 22:500 – 508, 2001.

[50] T. Dairay, V. Fortuné, E. Lamballais, and L.-E. Brizzi. Direct numerical simulation of a turbulent jet impinging on a heated wall. *J. Fluid Mech.*, 764:362 – 394, 2015.

[51] B.J Daly and F.H. Harlow. Transport equations in turbulence. *Phys. Fluids*, 13:2634 – 2649, 1970.

[52] A. Datta. Effects of gravity on structure and entropy generation of confined laminar diffusion flames. *Int. J. Therm. Sci.*, pages 429 – 440, 2005.

[53] D.W. Davis and B. Chehroudi. Measurements in an acoustically driven coaxial jet under sub-, near-, and supercritical conditions. *J. Propul. Power*, 23:364 – 374, 2007.

[54] G. De Vahl Davis. Natural convection of air in a square cavity: A bench mark numerical solution. *Int. J. Numer. Meth. Fl.*, 3:249 – 264, 1983.

[55] Eugene de Villiers. *The Potential of Large Eddy Simulation for the Modeling of Wall Bounded Flows*. PhD thesis, Imperial College of Science, Technology and Medicine, University of London, 2006.

[56] J.W. Deardorff. A numerical study of three-dimensional turbulent channel flow at large reynolds numbers. *J. Fluid Mech.*, 41:453–480, 1970.

[57] A. Dewan, R. Dutta, and B. Srinivasan. Recent trends in computation of turbulent jet impingement heat transfer. *Heat transf. Eng.*, 33:447 – 460, 2012.

[58] M. Draksler, B. Končar, B. Cizelj, and B. Ničeno. Large eddy simulation of multiple impinging jets in hexagonal configuration - flow dynamics and heat transfer characteristics. *Int. J. Heat Mass Transf.*, 109:16 – 27, 2017.

[59] M. K. Drost and M. D. White. Numerical predictions of local entropy generation in an impinging jet. *J. Heat Transfer*, 113(4):823 – 829, 1991.

[60] R. Dutta, A. Dewan, and B. Srinivasan. Comparison of various integration to wall (itw) rans models for predicting turbulent slot jet impingement heat transfer. *Int. J. Heat Mass Transf.*, 65:750–764, 2013.

[61] T.M. Eidson. Numerical simulation of the turbulent rayleigh-bérnard problem using subgrid modelling. *J. Fluid Mech.*, 158:245 – 268, 1985.

[62] J. A. Esfahani and P. B. Shahabi. Effect of non-uniform heating on entropy generation for laminar developing pipe flow of a high prandtl number fluid. *Energ. Convers. Manage.*, pages 2087 – 2097, 2010.

[63] R. Farran and N. Chakraborty. A direct numerical simulation-based analysis of entropy generation in turbulent premixed flames. *Entropy*, 15:1540 – 1566, 2013.

[64] L.A. Gabour and J.H. Lienhard. Wall roughness effects on stagnation-point heat transfer beneath an impinging liquid jet. *J. Heat Transf.*, 116:81 – 87, 1994.

[65] E. Garnier, A. Nikolaus, and P. Sagaut. *Large Eddy Simulation for compressible Flows.* Springer-Verlag Berlin Heidelberg New York, 2009.

[66] L.F.G. Geers, K. Hanjalić, and M.J. Tummers. Wall imprint of turbulent structures and heat transfer in multiple impinging jet arrays. *J. Fluid Mech.*, 546:255 – 284, 2006.

[67] M. Germano. A dynamic subgrid-scale eddy viscosity model. *Phys. Fluids*, 3(7):1760–1765, 1991.

[68] B.J. Geurts and J. Fröhlich. A framework for predicting accuracy limitations in large-eddy simulation. *Phys. Fluids*, 14:L41, 2002.

[69] S. Ghadi, K. Esmailpour, S.M. Hosseinalipour, and A. Mujumdar. Experimental study of formation and development of coherent vortical structures in pulsed turbulent impinging jet. *Exp. Therm. Fluid Sci.*, 74:382 – 389, 2016.

[70] T. Ghisu, F. Cambuli, P. Puddu, N. Mandas, P. Seshadri, and G.T. Parks. Numerical evaluation of entropy generation in isolated airfoils and wells turbines. *Meccanica*, pages 1 – 20, 2018.

[71] S. Ghosal, T.S. Lund, P. Moin, and K. Akselvoll. A dynamic localization model for large-eddy simulation of turbulent flows. *J. Fluid Mech.*, 286:229–255, 2006.

[72] S. Ghosal and P. Moin. The basic equations for the large eddy simulation of turbulent flows in complex geometry. *J. Comput. Phys.*, 118:24 – 37, 1995.

[73] L.Y.M. Gicquel, G. Staffelbach, and T. Poinsot. Large eddy simulations of gaseous flames in gas turbine combustion chambers. *Prog. Energ. Combust.*, 38:782 –817, 2012.

[74] R. Gojon, C. Bogey, and O. Marsden. Large-eddy simulation of supersonic planar jets impinging on a flat plate at an angle of 60 to 90 degrees. In *Proceedings of the 21st AIAA/CEAS Aeroacoustics Conference, Dallas, TX, USA, 22–26 June*, 2015.

[75] P. Gousseau, B. Blocken, and G.J.F. van Heijst. Quality assessment of large-eddy simulation of wind flow around a high-rise building: Validation and solution verification. *Comput. Fluids*, 79:120–133, 2013.

[76] C. J. Greenshields. Openfoam programmer's guide version 3.0.1.

[77] C.J. Greenshields, H.G. Weller, L. Gasparini, and J.M. Reese. Implementation of semi-discrete, non-staggered central schemes in a colocated, polyhedral, finite volume framework, for high-speed viscous flows. *Int. J. Numer. Meth. Fl.*, 63:1 – 21, 2010.

[78] P. Grenson and H. Deniau. Large-eddy simulation of an impinging heated jet for a small nozzle-to-plate distance and high reynolds number. *Int. J. Heat Fluid Flow*, 68:348 – 363, 2017.

[79] G. Grötzbach. Spatial resolution requirements for direct numerical simulation of the rayleigh-bérnard convection. *J. Comput. Phys.*, 49:241 – 264, 1983.

[80] PROPATH GROUP. Propath ver.13.1: A program package for thermophyical properties of fluids.

[81] P. Gulati, V. Katti, and S.V. Prabhu. Influence of the shape of the nozzle on local heat transfer distribution between smooth flat surface and impinging air jet. *Int. J. Therm. Sci.*, 48:602 – 617, 2009.

[82] M. Habiballah, M. Orain, F. Grisch, L. Vingert, and P. Gicquel. Experimental studies of high-pressure cryogenic flames on the mascotte facility. *Combust. Sci. Technol.*, 178:101 – 128, 2006.

[83] M. Hadžiabdić and K. Hanjalić. Vortical structures and heat transfer in a round impinging jet. *J. Fluid Mech.*, 596:221–260, 2008.

[84] H. Hattori and Y. Nagano. Direct numerical simulation of turbulent heat transfer in plane impinging jet. *Int. J. Heat Fluid Flow*, 25:749 – 758, 2004.

[85] H. Herwig and F. Kock. Local entropy production in turbulent shear flows: A tool for evaluating heat transfer performance. *J. Therm. Sci.*, 15:2205–2215, 2006.

[86] C. Hirsch. *Numerical Computation of Internal & External Flows: Fundamentals of Computational Fluid Dynamics*. John Wiley & Sons, 2 edition, 2007.

[87] J.O. Hirschfelder, C.F. Curtiss, and R.B. Bird. *Molecular theory of gases and liquids*. Wiley, New York, 1 edition, 1954.

[88] J. Holmen, T.J.R. Hughes, A.A. Oberai, and G.N. Wells. Sensitivity of scale partition for variational multiscale large-eddy simulation of channel flow. *Phys. Fluids*, 16(3):824–827, 2004.

[89] P. Hrycak. Heat transfer from round impinging jets to a flat plate. *Int. J. Heat Mass Transf.*, 26:1857 – 1865, 1983.

[90] Ying Huai. *Large eddy simulation in the scalar field*. PhD thesis, Technische Universität Darmstadt, 2006.

[91] S. Huang and Q.S. Li. A new dynamic one-equation subgrid-scale model for large eddy simulations. *Int. J. Numer. Meth. Eng.*, 81:835–865, 2009.

[92] H. Huo and V. Yang. Large-eddy simulation of supercritical combustion: model validation against gaseous h2o2 injector. *J. Propul. Power*, 33:1 – 13, 2017.

[93] K. Hutter. *Fluid- und Thermodynamik*. Springer-Verlag Berlin Heidelberg New York, 2 edition, 2003.

[94] M. Inagaki, T. Knodoh, and Y. Nagano. A mixed-time-scale sgs model with fixed model-parameters for practical les. *J. Fluids Eng.*, 27:13, 2005.

[95] F.P. Incropera and D.P. DeWitt. *Fundamentals of heat and mass transfer*. Wiley New York, 6 edition, 2007.

[96] R.I. Issa. Solution of the implicitly discretised fluid flow equations by operator-splitting. *J. Comput. Phys.*, 62:40 – 65, 1985.

[97] F.A. Jaberi and P.J. Colucci. Large eddy simulation of heat and mass transport in turbulent flows. part 2: scalar field. *Int. J. Heat Mass Tran.*, 46:1827 – 1840, 2003.

[98] K. Jambunathan, E. Lai, M.A. Moss, and B.L. Button. A review of heat transfer data for single circular jet impingement. *Int. J. Heat Fluid Flow*, 13:106–115, 1992.

[99] J. Janicka and A. Sadiki. Large eddy simulation of turbulent combustion systems. *P. Combust. Inst.*, 30:537 – 547, 2005.

[100] J.E. Jaramillo, F.X. Trias, A. Gorobets, C.D. Pérez-Segarra, and A. Oliva. Dns and rans modelling of a turbulent plane impinging jet. *Int. J. Heat Mass Transf.*, 55:789–801, 2012.

[101] Hrvoje Jasak. *Error Analysis and Estimation for the Finite Volume Method with Applications to Fluid Flows*. PhD thesis, Imperial College of Science, Technology and Medicine, University of London, 1996.

[102] R.J. Jefferson-Loveday and P.G. Tucker. Les of impingement heat transfer on a concave surface. *Numer. Heat Transf. Part A Appl.*, 58:247 – 271, 2010.

[103] Y. Ji, H.-C. Zhang, X. Yang, and L. Shi. Entropy generation analysis and performance evaluation of turbulent forced convective heat transfer to nanofluids. *entropy*, 19:108, 2017.

[104] D. Jou, J. Casas-Vázquez, and G. Lebon. *Extended irreversible thermodynamics*. Springer-Verlag Berlin Heidelberg New York, 2 edition, 1996.

[105] M. Juniper, A. Tripathi, P. Scouflaire, J.-C. Rolon, and S. Candel. Structure of cryogenic flames at elevated pressures. *P. Combust. inst.*, 28:1103 – 1109, 2000.

[106] K. K. Kiełczewski and E. Tuliszka-Sznitko. Numerical study of the flow structure and heat transfer in rotating cavity with and without jet. *Arch. Mech.*, 65:527 – 548, 2013.

[107] T. Kajishima and T. Nomachi. One-equation subgrid scale model using dynamic procedure for the energy production. *J. Appl. Mech.*, 73:368–373, 2006.

[108] V. Katti and S.V. Prahub. Experimental study and theoretical analysis of local heat transfer distribution between smooth flat surface and impinging air jet from a circular straight pipe nozzle. *Int. J. Heat Mass Transf.*, 51:4480 – 4495, 2008.

[109] H. Kawamura, H. Abe, and Y. Matsuo. Dns of turbulent heat transfer in channel flow with respect to reynolds and prandtl number effects. *Int. J. Heat Fluid Flow*, 20(3):196 – 207, 1999.

[110] J.G. Keenan. Availability and irreversibility in thermodynamics. *Brit. J. Appl. Phys.*, 2:183 – 192, 1951.

[111] K.-S. Kim. An experimental study on the flow and heat transfer characteristics of an impinging jet. *KSME J.*, 7:258 – 271, 1993.

[112] T. Kim, Y. Kim, and S.K. Kim. Numerical study of cryogenic liquid nitrogen jets at supercritical pressures. *J. Supercrit. Fluids*, 56:152 – 163, 2011.

[113] M. Klein. *Towards LES as an engineering tool*. habilitation, Technische Universität Darmstadt, 2008.

[114] M. Klein, A. Sadiki, and J. Janicka. A digital filter based generation of inflow data for spatially developing direct numerical or large eddy simulations. *J. Comput. Phys.*, 186:652 – 665, 2003.

[115] Ž. Knez, E. Markočič, M. Leitgelb, M. Primožič, M. Knez Hrnčič, and M. Škerget. Industrial applications of supercritical fluids: a review. *Energy*, 77:235–243, 2014.

[116] F. Kock and H. Herwig. Local entropy production in turbulent shear flows: A high-reynolds number model with wall functions. *Int. J. Heat Mass Transf.*, 47:2205–2215, 2004.

[117] T. Koide, K. Tsujimoto, T. Shakouchi, and T. Ando. Dns analysis of multiple impinging jets. *J. Fluid Sci. Technol.*, 9:JFST0027, 2014.

[118] W. Kollmann. *Fluid Mechanics in Spatial and Material Description*. University Readers, 1 edition, 2010.

[119] A. Kolmogorov. Dissipation of energy in locally isotropic turbulence. *Doklady Akademiia Nauk SSSR*, 32:16, 1941.

[120] A. Kolmogorov. The local structure of turbulence in incompressible viscous fluid for very large reynolds' numbers. *Doklady Akademiia Nauk SSSR*, 30:301 – 305, 1941.

[121] E. Komen, A. Shams, L. Camilo, and B. Koren. Quasi-dns capabilities of openfoam for different mesh types. *Comput. Fluids*, 96:87 – 104, 2014.

[122] M. D. Koretsky. *Engineering and chemical thermodynamics*. John Wiley & Sons, Inc, 2004.

[123] S. Kumar, M.K. Chauhan, and Varun. Numerical modeling of compression ignition engine: a review. *Renew. Sust. Energ. Rev.*, 19:517 – 530, 2013.

[124] G. Künne. *Large Eddy Simulation of Premixed Combustion Using Artificial Flame Thickening Coupled with Tabulated Chemistry*. PhD thesis, Technische Universität Darmstadt, 2012.

[125] J.D. Lambert. *Numerical Methods for Ordinary Differential Systems: The Initial Value Problem*. John Wiley & Sons, Inc. Hoboken, USA, 1 edition, 1992.

[126] P.E. Lapenna. Characterization of pseudo-boiling in a transcritical nitrogen jet. *Phys. Fluids*, 30:077106, 2018.

[127] P.E. Lapenna and F. Creta. Mixing under transcritical conditions: an a-priori study using direct numerical simulation. *J. Supercrit. Fluids*, 128:263 – 278, 2017.

[128] B.E. Launder and B.I Sharma. Application of the energy-dissipation model of turbulence to the calculation of flow near a spinning disc. *Lett. Heat Mass Trans.*, 1(2):131 – 138, 1974.

[129] J. Lee and S.-J. Lee. The effect of nozzle configuration on stagnation region heat transfer enhancement of axisymmetric jet impingement. *Int. J. Heat Mass Transf.*, 43:3497 – 3509, 2000.

[130] D.H. Lenschow, J. Mann, and L. Kristensen. How long is long enough when measuring fluxes and other turbulence statistics? *J. Atmos. Ocean Tech.*, 11:661 – 673, 1994.

[131] A. Leonard. Energy cascade in large-eddy simulations of turbulent fluid flows. *Adv. Geophys.*, 18:129–136, 1975.

[132] D.K. Lilly. The representation of small-scale turbulence in numerical simulation experiments. *Proceedings of IBM Scientific Computing Symposium on Environmental Sciences*, 62:195 – 210, 1967.

[133] D.K. Lilly. A proposed modification of the germano subgrid-scale closure method. *Phys. Fluids*, 4(3):633–635, 1992.

[134] P.J. Linstrom and W.G. Mallard. Number 69. 2016.

[135] K. Liu, Y. Wu, M.A. McHugh, H. Baled, R.M. Enick, and B.D. Morreale. Equation of state modeling of high-pressure, high-temperature hydrocarbon density data. *J. Supercrit. Fluid*, 55:701–711, 2010.

[136] G. Lodato, L. Vervisch, and P. Domingo. A compressible wall-adapting similarity mixed model for large-eddy simulation of the impinging round jet. *Phys. Fluids*, 21:035102, 2009.

[137] D. Lüdecke and C. Lüdecke. *Thermodynamik: Physikalische-chemische Grundlagen der thermischen Verfahrenstechnik*. Springer Berlin Heidelberg, 2012.

[138] M. M. Klein. An attempt to assess the quality of large eddy simulations in the context of implicit filtering. *Flow Turbul. Combust.*, 75:131–147, 2005.

[139] R. Manceau, R. Perrin, M. Hadžiabdić, and S. Benhamadouche. Investigation of the interaction of a turbulent impinging jet and a heated, rotating disk. *Phys. Fluids*, 26:035102, 2014.

[140] R. Mari, B. Cuenot, F. Duchaine, and L. Selle. Stabilization mechanisms of a supercritical hydrogen/oxygen flame. In *Center of Turbulence Research, Proceedings of the summer Programm*, 2012.

[141] H. Martin. Heat and mass transfer between impinging gas jets and solid surfaces. *Adv. Heat Transf.*, 13:1–60, 1997.

[142] J.J. Martin. Cubic equations of state - which? *Ind. Eng. Chem. Fundamen.*, 18:81–97, 1979.

[143] G. T. Mase and G. E. Mase. *Continuum mechanics for engineers.* CRC Press LLC, 2 edition, 1999.

[144] J. Matheis, H. Müller, C. Lenz, M. Pfitzner, and S. Hickel. Volume translation methhods for real-gas computational fluid dynamics. *J. Supercrit. Fluid*, 107:422–432, 2016.

[145] P.M. Mathias, T. Naheiri, and E.M. Oh. A density correction for the peng-robinson equation of state. *Fluid Phase Equilibr.*, 47:77 – 87, 1989.

[146] W. Mayer, A. Schik, M. Schäffler, and H. Tamura. Injection and mixing processes in high-pressure liquid oxygen/gaseous hydrogen rocket combustors. *J. Propul. Power*, 16:823 – 828, 2000.

[147] W. Mayer, A. Schik, B. Vielle, C. Chauveau, I. Gökalp, D.G. Talley, and R.D. Woodward. Atomization and breakup of cryogenic propellants under high-pressure subcritical and supercritical conditions. *J. Propul. Power*, 14:835 – 842, 1998.

[148] W. Mayer and H. Tamura. Propellant injection in a liquid oxygen/gaseous hydrogen rocket engine. *J. Propul. Power*, 12:1137 – 1147., 1996.

[149] W. Mayer, J. Telaar, R. Branam, G. Schneider, and J. Hussong. Raman measurements of cryogenic injection at supercritical pressure. *Heat and Mass Transfer*, 39:709–719, 2003.

[150] H.C. Meena, S.A. Reodikar, R. Vinze, and S.V. Prabhu. Influence of the shape of the orifice on the local heat transfer distribution between smooth flat surface and impinging incompressible air jet. *Exp. Therm. Fluid Sci.*, 70:292 – 306, 2016.

[151] S. Menon, P.-K-Yeung, and W.-W. Kim. Effect of subgrid models on the computed interscale energy transfer in isotropic turbulence. *Comput. Fluids*, 25:165 – 180, 1996.

[152] E. Messerschmid and S. Fasoulas. *Raumfahrtsysteme.* Springer-Verlag Berlin Heidelberg, 4 edition, 2011.

[153] J. Meyers. Error-landscape assessment of large-eddy simulations: a review of the methodology. *J. Sci. Comput.*, 49:65 – 77, 2010.

[154] J. Meyers, B. Geurts, and M. Baelmans. Database analysis of errors in large-eddy simulation. *Phys. Fluids*, 15(9):2740–2755, 2003.

[155] J. Meyers and P. Sagaut. Evaluation of smagorinsky variants in large-eddy simulations of wall-resolved plane channel flows. *Phys. Fluids*, 19, 2007.

[156] M. Mohensi and M. Bazargan. Entropy generation in turbulent mixed convection heat transfer to highly variable property pipe flow of supercritical fluids. *Energ. Convers. Manage.*, 87:552 – 558, 2014.

[157] P. Moin. Advances in large eddy simulation methodology for complex flows. *Int. J. Heat Fluid Fl.*, 23:710 –720, 2002.

[158] P. Moin, K. Squires, W. Cabot, and S. Lee. A dynamic subgrid-scale model for compressible turbulence and scalar transport. *Phys. Fluids*, 3:2746 – 2757, 1991.

[159] M. Molana and S. Banooni. Investigation of heat transfer processes involved liquid impingement jets: A review. *Braz. J. Chem. Eng.*, pages 413 – 435, 2012.

[160] H. Müller, C.A. Niedermeier, J. Matheis, M. Pfitzner, and S. Hickel. Large-eddy simulation of nitrogen injection at trans- and supercritical conditions. *Phys. Fluids*, 28:015102, 2015.

[161] I. Müller. *Thermodynamik: Die Grundlagen der Materialtheorie.* Bertelsmann Universitätsverlag, 1 edition, 1972.

[162] T. Natarajan, J.W. Jewkes, A.D. Lucey, R. Narayanaswamy, and Y.M. Chung. Large-eddy simulations of a turbulent jet impinging on a vibrating heated wall. *Int. J. Heat Fluid Flow*, 65:277 – 298, 2017.

[163] F. Nicoud and F. Ducros. Subgrid-scale stress modelling based on the square of the velocity gradient tensor. *Flow Turbul. Combust.*, 62:183 – 200, 1999.

[164] F. Nicoud, H. Baya Toda, O. Cabrit, S. Bose, and J. Lee. Using singular values to build a subrid-scale model for large eddy simulations. *Phys. Fluids*, 23:085106, 2011.

[165] M.A. Niederschulte, R.J. Adrian, and T.J. Hanratty. Measurements of turbulent flow in a channel at low reynolds numbers. *Exp. Fluids*, 9:222 – 230, 1990.

[166] W.L. Oberkampf and C.J. Roy. *Verification and Validation in Scientific Computing*. Cambridge University Press, New York, 1 edition, 2010.

[167] W.L. Oberkampf and T.G. Trucano. Verification and validation benchmarks. Technical report, Sandia Report SAND2007-0853, Sandia National Laboratories, 2007.

[168] A.M. Obukhov. Structure of the temperature field in turbulent flow. Technical report, DTIC Document, 1968.

[169] T.S. O'Donovan and D.B. Murray. Fluctuating fluid flow and heat transfer of an obliquely impinging air jet. *Int. J. Heat Mass Transf.*, 51:6169 – 6179, 2008.

[170] J. Oefelein. Mixing and combustion of cryogenic oxygen-hydrogen shear-coaxial jet flames at supercritical pressure. *Combust. Sci. and Tech.*, 178:229 – 252, 2006.

[171] N.A. Okong'o and J. Bellan. Direct numerical simulations of transitional supercritical binary mixing layers: heptane and nitrogen. *Int. J. Fluid Mech.*, 464:1 – 34, 2002.

[172] M. Olsson and L. Fuchs. Large eddy simulations of a forced semiconfined circular impinging jet. *Phys. Fluids*, 10:476, 1998.

[173] M. Oschwald and A. Schik. Supercritical nitrogen free jet investigated by spontaneous raman scattering. *Exp. Fluids*, 27:497–506, 1999.

[174] M. Oschwald, A. Schik, M. Klar, and W. Mayer. Investigation of coaxial ln2-gh2-injection at supercritical pressure by spontaneous raman scattering. In 35^{th} *AIAA/ASME/SAE/ASEE Joint Propulsion Conference and Exhibit: AIAA paper 99-2887*, 1999.

[175] M. Oschwald, J.J. Smith, R. Branam, J. Hussong, A. Schik, B. Chehroudi, and D. Talley. Injection of fluids into supercritical environments. *Combust. Sci. Technol.*, 178:49 – 100, 2006.

[176] I. Otic. One equation subgrid model for liquid metal forced convection. In *The* 8^{th} *International Topical Meeting on Nuclear Reactor Thermal-Hydraulics (NUTHOS-8), Operation and Safety, Shanghai, China, October 10-14*, 2010.

[177] H.F. Oztop and K. Al-Salem. A review on entropy generation in natural and mixed convection heat transfer for energy systems. *Renew. Sust. Energ. Rev.*, 16:911 – 920, 2011.

[178] N.R. Panchapakesan and J.L. Lumley. Turbulence measurements in axisymmteric jets of air and helium. part 2. helium jet. *J. Fluid Mech.*, 246:225–247, 1993.

[179] P. Pantangi, Y. Huai, and A. Sadiki. Mixing Analysis and Optimization in Jet Mixer Systems by Means of Large Eddy Simulation. *In:Micro and Macro Mixing - Analysis, Simulation and Numerical Calculation, Editors: H. Bockhorn, D. Mewes, W. Peukert, H.-J. Warnecke. Springer-Verlag Berlin Heidelberg*, pages 205 –226, 2010.

[180] S. Patankar and D. Spalding. A calculation procedure for heat, mass and momentum transfer in three-dimensional parabolic flows. *Int. J. Heat Mass Tran.*, 15:1787 – 1806, 1972.

[181] S.V. Patankar. *Numerical heat transfer and fluid flow*. Hemisphere Publishing Corporation, 1 edition, 1980.

[182] A. Péneloux, E. Rauzy, and R. Fréze. A consisten correction for redlich-kwong-soave volumes. *Fluid Phase Equilibr.*, 8:7–23, 1982.

[183] D.Y. Peng and D.P. Robinson. A new two-constant equation of state. *Ind. Eng. Chem. Fundamen.*, 15:59 – 64, 1976.

[184] S.H. Peng and L. Davidson. On a subgrid-scale heat flux model for large eddy simulation of turbulent thermal flow. *Int. J. Heat Mass Tran.*, 45:1393 – 1405, 2002.

[185] X. Petit, G. Ribert, G. Lartigue, and P. Domingo. Large-eddy simulation of supercritical fluid injection. *J. Supercrit. Fluids*, 84:61 – 73, 2013.

[186] T. Poinsot and D. Veynante. *Theoretical and Numerical Combustion.* by the authors, 3 edition, 2017.

[187] B. E. Poling, J. M. Prausnitz, and J.P. O'Connell. *The properties of gases and liquids.* The McGraw-Hill Companies, Inc, 5 edition, 2001.

[188] S.B. Pope. Ten questions concerning the large-eddy simulation of turbulent flows. *New J. Phys.*, 6(35), 2004.

[189] S.B. Pope. *Turbulent Flows.* Cambridge University Press, 2009.

[190] M. Popovac and K. Hanjalić. Large-eddy simulations of flow over a jet-impinged wall-mounted cube in cross stream. *Int. J. Heat Fluid Flow*, 28:1360 – 1378, 2007.

[191] P. Rauwoens, K. Nerinckx, J. Vierendeels, and B. Merci. Stability of pressure-correction algorithms for low-speed reacting and non-reacting flow simulations. In *Proceedings of the Fourth International Conference on Computational Fluid Dynamics, ICCFD4, Ghent, Belgium, 10-14 July*, 2006.

[192] O. Redlich and J.N.S. Kwong. On the thermodynamics of solutions. v. an equation of state. fugacities of gaseous solutions. *Chem. Rev.*, 44:233 – 244, 1949.

[193] D. Reichenberg. *The viscosities of gas mixtures at moderate pressures.* NPL Rept. Chem. 29, National Physical Laboratory, Teddington, England, 1974.

[194] L.F. Richardson. *Weather Predictions by Numerical Process.* Cambridge University Press, 2 edition, 1922.

[195] F. Ries, J. Janicka, and A. Sadiki. Thermal transport and entropy production mechanisms in a turbulent round jet at supercritical thermodynamic conditions. *Entropy*, 19:404, 2017.

[196] F. Ries, Y. Li, D. Klingenberg, K. Nishad, J. Janicka, and A. Sadiki. Near-wall thermal processes in an inclined impinging jet: Analysis of heat transport and entropy generation mechanisms. *energies*, 11(6):1354, 2018.

[197] P.L. Roe. Characteristic-based schemes for the euler equations. *Annu. Rev. Fluid Mech.*, 18:337 – 365, 1987.

[198] S. Roux, M. Fénot, G. Lalizel, L.-E. Brizzi, and E. Dorignac. Evidence of flow vortex signatures on wall fluctuating temperature using unsteady infrared thermography for an acoustically forced impinging jet. *J. Heat Mass Transf.*, 50:38 – 50, 2014.

[199] S. Roux, M. Fénot, G. Lalizel, L.E. Brizzi, and E. Dorignac. Experimental investigation of the flow and heat transfer of an impinging jet under acoustic excitation. *Int. J. Heat Mass Transf.*, 54:3277 – 3290, 2011.

[200] A. Ruiz, G. Lacaze, J. Oefeleing, R. Mari, B. Cuenot, L. Selle, and T. Poinsot. Numerical benchmark for high-reynolds-number supercritical flows with large density gradients. *AIAA Journal*, 54:1445 – 1460, 2016.

[201] D. Rundström and B. Moshfegh. Large-eddy simulation of an impinging jet in cross-flow on a heated wall-mounted cube. *Int. J. Heat Mass Transf.*, 52:921 – 931, 2009.

[202] M. Safari, F. Hadi, and M. Reza H. Sheikhi. Progress in the prediction of entropy generation in turbulent reacting flows using large eddy simulation. *entropy*, pages 5159 – 5177, 2014.

[203] P. Sagaut. *Large Eddy Simulation for incompressible Flows: An Introduction*. Springer-Verlag Berlin Heidelberg New York, 2006.

[204] A. Z. Sahin and R. Ben-Mansour. Entropy generation in laminar fluid flow through circular pipe. *Entropy*, 5:404 – 416, 2003.

[205] K. Salari and P. Knupp. Code verification by the method of manufactured solutions. Technical report, Sandia Report SAND2000-1444, Sandia National Laboratories, 2000.

[206] K.M. Saqr, A.I. Shehata, A.A. Taha, and M.A. ElAzm. Cfd modelling of entropy generation in turbulent pipe flow: Effects of temperature difference and swirl intensity. *Appl. Therm. Eeng.*, pages 999 – 1006, 2016.

[207] S. Satake and T. Kunugi. Direct numerical simulation of an impinging jet into parallel disks. *Int. J. Numer. Method Heat Fluid Flow*, 8:768 – 780, 1998.

[208] M. Schäfer. *Computational Engineering - Introduction to Numerical Methods*. Springer-Verlag Berlin Heidelberg, 1 edition, 2006.

[209] B. Schmandt and H. Herwig. Diffusor and nozzle design optimization by entropy generation minimization. *entropy*, 13:1380 – 1402, 2011.

[210] H. Schmidt and U. Schumann. Coherent structure of the convective boundary layer derived from large-eddy simulations. *J. Fluid Mech.*, 200:511 – 562, 1989.

[211] T. Schmitt, L. Selle, A. Ruiz, and B. Cuenot. Large-eddy simulation of supercritical pressure round jets. *AIAA Journal*, 48:2133 – 2144, 2010.

[212] U. Schumann. The counter gradient heat flux in turbulent stratified flows. *Nucl. Eng. Des.*, 100:255–262, 1986.

[213] A. Sciacovelli, V. Verda, and E. Sciubba. Entropy generation analysis as a desing tool - a review. *Renew. Sust. Energ. Rev.*, 43:1167 – 1181, 2015.

[214] A.M. Shehata and D.M. McEligot. Mean strucure in viscous layer of strongly-heated internal gas flows. measurements. *Int. J. Heat Mass Tran.*, 41:4297 – 4313, 1998.

[215] S.Z. Shuja, B.S. Yibas, and M.O. Budair. Local entropy generation in an impinging jet: minimum entropy concept evaluating various turbulence models. *Comput. Method. Appl. M.*, 190:3623 – 3644, 2001.

[216] L. Shunn and F. Ham. Method of manufactured solutions applied tp variable density flow solvers. Technical report, Annual Research Briefs. Center for Turbulence Research, Stanford University, 2007.

[217] J. Sierra-Pallares, J. García del Valle, P. García-Carrascal, and F.C. Ruiz. Numerical study of supercritical and transcritical injection using different prandtl numbers: a second law analysis. *J. Supercrit. Fluids*, 115:86 – 98, 2016.

[218] G. Singla, P. Scouflaire, J.C. Rolon, and S. Candel. Transcritical oxygen/transcritical or supercritical methane combustion. *P. Combust. inst.*, 30:2921 – 2928, 2005.

[219] G. Singla, P. Scouflaire, J.C. Rolon, and S. Candel. Flame stabilization in high pressure lo_x/gh_2 and gch_4 combustion. *P. Combust. inst.*, 31:2215 – 2222, 2007.

[220] J. Smagorinsky. General circulation experiments with primitive equations. *Mon. Weather Rev.*, 91(35):99–164, 1963.

[221] G. Soave. Equilibrium constants from a modified redlich-kwong equation of state. *Chem. Eng. Sci.*, 27:1197 – 1203, 1972.

[222] S.K. Som and A. Datta. Thermodynamic irreversibilities and exergy balance in combustion processes. *Prog. Energ. Combust.*, 34:351 – 376, 2008.

[223] D. B. Spalding. A single formula for the "law of the wall". *J. Appl. Mech.*, 28:455 – 458, 1961.

[224] S. Tavoularis and S. Corrsin. Experiments in nearly homogenous turbulent shear flow with a uniform mean temperature gradient. part 1. *J. Fluid Mech.*, 104:311–347, 1981.

[225] G.I. Taylor and A.E. Green. Mechanism of the production of small eddies from large ones. *Proc. R. Soc. A Math. Phys.*, 151:499 – 521, 1937.

[226] H. Tennekes and J.L. Lumley. *A First Course in Turbulence*. The Massachusetty Institute of Technology, 1999.

[227] N. Tramecourt, S. Menon, and J. Amaya. Les of supercritical combustion in a gas turbine engine. In 40^{th} *AIAA/ASME/SAE/ASEE Joint Propulsion Conference and Exhibit: Joint Propulsion Confereces*, 2004.

[228] X.T. Trinh, M. Fénot, and E. Dorignac. The effect of nozzle geometry on local convective heat transfer to unconfined impinging air jets. *Exp. Therm. Fluid Sci.*, 70:1 – 16, 2016.

[229] C. Tropea, A.L. Yarin, and J.F. Foss. *Handbook of Experimental Fluid Mechanics*. Springer, 2007.

[230] K. Tsujimoto, T. Ishikura, T. Shakouchi, and T. Ando. Direct numerical simulation of active-controlled impinging jets. *J. Fluid Sci. Technol.*, 4:279 – 291, 2009.

[231] N. Uddin, A.O. Neumann, and B. Weigand. Les simulations of an impinging jet: On the origin of the second peak in the nusselt number distribution. *Int. J. Heat Mass Transf.*, 57:356 – 368, 2013.

[232] J.D. van der Waals. *Over de continuiteit van den gas- en vloeistoftoestand*. PhD thesis, University of Leiden, netherlands, 1873.

[233] E.R. van Driest. On turbulent flow near a wall. *J. Aeronaut. Sci.*, 23(11):1007–1011, 1956.

[234] W.M. van Rees, A. Leonard, D.I. Pullin, and P. Koumoutsakos. A comparison of vortex and pseudo-spectral methods for the simulation of periodic vortical flows at high reynolds numbers. *J. Comput. Phys.*, 230:2794 – 2805, 2011.

[235] R. Vinze, S.M. Chandel, M.D. Lomaye, and S.V. Prabhu. Influence of jet temperature and nozzle shape on the heat transfer distribution between a smooth plate and impinging air jets. *Int. J. Therm. Sci.*, 99:136 – 151, 2016.

[236] R. Viskanta. Heat transfer to impinging isothermal gas and flame jets. *Exp. Therm. Fluid Sci.*, 6:106–115, 1993.

[237] P.R. Voke and S. Gao. Numerical study of heat transfer from an impinging jet. *Int. J. Heat Mass Transf.*, 41:671 – 680, 1998.

[238] A.W. Vreman. An eddy-viscosity subgrid-scale model for turbulent shear flow: algebraic theory and applications. *Phys. Fluids*, 16:3670 – 3681, 2004.

[239] B. Vreman, B.J. Geurts, and H. Kuerten. Comparison of numerical schemes in large-eddy simulation of the the temporal mixing layer. *Int. J. Numer. Meth. Fl.*, 22:297–311, 1996.

[240] V. Vuorinen, J.-P. Keskinen, C. Duwig, and B.J. Boersma. On the implementation of low-dissipative runge-kutta projection methods for time dependent flows using openfoam. *Comput. Fluids*, 93:153 – 163, 2014.

[241] B.-C. Wang, E. Yee, J. Yin, and D.J. Bergstrom. A general dynamic linear tensor-diffusivity subgrid-scale heat flux model for large-eddy simulation of turbulent thermal flows. *Numer. Heat Tr. B-Fund.*, 51:205–227, 2006.

[242] B.-C. Wang, E. Yee, J. Yin, and D.J. Bergstrom. New dynamic subgrid-scale heat flux models for large-eddy simulation of thermal convection based on the general gradient diffusion hypothesis. *J. Fluid Mech.*, 604:125–163, 2008.

[243] B.-C. Wang, J. Yin, E. Yee, and D.J. Bergstrom. A complete and irreducible dynamic sgs heat-flux modelling based on the strain rate tensor for large-eddy simulation of thermal convection. *Int. J. Heat Fluid Fl.*, 28:1227–1243, 2007.

[244] W. Wang, Y. Zhang, J. Liu, B. Li, and B. Sundén. Entropy generation analysis of fully-developed turbulent heat transfer flow in inward helically corrugated tubes. *Numer. Heat Tr. A-Appl*, 73:788 – 805, 2018.

[245] Z. Wang, P. He, Y. Lv, J. Zhou, J. Fan, and K. Cen. Direct numerical simulation of subsonic round turbulent jet. *Flow, Turbul. Combust.*, 84(4):669–686, 2010.

[246] B. Weigand and S. Spring. Multiple jet impingement - a review. *Heat transf. Res.*, 42:101 – 142, 2011.

[247] R. Wilke and J. Sesterhenn. Statistics of fully turbulent impinging jets. *J. Fluid Mech.*, 825:795 – 824, 2017.

[248] J.H. Williamson. Low-storage runge-kutta schemes. *J. Comput. Phys.*, 35:48 – 56, 1980.

[249] V.C. Wong and D.K. Lilly. A comparison of two dynamic subgrid closure methods for turbulent thermal convection. *Phys. Fluids*, 6:1016 – 1023, 1995.

[250] I. Wygnanski and H. Fiedler. Some measurements in the self-preserving jet. *J. Fluid Mech.*, 38(3):577–612, 1969.

[251] X. Yan and N. Saniei. Heat transfer from an obliquely impinging circular air jet to a flat plate. *Int. J. Heat Fluid Flow*, 18:591 – 599, 1997.

[252] H. Yapici, N. Kayataş, B. Albayrak, and G. Baştürk. Numerical calculation of local entropy generation in a methane-air burner. *Energ. Convers. Manage.*, pages 1885 – 1919, 2005.

[253] Z. Ying, L. Guiping, B. Xueqin, B. Lizhan, and W. Dongsheng. Experimental study of curvature effects on jet impingement heat transfer on concave surfaces. *Chin. J. Aeronaut.*, 30:586 – 594, 2017.

[254] A. Yoshizawa and K. Horiuti. A statistically-derived subgrid-scale kinetic energy model for the large-eddy simulation of turbulent flows. *J. Phys. Soc. Jpn.*, 54(8):2834–2839, 1985.

[255] B. A. Younis, C. G. Speziale, and T.T. Clark. A rational model for the turbulent scalar fluxes. *P. Roy. Soc. A-Math. Phy.*, 461:575 – 594, 2005.

[256] T.A. Zhang, R.B. Dahlburg, and J.P. Dahlburg. Direct and large-eddy simulations of three-dimensional compressible navier-stokes turbulence. *Phys. Fluids*, 4:127 – 140, 1992.

[257] N. Zuckerman and N. Lior. Impingement heat transfer: correlations, and numerical modeling. *J. Heat Transf.*, 127:544–552, 2005.

[258] N. Zuckerman and N. Lior. Jet impingement heat transfer: Physics, correlations, and numerical modeling. *Adv. Heat Transf.*, 39:565–631, 2006.